MODES OF CONTINENTAL DEFORMATION: STUDIES OF FOREDEEP BASINS, CONTINENTAL HOT SPOTS AND INTRACRATONIC BASINS

by

PAULA JEAN WASCHBUSCH

B.S. Drake University (1989)

Submitted to the Department of
Earth, Atmospheric, and Planetary Sciences
in partial fulfillment of the requirements for the degree of

DOCTOR OF PHILOSOPHY

at the

MASSACHUSETTS INSTITUTE OF TECHNOLOGY

September, 1994

Signature of Author _____
Department of Earth, Atmospheric, and Planetary Sciences
August 1994

Certified by _____
Leigh Royden
Thesis Supervisor

Certified by _____
Marcia McNutt
Thesis Co-Supervisor

Accepted by _____
Thomas H. Jordan
Department Head

MODES OF CONTINENTAL DEFORMATION: STUDIES OF FOREDEEP BASINS, CONTINENTAL HOT SPOTS AND INTRACRATONIC BASINS

PAULA J. WASCHBUSCH

Submitted to the Department of Earth, Atmospheric and Planetary Sciences in partial fulfillment of the requirements for the degree of Doctor of Philosophy

ABSTRACT

Surface manifestations of continental deformation processes can be used to infer properties of the underlying continental lithosphere, especially when compared to similar processes and their surface manifestation in the oceans. This thesis contains three studies investigating the properties of continental lithosphere and how those properties affect the observed geology. Each study was motivated by geologic observations that did not conform with the simple models developed in marine settings. By investigating why the models fail and how continental lithosphere must be different from oceanic lithosphere we can explain many of the geologic observations that earlier seemed anomalous. These studies combine a number of geophysical techniques but predominantly concentrates on integrating gravity and flexural analysis with geologic constraints in three fundamentally different tectonic settings: foredeep basins, hot spot swells, and intracratonic basins.

Lateral strength variations in foreland lithosphere in front of an advancing subduction zone (or thrust belt) can exert strong controls on the spatial and temporal evolution of the foredeep basin because local weak zones within the foreland serve to localize the position of the outer flexural bulge (with respect to the foreland) for extended periods of time. This occurs because the weak segment bends more easily than the surrounding, stiffer plate, so that plate bending is concentrated within the weak zone. With time, the dip of the down-going (foreland) plate becomes steeper, narrowing and/or deepening the foredeep basin. If several weak zones are present within the foreland, basin development can become episodic, with protracted periods of time during which the basin remains fixed with respect to the foreland, interspersed by brief periods of time during which the basin advances rapidly toward the foreland. The flexural behavior will be directly reflected in the stratigraphic record, producing facies belts which migrate toward the foreland in an episodic fashion. If the foreland lithosphere behaves as an elastic sheet, the weak zones must have a flexural rigidity about an order of magnitude lower than (or an elastic plate thickness about half of) the surrounding, stiffer plate in order to induce strongly episodic behavior. When the effects of inelastic yielding in a lithosphere of brittle-elastic-ductile rheology are considered, the strength contrast required to produce episodic behavior is reduced to about a factor of two in flexural rigidity (or 10 to 15% in initial elastic plate thickness). Examples taken from two foredeep basins show evidence for episodic foredeep basin development: in both the Early Proterozoic Kilohigok basin of

northern Canada and the Pliocene-Quaternary Apennine foredeep basin beneath the Adriatic Sea the outer flexural bulge appears to have remained fixed with respect to the foreland while the inner part of the basin deepened through time. In addition, the flexural geometry of the Pliocene-Quaternary Apennine foredeep basin is well modeled by an elastic plate varying laterally in strength of thickness $T_{elastic}$ = 8.5 km with a 20 km long weak zone of thickness T_{weak} = 4.25 km.

The Yellowstone hot spot has been identified mainly by its track of age-progressive volcanics; many smaller scale tectonic features serve to hide the long-wavelength hot spot-related swell. By employing averaging and filtering techniques, we are able to identify a swell in both the gravity and topography and use them to constrain the apparent depth of compensation of the Yellowstone hot spot at 70±10 km. This value is comparable to the deepest compensation depths for swells on old oceanic lithosphere. A compensation depth within the mid- to lower lithosphere combined with the only 15 m.y. known duration of the hot spot suggests either dynamic thinning of the thermal plate or compensation by upwelling in a low-viscosity asthenosphere, with some combination of the two explanations being consistent with seismic tomography results. Thus in many ways the Yellowstone hot spot appears quite similar to the oceanic analogues.

The cause of the formation of the circularly symmetric intracratonic basins of North America (including the Michigan and Williston Basins) is enigmatic; thermal processes, phase changes and effects due to in-plane stresses have all been suggested. These basins are filled by several kilometers of sediment and typically show a prolonged subsidence history with little deformation; a plate tectonics origin is not obvious. Analysis of gravity and subsidence in this paper shows long-wavelength positive isostatic gravity anomaly over the basins, which eliminates most in-plane stress formation mechanisms. The Williston Basin has a 25 mgal positive anomaly that decreases gradually over at least 600 km, and the Michigan Basin has a 15 mgal positive anomaly that decreases over 300 km. Gravity modeling suggests a shallow sub-crustal load in the shape of an inverted cone. In our opinion, the best interpretation of this anomaly and of the basin-forming mechanism is injection by a hot spot plume of suboceanic lithospheric material into the subcontinental lithosphere and cooling over 100's of m.ys. A chemical difference between suboceanic and subcontinental lithosphere results in the presence of a mass excess after complete cooling. The chemical density contrast between the two will depend on the thickness of the continental lithosphere; for continental lithosphere of thickness between 200 and 400 km, the chemical density contrast will be between 75 and 45 kg/m^3. In order for the hot material to be neutrally buoyant and rise beneath the lithosphere, this suggests temperature contrasts between 750 and 450°C. Comparing these thermal anomalies with those inferred at hot spots today suggests a thicker lithosphere (closer to the 400 km end) was probably present at the time of basin formation This model is consistent with theoretical modeling that shows several plumes forming at one time beneath a supercontinent, and may also explain why basin subsidence initiated shortly after breakup of the Late Proterozoic supercontinent. In this scenario, the intracratonic basins would be an ancient analog to the present day African hot spot swells (although there are some important differences between the two), which formed after breakup of the Mesozoic supercontinent.

Thesis supervisor: Leigh Royden

ACKNOWLEDGMENTS

So many people have affected my life and helped me along the way to my actually getting a Ph. D. that I hardly know where to start. Chronological order may make the most sense, and where better to start than with Mom and Dad. What can I say: I wouldn't be here if it weren't for them. I thank them for bringing me up in a loving, supportive family, so that I always knew that regardless of whatever else was bringing me down, home would be an oasis where I could get revitalized. I thank them for encouraging me as a scientist, even though they think what I do is rather esoteric (sometimes I even wonder if they're right). And I thank my Mom for her great advice through the years, which can be summed up with "get to bed at night" and "get your hair cut". I also want to thank my brothers and sister, my grandparents, and my whole extended family. I have really needed my vacations /visits home these last five years, and after every one of them I returned to Boston refreshed in spirit.

I owe a large debt of thanks to Art Lerner-Lam and the Lamont-Doherty summer intern program. I thought I was interested in Earth Science, and after working with Art, I was convinced. Art has an incredible ability to convey the excitement of science to the lay-person (as I was at the time), and also to find the words to turn mathematical equations into physical understanding. Art first introduced me to hot spots, and I've been interested in them ever since. He also went out of his way to introduce me to MIT and set up some interviews for me with faculty members here even before I seriously considered applying.
I also owe Dr. David Robinson and Dr. Dennis O'Brien at Drake University lots of thanks. Once I decided on geophysics they did everything in their power to help me get where I wanted to go (including to the aforementioned Lamont summer program).

I cannot express enough my gratitude for the inspiration and support I have received from my advisors, Wiki and Marcia. Wiki especially deserves thanks for boosting my morale when numerical difficulties in my first research project caused me to doubt whether science was worth it all. I am very glad that she was able to help me see the "big picture" that makes the annoying technical difficulties worthwhile. Wiki introduced me to geology, convincing me I really wanted to take regional tectonics and field camp my first year. I spent practically the whole first semester trying to figure out what all those words meant, but convincing me to get a working knowledge of geology was the greatest advice she could have ever given me. Wiki "held my hand" when I began grad school and needed a lot of direction, but showed confidence in my abilities by stepping back and letting me tackle problems on my own. Finally, I especially thank Wiki for organizing the Women in Science series in the department. One of the most interesting things I learned this past year was about the "Impostor Phenomena"; identifying this as a phenomenon common to

women at MIT helped me feel that maybe I am ready to go out and face the world, even if I do feel like an impostor at times. Marcia, too, was and is a constant source of inspiration, encouragement and advice. Marcia gave me the latitude to attack research projects on my own, yet was right there to set me straight whenever I ran into a wall (and she also made sure I was never running in the wrong direction too long). I have appreciated Marcia's political savvy this past year as I've been on my job search, several times I have had to tap into it and I've always received good advice. Marcia also allowed me to be a TA (and allowed me to lecture), thus getting a taste of professorial life in academia. Both Wiki and Marcia have been role models I can only hope to emulate some day.

I owe a big debt of thanks to many other faculty members at MIT as well, with John Grotzinger and Sam Bowring at the top of the list. They fed my interest in the evolution of lithosphere (especially the continental lithosphere) through time and brought me up to speed on what they consider the fundamental problems to be addressed; Sam's "Origin and Evolution of the Continental Crust" was probably my favorite class of my grad school career. I have also learned an incredible amount of field geology from John Grotzinger, and I thank him for allowing me to follow him around in the field from time to time. Regional tectonics with Clark Burchfiel has always been inspirational - Clark is a fount of information on anything and everything geologic. Tim Grove and Maartin deWitt also encouraged my interest in Archean tectonics, and had the patience to explain things to me in their field of specialty that I was having trouble with. Sean Solomon offered advice when I was nervous and stressed-out my first year.

I also appreciated the opportunities I've had to get in the field. I thank Kip, Clark, John and Wiki for everything they taught me in the field and for letting me (or even encouraging me to) attend field camp. I also thank Pete Kaufman for letting me be his field assistant, and Jim Knapp and the COCORP group for giving me a chance to see the Williston Basin up close and personal, for showing me how seismic experiments are run, and for detonating some dynamite right beneath a herd of cows so we could see them stampede! (That wasn't the goal, (really!) but it was an incredibly funny side effect!)

I also want to thank all the support people at MIT, especially Marie Senat, who is more of a friend than a co-worker, and Carol Gibbs, Anita Killian and Cindy Hanes, who have made the beauracratic part of grad-student life a very minor component.

My fellow grad students have been (and will continue to be) great friends. Pete Kaufman is first and foremost among them. There is no doubt in my mind that Pete is the reason I made it to this point. I would have left years ago if it weren't for him. I've said many prayers of thanks that Wiki took two new students our year so we have each other. I've talked through my grad school frustrations with him (even though 90% of the time he probably didn't care about them) and he's still my friend. He read and critiqued many (if

not all) of these chapters before I sent them on to my advisors, offering many salient comments and making sure I didn't say anything too dumb. He's also a great guy for ice cream/coffee breaks in the late afternoon, and for babbling on about nothing in particular. Pete also took me into the field with him, and we only got close to killing each other once! Pete is a great geologist and I'm looking forward to the time when we can collaborate on science. Carolyn Ruppel helped me when I first got to town - even earlier as I stayed with her on my visit to MIT - and has continued to help me ever since. I'm looking forward to actually being her equal so I can start helping her as much as she has helped me. Cecily Wolfe has also been a great friend. You can almost count on Cecily to have a positive outlook on something, so if you're down, she'll bring you up. The 8th floor crew, Helen Webb, Garrett Ito, Emily Hooft, Mousumi Roy, Yu Jin and Yu Zhou are all great people and have been great about putting up with Pete and me when we sometimes get a little loud (especially this last year when we'd go on some employment- (or lack thereof) related tirade). Matt Cordery and Paul Filmer, old 8th floor guys whose company I enjoyed, seemed like such pessimists to me when I started, but now their outlook seems realistic - I guess that's one sign I'm ready to be done!

The 5th floor folks, have been good about putting up with me since the computer situation on 8th floor got tight, and the 10th and 11th floor folks were great in helping me when I wasn't totally sure of the geologic implications of some data or some model. I especially want to mention Dave McCormick for his help when I was trying to figure out sequence stratigraphy and for his calming influence when I was paniced before giving my first professional talk, Lind Gee for setting me up on the computers when I first got to MIT, and Larry McKenna for showing me how to use a Brunton. The 7th floor folks have had me on their floor without complaint for 5 whole years. Margaretha Eckhardt (and Lynn Smith and Joanne Fredrich) deserves special thanks for never complaining about the state of my desk - which could almost be declared a disaster area (and has been that way for the majority of my grad school career, and the entire time she's been there). Mark Simons, Bev Saylor, Dawn Sumner, Dave Applegate, Dave Hawkins, C.J. Northrup, Jim Gaherty, Glen Gaetani, Pat McGovern, and Nori Namiki all made me think about problems I may not have thought about otherwise. Nick Fizman, Anne Sheehan, Martha House, Allison Macfarlane, Jen Edwards and Susan Evans made grad school a nicer place to be. Deb Zervas has been there the whole time for me, providing emotional and intellectual support. She's provided a nice balance to the intensity of MIT - helping me get a perspective on things where I think I'm starting to see crooked, and offering insights into life beyond academia. And of course, I want to thank Peter Puster. Peter's greatest contribution to this thesis came the afternoon before my defense, when I panicked thinking there was a bug in my program and wanted to re-generate all my figures. He got me off the computer and out

of the building before I could do any permanent damage to the code. But his contributions go beyond that. He's been a source of emotional solace and a scientific sounding board. I'm very happy with the time we've spent together, and I'm looking forward to having lots more.

I also want to thank my friends outside the department, including the whole theology discussion group and the TCC crowd, too numerous to mention individually, but they've all helped me keep my life in perspective. It's been nice to get away from the department at times, for either a theological debate or a wild game of pictonary. And it has also been a good exercise trying to explain what I do to some physicists, who were a lot more hung up on the mathematics than I. Julie McNamara, Tony Bogner, Bill Schmitt and Mike Cresciamano have been extra good friends that deserve extra commendation. Emily Huang, Lupe Rodrigues and Tanya Christiansen, who lived with me for years, and Chip and Larry Moreland provided a group of friends with interests so diverse they were the perfect MIT-antidote, keeping me sane when all I wanted to do was get out of here.

Finally thanks to my thesis committee, Wiki, Marcia, John Grotzinger, Brad Hager and Terry Jordan, for reading this tome and for passing me. I appreciate your time and comments, and you certainly have made this a better piece of work.

TABLE OF CONTENTS

CHAPTER ONE

INTRODUCTION

Almost thirty years ago, a revolution occurred in the Earth sciences in the form of the theory of plate tectonics. This theory fundamentally changed some of the most basic assumptions about the Earth. Plate tectonics describes quantitatively the kinematics of the rigid outer layer of the Earth. Within the plate tectonics paradigm, data sets as diverse as ocean depths, the spatial distribution of earthquakes and volcanoes, and patterns of sea floor magnetic lineations could be explained, and, more importantly, used to place constraints on Earth processes, such as describing the relative motions between plates or inferring a cooling history and thermal structure of the lithosphere.

Applying plate tectonics to the oceans has been far more successful than applying it to the continents. Most plate boundaries in the oceans are narrow and there is very little intra-plate deformation, consistent with the tenets of plate tectonics. On the continents, however, plate boundaries are much more diffuse, with deformation commonly occurring thousands of kilometers from the nearest plate boundary. Plate tectonics fails to describe continental kinematics because the continents cannot be reasonably approximated as rigid plates. In contrast to the relatively homogeneous ocean crust, which forms through a single process (i.e. sea floor spreading) continental crust forms through multiple deformational and igneous events, resulting in structural heterogeneities that can distribute deformation across great distances. Plate tectonics has, however, contributed enormously to continental tectonics. The realization that large scale lateral displacements could be as important or more important than vertical displacements profoundly affected interpretations of the geologic record. Perhaps more importantly, though, plate tectonics demonstrated the need for combining quantitative methods with what was largely an observational science, as indicated by the large number of geophysical techniques that address geologic problems.

Studies of continental tectonics suggest the converse is also true: to an extent far greater than in the oceans, geologic observations must be integrated with geophysical data before an understanding of active processes can be achieved.

Plate tectonics describes processes and mechanisms active in marine settings. Many of these processes also affect the continents, but their signals have been complicated by the heterogeneous continental lithosphere and thus their surface manifestations are distinct from, and commonly much more complex than, their oceanic analogs. A major focus of this thesis is how the processes creating tectonic features located in the oceans (such as subduction zones and hot spots) are transformed by the continental lithosphere, how the surface manifestations (i.e. the geology) are affected, and what can be learned from these transformations about the continental lithosphere.

OVERVIEW

The second chapter of my thesis concerns the flexing of continental lithosphere as it approaches a subduction zone. In an ideal plate tectonics model of subduction, the subducting plate would have a constant geometry throughout time, advancing steadily toward the plate boundary as described by the (constant) convergence velocity. In purely oceanic subduction zones, something close to this is seen. However, in contrast to the homogenous evolution recorded with downgoing oceanic lithosphere, observations from foredeep basins forming in front of subducting continental lithosphere may record evidence for spatial and/or temporal variations in subduction geometry. These variations can be explained once the effects of lateral variations in strength across the continental lithosphere and the effects of inelastic yielding, especially the weaker rheology in continents compared to oceans, are considered.

The third chapter concerns hot spots beneath the continents. In contrast to the oceans, where a large number of hot spots are observed at the surface, continental hot spots are relatively scarce. The Yellowstone hot spot and its track, the Snake River Plains, is one

of the best examples of a continental hot spot, and probably the best example of a hot spot on moving continental lithosphere. Techniques developed for oceanic hot spots must be modified to study the Yellowstone swell, as it is much more difficult to isolate a single tectonic feature in the continents as compared to the oceans. Many of the features of the Yellowstone hot spot appear to be analogous to oceanic hot spots, (perhaps suggesting plumes initiate deeper than the base of the lithosphere), and studying a hot spot in a continental setting even may help resolve thermal questions difficult to address in oceanic settings due to the large amount of hydrothermal circulation.

The fourth chapter concerns intracratonic basins. These features have no obvious analog in the oceans, nor any obvious tectonic explanation. They are generally circular and contain several kilometers of sediments. Four intracratonic basins formed on the North American craton at roughly the same time, suggesting a common mechanism of formation. Two of the basins are studied in detail, the Michigan Basin and the Williston Basin. Both of these basins are associated with an isostatic gravity high, which suggests a subsurface mass excess. A model is developed to explain the observed mass excess which relates the intracratonic basins to mantle plumes (hot spots) that arose beneath the Late Proterozoic supercontinent. In this model, the chemical difference between suboceanic and subcontinental lithosphere is utilized, with the rising mantle plume injecting suboceanic lithosphere into the subcontinental lithosphere, thus leaving a chemical mass excess upon cooling. This model also explains why there are no oceanic analogs to the intracratonic basins: Mantle plumes beneath the ocean would not result in a chemically distinct mass being deposited, so upon cooling no basin would be formed. Instead of an oceanic analog, a more reasonable analog for these basins may be the hot spots of Africa, another case of mantle plumes located beneath continental lithosphere shortly after breakup of a supercontinent.

Finally, based largely on the conclusions of chapters three and four, I draw some tentative conclusions on the presence (or lack thereof) of hot spots beneath continental

lithosphere. It is clear from looking at the surface distribution of hot spots on the Earth that hot spots are predominantly observed on oceanic lithosphere. This may be a result of lower mantle dynamics producing fewer mantle plumes beneath the oceans or it may be a result of the continental lithosphere filtering out the plumes so fewer are observed at the surface. I explore the possibility that plume distribution is lithosphere controlled and conclude that in order to penetrate the continental lithosphere and produce as surface expression, the hot spot must either be a strong plume or must have formed when the continental lithosphere was at rest with respect to the hot spot frame of reference for an extended period of time. To support this assumption, an ancient and a modern example of each case is discussed.

CHAPTER TWO

SPATIAL AND TEMPORAL EVOLUTION OF FOREDEEP BASINS: LATERAL STRENGTH VARIATIONS AND INELASTIC YIELDING IN CONTINENTAL LITHOSPHERE

Paula J. Waschbusch and Leigh H. Royden

(Published in *Basin Research*, vol 4, pp. 179-196, 1992)

ABSTRACT

Lateral strength variations in foreland lithosphere in front of an advancing subduction zone (or thrust belt) can exert strong controls on the spatial and temporal evolution of the foredeep basin because local weak zones within the foreland serve to localize the position of the outer flexural bulge (with respect to the foreland) for extended periods of time. This occurs because the weak segment bends more easily than the surrounding, stiffer plate, so that plate bending is concentrated within the weak zone. With time, the dip of the down-going (foreland) plate becomes steeper, narrowing and/or deepening the foredeep basin. If several weak zones are present within the foreland, basin development can become episodic, with protracted periods of time during which the basin remains fixed with respect to the foreland, interspersed by brief periods of time during which the basin advances rapidly toward the foreland. The flexural behavior will be directly reflected in the stratigraphic record, producing facies belts which migrate toward the foreland in an episodic fashion. If the foreland lithosphere behaves as an elastic sheet, the weak zones must have a flexural rigidity about an order of magnitude lower than (or an elastic plate thickness about half of) the surrounding, stiffer plate in order to induce strongly episodic behavior. When the effects of inelastic yielding in a lithosphere of brittle-elastic-ductile rheology are considered, the strength contrast required to produce episodic behavior is reduced to about a factor of two in flexural rigidity (or 10 to 15% in initial elastic plate thickness). Examples taken from two foredeep basins show evidence for episodic foredeep basin development: in both the Early Proterozoic Kilohigok basin of northern Canada and the Pliocene-Quaternary Apennine foredeep basin beneath the Adriatic Sea the outer flexural bulge appears to have remained fixed with respect to the foreland while the inner part of the basin deepened through time. In addition, the flexural geometry of the Pliocene-Quaternary Apennine foredeep basin is well modeled by an elastic plate varying laterally in strength of thickness $T_{elastic}$ = 8.5 km with a 20 km long weak zone of thickness T_{weak} = 4.25 km.

INTRODUCTION

Studies of the ocean basins have shown that oceanic lithosphere acts elastically on geologic time scales and to first order can be treated as a thin, laterally homogeneous elastic sheet floating on a fluid substratum (e.g. *Gunn* [1943], *Walcott* [1970]). Continental lithosphere has also been successfully treated the as a thin, laterally homogeneous elastic plate in several studies of the development of foredeep basins (e.g. *Jordan* [1981], *Karner and Watts* [1983], *Lyon-Caen and Molnar* [1983, 1985], *Royden and Karner* [1984]). Yet while oceanic lithosphere is relatively homogeneous, the multiple deformational and igneous events which form the continental crust have resulted in significant structural inhomogeneities within the continents; this structural heterogeneity is almost certainly accompanied by lateral variations in lithospheric strength.

Experimental rock mechanics studies also suggest that the approximation of the lithosphere as a homogeneous elastic plate is less accurate on the continents than the oceans, as rheological differences suggest that inelastic yielding of the continental lithosphere commonly occurs at much lower stresses than does inelastic yielding of the oceanic lithosphere (e.g. *Goetze and Evans* [1979], *Brace and Kohlstedt* [1980]). Inelastic yielding may also be of more importance in continental lithosphere because of the higher curvatures observed at continental subduction zones as compared to oceanic subduction zones [*Jarrad*, 1986]. Thus, while a perfectly elastic plate of uniform thickness may be a sufficient approximation to the homogeneous oceanic lithosphere, lateral variations in flexural strength and inelastic yielding during flexure are likely to play a more important role in the flexure of continental lithosphere.

Several previous studies have looked at lateral strength variations and inelastic yielding in the lithosphere in a preliminary way. For example, *Lyon-Caen and Molnar* [1983,1985] and *Sheffels and McNutt* [1986] incorporated lateral variations in lithospheric strength into their analysis of foredeep basin development, and *Judge and McNutt* [1991] showed that curvatures reached at oceanic subduction zones can be high enough that

inelastic yielding has a significant effect on plate flexure. Nevertheless, a systematic study of the effects of lateral strength variations and inelastic yielding on flexural behavior has not been undertaken. In this paper we address how these two effects, separately and in combination, affect the flexural behavior of continental lithosphere and the geometric and temporal development of continental foredeep basins.

DEVELOPMENT OF FOREDEEP BASINS BY FLEXURE OF HOMOGENEOUS ELASTIC LITHOSPHERE

Before considering the effects of lateral strength variations and inelastic yielding on foredeep basin evolution, a brief review of the fundamental features of the simple, homogeneous elastic case is warranted. This will provide the reference frame within which we may interpret the effects of additional rheological complexity.

Foredeep (or foreland) basins that develop in front of active orogenic belts form primarily by the flexural bending of the lithosphere under applied loads [*Price*, 1973]. These loads may be both supracrustal, such as load applied during emplacement of thrust sheets (e.g. *Karner and Watts* [1983]), and subcrustal, loads transmitted from the subduction zone itself (e.g. *Royden and Karner* [1984], *Royden* [1994]). Continuing plate convergence is accommodated by spatial translation of the thrust belt and the associated subduction zone toward the foreland, and this translation results in the flexurally induced basin also being translated, or migrating, toward the foreland in front of the advancing loads. If the foreland lithosphere is laterally homogeneous, and if the forces associated with thrust-sheet emplacement and subduction are constant in time, the geometry of the advancing foredeep basin will also remain constant through time. To a viewer sitting on the downgoing (subducting) plate, the foredeep basin and its associated outer flexural bulge appear to be migrating continuously towards the foreland without changing shape.

Figure 2.1a shows the simplified geometry of a foredeep basin assumed to have formed on a homogeneous, perfectly elastic lithosphere ($T_{elastic}$ = 32 km, see Table 2.1)

subject to a constant subduction load (= 1.8×10^{12} N/m) at the effective plate end. The location of the plate end, at which the subduction load is applied, is assumed to advance toward the foreland at a constant rate. As discussed above, the basin geometry does not change in time - the profiles are of identically shaped basins that are merely shifted horizontally toward the foreland as subduction advances. Although a simple elastic model has been used here, the same effect will occur with any reasonable foreland rheology, provided that the foreland lithosphere is laterally homogeneous. (Note also that if the effective plate end does not advance at a constant rate the basin shape still remains constant with time, but the basin will not advance at a constant rate.) Figure 2.1b, showing sediment deposition rates as a function of time and space also demonstrates the steady-state nature of the system. If rates of deposition can be simplistically correlated with sedimentary facies, then the "facies" zones follow the plate boundary and advance toward the foreland at the same rate as the subduction system and thrust belt.

If the idealized basin remains filled to sea level by sediment throughout its history, then a synthetic stratigraphy of the foredeep basin can be constructed (Figure 2.1c). A stratigraphic cross section consists of wedge-shaped units, bounded by time lines tracking the position of originally horizontal depositional surfaces. The wedges, which are thickest near the thrust belt and thin toward the foreland, are a result of the lateral gradient in subsidence rate across the basin and the spatial translation of the basin toward the foreland with respect to the underlying plate. The effect of the continuous migration is to shift the wedges laterally, causing onlap of successively younger strata onto the foreland.

MIGRATION(?) OF ANCIENT AND MODERN FOREDEEP BASINS

Analyses based on homogeneous elastic flexure have produced results consistent with the stratigraphic development of both ancient and modern foredeep basins (e.g. the Appalachians [*Karner and Watts*, 1983], the Taconic Orogen [*Bradley and Kusky*, 1986], the Rocky Mountains [*Jordan*, 1981] and the Himalaya [*Lyon-Caen and Molnar*, 1983,

1985]). However, there are a number of examples of foredeep basins that contain stratigraphic observations that are better explained by a discontinuous geometric evolution with time, such as the ancient Kilohigok basin and the modern Apennine foredeep. Flexural studies from the well preserved stratigraphy of these two basins suggest an evolutionary history distinct from that of the homogeneous elastic case, as discussed in more detail below.

The Kilohigok Basin

The Early Proterozoic Kilohigok Basin (Figure 2.2a), located on continental crust of the Archean Slave craton in northern Canada, is bounded to the west by Archean basement rocks of the Slave craton and to the east by the Thelon orogenic belt. Sediment deposition within the basin was contemporaneous with thrusting and convergence in the Thelon orogenic belt. Reconstruction of original basin geometry from stratigraphic data reveals an asymmetric basin deepening eastward. These observations are consistent with formation as a flexurally induced foredeep basin in front of the Thelon orogenic belt [*Grotzinger and McCormick*, 1988; *Grotzinger and Royden*, 1990]. During initial foredeep basin development the lowest basin sequence, a passive margin sequence, underwent drowning at its outer (eastern) edge and uplift in the interior (marked by an erosional unconformity). With time, the underlying lithosphere became more flexed and the basin deepened, reaching a maximum subsidence of 5 km in its deepest (eastern) part. However, the location of the flexural bulge did not change. This is particularly clear because all formations thin significantly in a localized zone due to both lateral pinch-out and erosion of upper units, documenting the location of the outer flexural bulge (the point of maximum elevation) throughout most of the basin's evolution. In addition, the fabrics indicative of subaerial exposure and erosion are most strongly developed in this zone, and become less well developed to the east (toward the subduction zone) where formations are thicker [*Grotzinger et al.*, 1987]. Because the vertical stacking of the stratigraphic pinch-

outs and the erosional surfaces indicates that the flexural bulge formed and remained fixed to the downgoing plate with time, we need a mechanism that will fix the flexural bulge with respect to the downgoing plate while deepening the basin's interior.

The Apennine Foredeep

The Apennine foredeep, located on the Adriatic plate lies northeast of and trends parallel to the Apennine thrust belt. It forms a northwest trending asymmetric basin with a steep western flank and a much more gradual eastern flank [*Pieri and Groppi*, 1981; *Dondi et al.*, 1985]. A steeply dipping Benioff zone [*Gasparini et al.*, 1982] and Miocene to Recent volcanism west of the Apennine thrust belt [*Barberi et al.*, 1974, *Civetta et al.*, 1978] indicate a westward direction of subduction. The foredeep basin sequence contains turbiditic and conglomeratic sedimentary rocks as old as middle Miocene in the northern part of the belt, but only as old as lower to middle Pliocene in the central and southern parts. Depth data (to the base of the Tertiary, base of the Pliocene and middle Pliocene) determined from seismic stratigraphy combined with paleontological information from open-file well logs in the Adriatic Sea can be used to reconstruct earlier foredeep basin geometries [*Kruse*, 1989; *Kruse and Royden*, 1994]. These foredeep basin reconstructions suggest that the basin narrowed and deepened with time, without associated migration toward the foreland. This is particularly clear in the reconstructions of their profile B-B' (Figure 2.2b) where the base Pliocene and the middle Pliocene profiles within the basin are separated by approximately two km of deposition, yet pinch together at the basin edge and are virtually indistinguishable from that point forelandward. In addition, flexural modeling [*Kruse*, 1989] of the basin indicates that the location of the flexural bulge, with respect to the foreland, is the same for both time intervals. Thus, while sedimentation continued within the basin, flexural modeling and the lack of onlap deposition both suggest the area of maximum elevation (the bulge) remained fixed during this time period. In this way, the geometry of the Apennine foredeep is similar to that of

the Kilohigok basin: the internal part of the basin appears to deepen with time while the flexural bulge remains fixed to the downgoing plate.

Taken together, the observations of these two basins indicate that not all foredeep basins form by continuous cratonward migration as suggested by the homogeneous elastic model. Instead, to explain these basins we require a mechanism which allows development of successive basins that deepen through time without lateral migration of the bulge. One naturally occurring phenomena that might be responsible for the localization of the flexural bulge on the downgoing plate is the presence of pre-existing inhomogeneities in the foreland lithosphere.

FLEXURE OF AN INHOMOGENEOUS ELASTIC LITHOSPHERE

Continental lithosphere, as a result of its complex and protracted formation and evolution, may contain significant inhomogeneities. Zones within the lithosphere which appear weak (or thin) will be more likely to bend under applied flexural stresses and serve to localize curvature during bending. Thus weak zones cause the flexural bulge to localize with respect to the downgoing lithosphere and determine the resultant flexural geometry of the basin, as discussed below.

Geometric Evolution

Figure 2.3a shows the time evolution of the geometry of a simplified foredeep basin assumed to have formed on an inhomogeneous, perfectly elastic lithosphere, and subject to a constant subduction load (1.8×10^{12} N/m) at the effective plate end. In this idealized foreland, the lithosphere was assumed to be an elastic sheet of uniform strength ($T_{elastic}$ = 32 km) with two weaker segments (T_{weak} = 16 km) embedded in it (thus, the flexural rigidity of the weaker segments is one-eighth the background rigidity). The width of the weak segments were taken to be 75 km, or $2\alpha / 3$, where α is the flexural parameter of the homogeneous portion of the plate, given by $\alpha^4=(4D/\Delta\rho g)$. (For an elastic plate thickness

of 32 km and a density contrast $\Delta\rho$=600 kg/m^3, α=112 km.) The lateral change in elastic plate thickness (flexural rigidity) is assumed to occur linearly over a narrow transition zone, as seen in Figure 2.3a, so as to avoid sharp discontinuities in the flexural strength of the plate. The width of the weak zone is defined as the distance between the mid-points of the two transition zones. The two weak zones shown in Figure 2.3a were separated by 450 km (or 4α). Flexural profiles for this broken plate with non-uniform rigidity were computed from explicit finite difference equations, modified after Bodine (1981). Plate deflections were calculated out to a distance of 900 km (or 8α) from the subduction zone to avoid effects of a plate end.

The effect of the weak segments is significant and introduces a time dependence to the basin geometry (Figure 2.3a). While the weak zones remains located in front of (towards the foreland from) the flexural bulge, they do not have a significant effect on the basin geometry and the plate behaves as though it were homogeneously elastic. With time, the basin approaches the weak segments and their effect can be seen in the basin geometry and apparent rate of migration toward the foreland. This occurs because the weak segment bends more easily than the surrounding, stiffer plate, so that plate bending is concentrated within the weak zone. Consequently, the flexural bulge becomes localized within the weak zone. In effect the bulge becomes "fixed" to the zone of weakness and travels with the weak zone toward the plate end. While the flexural bulge is localized within the weak segment of the lithosphere, its width scales with the width of the weak zone and not with the flexural wavelength of the plate. As the weak segment nears the subduction zone, it continues to absorb a large portion of the plate bending. In addition, the dip of the downgoing plate becomes steeper with time, narrowing and/or deepening the foredeep basin.

The flexural bulge remains fixed to the weak segment of the foreland until the subduction system and thrust belt advance to a point where the weak segment is near the subduction zone and the zone of positive (upward) deflections occurs almost completely

within the strong, background lithosphere. At this time the flexural bulge ceases to be localized within the weak segment and the upward deflections that define the flexural bulge advance quickly toward the foreland. In the example shown in Figure 2.3a, the flexural bulge quickly becomes localized within the next zone of weakness in the foreland, starting the process over again (although the way in which this occurs is clearly dependent on the spacing between weak segments and their strength relative to each other and to the rest of the foreland lithosphere).

Figure 2.3a thus shows an episodic history of basin evolution, where the flexural bulge remains roughly fixed with respect to the downgoing plate for long periods of time, during which its amplitude increases and reaches a maximum just prior to abandonment of the weak zone as the locus of the flexural bulge. In between periods where the bulge is localized within the weak zones it advances quickly to the next zone of weakness in the foreland and its amplitude during this period of rapid advance is greatly reduced. In the example in Figure 2.3a the flexural bulge spends most of its time localized within the weak zones in the lithosphere, and relatively little time advancing from one weak zone to the next. The depth of the deepest part of the foredeep basin also varies with time, reaching its greatest value just as the weak segment in the lithosphere is abandoned as the flexural bulge. One of the implications of Figure 2.3a is that the basin geometry at a particular point in time may not necessarily be the same as the geometry of the basin at other times. Instead it is only a single snap-shot of a basin whose geometry is continuously evolving.

A comparison of depositional rates on a time versus distance diagram (Figure 2.3b) offers another representation of the changing nature of basin geometry. Again making the simplistic correlation between deposition rates and facies, the initial "facies" pattern (across the lowermost part of the plot), developed while the weak zone is still far from the basin, closely resembles the homogeneous elastic basin case. As the weak zone begins to affect basin shape, the distribution of the "facies" zones is affected, increasing the height of the flexural bulge (note the increased erosion rate over the bulge), increasing the basin depth

(and the rate of deposition in the deepest part of the basin), and localizing the flexural bulge with respect to the foreland for a significant period of time.

Stratigraphic cross sections through this basin are not much different than those resulting from flexure of a homogeneous elastic plate. Figure 2.3c shows the synthetic stratigraphy generated up to the point where the weak zone is abandoned. As in Figure 2.1c, sedimentary wedges, bounded by time-lines and thinning toward the foreland, are the result of a lateral gradient in subsidence across the basin and dominate the stratigraphy. Closer inspection reveals that while the lateral subsidence gradient is constant in time in Figure 2.1c, variations in onlap spacing and wedge thickness in Figure 2.3c reveal a non-constant subsidence gradient due to inhomogeneous strength variation of the lithosphere. Onlapping of younger units is also apparent in both basins, although it results from two different processes. Onlap in the homogeneous case results from continuous migration of the basin at a constant rate. In the inhomogeneous case, onlap is also the result of the bulge growing narrower and higher within the weak zone. The final result is that it may be very difficult, if not impossible, to distinguish between a continuous and a discontinuous basin evolution on the basis of onlap patterns alone, especially when a more complex system (incorporating important eustatic and other tectonic factors) is considered. Additional constraints, such as location and extent of erosion surfaces may help to determine the foredeep basin's evolution, but quantitative flexural modeling remains the best way to distinguish between a continuous or episodic foredeep basin evolution. An example of such modeling will be discussed in more detail later.

Note that the model stratigraphy results discussed above (Figures 2.3b and 2.3c) are solely for illustrative purposes and the actual facies produced may be considerably different from this simple model. For example, the correlation between depositional rates and facies becomes too simplistic as the plate with laterally varying strength is overthrust. Note also that the effect of erosion is not incorporated into the theoretical stratigraphy generated in Figure 2.3c. Clearly a large number of other stratigraphy-influencing factors

(eustacy, sediment supply, etc...) will affect the final stratigraphic geometry and a thorough discussion of them is beyond the scope of this paper.

Incorporating flexurally weak zones into the lithosphere introduces three more variables to be considered: the strength contrast between the weak zones and the background lithosphere, the width of the weak zones, and the spacing between weak zones. In constructing Figure 2.3 we arbitrarily chose the contrast in flexural rigidity between the background foreland lithosphere and the weak zones imbedded in it to be one eighth, the width of the weak zones to be 75 km ($2\alpha/3$), and the spacing between weak zones to be 450 km (4α). Clearly, the temporal evolution of the basin will depend on the particular combination of these three parameters.

Figure 2.4 shows the effect of varying the rigidity contrast between the background foreland lithosphere and the weak zones. Large contrasts in flexural rigidity (Figure 2.4a) (i.e. roughly any rigidity contrasts $D_{weak} < 1/8\ D_{elastic}$ can be considered large) produce results qualitatively similar to Figure 2.3a: a discontinuous evolution of the basin with distinct localization of the flexural bulge in the weak zones. However, a greater strength contrast allows even more bending to occur in the localized zone, resulting in greater deviations from the homogeneous elastic geometry with time. With a small contrast in flexural rigidity (Figure 2.4b) ($D_{weak} > 1/8\ D_{elastic}$) the effect of the weak zone on basin geometry becomes relatively insignificant and the profiles resemble the homogeneous elastic case.

Decreasing the width of the weak zone (Figure 2.5a) results in short term and relatively minor localization of the weak zone. If the weak zone is extremely narrow (length $< \alpha/60$), the effect of the weak zone on the flexural profile is almost negligible. Increasing the width of the weak zone by a significantly large amount (length $> \alpha$) initially localizes the flexural bulge within the weak zone, but then produces plate flexure similar to that of an elastic plate with uniform rigidity equal to that of the weak zone (Figure 2.5b). The plate profile remains similar to that of an elastic plate of the weak zone thickness until

the edge of the weak zone nears the subduction zone and the strong, background lithosphere increases the flexural wavelength.

Increasing the spacing between the weak segments (Figure 2.6a) generates a flexural bulge that spends a greater proportion of its time in a continuously migrating evolution between weak segments. Significantly decreasing the spacing between weak segments (Figure 2.6b) creates a flexural bulge that is nearly always localized on a weak segment and can result in some unexpected plate geometries because the plate may be effected by more than one weak zone at any given time.

Apparent Plate Thickness

Apparent flexural rigidity (or apparent elastic plate thickness) of the lithosphere is commonly used to infer properties of the lithosphere that cannot be directly observed, such as temperature structure (e.g. *Watts* [1978], *McNutt and Menard* [1982]) and paleo-temperature (e.g. *Karner, Steckler and Thorne* [1983]). Changes in apparent plate thickness with time have then been used to infer changes in lithospheric properties with time (e.g. *Grotzinger and Royden* [1990]). Our results indicate that the shape of a foredeep basin changes in time due to lateral variations in lithospheric strength, which suggests that the apparent flexural rigidity (or apparent plate thickness) may also change in time. To assess the importance of this phenomena, we computed the apparent plate thicknesses through time of idealized cases of an elastic lithosphere with lateral strength variations.

A synthetic data set of 35 points was constructed from each of the profiles shown in Figure 2.3a, using only values shallower than 4 km depth (a reasonable estimate for maximum depth of real foredeep basins) and located within a distance of 4α of the plate end (out to the small basin located forelandward of the flexural bulge). Each of these synthetic data sets was then treated as if this plate geometry had resulted from the bending of a homogeneous elastic lithosphere. A range of different uniform elastic plate thicknesses were used to fit these synthetic data (setting the initial (pre-flexural) depth constant and

using the method described by *Royden* [1988]). The uniform plate thickness that produced the minimum error was defined as the apparent plate thickness (T_{app}). By computing the apparent plate thickness of flexural profiles throughout the basin's evolution, we can observe how the apparent plate strength of an elastic plate with lateral strength inhomogeneities will change in time. In order to give less weight to the deeper (and usually less reliable) data and also to prevent the near zero (non-deflected) depths from providing overly strong constraints, errors were computed by summing over all N data points $((w_{obs} - w_{calc}) / w_{obs}^{*})^2$, where w_{obs} is the observed basin depth at a particular point, w_{calc} is the calculated basin depth, and w_{obs}^{*} is equal to the observed basin depth if greater than one half kilometer depth, or is equal to one half kilometer if the observed basin depth is less than one half kilometer depth.

A range of acceptable fits around each best fit value were also calculated, where acceptable fits are defined as plate thicknesses whose root mean square (rms) error (defined as the square root of the error divided by (N+1)) is less than a constant value (0.15) Using this criteria, some of the data sets are not acceptably fit by any apparent plate thickness. To illustrate the range of what are considered acceptable fits, Figure 2.7a shows the flexural profiles of the minimum and maximum plate thickness that acceptably fit a data set from a homogeneous elastic plate ($T_{elastic}$ = 32). In contrast, Figure 2.7b shows a data set from an inhomogeneous plate that has no acceptable fits (the 5th profile of Figure 2.3a) and the best fit flexural profile, which is still not an acceptable fit. One other point worth noting is that the with poorly fit data sets (few or no acceptable fit values) large changes in apparent plate thickness have a small effect on the error. In contrast, with a well fit data set, even small deviations in apparent plate thickness from the best fit value cause large increases in the error. Figure 2.7c compares the variation in error with apparent plate thickness of a well fit and a poorly fit data set. Note the distinctive minimum at the best fit value of the homogeneous plate versus the broad best fit minimum of the inhomogeneous, poorly fit plate. Thus, for a data set that is not acceptably fit by a uniform elastic plate, the range of

plate thicknesses that produce a fit almost as good as the best fit can become so large the significance of the best fit plate thickness value becomes questionable.

Figure 2.8b shows the apparent plate thickness (and acceptable bounds) as a function of time for the idealized foreland basin of Figure 2.3a. In general, the apparent elastic plate thicknesses stays approximately between the background elastic plate thickness ($T_{elastic}$ = 32) and the weak zone thickness (T_{weak} =16). During the transition from strong to weak (or vice versa) the plate is not acceptably fit by either strong or weak plates, and the best fit plate thickness is an intermediate value. The apparent plate thickness is most sensitive to the strength of the lithosphere located atop and slightly trenchward from the flexural bulge, where curvature reaches its maximum values. Note that in Figure 2.8 the apparent plate thickness is plotted as a function of the first zero crossing, near the point of maximum curvature.

Variations in strength contrast have the effect of varying the minimum and maximum T_{app} in a predictable manner. With a large rigidity contrast (Figure 2.8c), bending may become so substantial that the plate can only be acceptably fit by a uniform elastic plate when the weak zone is far from the zone of high curvature. As the weak zone is about to be abandoned the plate may even appear weaker than its strength within the weak zone. With only a small rigidity contrast the weak zone still has an effect on the apparent plate thickness (Figure 2.8d), as a decrease in apparent strength due to the weak zones can be seen. However, this decrease is minor and the plate can be acceptably fit by a uniform elastic plate at any point during its evolution. If the lateral extent of the weak zone is decreased (Figure 2.8e), the plate may never appear to be as weak as the weak zone, having a minimum T_{app} that is between $T_{elastic}$ and T_{weak}. In fact, the effect of a narrow weak zone could easily be mistaken for the effect of a small strength contrast (compare Figure 2.8e and 2.8d). Increasing the lateral extent of weak zones increases the amount of time the plate appears to have a rigidity equal to that in the weak zone (Figure 2.8f). Increasing the spacing between weak zones increases the amount of time T_{app} reflects the

strength of the strong part of the lithosphere (Figure 2.8g). The effect of decreasing the spacing between weak zones (Figure 2.8h) is to increase the uncertainty in the apparent plate thickness, as more of the profile is influenced by both the strong and weak parts of the plate and thus take an intermediate value and are generally not acceptably fit.

Note that plate profiles can generally be well fit by a uniform elastic plate when the zone of maximum curvature (trenchward of the flexural bulge) is entirely composed of either the strong plate or the weak zone. It is the intermediate, transition values that are more poorly fit by a uniform elastic plate. Figure 2.8 thus shows that apparent plate thickness determined by fitting the shape of the basin profile can not be applied to the lithosphere as a whole, but applies only to the zone of maximum curvature. The results obtained may not be directly applicable to adjoining areas. Care must be taken to assess the role of strength inhomogeneities and the temporal evolution of the basin before inferences about the strength of the lithosphere as a whole can be made.

Flexural Modeling of the Apennine Foredeep

As mentioned above, the effects of lateral strength variations are most easily observed through quantitative flexural modeling. One example of a flexural profile that appears to show a subducting plate with laterally varying strength is shown by the geometry of the base Pliocene in the Apennine foredeep basin. *Kruse* [1989] and *Kruse and Royden* [1994] applied a backstripping technique to existing seismic stratigraphic and open-file well log data to reconstruct the flexural geometry and initial water and sediment thickness of the Apennine foredeep basin at time horizons with identifiable paleontological markers. Figure 2.9 shows the depth to the base of the Pliocene at points in the basin where depth reconstructions were possible. We assumed the initial water depth (shown in Figure 2.9) and infilling sediment density profile (increasing density with depth from 2300 to 2600 kg/m^3) of *Kruse and Royden* [1994] then fit the observed base Pliocene deflection data as

described above. We obtained a best fit uniform elastic plate thickness of 9.5 km (Figure 2.9) in good agreement with the 10 km best fit of *Kruse and Royden* [1994]

However, it is clear from Figure 2.9 that a 10 km uniform elastic plate does not adequately fit the data, especially between kilometers 240 and 260, where the reconstructed deflections reach their maximum height, and forelandward of kilometer 260 where deflection heights begin to decrease. The computed deflection is not able to mimic either of these observations. The observed deflection data, with its localized zone of positive deflection and abrupt change of slope near that localized zone, has a form similar to that of the "unacceptably fit" profile of Figure 2.7b, suggestive of a subducting lithosphere varying laterally in strength. Figure 2.9 shows the result of incorporating into the subducting plate a 20 km long weak zone (located between kilometers 240 and 260) of half the surrounding plate thickness (T_{weak} = 1/2 $T_{elastic}$). Clearly a better fit to the data (with $T_{elastic}$ = 8.5 km, T_{weak} = 4.25 km) has been obtained, and the computed profile is now able to mimic the data in reaching a minimum depth between kilometers 240 and 260 , with a local increase in depth toward the foreland. It should also be noted that while the 10 km uniform elastic plate fit is a true "best fit" to the data (found using an inverse technique), the fit with the incorporated weak zone is not a best fit, but simply one example of a fit (found by trial and error) which is clearly better than the uniform elastic case. Relaxing the constraints on the location, extent and strength contrast of the weak zone may also improve the fit of the model to the data.

ENHANCEMENT OF EPISODICITY BY INELASTIC YIELDING

Rheology

The preceding section indicates that basin episodicity can result from application of a constant load, migrating in time, to a perfectly elastic plate with lateral inhomogeneities in flexural strength. Significant episodicity in basin development results only when the strength

variations are equivalent to roughly an order of magnitude in flexural rigidity (or a factor of two in effective elastic plate thickness). However, the effects of weak segments within the foreland lithosphere are greatly enhanced when brittle and ductile yielding are included, as inelastic yielding concentrates bending of the lithosphere into localized, highly flexed zones and reduces the bending in the adjacent parts of the lithosphere (e.g. *McNutt and Menard* [1982], *McAdoo et al.* [1978], *Beaumont* [1978]).

The effects of inelastic yielding can be illustrated by using a lithospheric rheology constructed after *Goetze and Evans* [1979] (based on olivine deformation parameters) that incorporates brittle failure in the upper lithosphere and ductile failure in the lower lithosphere at high differential stresses. In between the zones of brittle and ductile failure, an "elastic core" develops where strains are recoverable when the stresses fall to zero. In this zone, strain is directly proportional to differential stress, and thus to the curvature of the plate. Curvature therefore plays an important role in determining the amount of yielding - higher curvatures produce greater yielding. Note that incorporation of a more continental rheology, i.e. using quartz flow laws in the lower crust, will further enhance the effects of inelastic yielding and in the extreme could decouple bending of the crust and mantle parts of the plate (e.g. *McNutt et al.* [1988]). For simplicity we have used an olivine rheology throughout this paper.

When inelastic yielding occurs, the state of stress of the lithosphere is controlled not only by the final curvature of the plate, but also by its entire strain history. Beginning from a state of lithostatic stress, initial bending stresses may be sufficiently small such that they do not exceed the yield criteria (Figure 2.10a). Flexure is perfectly elastic and strains are entirely recoverable. In the absence of yielding, the mechanical plate thickness, T_{mech}, defined as the elastic plate thickness at zero curvature, is the same as the elastic plate thickness for a small increment of bending, T_{inc}, which is defined as the thickness of the elastic core of the lithosphere during that bending increment (shown by the vertical bar to the right of the yield envelopes in Figure 2.10). T_{inc} can also be computed mathematically from D_{inc} =

$-\Delta M/\Delta w_{xx}$, where D_{inc} is the flexural rigidity during an increment of curvature and ΔM is the incremental increase in moment generated by an incremental increase in curvature, Δw_{xx}. As curvature increases so do the bending stresses within the elastic core. When the bending stresses become large enough to reach the yield criteria, brittle and ductile yielding occur at the top and the bottom of the plate respectively, decreasing the thickness of the elastic core. Thus, at curvatures high enough to cause yielding, T_{inc} will be less than T_{mech} (Figure 2.10b). As the curvature continues to increase, more yielding occurs and the moment generated during each increment of curvature decreases. T_{inc} can decrease to almost zero, so that an increase in curvature has almost no effect on the generated moment, a condition known in the engineering literature as "moment saturation".

When the plate is unflexed and curvature decreases, elastic stresses and strains stored in the lithosphere must be relieved but inelastic strains are not recoverable. As a result, for a small initial decrease in curvature, the release of stored elastic stresses causes T_{inc} to return its original thickness, equal to T_{mech}, regardless of the amount of previous yielding during flexure (Figure 2.10c). As unflexing continues, the residual elastic stresses are relieved and bending stresses on the other side of the yield envelope accumulate until the yield criteria is exceeded, causing the incremental elastic thickness to decrease once again, so that $T_{inc} < T_{mech}$, (Figure 2.10d). The incremental strength of the lithosphere is thus controlled by both the yield history of the plate and by the plate's present curvature. The stress distribution within the plate can become rather complicated when the plate has been flexed and then unflexed.

Figure 2.11a shows the relationship between T_{mech} and T_{inc} for the last increment of bending assuming unidirectional flexure starting from a lithostatic stress distribution, As discussed above, at zero curvature $T_{inc} = T_{mech}$, but even at relatively small curvatures, $T_{inc} < T_{mech}$. At high curvatures we approach moment saturation and T_{inc} may become very small. However, this does not mean the lithosphere as a whole appears extremely thin. As defined by *McNutt* [1984], an "effective" elastic plate strength of the lithosphere as a whole, D_{eff}, can

be found from the total moment divided by the total curvature (Figure 2.11b). In other words, the effective elastic plate thickness, T_{eff}, will be thickness of a perfectly elastic layer required to generate a moment equal to the moment generated by the stresses stored in the brittle-elastic-ductile lithosphere at the observed curvature. Under uni-directional bending and yielding, T_{eff} will be greater than T_{inc}. As defined in this way, T_{eff} gives an average measure of the plate strength during bending. In contrast, T_{inc} gives a measure of the plate strength during bending from its present curvature to a slightly larger or smaller curvature. Thus it is T_{inc} that accurately represents the response of the inelastic lithosphere to changes in curvature.

Method

Using the rheology described above, plate deflections for the case of inelastic yielding were found by solving the flexure equation with flexural rigidities, D_{inc}, that varied as a function of plate bending and yield history. An initial deflection profile was found by applying a subduction load, P_{end}, to the end of the plate in small increments. For each increment of load added to the plate end, an iterative process was used to compute the incremental deflection and incremental rigidity such that $D_{inc} = - \Delta M/\Delta w_{xx}$ at each point. After each increment of loading, the deflection increment is added to the total deflection and the stress state at each location along the plate is recorded so that D_{inc} for the next increment of loading can be computed.

After the initial deflection of the plate has been computed, the load is advanced toward the foreland at a constant rate to simulate subduction. For a plate with a uniform mechanical strength, T_{mech}, this will eventually result in a steady-state plate profile that will be different from the initial deflection profile (because of the dependence of D_{inc} on the yield history at each point). In this study we neglect the pre-steady state deflections of the plate. Note that in the case of a plate with strength inhomogeneities, the weak zones are initially located far behind the flexural bulge so they neither affect nor are affected by the minor fluctuations prior to achieving steady state.

Computationally, advancing the subduction load toward the foreland involves finding the difference between the vertical shear force and the bending moment at the plate end (at node 0) and at the node adjacent to (and toward the foreland from) the plate end (node 1). The load and moment at the plate end, P_0 and M_0, are those specified as the subduction load ($P_0 = P_{end}$, $M_0 = 0$). P_1 was computed by integrating the deflection (times gravity and the density contrast between the material above and below the flexing lithosphere) from node 1 to "infinity" (node 300) and requiring all the vertical forces acting on the plate between node 1 and node 300 to sum to zero. M_1 was found by summing $D_{inc}*\Delta w_{xx}$ over the entire bending history at node 1. The "subduction load" was then transferred from node 0 to node 1 by incrementally applying an additional load and moment, ΔP ($= P_{end} - P_1$) and ΔM ($= 0 - M_1$), to node 1, iterating as described above. After all increments of ΔP and ΔM have been applied to the plate, the load and moment at node 1 will be P_{end} and 0 and node 0 will effectively have been "subducted". By advancing the load in this manner and recording the stress state after each increment of load, we achieve the effect of incorporating very small increments of bending into the yield envelope without needing an intractably fine node spacing.

A finite point spacing introduces an intrinsic trade off between numerical precision and accuracy of the finite difference method. At fine point spacing high accuracy is attained, but numerical precision is lost. To ensure at least 99% accuracy of the finite difference code and to minimize the effect of loss of precision, we apply a constraint that D_{inc} cannot be less than 0.035% of the original plate rigidity, D_{mech} (T_{inc} cannot be less that about 7 % of T_{mech}). (Accuracy is tied to the absolute point spacing and we have chosen the point spacing to be a function of D_{mech}, thus there is a correlation between D_{mech} and the minimum D_{mech} for which accuracy can be maintained.) Although this is a numerical constraint, a minimum bound on the effective plate thickness is not geologically unreasonable, as extremely small effective plate thicknesses (much less than about 1 km) are seldom seen, even in extremely hot, weak, extended regions such as the Basin and Range [*Block and Royden* 1990; *Weissel and Karner* 1989].

Results

Figure 2.12a shows the geometry of a foreland basin constructed using the rheology shown in Figure 2.10. The assumptions were the same as those used in constructing Figure 2.1 except that the initial elastic plate thickness (T_{mech}) was chosen to be 40 km. This was done because inelastic yielding of the lithosphere makes the plate weaker; this value of T_{mech} produced a foredeep basin geometry similar in wavelength to that produced by flexure of a perfectly elastic plate with an elastic plate thickness of 32 km (Figure 2.1a) under an applied end load of 1.8×10^{12} N/m. As in the perfectly elastic case, the foredeep basin geometry remains constant through time, but is shifted progressively toward the foreland. Note, however, that the overall shape of the basin and the flexural bulge differs somewhat from the perfectly elastic case.

Figure 2.12b shows the geometry of the foredeep basin when the foreland lithosphere has a background strength that is defined by T_{mech}=40 km, but with two weak zones embedded in the lithosphere. The strength of these weak zones is defined by T_{weakm}=35 km, and their spacing and width are the same as those used in Figure 2.3a. The resulting basin geometry is episodic in time, and behaves in much the same way as the episodic basin generated in the perfectly elastic case (i.e. varying spacing and width of the weak zones has the same effect as in the elastic case.) However, the strength contrast within the foreland needed to generate this episodic behavior is much less that in the perfectly elastic case, requiring in this case only a 12.5 % difference in T_{mech}. Thus, when the effects of inelastic yielding are included, even relatively minor strength variations in the foreland lithosphere can produce an irregular and episodic foredeep basin development.

It should be noted that when considering inelastic yielding, episodic behavior depends on both the mechanical plate thickness and the magnitude of the lateral strength contrast. For example, Figure 2.12c shows the deflection of a plate with a mechanical plate thickness of 80 km, double that of Figure 2.12b, and with embedded weak zones that have

T_{weakm} = 70 km, 12.5% less than the surrounding areas. The load applied to the 80 km plate is increased to give the same end deflection on an 80 km elastic plate as occurs with a 40 km elastic plate. The resulting deflections in Figure 2.12c are a series of plate profiles whose geometry does not vary in time, but are merely translated toward the foreland. Thus, the strength contrast required to induce bulge localization is a function of initial plate thickness. This occurs because, under a specified bending stress, a weaker plate will have greater curvature and undergo greater inelastic yielding than a stronger plate. Weaker lithosphere is therefore more likely to display episodic behavior than stronger lithosphere and also requires a smaller strength contrast to induce *any* episodic behavior.

The lateral contrast in lithospheric strength required to cause deviations from the homogeneous elastic profile is decreased by including inelastic yielding, but it is still non-negligible (generally greater than 10% of T_{mech}, depending on the rheology and initial plate thickness). We might therefore expect relatively homogeneous oceanic lithosphere to be less likely than the inhomogeneous continental crust to display episodic flexure.

Apparent plate thickness

Two primary factors control the apparent plate thickness of inelastically yielded lithosphere. The first is the apparent weakening of the plate due to inelastic yielding, the second is the change in apparent plate thickness induced by the weak zones within the lithosphere. The latter has been discussed above in the perfectly elastic case, so we now turn our attention to the change in apparent plate thickness due to inelastic yielding. In an earlier study, *McNutt* [1984] suggested that correcting for the amount of yielding at the point of maximum curvature should be sufficient to recover the initial (or pre-flexural) elastic plate thicknesses (T_{mech}).

To test this idea, we computed flexural profiles due to bending of a plate with a uniform mechanical plate thickness (40 km). The apparent elastic plate thickness was then determined by generating a synthetic deflection data set and fitting these data with a uniform

elastic model, (as described above in the section on perfectly elastic lithosphere). Once the best fit uniform elastic plate deflection profile is found, the curvature of the best fit profile is also known, and we can attempt to recover T_{mech} from T_{app} using the maximum curvature attained along the elastic profile and the relationships (illustrated in Figure 2.11b) between T_{mech}, T_{app} (equated with T_{eff}), and curvature. If correcting for yielding based on the maximum curvature is sufficient, the recovered mechanical plate thicknesses will be the mechanical plate thickness used to generate the synthetic data set.

Figure 2.13 shows the results of our attempt to recover the mechanical plate thickness of profiles generated by a plate of T_{mech} = 40 km. A range of apparent plate thicknesses can result from the same T_{mech} = 40 by varying the applied end load, thereby changing the curvature and the amount of yielding within the plate, producing different flexural geometries. If the correction for inelastic yielding is sufficient, all recovered T_{mech} values should plot on a line of T_{mech} = 40 km, regardless of the apparent plate thickness. What we see instead in Figure 2.13 is a consistent trend of underestimating the correction for yielding when this technique is applied. Thus, the estimated value for the mechanical plate thickness can be considered a lower bound for the true mechanical plate thickness. In lieu of a better recovery method, this correction is applied to the following results with the caveat that the true mechanical plate thickness must be greater than the estimated mechanical plate thickness (except where curvature is very small, making inelastic yielding unimportant; in these cases, the recovered plate thickness should be equal to the initial plate thickness).

The results of fitting the synthetic data from the profiles of Figure 2.12b and 2.12c to perfectly elastic plates are shown in Figure 2.14, as is an attempt to estimate the mechanical plate thickness from the profiles of Figure 2.12b by correcting for inelastic yielding as described above. The results found for the elastic case hold true. When episodicity is observable (Figure 2.14a) and the zone of maximum curvature contains both strong and weak lithosphere, the plate cannot be acceptably fit by an elastic plate of any thickness.

However, when one strength dominates the zone of maximum curvature, a single plate thickness can acceptably fit the generated data set. Figure 2.14b shows the same values of T_{app} and the estimated values of T_{mech}. While these values are close to the mechanical plate thickness, they underestimate the plate's strength, as discussed above. Figure 2.14c shows that even the very small rigidity contrast, such that weak zones are not discernible in the profiles, affects the best fit value.

CONCLUSION

We can make the following conclusions from this study of the effect of lateral strength variations and inelastic yielding on continental foredeep basins:

1) Some basins exist, both modern (e.g. the Apennine foredeep) and ancient (e.g. the Kilohigok basin) that contain stratigraphy consistent with evolution through time of a deepening foreland basins adjacent to a localized flexural bulge. The localized flexural bulge could possibly be caused by lateral variation in strength of the lithosphere (weak zones) that serve to localize plate curvature.

2) Lithospheric inhomogeneities can cause episodic behavior of the lithosphere even under constantly migrating loads.

3) Incorporating weak zones introduces three new variables to the system: strength contrast, weak zone length, and spacing between weak zones. For an elastic rheology, a 50% contrast in effective elastic thickness and a minimum length of $\alpha/60$ are required to induce significant episodic behavior.

4) The apparent plate thickness (T_{app}) computed from fitting uniform elastic profiles to a laterally varying lithosphere is going to be biased by the lithospheric strength beneath and just trenchward of the flexural bulge, where curvatures are the highest. The results may be so biased by this small area of lithosphere as to not be applicable even to the adjacent lithosphere.

5) When inelastic yielding is important, plate deflection computations will be sensitive to curvature and stress state. When computing how the plate will react to continued bending, the entire strain history and the strength of the plate at that point (D_{inc}) must be considered. The average strength of the lithosphere (D_{eff}) is not sufficient. In addition, loading must be modeled as an incremental process as even small changes in curvature (particularly changes in the direction of curvature) can have a dramatic effect on incremental plate strength (D_{inc}).

6) Inelastic yielding in and of itself serves to localize curvature and thus to decrease the magnitude of the strength contrast needed for a weak zone to cause plate episodicity. Because larger loads will cause greater curvatures (and thus greater amounts of inelastic yielding), the magnitude of the strength contrast needed to cause episodicity will be a function of the load size and mechanical plate strength. As a rough estimate, only a 10-15% strength contrast is needed for significant episodicity in a 20-40 km mechanical plate, but a larger strength contrast is needed for a thicker (80 km) plate since less inelastic yielding occurs in a thicker plate. (Incorporation of a continental rheology may further decrease the required strength contrast.)

7) Attempts to recover the initial (pre-flexural) plate thickness based on correcting best fit elastic plate profiles for the maximum curvature attained will systematically underestimate the initial plate thickness, but the plate thickness recovered by this correction may be considered as a minimum bound on the initial plate thickness.

REFERENCES

Barberi, F., F. Innocenti, G. Ferrara, J. Keller, and L. Villari, 1974, Evolution of eolian arc volcanism (southern Tyrrhenian Sea), *Earth Planet. Sci. Lett.*, **21**, 269-276.

Beaumont, C., 1978, The evolution of sedimentary basins on a viscoelastic lithosphere: theory and examples, *Geophys. J. R. astr. Soc.*, **55**, 471-497.

Block, L. and L. H. Royden, 1990, Core complex geometries and regional scale flow in the lower crust, *Tectonics*, **9**, 557-567.

Bodine, J. H., 1981, Numerical computations of plate flexure in marine geophysics, *Technical Report 1*, Columbia University, 153 pp.

Brace, W. F. and D. L. Kohlstedt, 1980, Limits on lithospheric stress imposed by laboratory experiments, *J. Geophys. Res.*, **85**, 6248-6252.

Bradley, D. C., and T. M. Kusky, 1986, Geologic evidence for rate of plate convergence during the Taconic arc-continent collision, *J. of Geology*, **94**, 667-681.

Civetta, L., G. Orsi and P. Scandone, 1978, Eastwards migration of the Tuscan anatectic magmatism due to anticlockwise rotation of the Apennines, *Nature*, **276**, 604-606.

Dondi, L., A. Rizzini, and P. Rossi, 1985, Recent geological evolution of the Adriatic Sea, *in* Geological Evolution of the Mediterranean Basin, D. J. Stanley and F. C. Wezel, eds., pp. 195-214.

Gasparini, C., G. Iannaccone, P. Scandone and R. Scarpa, 1982, Seismotectonics of the Calabrian Arc, *Tectonophysics*, **84**, 267-286.

Goetze, C., and B. Evans, 1979, Stress and temperatures in the bending lithosphere as constrained by experimental rock mechanics, *Geophys. J. R. astr. Soc.*, **59**, 463-478.

Grotzinger, J. P., and D. S. McCormick , 1988, Flexure of the Early Proterozoic lithosphere and the evolution of the Kilohigok Basin (1.9 Ga), Northwest Canadian shield, in New Perspectives in Basin Analysis, K. L. Kleinspehn and C. Paola, eds., pp. 405-430.

Grotzinger, J. P., D. S. McCormick, and S. M. Pelechaty, 1987, Progress report on the stratigraphy, sedimentology and significance of the Kimerot and Bear Creek group, Kilohigok Basin, District of Mackenzie, Current Research Part A, Geological Survey of Canada, Paper 87-1A, pp. 219-238.

Grotzinger, J., and L. Royden, 1990, Elastic strength of the Slave craton at 1.9 Ga and implications for the thermal evolution of the continents, *Nature*, **347**, 64-66.

Gunn, R., 1943, A quantitative study of isobaric equilibrium and gravity anomalies in the Hawaiian Islands, *Franklin Inst. J.*, **236**, 373-390.

Jarrad, R. D., 1986, Relations among subduction parameters, *Rev. of Geophys.*, **24**, 217-284.

Jordan, T. E., 1981, Thrust loads and foreland basin evolution, Cretaceous, western United States, *AAPG Bulletin*, **65**, 2506-2520.

Judge, A. V., and M. K. McNutt, 1991, The relationship between plate curvature and elastic plate thickness: a study of the Peru-Chile trench, *J. Geophys. Res.*, **96**, 16,625-16,639.

Karner, G. D., M. S. Steckler and J. A. Thorne, 1983, Long-term thermo-mechanical properties of the continental lithosphere, *Nature*, **304**, 250-253.

Karner, G. D., and A. B. Watts, 1983, Gravity anomalies and flexure of the lithosphere at mountain ranges, *J. Geophys. Res.*, **88**, 10,449-10,477.

Kruse, S. E., 1989, Deformation of continental lithosphere: studies in the Ural Mountains, the Adriatic region and the western United States, Ph.D. Thesis, MIT, pp. 215.

Kruse, S. E., and L. H. Royden, 1994, Bending and unbending of an elastic lithosphere: The Cenozoic history of the Apennine and Dinaride foredeep basins, *Tectonics*, **13**, 278-302.

Lyon-Caen, H., and P. Molnar, 1983, Constraints on the structure of the Himalaya from an analysis of gravity anomalies and a flexural model of the lithosphere, *J. Geophys. Res.*, **88**, 8171-8191.

Lyon-Caen, H., and P. Molnar, 1985, Gravity anomalies, flexure of the Indian plate and the structure, support and evolution of the Himalaya and Ganga basin, *Tectonics*, **4**, 513-538.

McAdoo, D. C., J. G. Caldwell, and D. L. Turcotte, 1978, On the elastic-perfectly plastic bending of the lithosphere under generalized loading with application to the Kuril Trench, *Geophys. J. R. astr. Soc.*, **54**, 11-26.

McCormick, D. S., and J. P. Grotzinger, 1992, Stratigraphic evolution of the early Proterozoic (1.9 Ga) Burnside Formation alluvial foreland basin sequence, Kilohigok Basin, N.W.T., Canada, *Basin Research*, **4**, 253-278.

McNutt, M. and H. Menard, 1982, Constraints on yield strength in the oceanic lithosphere derived from observations of flexure, *Geophys. J. R. astr. Soc.*, **71**, 363-394.

McNutt, M. K., 1984, Lithospheric flexure and thermal anomalies, *J. Geophys. Res.*, **89**, 11,180-11,194.

McNutt, M. K., M. Diament and M. G. Kogen, 1988, Variations of elastic plate thickness at continental thrust belts, *J. Geophys. Res.*, **93**, 8825-8838.

Pieri, M. and G. Groppi, 1981, Subsurface geological structure of the Po plain, Italy, *Publ. 414*, Final Geodyn. Proj., Italy, 1-13.

Price, R. A., 1973, Large-scale gravitational flow of supracrustal rocks, southern Canadian Rockies, in Gravity and Tectonics, K. A. DeJong and R. Scholte, eds., pp. 491-502.

Royden, L. and G. D. Karner, 1984, Flexure of lithosphere beneath Apennine and Carpathian foredeep basins: evidence for an insufficient topographic load, *AAPG Bulletin*, **68**, 704-712.

Royden, L., 1988. Flexural behavior of the continental lithosphere in Italy: constraints imposed by gravity and deflection data, *J. Geophys. Res.*, **93**, 7747-7766.

Royden, L.H., 1994 , The tectonic expression of slab pull at continental convergent boundaries, *Tectonics*, **12**, 303-325.

Sheffels, B., and M. McNutt, 1986, Role of subsurface loads and regional compensation in the isostatic balance of the Traverse Ranges, California: evidence for intracontinental subduction, *J. Geophys. Res.*, **91**, 6419-6431.

Walcott, R. I., 1970, Flexural rigidity, thickness and viscosity of the lithosphere, *J. Geophys Res.*, **75**, 3941-3954.

Watts, A. B., 1978, An analysis of isostasy in the worlds oceans 1. Hawaiian - Emperor seamount chain, *J. Geophys. Res.*, **83**, 5989-6004.

Weissel, J. K., and G. D. Karner, 1989, Flexural uplift of rift flanks due to mechanical unloading of the lithosphere during extension, *J. Geophys. Res.*, **94**, 13,919-13,950.

Table 2.1. Definition of Variables Relating to Plate Thickness (or Flexural Rigidity)[a]

$T_{elastic}$ ($D_{elastic}$)	Thickness (flexural rigidity) of a uniform elastic layer (lithosphere)
T_{weak} (D_{weak})	Thickness (flexural rigidity) of a localized area of elastic lithosphere surrounded by lithosphere of thickness $T_{elastic}$
T_{mech} (D_{mech})	Thickness (flexural rigidity) of a brittle-elastic-ductile lithosphere at zero curvature (prior to yielding)
T_{weakm} (D_{weakm})	Thickness (flexural rigidity) of a localized area of brittle-elastic-ductile lithosphere at zero curvature (prior to yielding) surrounded by lithosphere of thickness T_{mech}
T_{app} (D_{app})	Thickness (flexural rigidity) of a uniform elastic layer that best fits the observed data points (see text for details)
T_{inc} (D_{inc})	Thickness (flexural rigidity) of the elastic core of a brittle-elastic-ductile lithosphere during a small increment of curvature
T_{eff} (D_{eff})	Thickness (flexural rigidity) of a uniform elastic layer required to generate a bending moment and curvature equal to those obtained by bending of brittle-elastic-ductile lithosphere

[a] Plate thickness can be converted to a flexural rigidity through the equation $D = E\,T^3 / 12 / (1-\nu^2)$ where $E = 8.53 \times 10^{10}$ N/m^2 and $\nu = 0.25$ (value of E from *McNutt* [1984])

FIGURE CAPTIONS

Figure 2.1: Flexural behavior of a subducting elastic plate of uniform strength. (a) Flexural geometry through time as shown by profiles at equally spaced time intervals. The frame of reference is fixed with respect to the foreland and the trench advances to the right with time. Circles above each profile locate the point of maximum elevation over the top of the flexural bulge (also at equally spaced time intervals). Elastic plate thickness (32 km) is shown at top. (b) Time - space diagram of basin evolution. Shading patterns reflect variations in subsidence (sediment depositional) rates. (c) Synthetic stratigraphy of a basin formed on a uniform elastic plate shown by equally spaced time lines that were all originally horizontal depositional surfaces.

Figure 2.2: Examples of foredeep basins with possible non-continuous evolutionary development. (a) Basin stratigraphy through the Early Proterozoic Kilohigok basin (simplified from *McCormick and Grotzinger*, [1992] and (b) depth to the middle Pliocene and base Pliocene within the modern Apennine foredeep basin (of Pliocene-Quaternary age). Symbols show the current depth within the basin, lines show the best-fitting model depth computed by *Kruse and Royden* [1994] (simplified from *Kruse and Royden* [1994]).

Figure 2.3: Flexural behavior of a subducting elastic plate of non-uniform strength. (a) Flexural geometry through time as shown by profiles at equally spaced time intervals The frame of reference is fixed with respect to the foreland and the trench advances to the right with time. Circles above each profile locate the point of maximum elevation over the top of the flexural bulge (also at equally spaced time intervals). Elastic plate thickness (32 km with two weak segments of 16 km) is shown at top. (b) Time - space diagram of basin evolution. Shading patterns reflect variations in subsidence (sediment

depositional) rates. (c) Synthetic stratigraphy of a basin formed on a non-uniform elastic plate shown by equally spaced time lines that were all originally horizontal depositional surfaces.

Figure 2.4: Flexural geometry of a subducting elastic plate of non-uniform strength through time as shown by profiles at equally spaced time intervals. The frame of reference is fixed with respect to the foreland and the trench advances to the right with time. Circles above each profile locate the point of maximum elevation over the top of the flexural bulge (also at equally spaced time intervals). Elastic plate thickness (32 km with two embedded weak zones) is shown at top. (a) Weak zones with elastic plate thickness of 8 km. (b) Weak zones with elastic plate thickness of 24 km.

Figure 2.5: Flexural geometry of a subducting elastic plate of non-uniform strength through time as shown by profiles at equally spaced time intervals. The frame of reference is fixed with respect to the foreland and the trench advances to the right with time. Circles above each profile locate the point of maximum elevation over the top of the flexural bulge (also at equally spaced time intervals). Elastic plate thickness (32 km with two weak segments of 16 km) is shown at top. (a) Narrow weak zones width ($\alpha/30$). (b) Wide weak zones width($4\alpha/3$).

Figure 2.6: Flexural geometry of a subducting elastic plate of non-uniform strength through time as shown by profiles at equally spaced time intervals The frame of reference is fixed with respect to the foreland and the trench advances to the right with time. Circles above each profile locate the point of maximum elevation over the top of the flexural bulge (also at equally spaced time intervals). Elastic plate thickness (32 km with two weak segments of 16 km) is shown at top. (a) Large spacing between two weak zones. (b) Close spacing between three weak zones.

Figure 2.7: a) Examples of the limits of acceptable fits to a synthetic data set from a uniform elastic plate with Te = 32 km. Solid line is profile from maximum acceptable elastic plate thickness, T_{app} = 39.5 km. Dashed line is profile from minimum acceptable elastic plate thickness, T_{app} = 23.5 km. b) Example of a synthetic data set (from the fifth profile of Figure 2.3a) for which there are no acceptable fits. Profile shown is the best fit profile (although not an acceptable fit). c) RMS error for fits to synthetic data sets shown in (a) (dashed line) and (b) (solid line) as a function of T_{app}.

Figure 2.8: Apparent plate thickness through time for deflection profiles shown in Figures 2.1 and 2.3 - 2.6. Apparent plate thickness is plotted as a function of the location of the first zero crossing (closest to the plate end). Solid line indicates strength of the lithosphere for each model case, short dashed line indicates best fit apparent plate thickness at each time step, long dashed lines are the minimum and maximum acceptable plate thicknesses. Points represent the apparent plate thickness fit to the profiles shown in the corresponding figure.

Figure 2.9: Data points from the reconstructed flexural geometry of the base Pliocene in the Apennine foredeep basin (from *Kruse* [1988]). Long dashed line is initial water depth. Short dashed line is best fit model using a uniform elastic plate thickness 9.5 km. Solid line is fit of a elastic plate ($T_{elastic}$ = 8.5 km) with an incorporated weak zone (from kilometers 240 to 260) of thickness T_{weak} = 4.25 km.

Figure 2.10: State of stress and incremental elastic plate thickness in a brittle-elastic-ductile lithosphere as a function of depth and yield (bending) history (failure criteria after *Goetze and Evans* [1979]; tension is defined as positive). Initial thickness of the "elastic core" at zero curvature is 40 km. Apparent plate thickness from incremental

bending (each bending increment shown is 10^{-7} m^{-1}) is shown by the vertical bar. a) stress state for initial lithospheric flexing ($T_{inc} \approx T_{mech}$). b) stress state after considerable lithospheric flexing ($T_{inc} < T_{mech}$). c) stress state immediately following initiation of unflexing ($T_{inc} \approx T_{mech}$). d) stress state after considerable unflexing ($T_{inc} < T_{mech}$).

Figure 2.11: (a) Incremental elastic plate thickness (due to inelastic yielding) as a function of curvature for T_{mech} = 100, 80, 60, 40 20, 10 km. (see Figure 2.9) (b) Effective elastic plate thickness as a function of curvature for T_{mech} = 100, 80, 60, 40 20, 10 km.

Figure 2.12: Flexural geometry through time of a subducting plate with a brittle-elastic-ductile rheology as shown by profiles at equally spaced time intervals. The frame of reference is fixed with respect to the foreland and the trench advances to the right with time. Circles above each profile locate the point of maximum elevation over the top of the flexural bulge (also at equally spaced time intervals). Mechanical plate thickness shown at top (a) Geometry of a uniform plate (T_{mech} = 40 km). (b) Geometry of a yielded plate (T_{mech} = 40 km) with two weak zones (T_{weakm} = 35 km). (c) Geometry of a yielded plate (T_{mech} = 80 km) with two weak zones (T_{weakm} = 70 km).

Figure 2.13: Effect of correcting apparent plate thickness for inelastic yielding using the method of *McNutt* [1984]. All points derived from a 40 km mechanical plate subject to various end loads. Points represent the best fit apparent elastic plate thickness and the recovered mechanical plate thickness from the correction for inelastic yielding. Error bars run from the minimum acceptable apparent plate thickness (and the associated recovered mechanical plate thickness) to the maximum acceptable apparent plate thickness (and the associated recovered mechanical plate thickness). All points would

plot on the dashed line through T_{mech} = 40 km if the correction for inelastic yielding was sufficient. The correction consistently underestimates the mechanical plate thickness.

Figure 2.14: (a) Apparent plate thickness through time for deflection profiles shown in Figure 2.12b. Short dashed lines indicate best fit apparent plate thickness at each time step, long dashed lines are the minimum and maximum acceptable plate thicknesses. (b) Apparent plate thickness (dashed line) and recovered mechanical plate thickness (dotted line) through time from the deflection profiles of Figure 2.12b. (c) Apparent plate thickness through time for deflection profiles shown in Figure 2.12c. Short dashed lines indicate best fit apparent plate thickness at each time step, long dashed lines are the minimum and maximum acceptable plate thicknesses. The plate thicknesses of (a), (b), and (c) are all plotted as a function of the location of the first zero crossing (closest to the plate end).

Figure 1a

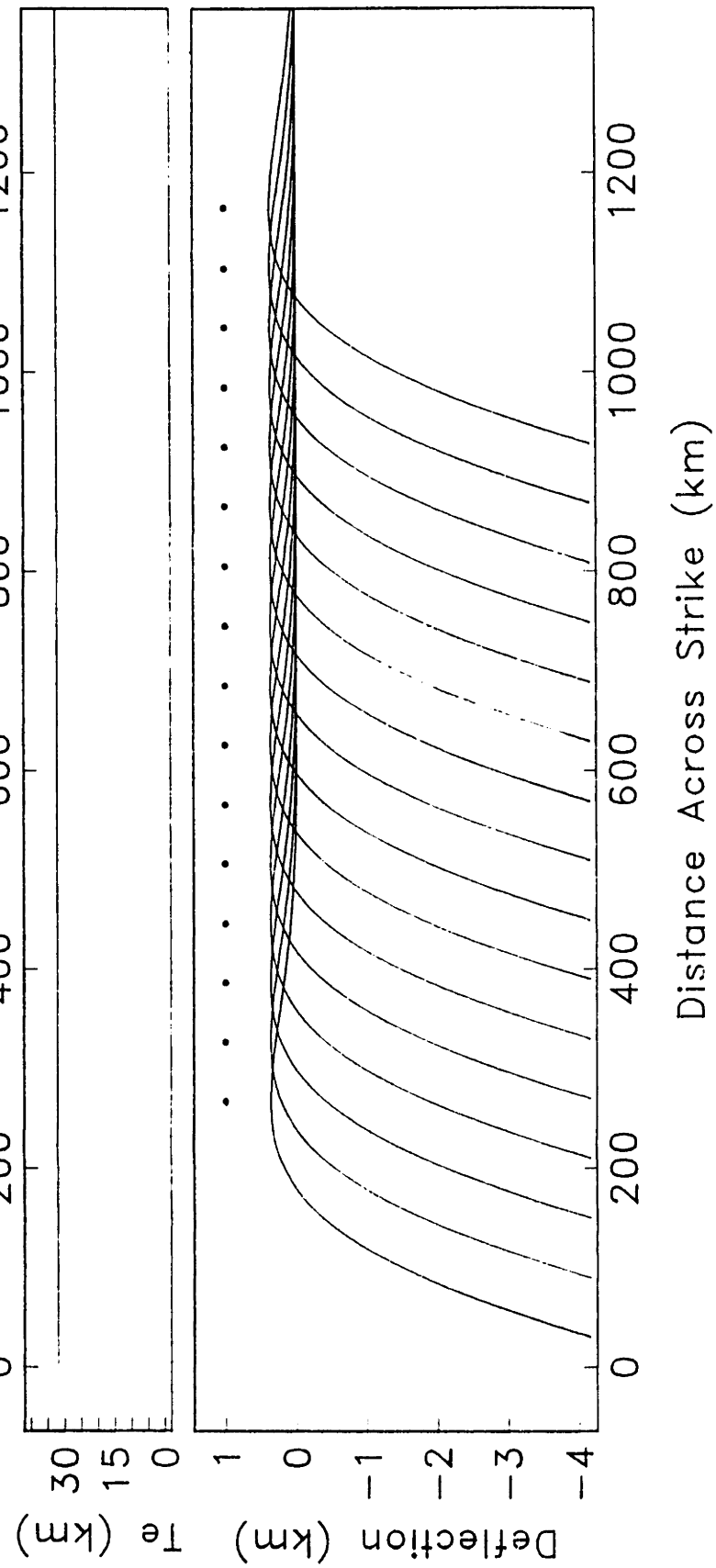

Figure 2.1a

Figure 1b

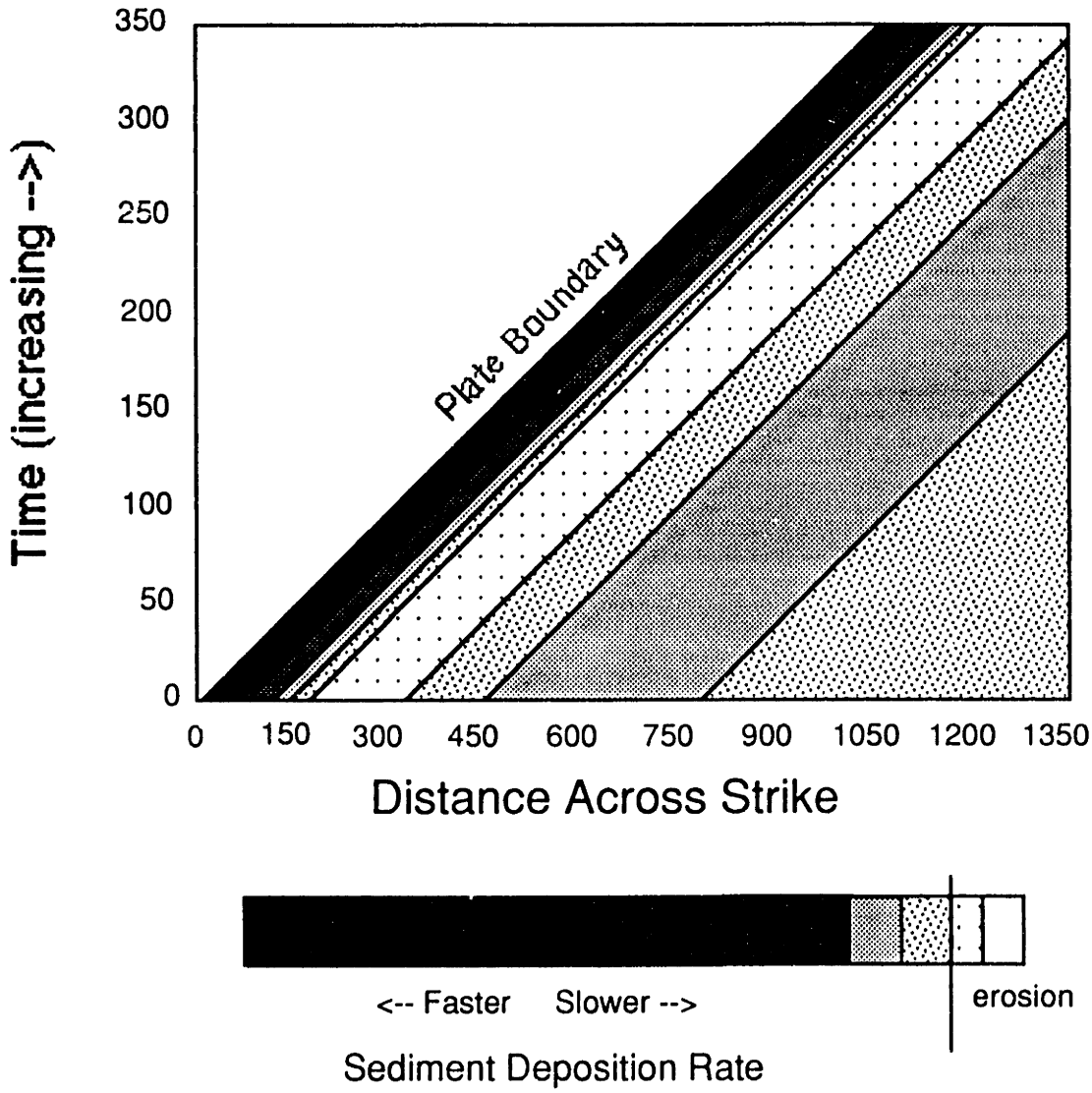

Figure 2.1b

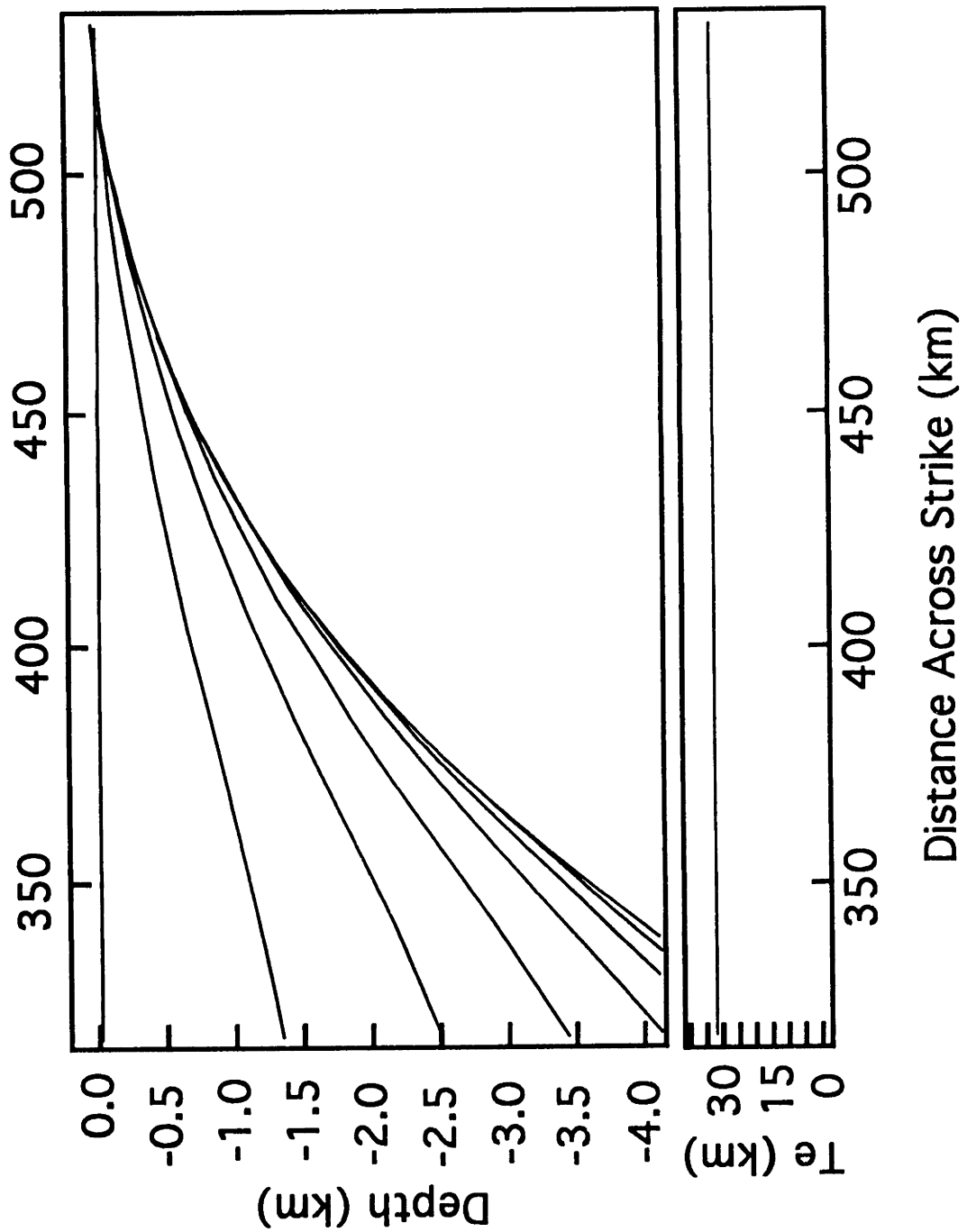

Figure 1c

Figure 2.1c

Kilohigok Basin Stratigraphy

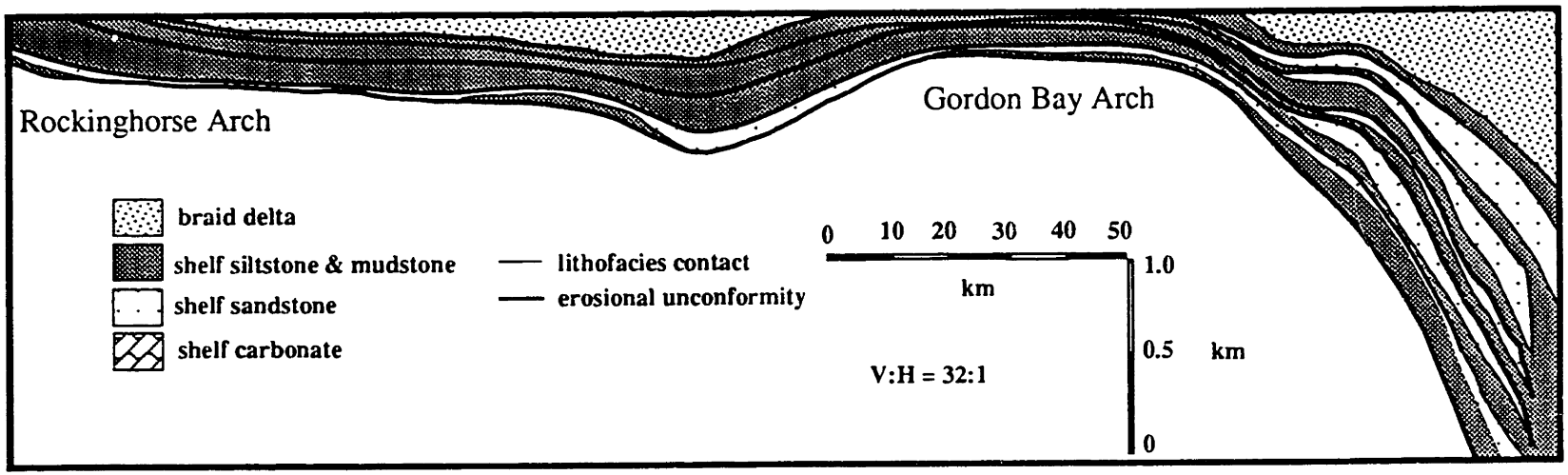

simplified after Grotzinger and McCormick, 1992

Figure 2a

Figure 2.2a

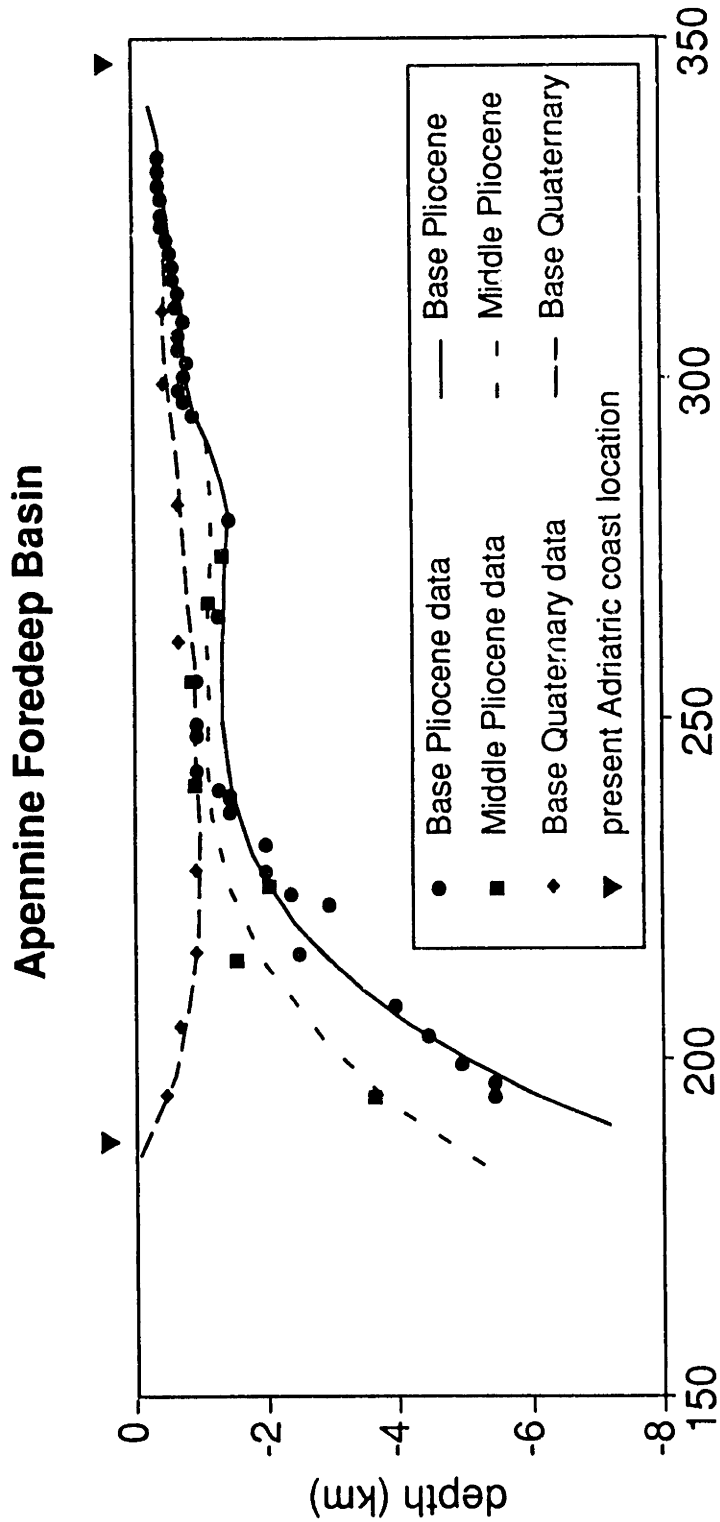

Figure 2b

Figure 2.2b

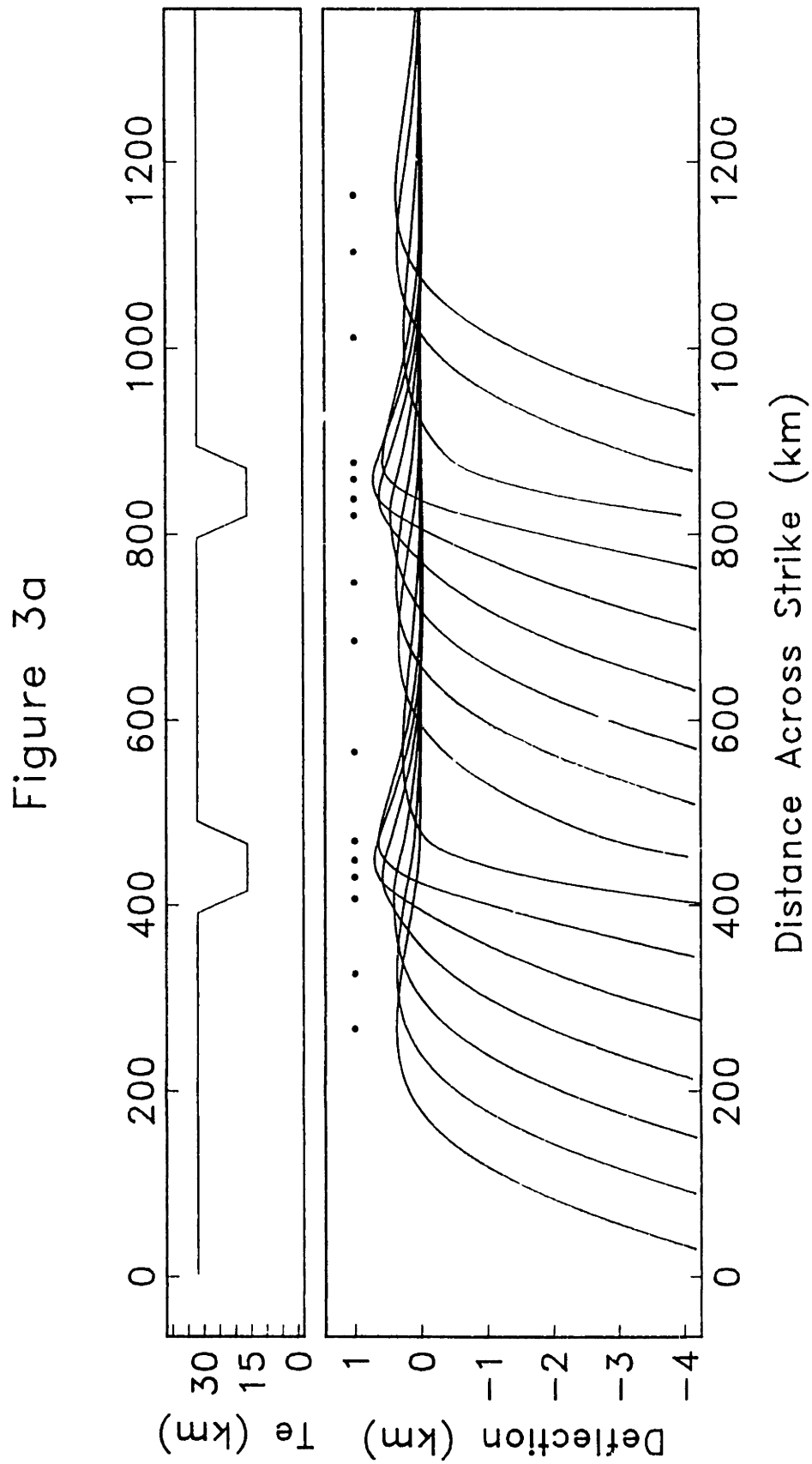
Figure 3a
Te (km)
30
15
0
Deflection (km)
1
0
−1
−2
−3
−4
0
200
400
600
800
1000
1200
Distance Across Strike (km)

Figure 2.3a

Figure 3b

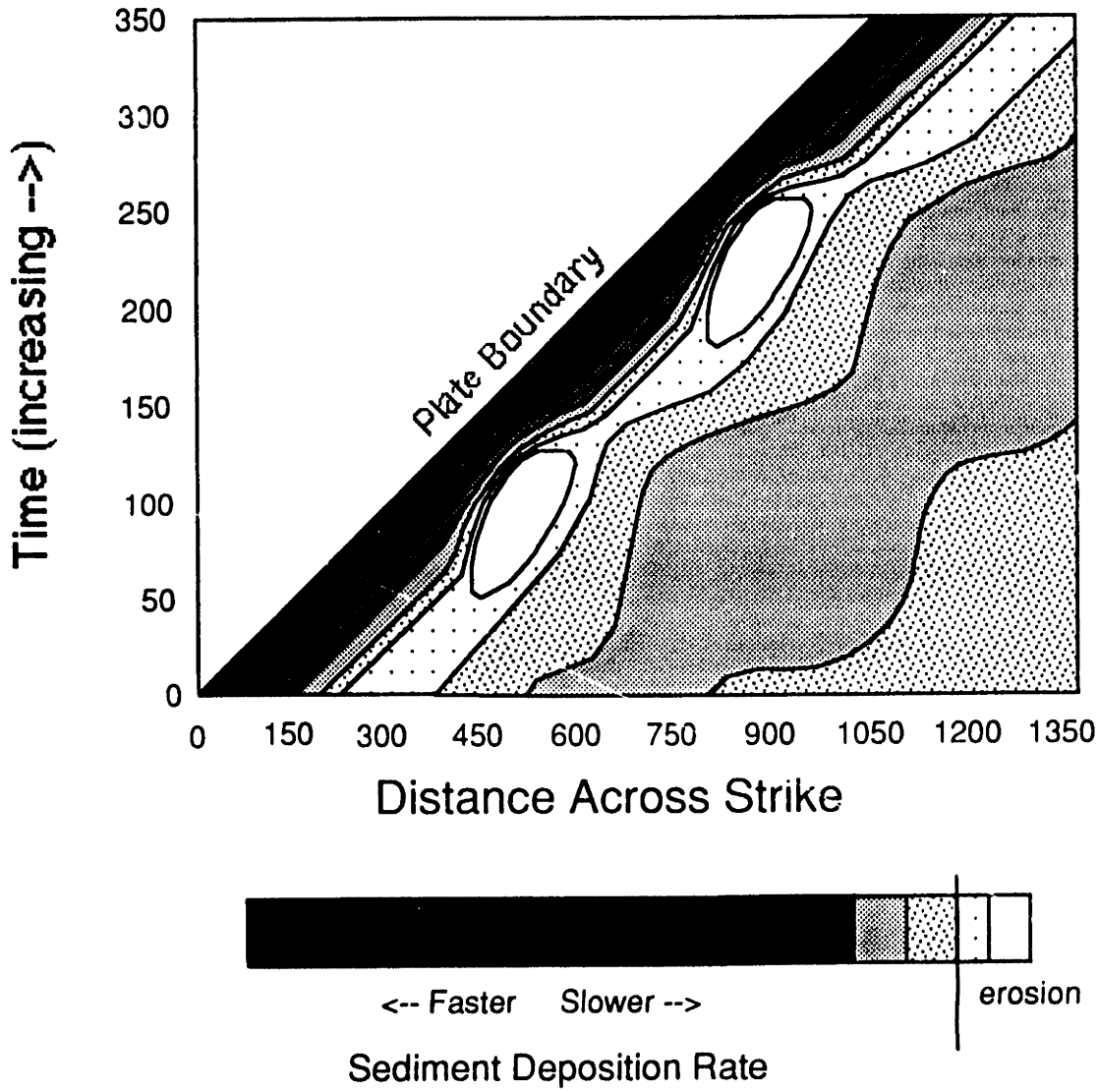

Figure 2.3b

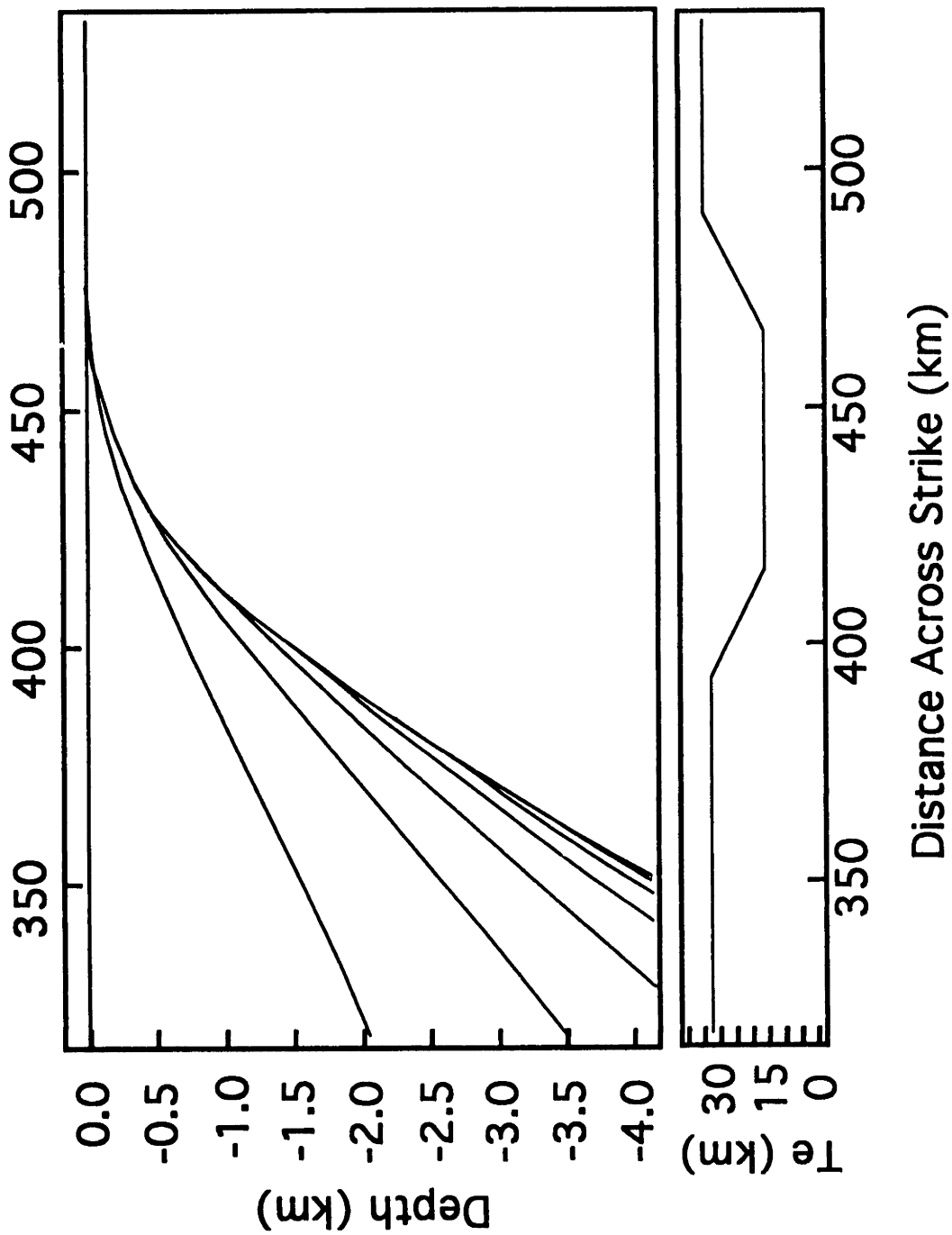

Figure 3c

Figure 2.3c

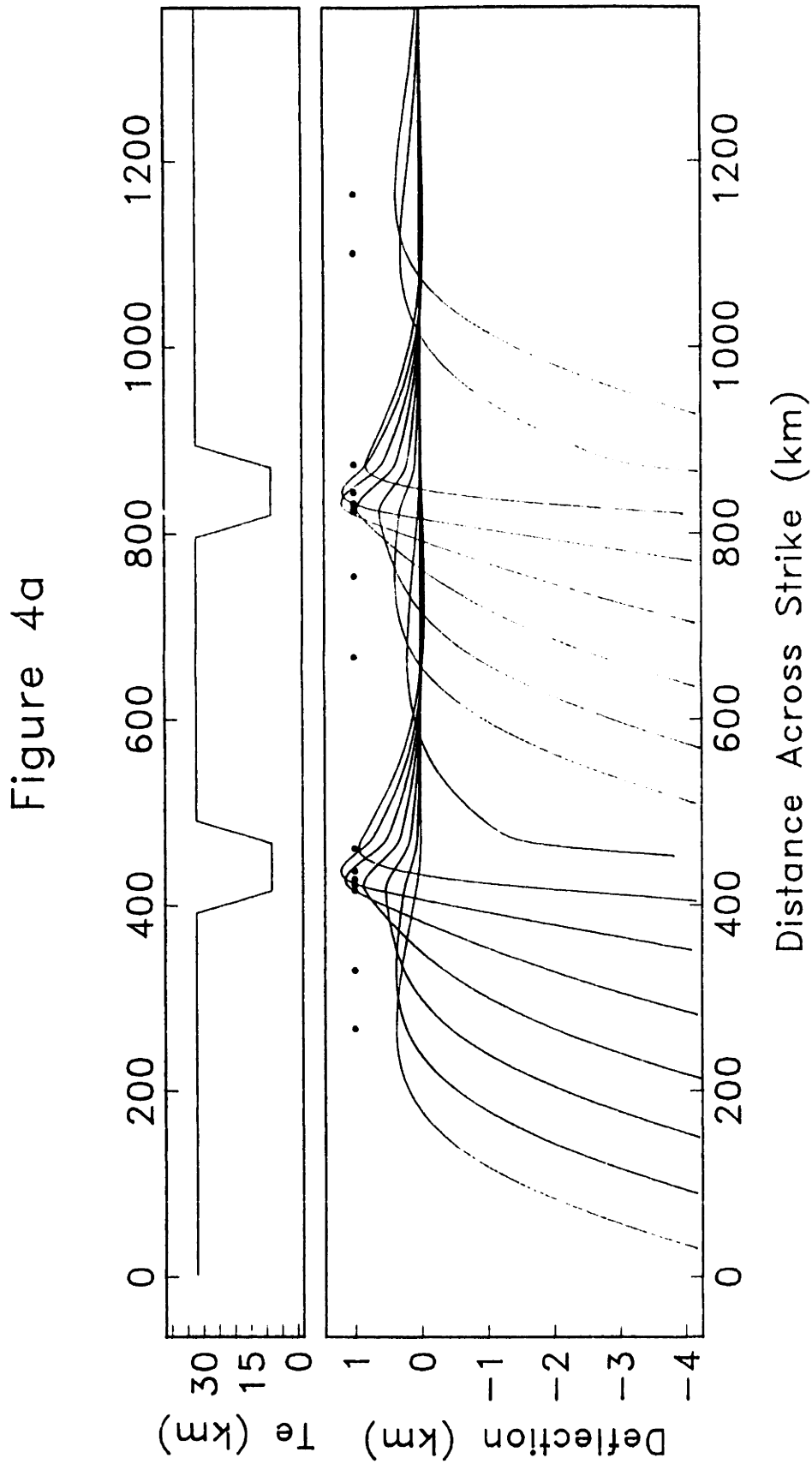
Figure 4a
Te (km)
30
15
0
Deflection (km)
1
0
−1
−2
−3
−4
0
200
400
600
800
1000
1200
Distance Across Strike (km)

Figure 2.4a

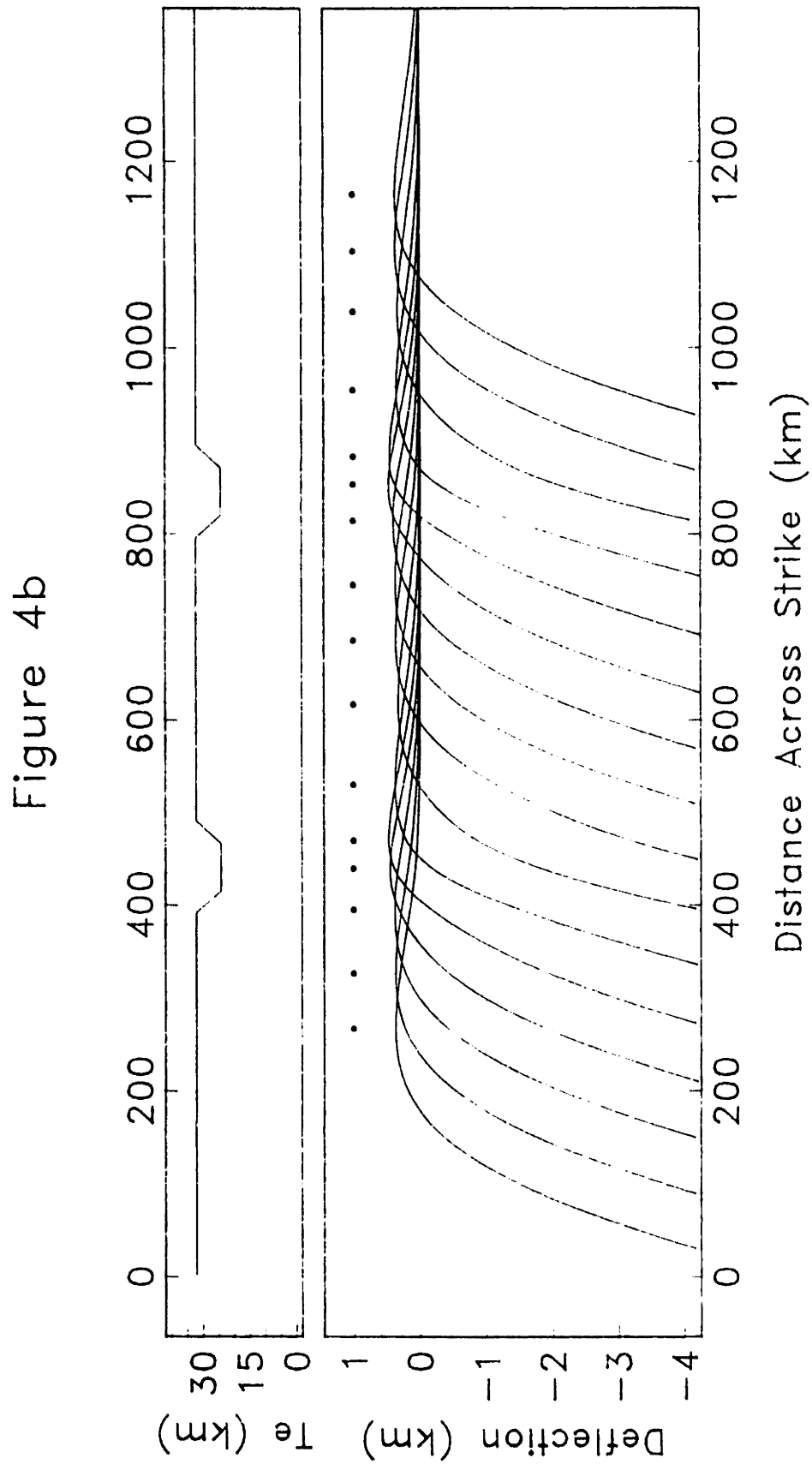
Figure 4b
Te (km)
30
15
0
Deflection (km)
1
0
−1
−2
−3
−4
0
200
400
600
800
1000
1200
Distance Across Strike (km)

Figure 2.4b

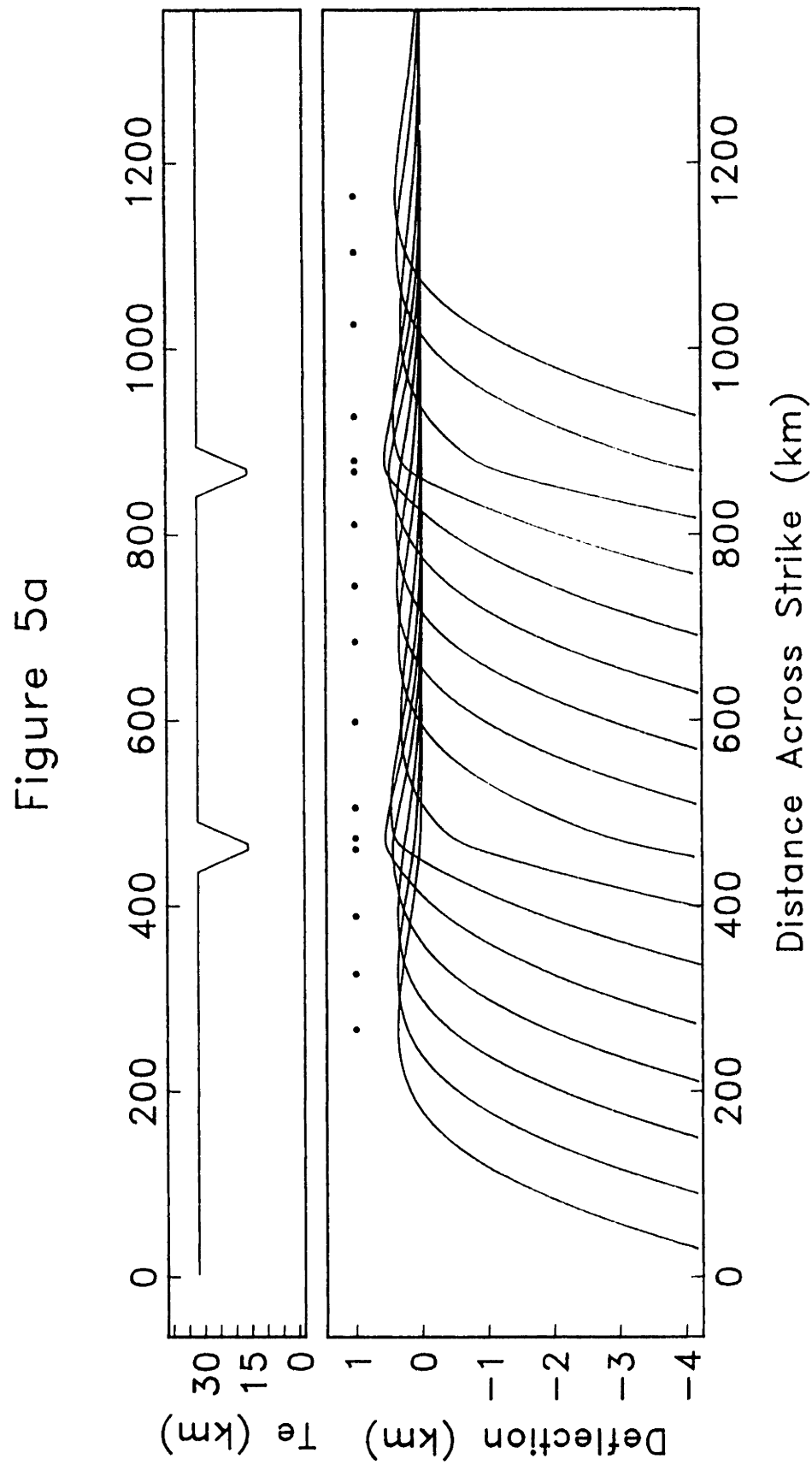
Figure 5a
Te (km)
0
15
30
Deflection (km)
1
0
−1
−2
−3
−4
0
200
400
600
800
1000
1200
Distance Across Strike (km)

Figure 2.5a

Figure 5b

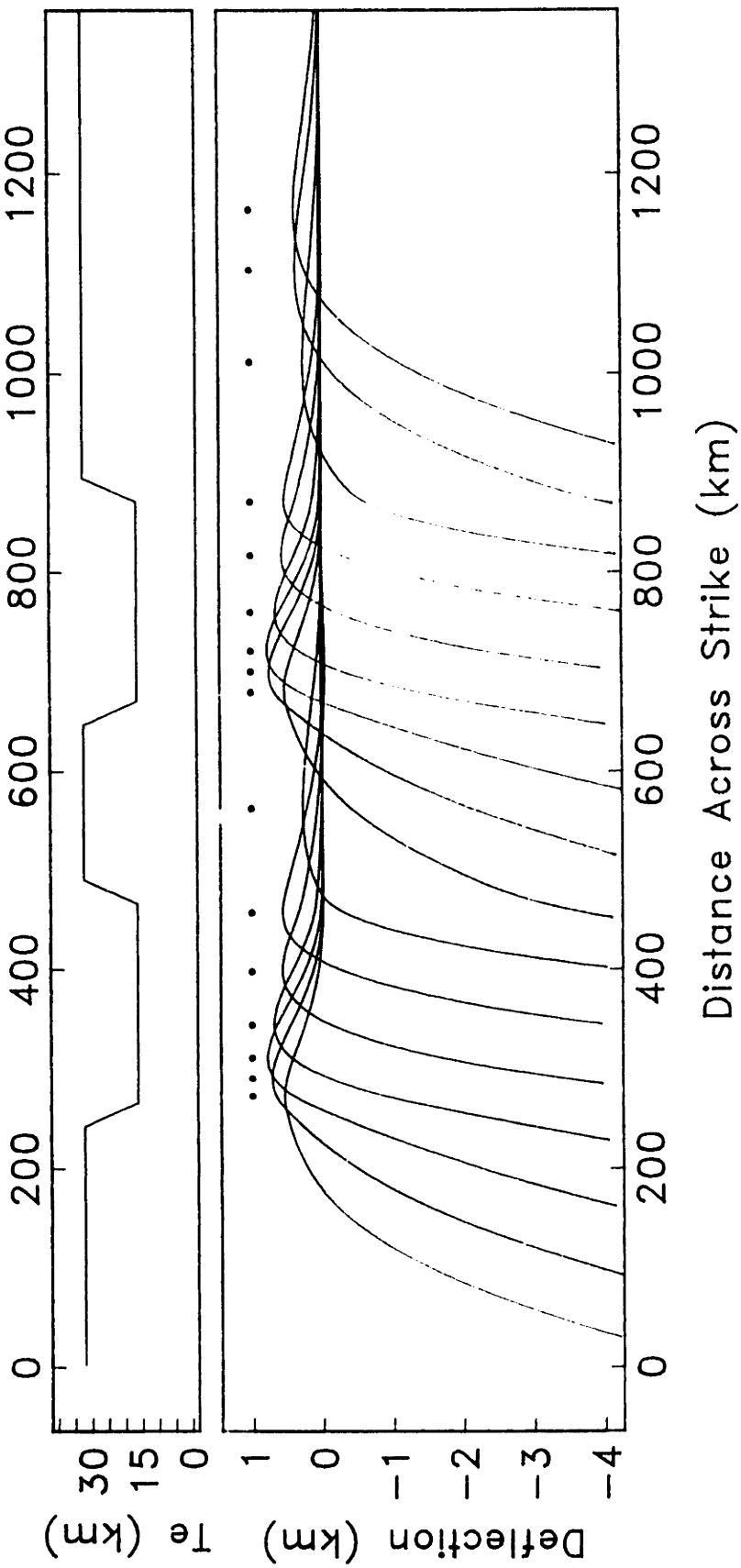

Figure 2.5b

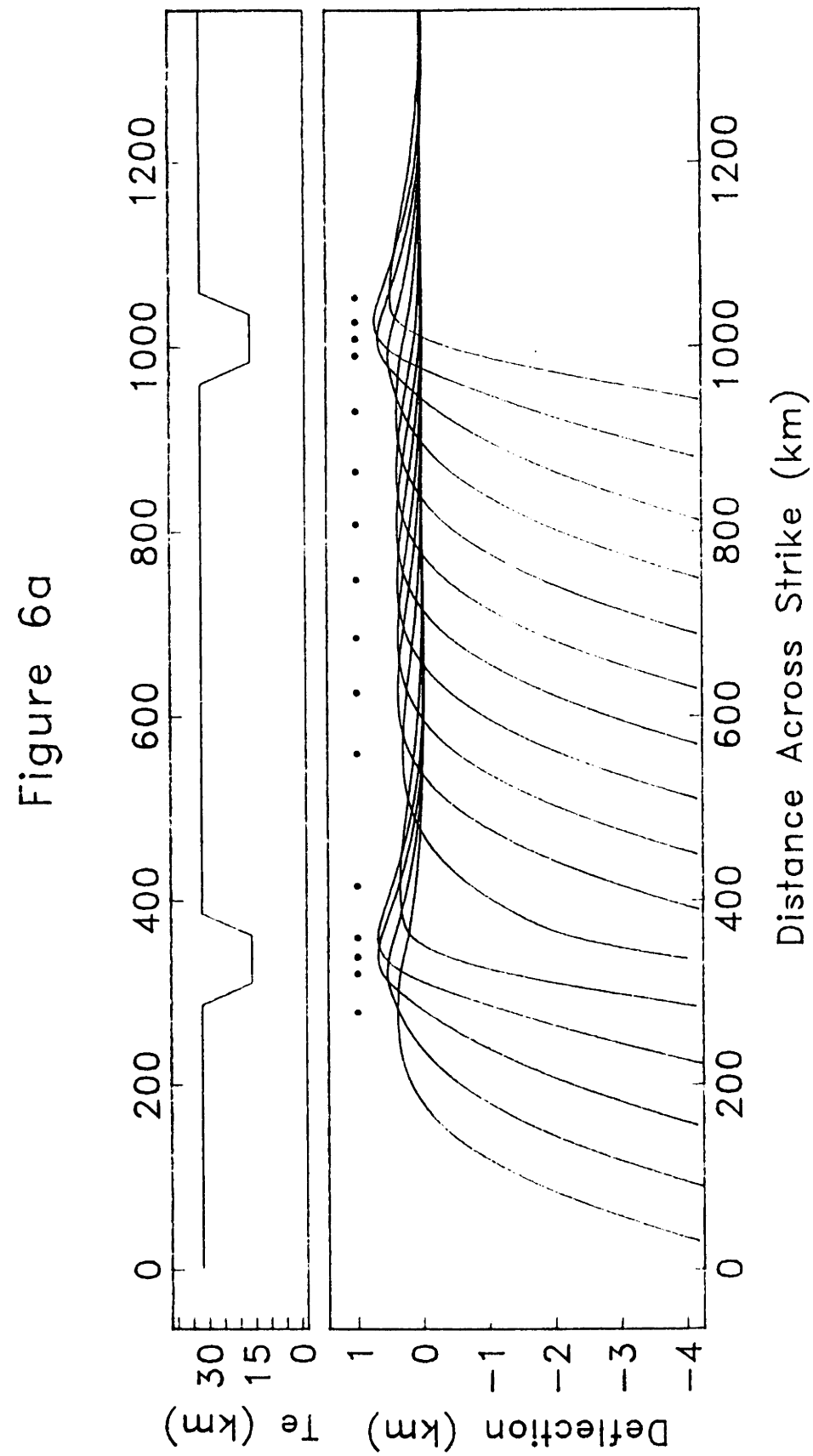
Figure 6a
Te (km)
30
15
0
Deflection (km)
1
0
−1
−2
−3
−4
0
200
400
600
800
1000
1200
Distance Across Strike (km)

Figure 2.6a

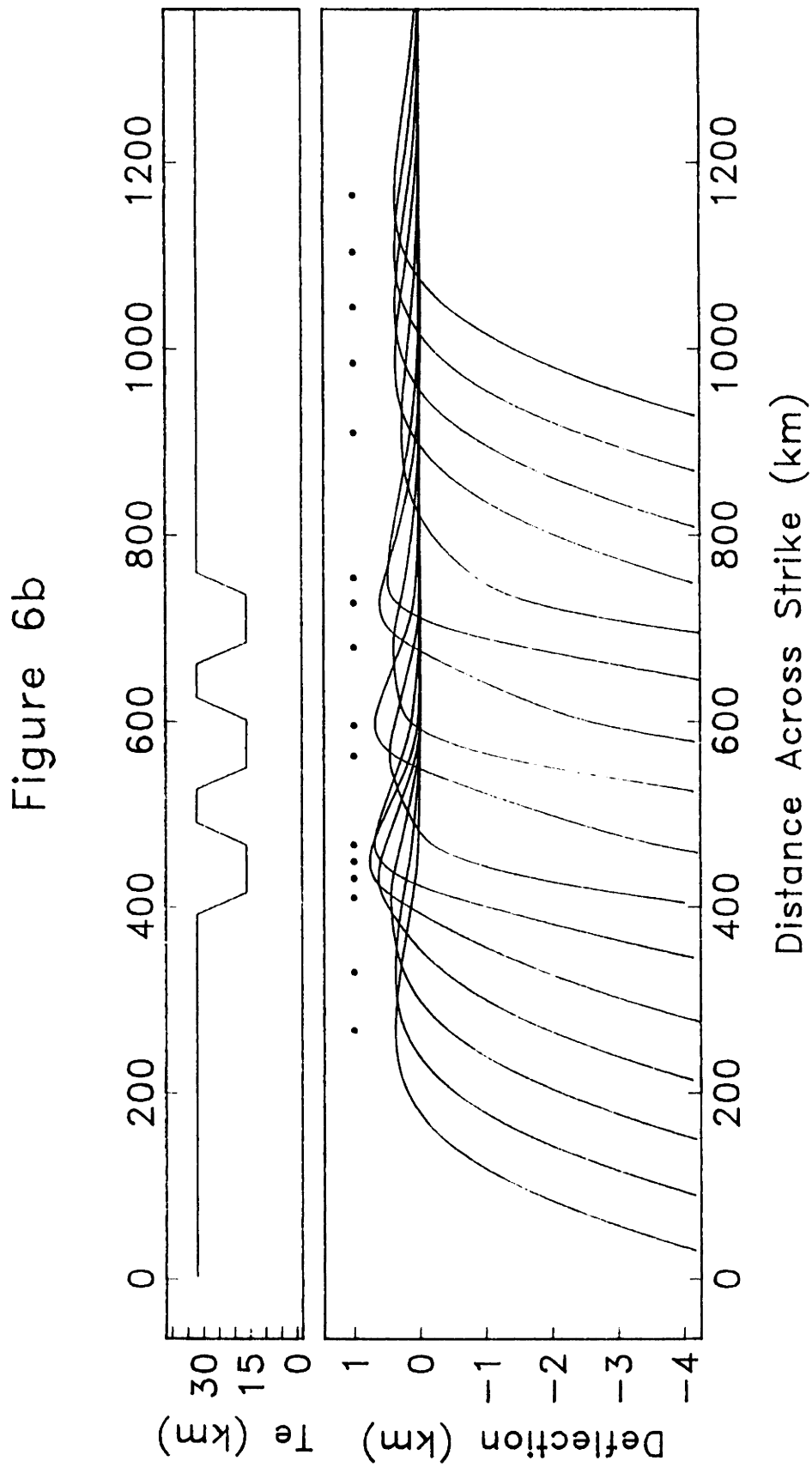
Figure 6b
Te (km)
30
15
0
Deflection (km)
1
0
-1
-2
-3
-4
0
200
400
600
800
1000
1200
Distance Across Strike (km)

Figure 2.6b

Figure 7

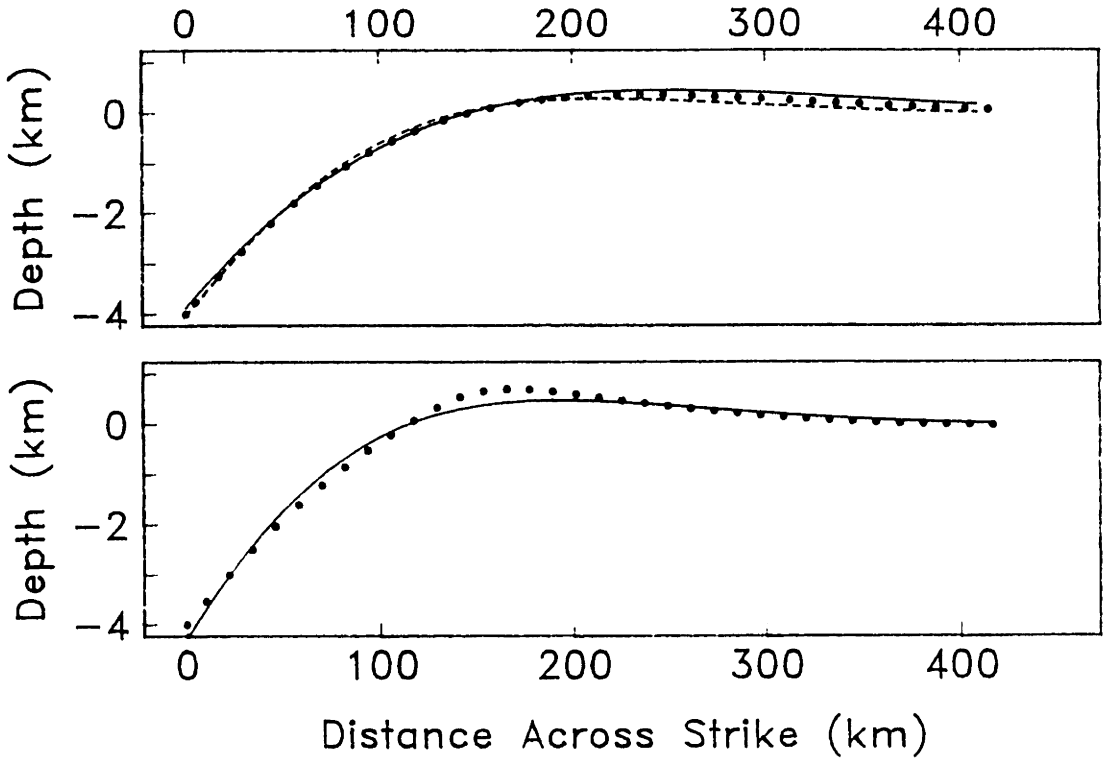

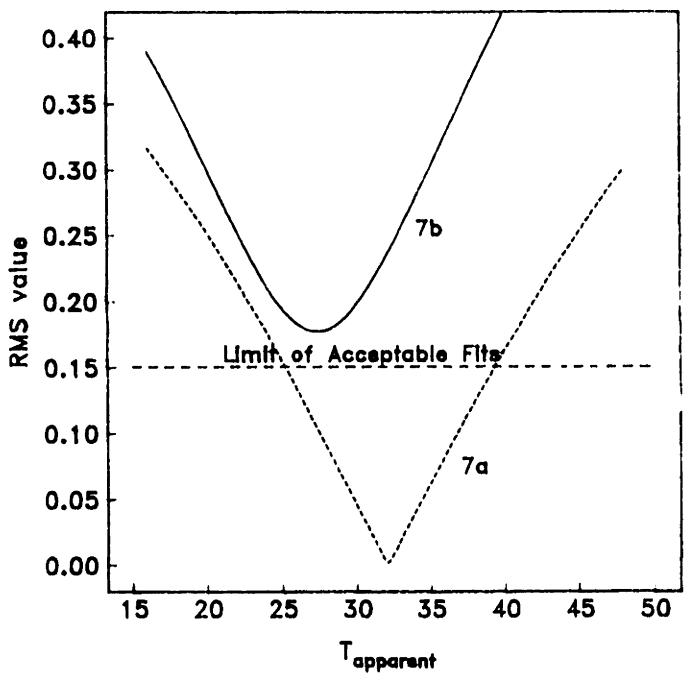

Figure 2.7

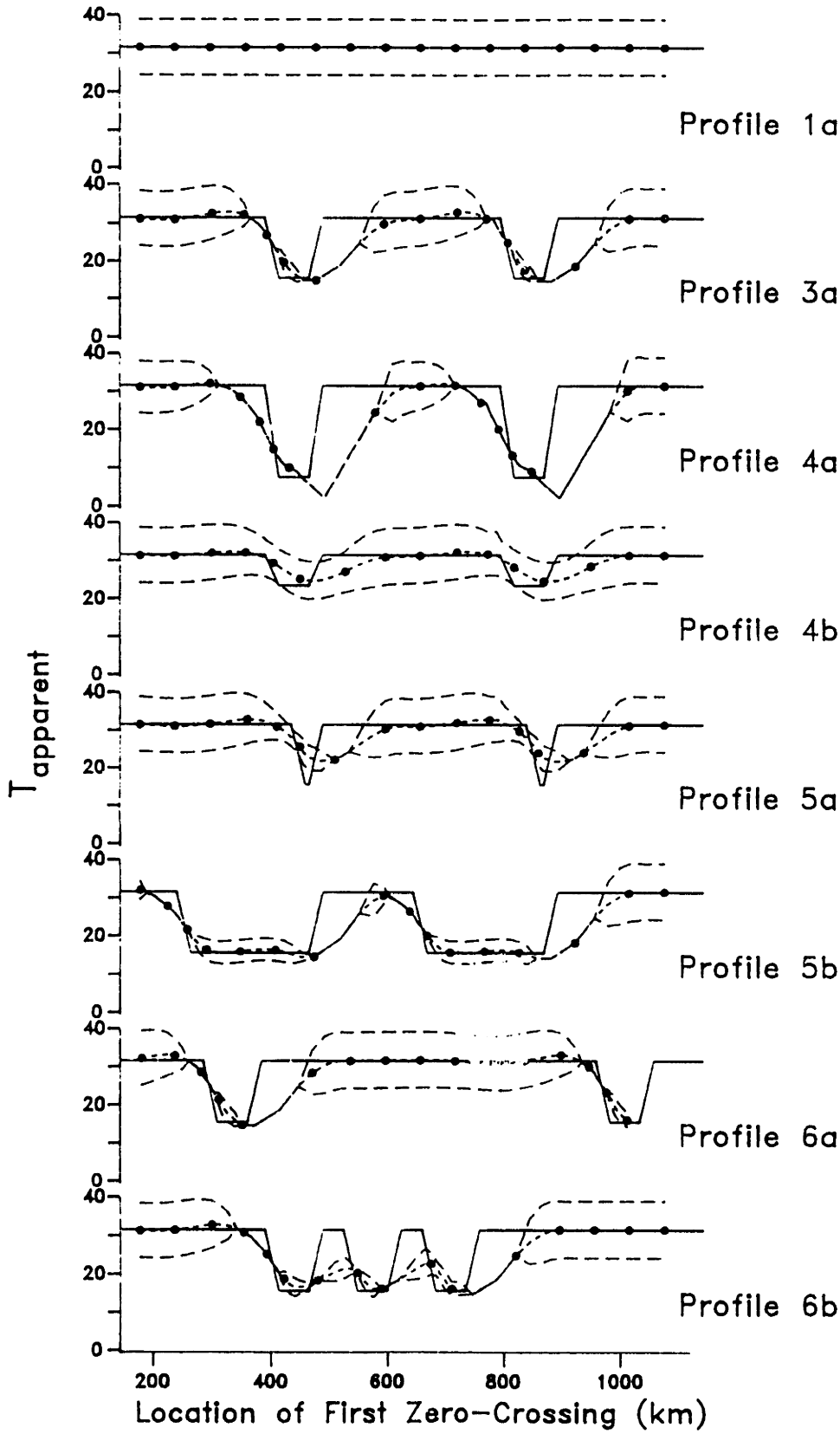
Profile 1a
Profile 3a
Profile 4a
Profile 4b
Profile 5a
Profile 5b
Profile 6a
Profile 6b
T apparent
40
20
0
200
400
600
800
1000
Location of First Zero-Crossing (km)

Figure 2.8

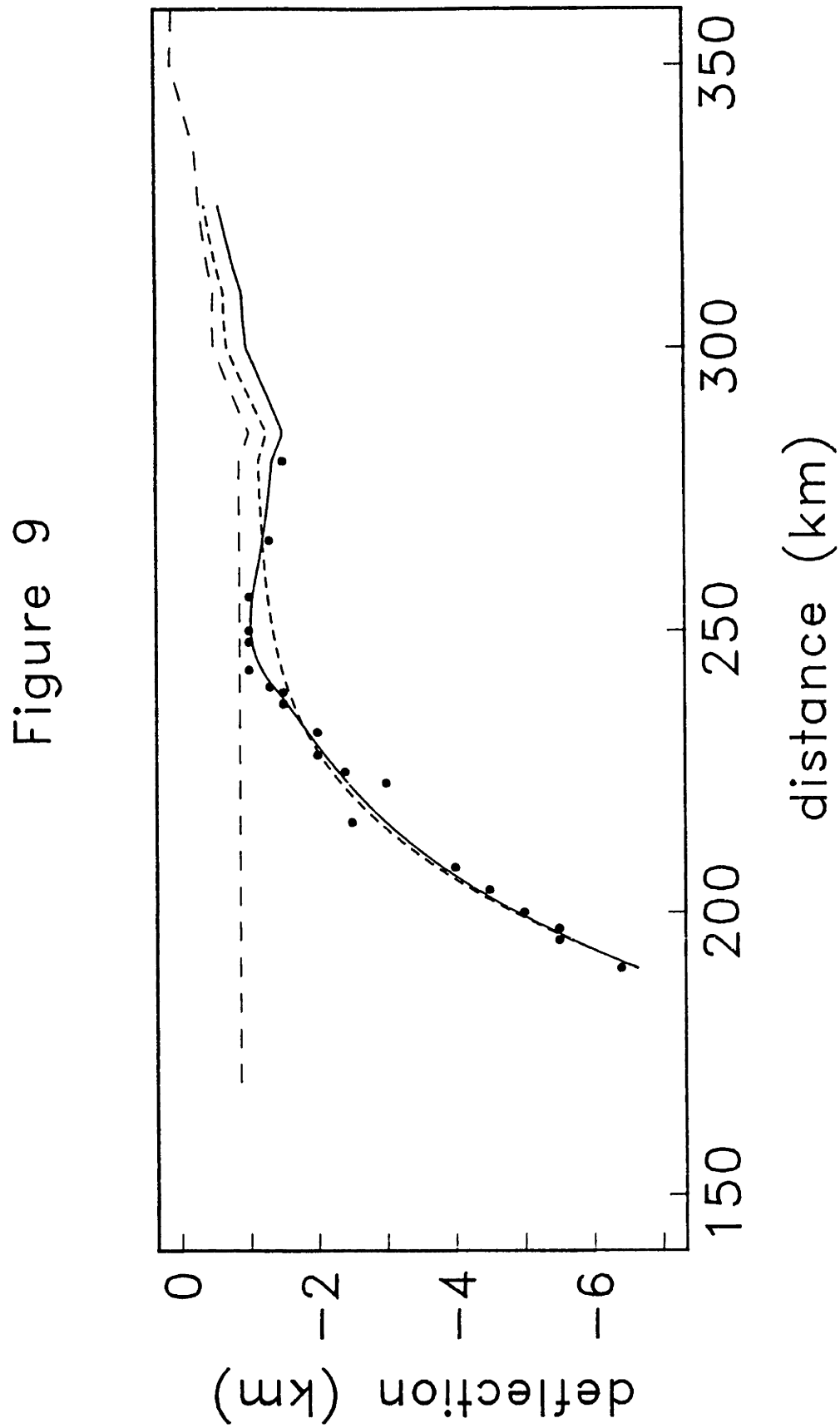

Figure 2.9

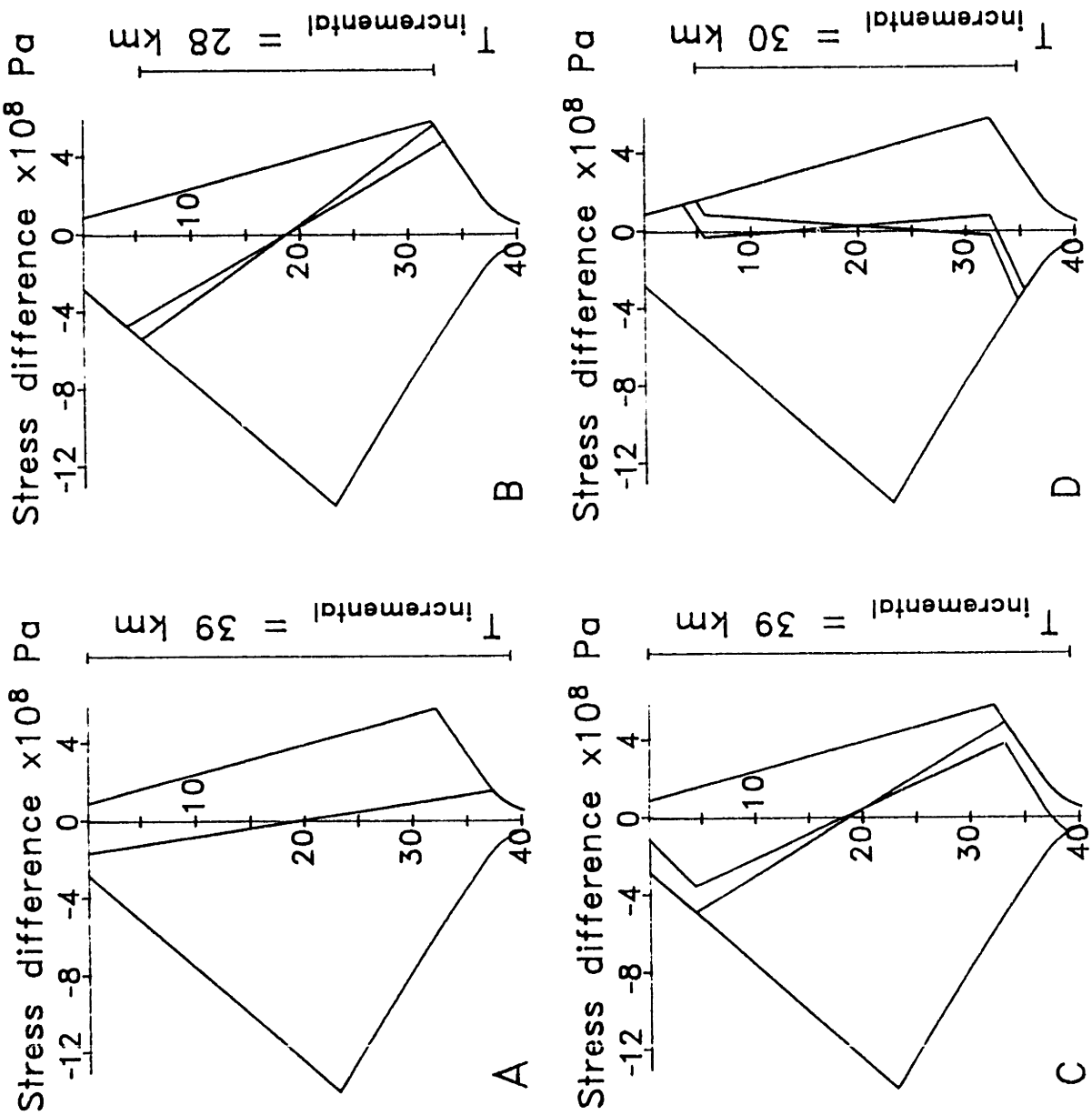
Stress difference x10^8 Pa
-12
-8
-4
0
4
10
20
30
40
T incremental = 39 km
A
T incremental = 28 km
B
T incremental = 39 km
C
T incremental = 30 km
D

Figure 2.10

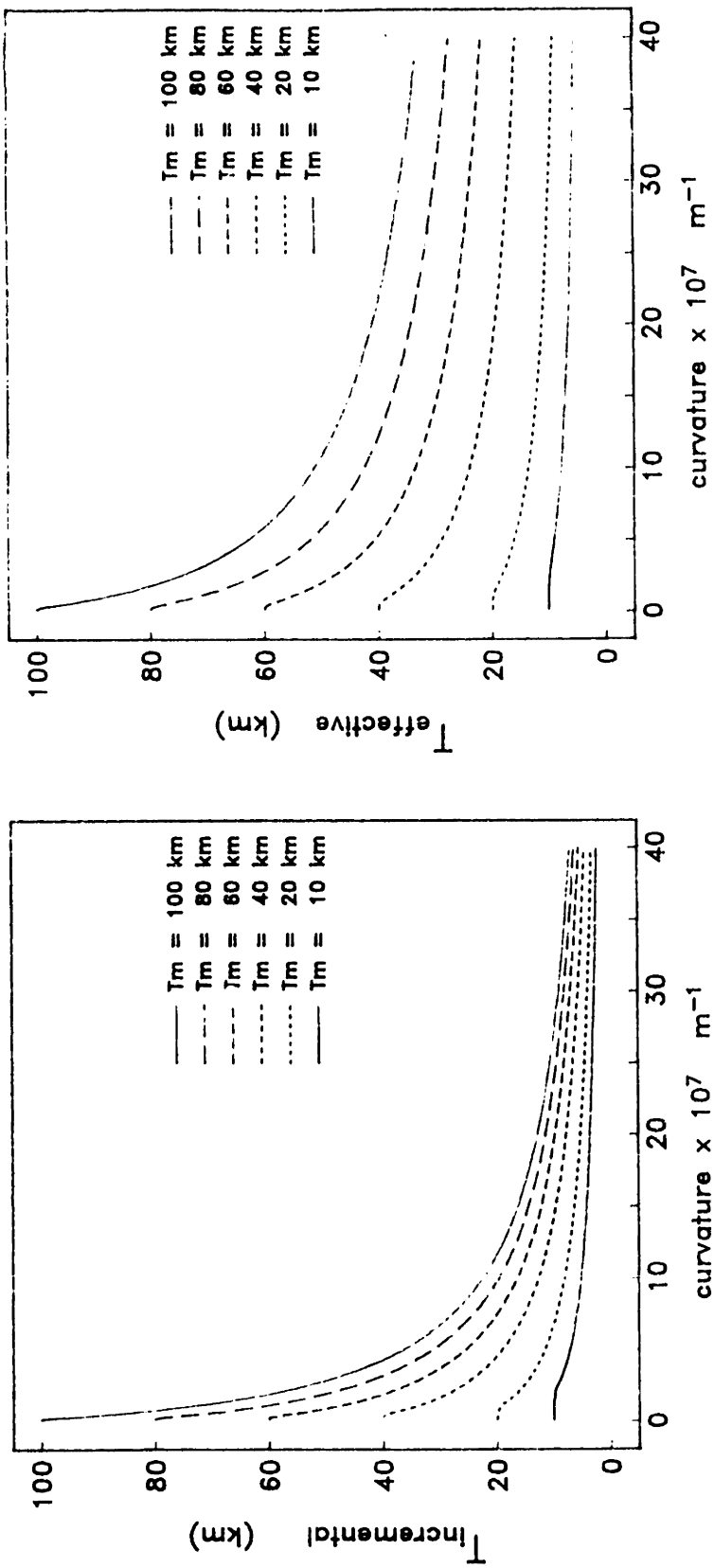
T effective (km)
T incremental (km)
curvature x 10^7 m^-1
Tm = 100 km
Tm = 80 km
Tm = 60 km
Tm = 40 km
Tm = 20 km
Tm = 10 km
0
20
40
60
80
100
10
30

Figure 2.11

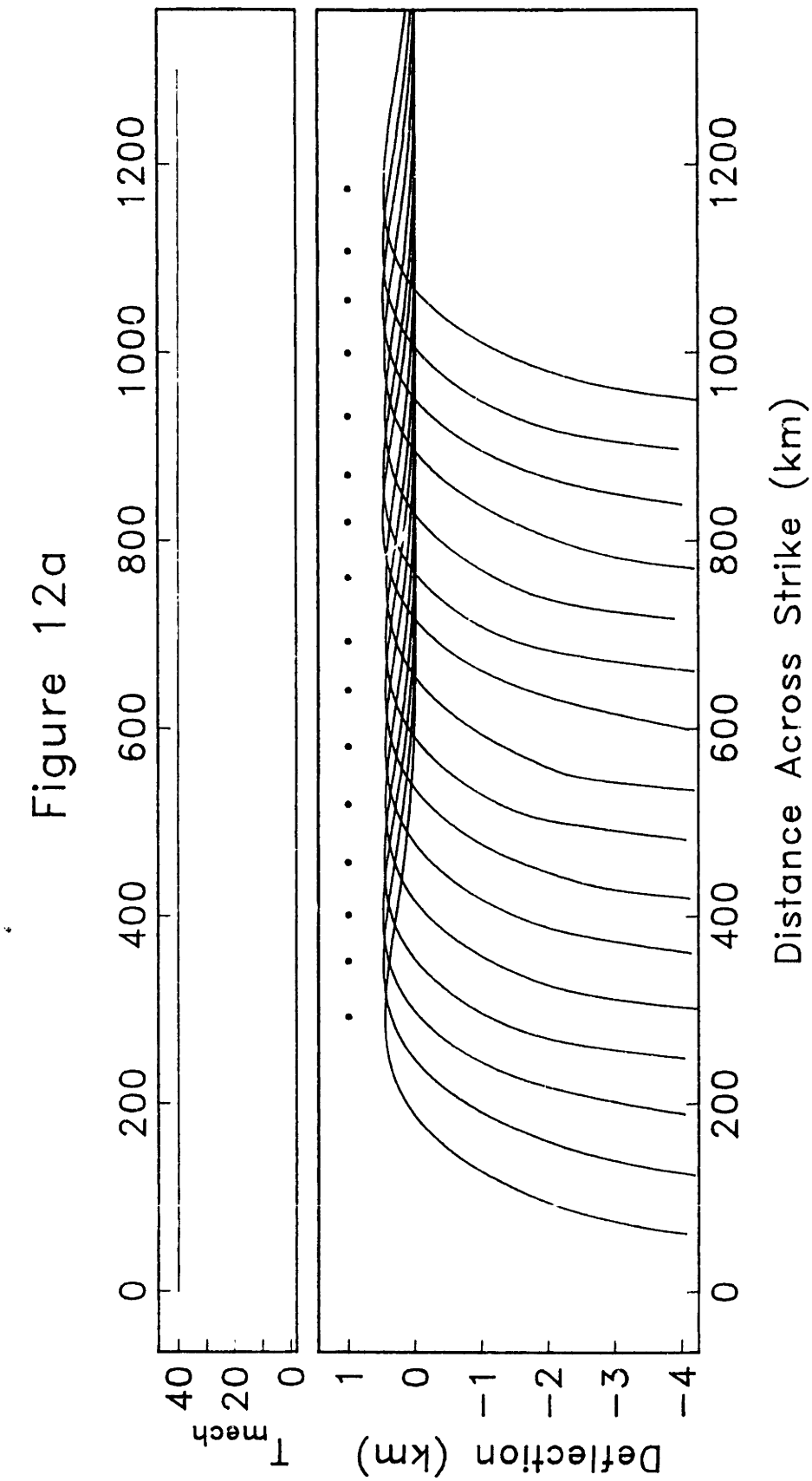
Figure 12a
0
200
400
600
800
1000
1200
Distance Across Strike (km)
Deflection (km)
1
0
−1
−2
−3
−4
T mech
40
20
0

Figure 2.12a

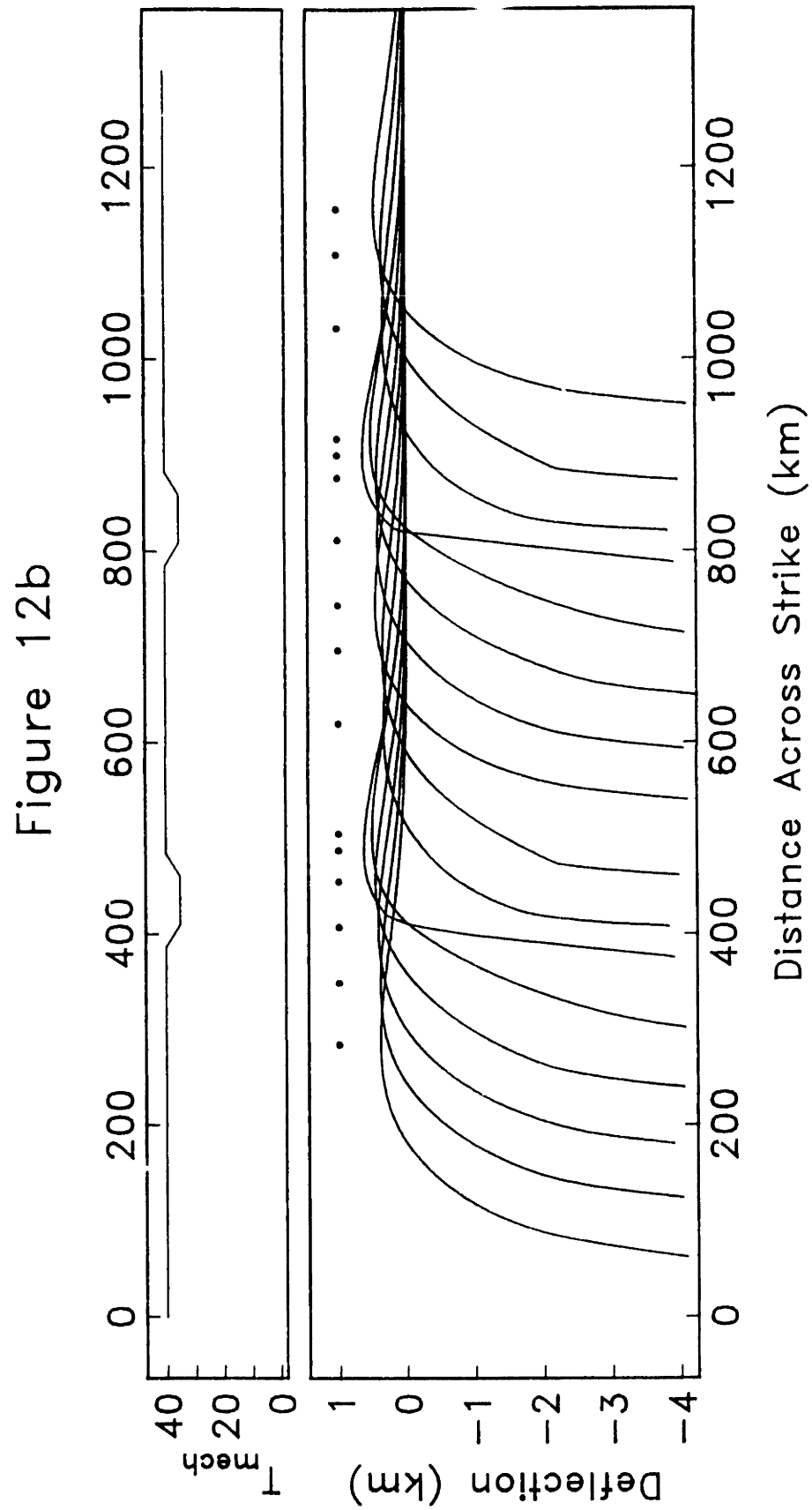
Figure 12b
0
200
400
600
800
1000
1200
Distance Across Strike (km)
Deflection (km)
1
0
−1
−2
−3
−4
T
mech
40
20
0

Figure 2.12b

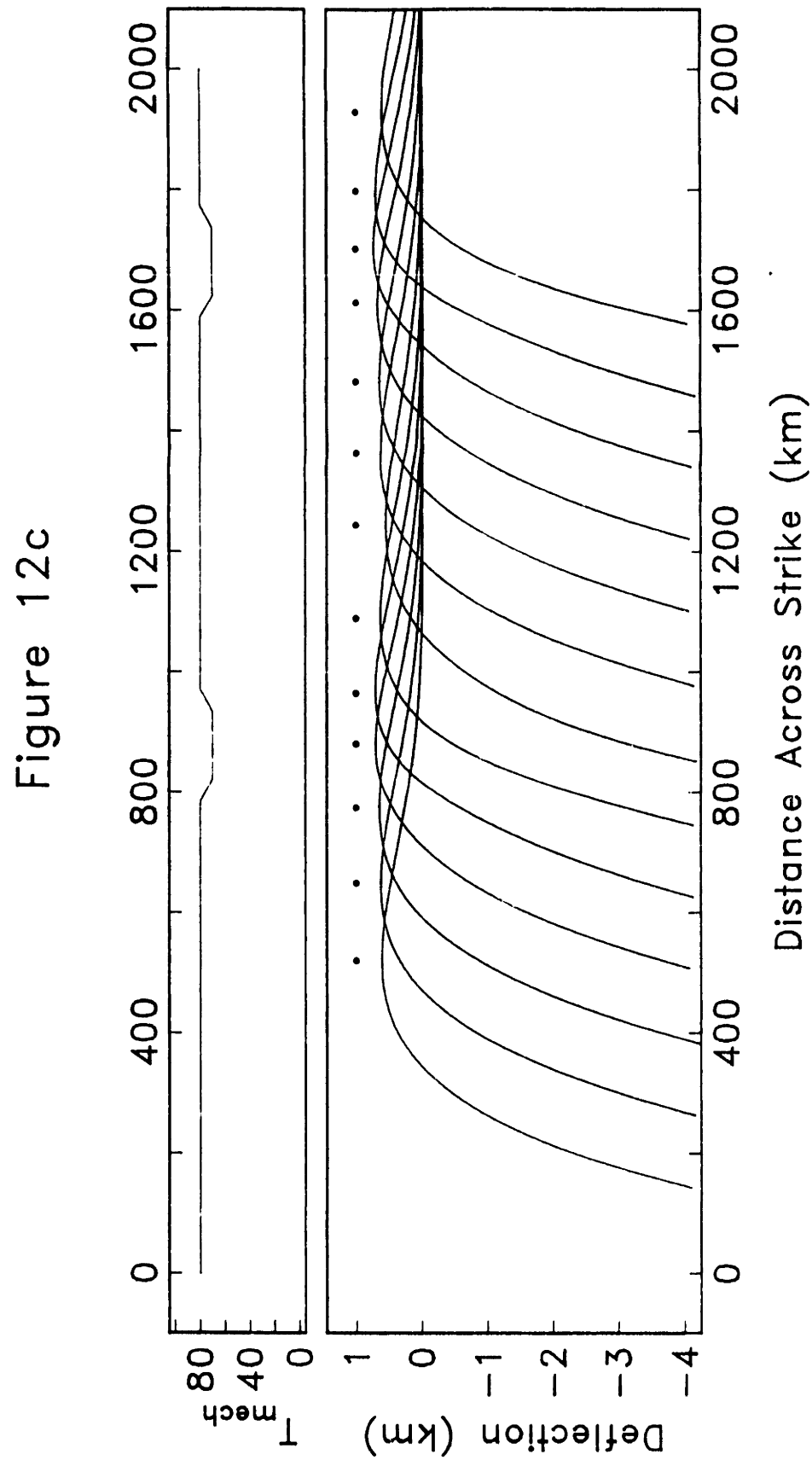
Figure 12c
0
400
800
1200
1600
2000
Distance Across Strike (km)
Deflection (km)
1
0
−1
−2
−3
−4
T_{mech}
80
40
0

Figure 2.12c

Figure 13

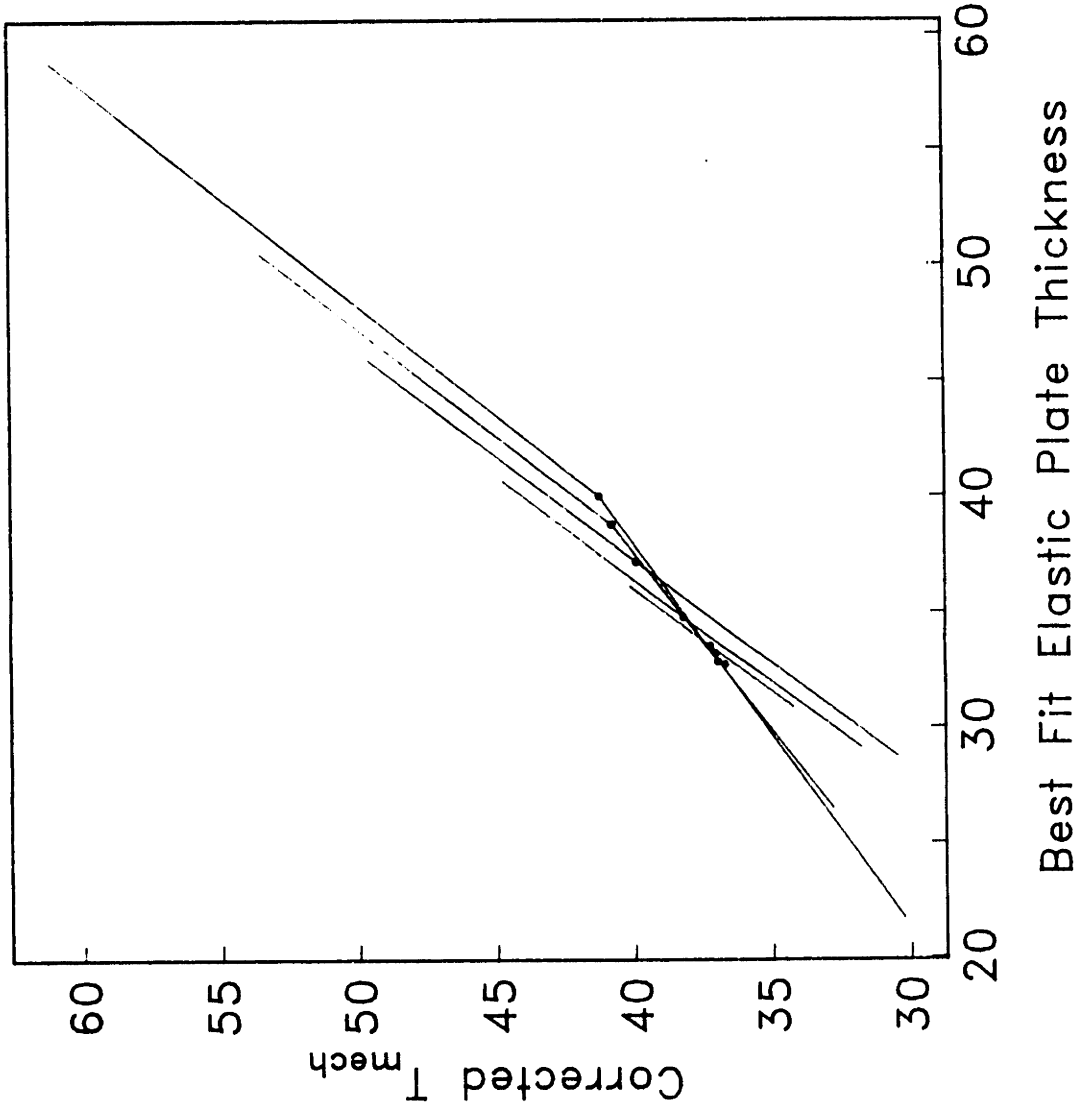

Figure 2.13

Figure 14

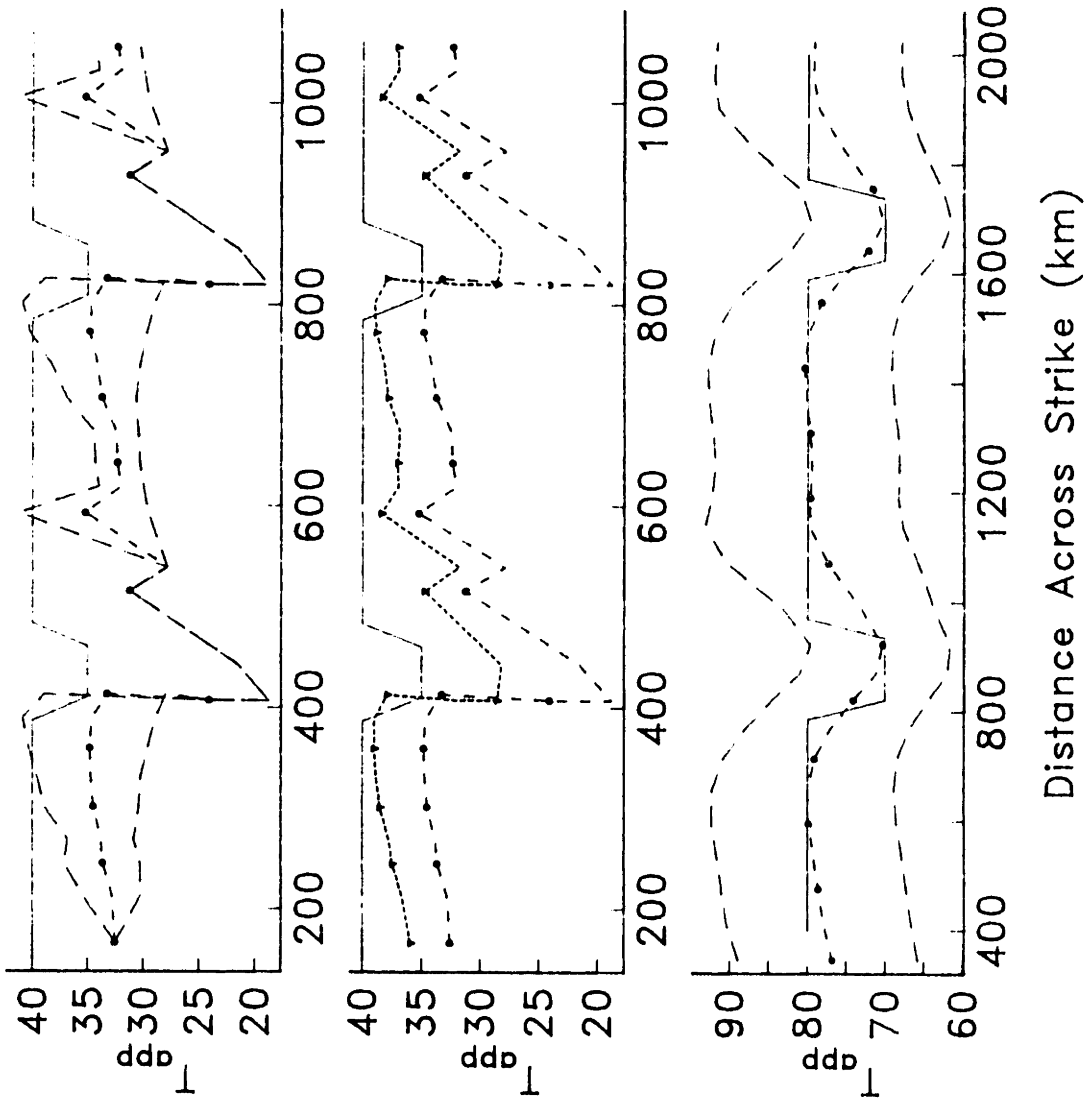

Figure 2.14

CHAPTER THREE

YELLOWSTONE: A CONTINENTAL MIDPLATE (HOT SPOT) SWELL

P. J. Waschbusch and M. K. McNutt

(Published in *Geophysical Research Letters*, vol. 21, pp. 1703-1706, 1994)

ABSTRACT

The Yellowstone hot spot has been identified mainly by its track of age-progressive volcanics; many smaller scale tectonic features serve to hide the long-wavelength hot spot-related swell. By employing averaging and filtering techniques, we are able to identify a swell in both the gravity and topography and use them to constrain the apparent depth of compensation of the Yellowstone hot spot at 70±10 km. This value is comparable to the deepest compensation depths for swells on old oceanic lithosphere. A compensation depth within the mid- to lower lithosphere combined with the only 15 m.y. known duration of the hot spot suggests either dynamic thinning of the thermal plate or compensation by upwelling in a low-viscosity asthenosphere, with some combination of the two explanations being consistent with seismic tomography results. Thus in many ways the Yellowstone hot spot appears quite similar to the oceanic analogues.

INTRODUCTION

The Yellowstone - Snake River Plains (SRP) volcanic system is one of the most strikingly anomalous volcanic-tectonic features of the continental United States. It extends as an arcuate depression approximately 600 km long and 100 km wide composed mainly of a bimodal suite of rhyolites and basalts. The Yellowstone Caldera, located on the northeasternmost point of the SRP is a site of unusually high heat flow (approximately 30 times the continental average [*Blackwell*, 1989]).

Morgan [1972] first suggested a mantle plume (hot spot) origin for Yellowstone. This hypothesis was subsequently strengthened when *Armstrong et al.* [1975] reported a

systematic decrease in the age of silicic volcanism along the eastern arm of the SRP corresponding to a migration of the volcanic center northeastward (~N60W) about 35 mm/yr, similar in magnitude and approximately parallel, but opposite, in direction to the plate motion vector of NUVEL-HS2 [*Gripp and Gordon*, 1990], which predicts plate motion N58W, 23 mm/yr. A large magnitude geoid anomaly (~+10 m) is centered over Yellowstone National Park and has an amplitude and wavelength similar to the geoid highs found over oceanic hot spot swells.

However, there is no obvious topographic anomaly above the presumed Yellowstone mantle plume that would be analogous to a hot spot swell. This lack of an obvious topographic anomaly may result from the inability to define a "reference topography" from which anomalies could be computed (i.e. no simple thermal model, such as a cooling plate model, satisfactorily explains large-scale continental elevations). Alternatively, a topographic anomaly due to a hot spot source could exist, but may not be immediately discernible due to overprinting by smaller regional tectonic features. Several authors have discussed the evidence for a topographic anomaly in detail; *Pierce and Morgan* [1992] is an excellent review of the geologic evidence of uplift and anomalous topography in the Yellowstone area. In this paper we employ averaging and filtering techniques to reduce overprinting by regional tectonic features and isolate a long-wavelength topographic swell. This swell, combined with a long-wavelength gravity feature, can be used to constrain the depth of compensation of the hot spot related features. The depth of compensation for Yellowstone can then be compared to depths of compensation for oceanic swells and with preliminary 3-D seismic velocity models.

GEOLOGIC SETTING

Surrounding the Yellowstone/SRP area are major rock units of Archean, Proterozoic, Paleozoic, Mesozoic and Tertiary ages. The Archean crystalline basement is cut by widespread Proterozoic dikes [*Ruppel*, 1972; *Baadsgaard and Mueller*, 1973].

Paleozoic and Mesozoic rocks are mainly sedimentary and were deposited in shallow marine basins on a subsiding cratonic platform. In the latest Cretaceous and earliest Eocene the Laramide orogeny disturbed the cratonic foreland, forming large northwest to west trending thrust bound anticlinal uplifts and deep adjacent basins that accumulated orogenic sediments [*Ruppel*, 1972; *Love and Keefer*, 1975]. Since the mid-Miocene this part of the Basin and Range tectonic system has been broken by extensional normal faults [*Stewart*, 1971].

The SRP has two distinct sub-provinces, a northeast trending eastern sector (ESRP) and a northwest trending western sector (WSRP). Gravity and aeromagnetic anomalies suggest the normal fault-bounded WSRP probably formed as a graben in response to northeast/southwest trending extension [*Leeman*, 1989; *Mabey*, 1976], and as such is unrelated to hot spot structure. The northeast trending ESRP is composed mainly of rhyolites and basalts; intermediate composition rocks are notably absent. *Armstrong et al.* [1975] first reported the systematic decrease in silicic volcanism along the ESRP (from 12-14 m.y. in southwestern Idaho to about 0.6 m.y. in western Wyoming); more recent refinements in geochronometry have not changed his primary results. Basaltic activity along the ESRP appears to have begun at about the same times as the corresponding silicic activity but continued intermittently even into the present [*Brott et al.*, 1981]. The topography along the ESRP decreases in elevation from about 2200 m over the present day Yellowstone Plateau to about 700 km at the southwest end. This decrease in elevation is interpreted to be a result of thermal cooling, which is further supported by a decrease in heat flow along the same path [*Brott et al.*, 1981]. Heat flow across the SRP averages around 100 mW/m^2, significantly above the average continental heat flow. Lower heat flow measurements over the central part of the ESRP results from cold groundwater circulation in the major SRP aquifer. However, when only the data from deep wells is considered, (greater than 500 m deep, below the SRP aquifer), the heat flow values along the ESRP show a systematic trend of higher values in the east (90-110 mW/m^2) decreasing to the west (to 75-90 mW/m^2). Above the Yellowstone Caldera, heat flow values average as high as 2500 mW/m^2, 30 times

the continental heat flow average [*Blackwell*, 1991]. Further evidence for active migration of the underlying volcanic source comes from a parabolic distribution of historic seismic activity, centered about the axis of the ESRP and opening to the southwest. *Anders et al.* [1989] suggest this distribution results from a decrease in integrated lithospheric strength due to thermal effects from an assumed mantle plume. Lithosphere that has been affected will yield more easily, thus the opening parabola records the lateral spreading of thermal effects away from the center of the ESRP after the passing of the thermal anomaly. *Smith and Braile* [1994] review more thoroughly the evidence for the ESRP being the track of the Yellowstone hot spot.

DATA

The two primary data sets used in this paper are topographic heights (Figure 3.1a) and Bouguer gravity anomalies (Figure 3.1b) from 243°-255° E longitude and 41°-48° N latitude. Topographic data comes from the ETOPO-5 data set [*National Geophysical Data Center*, 1988]. The Bouguer gravity data comes from the Geological Society of American gravity anomaly map of North America [*Committee for the Gravity Anomaly Map of North America*, 1987]. A crustal density of 2670 kg/m^3 was used to generate anomalies. Both sets of data were gridded onto 0.05° by 0.05° bins using a minimum curvature method. Errors in the gravity field are estimated at less than 5 mgals.

A hot spot-related swell is not obvious in the topography. We can emphasize the swell's topographic anomaly by averaging the topography radially about the (inferred) current hot spot location in order to minimize the signature of the individual tectonic features. Radially averaging to enhance the swell signal assumes that the hot upwelling plume radiates out in all directions equally. This assumption is certainly valid where the overlying lithospheric plate is slow-moving, such as at Cape Verde (plate velocity ~ 1.2 km/my), and there the swell is indeed circular. Plumes rising beneath fast-moving plates may also radiate hot, less-dense material equally in all directions, but the rapidly moving

lithosphere above effectively carries the hot material "downstream", producing a much more tear-drop-shaped swell (such as the Hawaiian swell, plate velocity ~ 8.6 km/my). Since we are only seeking general evidence for a hot spot swell and since the plate velocity at Yellowstone is a moderate ~2.3 km/my, averaging radially about the current location of the Yellowstone hot spot should give a reasonable signal if a hot spot swell is present.

Figure 3.2 shows the result of the radial averaging about 44.5°N lat and 249.5°E long, our best estimate for the current location of the hot spot. After averaging, a long wavelength feature is evident in both the gravity and in the topography. This feature is of the right magnitude (~1000 m in topography, 60 mgals in gravity) and half-wavelength (~500 km) to be the conjectured hot spot swell. These long-wavelength features are even more evident when the effect of the Laramide uplifts and associated basins are smoothed (via band-pass filtering in the range 10 to 60 km prior to radial averaging) to reduce their signature in the data (Figure 3.2). These mountain ranges, such as the Wind River, Beartooth and Bighorn Ranges, are clearly older than the Yellowstone hot spot and show a distinctly coupled short-wavelength high-low pattern in the Bouguer gravity that suggest shallow compensation. By smoothing this signal in the data, we are better able to concentrate on the long-wavelength, deep compensation signal we wish to study.

DEPTH OF COMPENSATION

We estimate the depth of compensation of a the swell using linear filtering [*McNutt and Shure*, 1986]. This technique utilizes the difference in sign and amplitude of Moho deflections cause by surface topography (Moho downwarping) and subsurface topography (Moho upwarping) to determine the depth of subsurface loading. Two filters are applied to the data in the wavenumber domain. The first computes the gravity due to local (flexural) compensation of all surface topography at the Moho. By subtracting this computed gravity from the observed, we are left with an isostatic gravity anomaly. The isostatic gravity anomalies reflect the signal that cannot be explained by Moho compensation, and thus

should be dominated by the signal from subsurface loading. A second filter acts on the isostatic gravity to correct for the (erroneous) assumption that all surface loads are compensated at the Moho (specifically that the subsurface-loading generated topography is not Moho compensated), and computes the topography due to loading at z_l, the apparent depth of compensation. In practice, z_l is varied until the swell predicted by the second filter is similar to the observed swell.

Figure 3.3 shows the predicted swell topography for several depths of compensation from the filtered topography and gravity of Figure 3.1. Depths of compensation from 60 to 80 km model the observed topography reasonably well. With a 60 km depth of compensation, the slope of the predicted topography is steeper than that observed, but the swell amplitude is closest to the observed; with an 80 km depth of compensation, the amplitude of the predicted swell is too small but the wavelength is closely matched. The geoid is a more sensitive indicator of deep structure than the Bouguer gravity because its long-wavelength signal is enhanced by 1/k (where k is the wavenumber) relative to the shorter wavelength surface sources, and thus might be considered a better estimator of the depth of compensation. However, when we repeated the analysis with the as yet unpublished GEOID93 data set [*Milbert and Schultz*, 1993], which shows a strong positive anomaly over Yellowstone (estimated between 8 m [*Pierce et al*, 1992] and 10-12 m [*Smith and Braile*, 1994]), our result did not change within the error limits. We take this to mean the determined depth of compensation is robust. We thus conclude that the apparent depth of compensation of the Yellowstone hot spot is 70±10 km.

DISCUSSION

Our value 70±10 km for the depth of compensation is one of the deepest values in the literature, but is consistent with the range for oceanic hot spot swells, such as Hawaii (60±15 [*Crough*, 1978], 70±10 [*McNutt and Shure*, 1986]) and Cape Verde (69±10 [*McNutt*, 1988]). Preliminary results from other continental hot spots suggest shallower

compensation depths. Two of the African hot spot swells, Hoggar and Dafur, have depths of compensation estimated at 60 km [*Crough*, 1981a] and 50 km [*Crough*, 1981b], respectively, and *Banks and Swain* [1978] estimated the East African Plateau's depth of compensation at 40 km. However, these other continental estimates were derived using simple regression of potential field data versus topographic elevation, a method that underestimates apparent depths of compensation compared to those derived using the linear filtering approach [*McNutt*, 1988]. A more recent study of the East African Plateau by *Ebinger et al.* [1989] suggested the need for a dynamic component of uplift and a much greater depth of compensation, although they could only loosely constrain the depth to between 70 and 400 km.

One importance of Yellowstone as a continental analog of oceanic midplate swells is in the quality of heat flow data over the swell. If the amount of heat flow through a midplate swell was known with some certainty, it could be used to place constraints on the possible mechanism of origin of the swell (i.e. thermal vs dynamic). However, as discussed by *Von Herzen et al.*[1989], one of the major problems in oceanic settings is knowing the background heat flow from "normal" oceanic lithosphere. While Cape Verde and Bermuda both show small heat flow anomalies, there is no significant heat flow anomaly over the Hawaiian swell, leading some to conclude that thermal mechanisms must be subordinate to dynamic mechanisms in supporting midplate swells. The Yellowstone case suggests this isn't so. As discussed above, a significant heat flow anomaly does exist above Yellowstone, and decreases away from the swell as a thermal compensation model would predict. This pattern is especially clear in the deep wells, where hydrothermal circulation has not had much of an effect. Taking Yellowstone as an analog for oceanic swells suggests that the low heat flow around oceanic midplate swells is largely a factor of hydrothermal circulation in the oceanic crust dissipating any heat flow anomaly.

A compensation depth of 70±10 km suggests the presence of anomalously buoyant material within or just beneath the lithosphere. This apparent depth of compensation was

determined by assuming that an infinitely thin layer of low density material resides at a single depth (Figure 3.4, Model A), a physically unrealistic case. A better model is that of a swell compensated by a column of low density material (Figure 3.4, Model B). If we equate the compensation depth we determined by assuming an infinitely thin layer of low-density material to that due to a column of low density material, some of the low density column may be 10's of km shallower than z_l, but the column cannot be everywhere deeper than z_l [*McNutt and Shure*, 1986] unless the compensation for the swell is provided by dynamic upwelling in a low-viscosity zone beneath the plate [*Robinson and Parson*, 1988]. Thus the depth of compensation is deep enough to rule out shallow crustal anomalies as sources of the swell, but is insufficient to distinguish between models of deeper compensation such as lithospheric reheating, dynamic compensation, or combinations of the two.

A column of low density material extending from the asthenosphere well into the lithosphere beneath the Yellowstone hot spot is consistent with the results of seismic tomography beneath the Yellowstone/SRP. *Dueker and Humphreys* [1990] inverted over 5000 P and PKIKP teleseismic travel times to image the upper mantle velocity of the Great Basin region of the western U. S. (including the Yellowstone/SRP region). They found a 1-3% low velocity anomaly that extends from 40 to 150±50 km beneath Yellowstone and to 200±50 km beneath southeastern Idaho (i.e., the ESRP). The shallow low-velocity anomalies support some amount of lithospheric reheating, but there is also evidence that the thermal anomalies extend well into the asthenosphere where they must be dynamically maintained. Simplistically correlating the change in velocity with a change in temperature (and thus, with a change in density), a 1% velocity contrast will produce approximately a 200° thermal anomaly, which would generate a 660 m topographic anomaly and a 7.2 m geoid anomaly when integrated over the length of the low-density column (from 40-150 km, Figure 3.4, Model B), assuming a high-viscosity layer in local isostatic equilibrium. While the estimated topographic anomaly seems a bit small, these values are in reasonable

agreement with the observations considering the number of assumed values in these rough calculations. If additional support for the swell is provided by upwelling in a low-viscosity zone (LVZ) at the base of the plate (Figure 3.4, Model C), the topographic uplift would increase with no increase (or even a decrease for a dramatic LVZ) in the geoid [*Robinson and Parsons*, 1988], bringing the predictions even more in line with the observations. However, there is presently no independent evidence for density anomalies below 150 km, so any model that reduces the viscosity above 150 km without increasing the amplitude of the density anomalies would further decrease the amplitude of the predicted swell.

Purely thermal (conductive) processes cannot explain the thermal anomalies as shallow as 40-70 km. Solving the one dimensional heat flow equation for pure conduction and even assuming the thinnest suggested continental lithosphere (125 km from *Sclater et al.* [1981]), approximately 30 m.y. are required for a thermal anomaly to propagate from the base of the lithosphere to 70 km depth. The Yellowstone hot spot, however, can only be traced back about 15 m.y. This suggests that either there were no surface expressions of the Yellowstone hot spot for at least the first 15 m.y. of its evolution, or that some non-conductive mechanism (magmatic advection?) must be called upon to inject heat into the middle lithosphere.

REFERENCES

Anders, M. H., J. W. Geissman, L. A. Piety, and J. T. Sullivan, 1989, Parabolic distribution of circumeastern Snake River Plain seismicity and latest Quaternary faulting: migratory pattern and association with the Yellowstone hot spot, *J. Geophys. Res.*, **94**, 1589-1621.

Armstrong, R. L., W. P. Leeman, and H. E. Malde, 1975, K-Ar dating, Quaternary and Neogene rocks of the Snake River Plain, Idaho, *Amer. J. of Sci.*, **275**, 225-251.

Baadsgaard, H. and P. A. Mueller, 1973, K-Ar and Rb-Sr ages of intrusive Precambrian mafic rocks, Southern Beartooth Mountains, Montana and Wyoming, *Geol. Soc. Am. Bull.*, **84**, 3635-3644.

Banks, R. J., and C. J. Swain, 1978, The isostatic compensation of East Africa, *Proc. R. Soc. Lond. A*, **364**, 331-352.

Blackwell, D. D., 1989, Regional implications of the heat flow of the Snake River Plain, northwestern United States, *Tectonophysics*, **164**, 323-343.

Brott, C. A., D. D. Blackwell, and J. P. Ziagos, 1981, Thermal and tectonic implications of heat flow in the Eastern Snake River Plain, Idaho, *J. Geophys. Res.*, **86**, 11,709-11,734.

Committee for the Gravity Anomaly Map of North America, 1987, Gravity anomaly map of North America, Geol. Soc. of Amer., 5 sheets, scale 1:5,000,000.

Crough, S. T., 1978, Thermal origin of mid-plate hot-spot swells, *Geophys. J. R. astro. Soc.*, **55**, 452-469.

Crough, S. T., 1981a, Free-air gravity over the Hoggar Massif, Northwest Africa: evidence for alteration of the lithosphere, *Tectonophysics*, **77**, 189-202.

Crough, S. T., 1981b, The Dafur Swell, Africa: gravity constraints on its isostatic compensation, *Geophys. Res. Lett.*, **8**, 877-879.

Dueker, K., and E. Humphreys, 1990, Upper-mantle velocity structure of the Great Basin, *Geophys. Res. Lett.*, **17**.

Ebinger, C. J., T. D. Bechtel, D. W. Forsyth, and C. O. Bowin, 1989, Effective elastic plate thickness beneath the East African and Afar plateaus and dynamic compensation of the uplifts, *J. Geophys. Res.*, **94**, 2883-2901.

Gripp, A. E. and R. G. Gordon, 1990, Current plate velocities related to hotspots incorporating the NUVEL-1 global plate motion model, *Geophys. Res. Lett.*, **17**, 1109-1112.

Leeman, W. P., 1989, Origin and development of the Snake River Plain (SRP) - and overview, *in* Volcanism and plutonism of Western North America, AGU Field Trip Guidebook T305, p. 4-12.

Love, J. D, and W. R. Keefer, 1975, Geology of sedimentary rocks in Southern Yellowstone National Park, Wyoming, *U.S. Geol. Surv. Prof. Paper, 729-D*, 60 pp.

Mabey, D. R., 1976, Interpretation of a gravity profile across the Western Snake River Plain, Idaho, *Geology*, **4**, 53-55.

McNutt, M. K., 1988, Thermal and mechanical properties of the Cape Verde Rise, *J. Geophys. Res.*, **93**, 2784-2794.

McNutt, M. K., and L. Shure, 1986, Estimating the compensation depth of the Hawaiian Swell with linear filters, *J. Geophys. Res.*, **91**, 13,915-13,923.

Milbert, D. G., and D. G. Schultz, 1993, GEOID93: A new geoid model for the United States, *EOS Transactions of the American Geophysical Union*, **74**, 96.

Morgan, W. J., 1972, Deep mantle convection plumes and plate motions, *Amer. Assoc. Petrol. and Geol. Bull.*, **56**, 203-213.

National Geophysical Data Center, 1988, ETOPO-5 bathymetry/topography data, Data Announcement 88-MGG-02, Natl. Oceanic and Atmos. Admin., U.S. Dep. Commer., Boulder, Colo.

Pierce, K. L., and L. A Morgan, 1992, The track of the Yellowstone hot spot: volcanism, faulting and uplift, *in* Regional geology of Eastern Idaho and Western Wyoming, P. K. Link, M. A. Kuntz, and L. B. Platt, eds., *Geol. Soc. Am. Mem.*, **179**, 1-53.

Pierce, K. L., D. G. Milbert, and R. W. Smith, 1992, Geoid dome culminates on Yellowstone: Yellowstone hotspot fed by a thermal mantle plume?, *EOS Transactions of the American Geophysical Union*, **73**.

Robinson, E. M., B. E. Parsons, 1988, The effect of a shallow low-viscosity zone on the formation of midplate swells, *J. Geophys. Res.*, **93**, 3144-3156.

Ruppel, E. T., 1972, Geology of Pre-Tertiary rocks in the northern part of Yellowstone National Park, Wyoming, *U. S. Geol. Surv. Prof. Paper, 729-A*, 66 pp.

Sclater, J. G., B. Parsons, and C. Jaupart, 1981, Oceans and continents: Similarities and differences in the mechanisms of heat loss, *J. Geophys. Res.*, **86**, 11,535-11,552.

Smith, R. B., and L. W. Braile, The Yellowstone Hotspot, *J. of Volcanology, in press*, 1993

Von Herzen, R. P., M. J. Cordery, R. S. Detrick, and C. Fang, 1989, Heat flow and the thermal origin of hot spot swells: the Hawaiian swell revisited, J. Geophys. Res., 94, 13,783-13,799.

FIGURE CAPTIONS

Figure 3.1: a) Topography of the Yellowstone/SRP study area. Contour interval is 400 meters; bold contour is 2000m b) Bouguer gravity anomaly of the Yellowstone/SRP study area. Contour interval is 20 mgals; bold contour is -200 mgals A white dot marks inferred current location of the Yellowstone hot spot.

Figure 3.2: Radial topography and Bouguer gravity obtained by circularly averaging about the current hot spot location. Thick line averages all data, thin line averages data after band-pass filtering to remove Laramide structures (see text for details).

Figure 3.3: Comparison of predicted topographic swells generated from compensation depths of 50 km (a), 70 km (b), and 90 km (c). Contour interval is 400m; bold contour is 0 m. A white dot marks inferred location of the Yellowstone hot spot. The topographic lows south and west of Yellowstone probably result from using either too low an elastic plate thickness or too high a crustal density to estimate crustal compensation in those areas; as a result, there are "artifact" gravity anomalies that are interpreted as low topography that overlaps the Yellowstone swell topography, hindering our ability to estimate the total wavelength of the swell.

Figure 3.4: Three models for the support of the Yellowstone swell. Model A assumes the swell is supported by a thin spike of low-density material at 70 km depth. By varying laterally the amplitude of the spike, this model provides a good fit to the amplitude and wavelength of the topography and geoid signals. Model B assumes that the low-density material is distributed uniformly in a column between 40 and 150 km depth, as suggested by seismic tomography. This model slightly underestimates the swell height, but the parameters used in converting seismic velocity anomalies to density anomalies

are uncertain. Model C allows some further uplift of the swell by dynamic support in a low-viscosity zone beneath the lithosphere. The effect of the low-viscosity zone is to allow very deep density anomalies to increase the height of the swell without increasing the geoid anomaly.

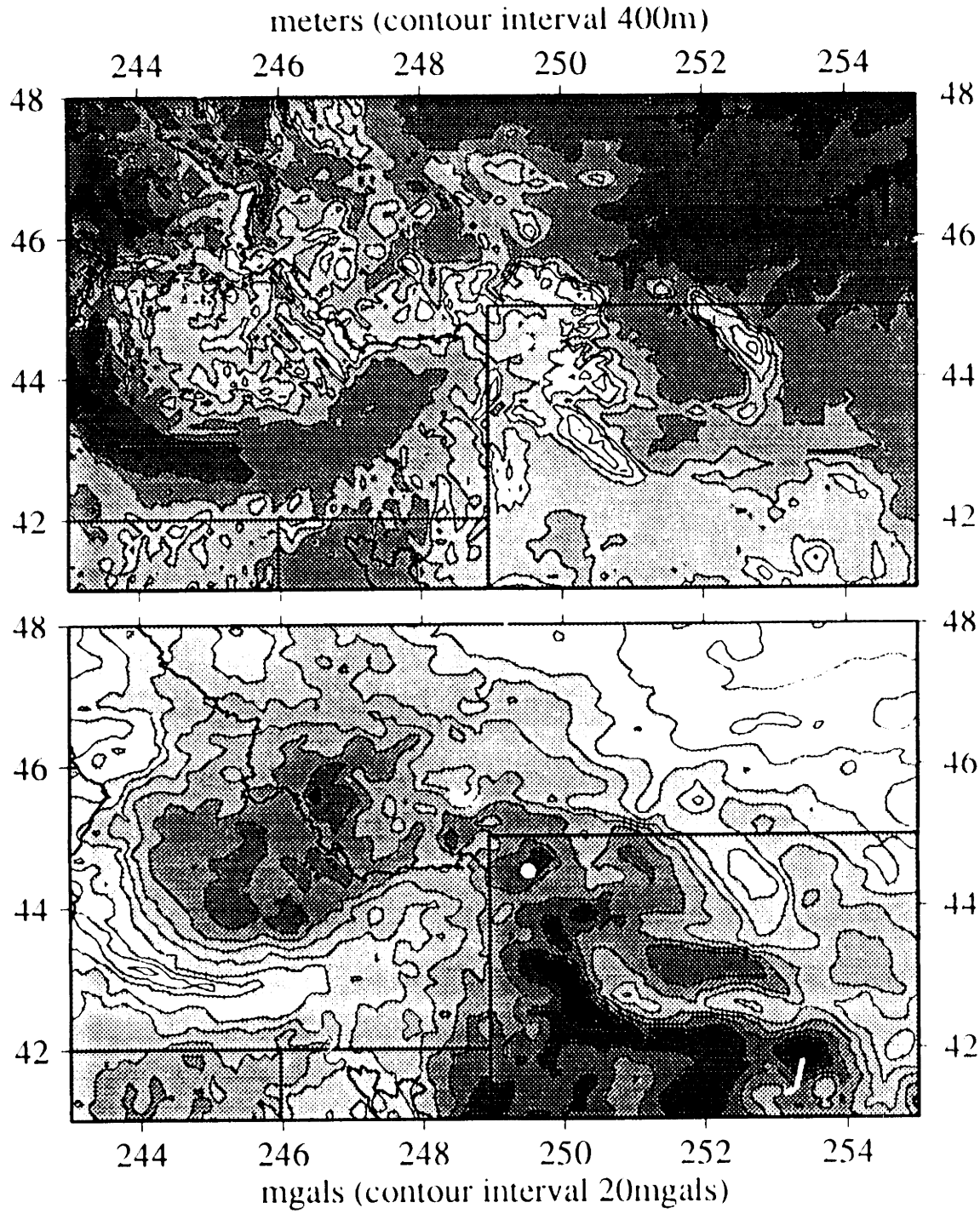
meters (contour interval 400m)
244
246
248
250
252
254
48
46
44
42
mgals (contour interval 20mgals)

Figure 3.1

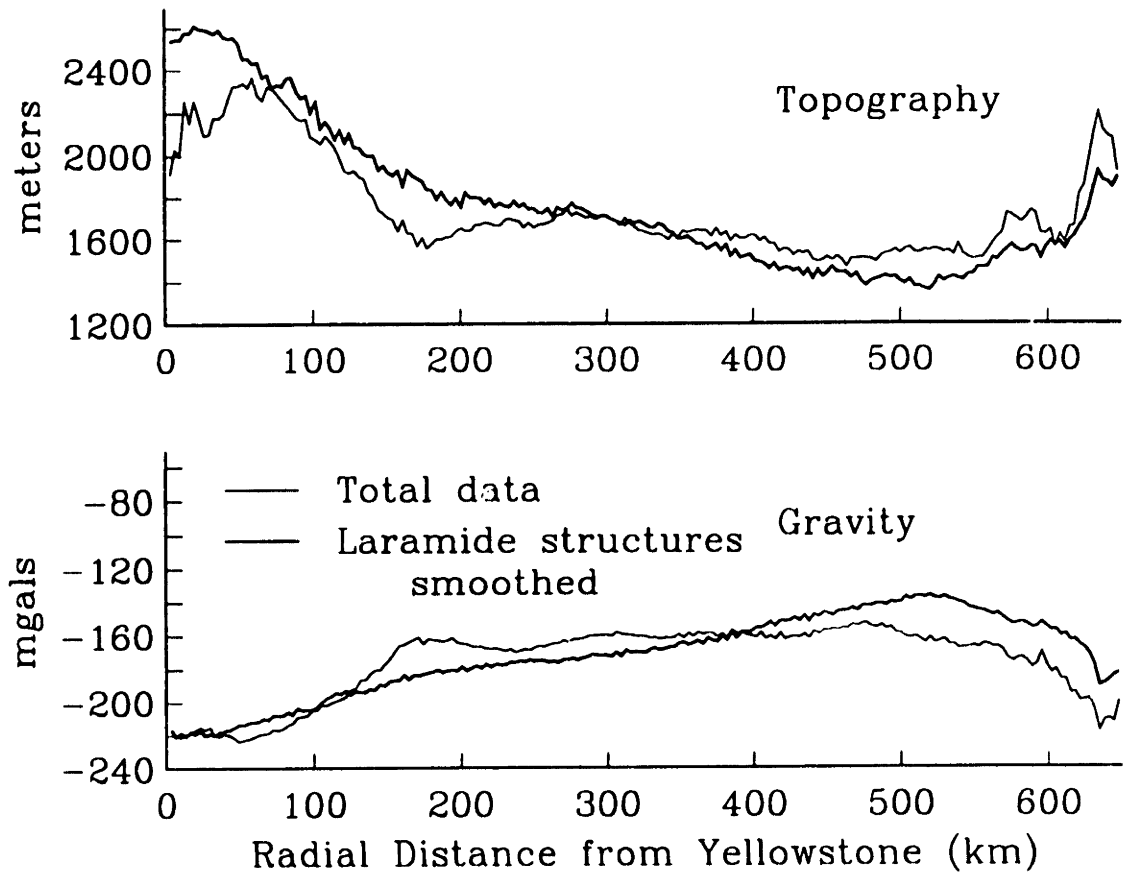
meters
2400
2000
1600
1200
Topography
0
100
200
300
400
500
600
mgals
-80
-120
-160
-200
-240
Total data
Laramide structures smoothed
Gravity
0
100
200
300
400
500
600
Radial Distance from Yellowstone (km)

Figure 3.2

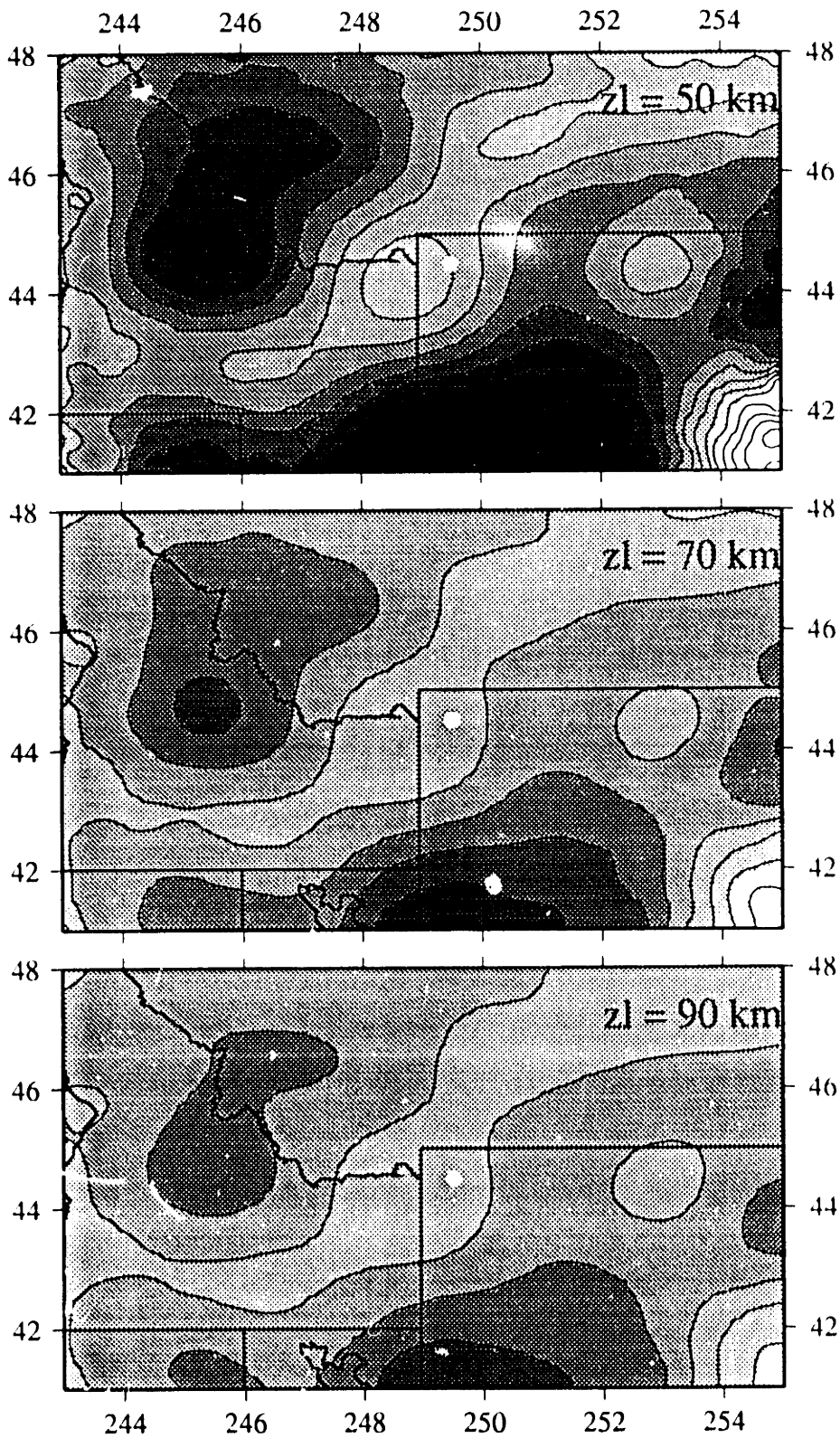

contour interval 400m

Figure 3.3

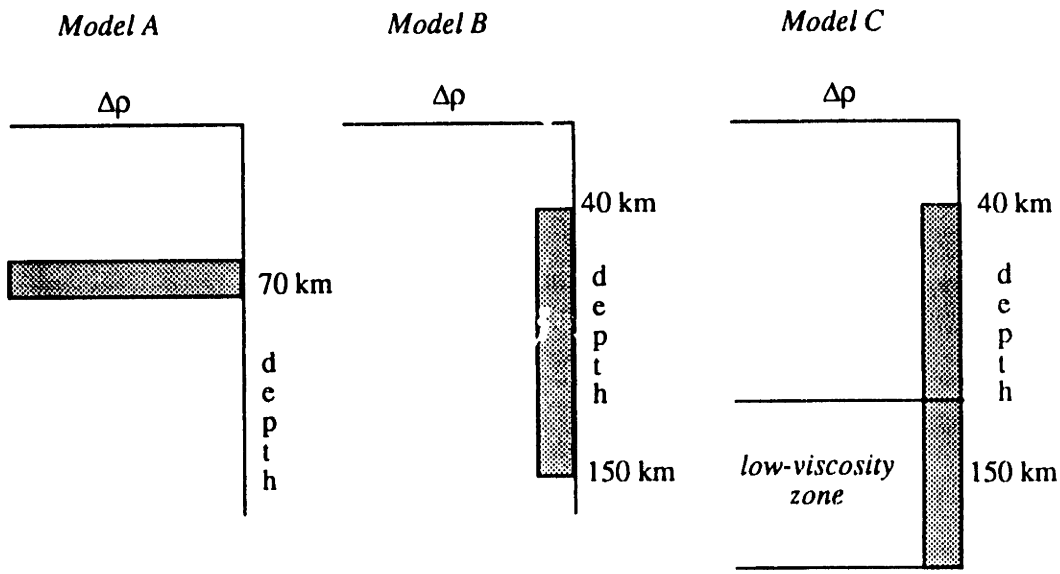
Model A
Δρ
70 km
depth
Model B
Δρ
40 km
depth
150 km
Model C
Δρ
40 km
depth
low-viscosity zone
150 km

Figure 3.4

CHAPTER FOUR

GRAVITY AND FLEXURE OF THE INTRACRATONIC WILLISTON AND MICHIGAN BASINS AND THEIR IMPLICATIONS FOR A BASIN-FORMING MECHANISM

Paula J. Waschbusch

ABSTRACT

The cause of the formation of the circularly symmetric intracratonic basins of North America (including the Michigan and Williston Basins) is enigmatic; thermal processes, phase changes and effects due to in-plane stresses have all been suggested. These basins are filled by several kilometers of sediment and typically show a prolonged subsidence history with little deformation; a plate tectonics origin is not obvious. Analysis of gravity and subsidence in this paper shows long-wavelength positive isostatic gravity anomaly over the basins, which eliminates most in-plane stress formation mechanisms. The Williston Basin has a 25 mgal positive anomaly that decreases gradually over at least 600 km, and the Michigan Basin has a 15 mgal positive anomaly that decreases over 300 km. Gravity modeling suggests a shallow sub-crustal load in the shape of an inverted cone. In our opinion, the best interpretation of this anomaly and of the basin-forming mechanism is injection by a hot spot plume of suboceanic lithospheric material into the subcontinental lithosphere and cooling over 100's of m.ys. A chemical difference between suboceanic and subcontinental lithosphere results in the presence of a mass excess after complete cooling. The chemical density contrast between the two will depend on the thickness of the continental lithosphere; for continental lithosphere of thickness between 200 and 400 km, the chemical density contrast will be between 75 and 45 kg/m^3. In order for the hot material to be neutrally buoyant and rise beneath the lithosphere, this suggests temperature contrasts between 750 and 450°C. Comparing these thermal anomalies with those inferred at hot spots today suggests a thicker lithosphere (closer to the 400 km end) was probably present at the time of basin formation. This model is consistent with theoretical modeling that shows several plumes forming at one time beneath a supercontinent, and may also explain why basin subsidence initiated shortly after breakup of the Late Proterozoic supercontinent. In this scenario, the intracratonic basins would be an ancient analog to the present day African hot spot swells (although there are some important differences between the two), which formed after breakup of the Mesozoic supercontinent.

INTRODUCTION

The mechanism of formation of intracratonic sedimentary basins is controversial. These basins are large (a few hundred kilometers in radius), generally circular and filled with several kilometers of sediments. Four such basins exist in North America (Figure 4.1), the Williston, Michigan, Illinois and Hudson Bay Basins. Because these basins formed in cratonic settings where there has generally been little tectonic deformation aside from the formation of the basin itself, a plate tectonics explanation for their origin is not obvious. The sediments within these basins thicken toward the center, precluding a formation mechanism of purely eustatic sea level changes. In addition, the presence of deeper-water sediments near the basin center and the general concordance of isopachs and facies indicate that these basins subsided relative to their surroundings during deposition.

Hypothesized intracratonic basin formation mechanisms generally fall into one of three categories: 1) decay of thermal anomalies (with or without emplacement of an excess intrusive mass), 2) increase in density due to a phase transition (basalt to eclogite and greenschist to amphibolite are the most common suggestions), or 3) deflection due to large in-plane lithospheric stresses, perhaps relating to adjacent foreland processes.

Sleep and Snell [1976] and *Haxby et al.* [1976] were the first to test rigorously the model of decaying thermal anomalies. In these models, a heated region within the lithosphere cools predominantly by conductive heat transfer to the isothermal upper and lower boundaries of the thermal plate. Both *Sleep and Snell* [1976] and *Haxby et al.* [1976] found thermal cooling produced a subsidence pattern similar to the subsidence observed in the Michigan Basin. Similar thermal cooling models have since been applied to the Williston Basin (e.g. *Ahern and Mrkvicka* [1984]) and to the Illinois Basin (e.g. *Heidlauf et al.*, [1986]). The main problem with the thermal cooling model is that simple heating followed by conductive cooling will not produce any net subsidence. In order to produce subsidence beyond the pre-heating elevation, some additional process must occur to increase the average density beneath the basin, driving basin subsidence.

One variation of the thermal cooling model relates formation of the intracratonic basins to break-up of the Late Proterozoic supercontinent [*Klein and Hsui*, 1987; *Hamdani et al.*, [1994]. The synchroneity in episodes of deposition and erosion within the basins has long been noted [*Sloss*, 1963], and correlations of these sedimentation cycles with cycles in Brazil, the Russian platform, and North Africa have been drawn [*Sloss*, 1972, 1979; *Sloss and Scherer*, 1975]. Coupled with the observation that the intracratonic basins of North America all began subsiding at roughly the same time [*Hamdani et al.*, 1994; *Klein and Hsui*, 1987; *Quinlan*, 1987] (Figure 4.2), the global synchroneity of sediment cycles suggests a common global formation process. *Klein and Hsui* [1987] suggest that the same thermal process that initiated rifting of the Late Proterozoic supercontinent (constrained between 625 - 555 Ma [*Bond et al.*, 1984]) emplaced thermal anomalies in the lithosphere that eventually cooled, forming the intracratonic basins.

Phase changes have been considered an alternative to thermal models. *Lovering* [1958] and *Kennedy* [1959] first suggested uplift and subsidence could be explained by a transition from a less dense phase to a more dense phase at Moho depth. Two phase changes are commonly suggested: greenschist to amphibolite facies (e.g. *Falvey and Middleton*, [1981], *Falvey*, [1974]), and gabbro or basalt to eclogite (e.g. *Fowler and Nisbet*, [1985], *Haxby et al.*, [1976], *Hamdani et al.*, [1991], [1994]). These models require the lower crust and/or upper mantle to be in a meta-stable phase prior to basin initiation, then convert to a more stable (and more dense) phase. Since the more stable phase is more dense, the average density of the lithosphere increases, driving the basin down. Many of these models invoke a small temperature anomaly to initiate the phase transition.

Most models which involve large in-plane stresses attempt to correlate basin subsidence with uplift of nearby intra-basinal arches. As seen in Figure 4.1, the Michigan, Williston and Illinois Basins are all located within 500-600 km of one or more of the Appalachian, Ouachita, and Rocky Mountain belts, a distance in which foreland tectonics will still have a strong influence. *Quinlan and Beaumont* [1984] argue that the sedimentation patterns within the intracratonic basins can be explained by orogenic foreland processes, but they provide no mechanism for the ultimate cause of localized subsidence. *Lambeck* [1983a,b] showed how in-

plane stresses can amplify pre-existing downwarps to form deep basins and suggested a model of alternating upwarps (arches) and downwarps (basins) that form in a quasi-linear pattern. This model requires a persistent compressive stress to maintain the warping. *De Rito et al.* [1983], and more recently *Cloethingh* [1988], suggested similar models, amplifying pre-existing lithospheric curvature to create downwarpings, but with a more complicated temperature-dependent rheology. With this rheology, part of the basin curvature remains even after removal of the in-plane stress, creating a shallow basin. After several cycles of stress application and removal, a deep basin can be formed. One of the major problems with the in-plane stress models is that they generally produce quasi-linear or rhombehedral basins, inconsistent with the observed basin circularity.

One under-utilized data source and technique that may help distinguish between intracratonic basin formation mechanisms is gravity anomalies and gravity modeling. Studies of lithospheric flexure coupled with gravity anomalies have been successful at constraining geometries and magnitudes of subsurface loads in other tectonics settings, such as foreland basins [*Lyon-Caen and Molnar*, 1983, 1985; *Kruse and Royden*, 1994], extensional margins [*Karner and Watts*, 1982] and uplifted thrust blocks [*Hall and Chase*, 1989]. To date, little work has been done using both gravity and flexure to constrain subsurface structures beneath the intracratonic basins. Several studies have focused on the constraints on formation of the intracratonic basins supplied by lithospheric flexure [*e.g. Haxby et al.*, 1978 and *Nunn and Sleep*, 1984, in the Michigan Basin, *Ahern and Mrkvicka*, 1984 in the Williston Basin], but the gravity anomalies have not received the same attention.

Nunn and Sleep [1984] used upward continuation of the gravity anomaly at the Michigan Basin to constrain the depth of the driving load to be "shallow" in order to produce the observed gravity high. However, the authors themselves point out that their first order analysis was undertaken only to provide a rough sense of the depth of the load and was not meant to be taken rigorously. Several other authors [*e.g. Haxby et al.*, 1976, in the Michigan Basin and *Ahern*, 1992, in the Williston Basin] have pointed to the observed gravity anomalies as supporting evidence for a proposed subsidence model without modeling the gravity anomalies in detail. In

this study, we use the gravity anomalies along with lithospheric flexure to place constraints on the mechanism of formation of the intracratonic basins. We focus here on the Williston and Michigan Basins since they show little tectonic deformation after formation of the basins, and for which, due to their oil-producing nature, large data bases of well log depths exist.

TECTONIC SETTING:

Williston Basin:

The Williston Basin, located mainly in Montana, North Dakota and Saskatchewan, is a broad, circular depression approximately 400 km in radius with over 4900 m of sediment at its deepest point (Figure 4.3). The basin formed atop Archean age basement of the Superior Province in its eastern part, the north-south striking Trans-Hudson Orogeny in its central part, and the Archean Wyoming Province in its western part. Some authors argue for a Middle Ordovician age of basin initiation [*Ahern and Mrkvicka*, 1984; *Porter et al.*, 1982], but more recent work suggests a Late Cambrian age of initiation [*Fowler and Nisbet*, 1985; *Haid*, 1991; *Hamdani et al.* 1984], with subsidence rates increasing in the Middle Ordovician. An initiation age of 520 Ma suggests the Williston Basin begin forming roughly 35 m.y. after breakup of the Late Paleozoic supercontinent. Termination of the basin's localized, circularly symmetric subsidence occurred approximately 120 Ma [*Hamdani et al.*, 1994], after which the Williston basin became part of the larger Cordilleran foreland basin. (See *Hamdani et al.*, [1994] for a more detailed review of the subsidence history of the Williston Basin). The long duration of subsidence (more than 350 m.y.) strongly argues for a thermal component to the basin's history.

Aside from the basin itself, there has been very little tectonic deformation in the Williston area [*Ahern and Mrkvicka*, 1984]. Crustal thickness beneath the Williston Basin is 50-55 km [*Hajnal et al.*, 1984; *Nelson et al.*, 1993] and apparently thickens smoothly toward the center of the basin. Although early seismic studies suggested evidence of an underlying rift basin [*Stewart*, 1972; *Kent*, 1987], the most recent COCORP reflection profiles in Montana and North Dakota present no evidence for a precursor rift basin beneath the Williston Basin [*Knapp et al*, 1993]. *Fowler and Nisbet* [1985] report that there is no evidence for any Cambrian

igneous event, as no K/Ar isotopic clocks show Cambrian ages. However, Rb-Sr dating on biotite of basement rocks near the center of the Williston Basin gives and age of 520 ± 30 m.y [*Hamdani et al.* 1994] and a study of apatite fission tracks gives an apparent age of 554 Ma, and suggests at least 3 km of erosion prior to subsidence of the Williston Basin [*Crowley et al.*, 1985].

Flexural modeling of the shape of the Williston Basin through time suggests the geometric center of the basin moved less than 20 km throughout its subsidence history [*Ahern and Mrkvicka*, 1984]. This small amount of movement suggests the basin driving load was probably fixed in space and the apparent motion with time of the basin center is due to scatter in the well-log depth data used in the flexural reconstructions. In addition, flexural modeling suggests that subsidence was caused by a load increasing with time near the center of the basin and that the elastic strength of the lithosphere (or flexural rigidity) also increased with time [Ahern and Mrkvicka, 1984].

Michigan Basin:

The Michigan Basin, centered on Michigan's lower peninsula, is also a broad, circular basin, approximately 300 km in radius with over 4 km of sediment in the basin's center (Figure 4.4). The basin formed atop Early Proterozoic Penokian basement except in its eastern third, which formed atop Grenville basement. As in the Williston Basin, the basal sediments in the Michigan Basin are Upper Cambrian to Lower Ordovician units, but it is debated whether these units are related to localized basin subsidence or to a more regional process, which would suggest a Middle Ordovician age of basin initiation [*Sleep et al.*, 1980; *Nunn and Sleep*, 1984; *Howell and van der Pluijm*, 1990]. This places initiation of basin subsidence either 35 m.y. or 95 m.y. after breakup of the Late Paleozoic supercontinent. Subsidence in the Michigan Basin lasted at least 160 m.y., as the Pennsylvanian sediments show a circular depositional pattern. Localized subsidence probably continued throughout the Paleozoic and into the Mesozoic, however, as a sequence of poorly consolidated "red beds" (sands and shales), probably of Jurassic age, overlie the Pennsylvanian rocks and also have a circular outcrop pattern. These

units have not been rigorously distinguished from the Pennsylvanian strata [*Nunn and Sleep,* 1984;, *Haxby et al.*, 1986], but if a more detailed study concludes these units do suggest localized subsidence was occurring into the Jurassic, subsidence in the Michigan Basin may have continued for more than 250 m.y.

While there has been virtually no secondary structural deformation since the basin formed, the Michigan Basin formed atop highly deformed crust. Gravity and magnetic anomalies and trends in petroleum production show a series of northwest trending structures of a few to a few tens of kilometers wavelength [*Ells*, 1962; *Hinze and Merritt*, 1969]. These features are believed to be related to the Proterozoic Midcontinental Rift (MCR), which formed at ~1.1 -1.2 Ga. *Brown et al.* [1982] describe COCORP seismic reflection data from the central part of the Michigan Basin in which a feature believed to be the MCR is prominent. However, reprocessing and refining of the data by *Zhu and Brown* [1986] shows the Moho beneath the rift to be no shallower than the Moho in the absence of the rift (~43 km in both cases). Thus, while presence of a rift structure implies crustal extension, the Moho position suggests that either no significant crustal thinning accompanied this rifting or that subsequent events modified the Moho back to its original thickness [*Quinlan,* 1987]. In either case, the MCR rifting preceded basin deposition by 500-600 m.y., making a correlation between events unlikely. It should be noted that the seismic reflection line discussed here is limited to 87 km long and samples only the central part of the basin and one ancient rift graben. It remains to be seen if this result (no crustal thinning) holds for the entire basin.

Flexural modeling of the shape of the Michigan Basin through time suggests the geometric center of the basin moved less than 50 km throughout its subsidence history [*Nunn and Sleep,* 1984]. In addition, the flexural modeling suggests that the elastic strength of the lithosphere (or flexural rigidity) increased with time [*Ahern and Dikeou*, 1989].

DATA:

The three primary data sets used in this paper are 1) topographic elevations, 2) Bouguer gravity anomalies, and 3) well-log depths to the oldest sedimentary horizon that shows the

basin's characteristic circular deflection. Topographic elevations and Bouguer gravity anomalies from 93° - 113° W longitude and 33° - 63° N latitude and from 74.5° - 94.5° W longitude and 29° - 59° N latitude were used to study the Williston Basin (Figure 4.5) and the Michigan Basin (Figure 4.6) respectively. Topographic data comes from the ETOPO-5 data set [*National Geophysical Data Center,* 1988]. The Bouguer gravity data comes from the Geological Society of America gravity anomaly map of North America [*Committee for the Gravity Anomaly Map of North America,* 1987]. A crustal density of 2670 kg/m^3 was used to generate anomalies. Both sets of data were gridded onto 0.05° by 0.05° bins using a minimum curvature method. Errors in the gravity field are estimated at less than 5 mgals.

The oldest unit in the Williston Basin to show circular deflection patterns is the Middle Ordovician Winnipeg Formation, a thin clastic unit. However, this formation is not often identified in well logs, so following *Ahern and Mrkvicka* [1984] we use instead the 681 recorded log depths to the top of the Upper Ordovician Red River Formation as a proxy for the total amount of basin subsidence. The *Ahern and Mrkvicka* [1984] paper contains a map showing the location of the wells used in this study. Due to the large number of data points in the Williston Basin, the depth data used in the inversion (and shown in the figures) will be the radially averaged depth data. Figure 4.7a shows the radially averaged depth data along with the errors (one standard deviation) produced by the radial averaging. Note that the zero error at points far from the basin center is a result of only having one data point at that distance from the basin center, (and thus averaging over one point) and should not be taken to mean the model must fit the subsidence data tightly at these points. In the Michigan basin the Middle Ordovician Trenton Limestone is the oldest unit to show a localized circular deflection pattern. This data set, originally published in *Hinze and Merritt* [1969], contains 91 wells, all of which are located in a quadrant southwest of the basin center (see their paper for a map of locations). Because this is a small data set and may not reflect the range of depth data values across the whole basin, we ascribe errors to the radially-averaged depth data that are equal to the errors found at the same radial distance in the Williston Basin (Figure 4.7b). The whole of the Williston Basin was

sampled, and thus the Williston Basin errors should be a more accurate reflection of basin-wide variations than the standard deviation from solely the points in the southwest quadrant.

Isostatic Gravity Anomalies

The Bouguer gravity anomaly can be considered to be derived from two sources: 1) the deflection of subsurface density interfaces by compensation of surficial topography (mainly deflection of the Moho) and 2) additional (anomalous) subsurface density contrasts and the deflections of density interfaces (the Moho and the surface) caused by these loads. Assuming isostatic equilibrium and a compensation model, we can compute the gravity anomaly from the first source (deflection of the Moho due to surface topography) and subtract it from the Bouguer gravity anomaly, leaving isostatic gravity anomalies, which reflect additional subsurface loads (such as the load driving basin subsidence) and the deflections of interfaces caused by these loads. As discussed in more detail below, both the Williston and the Michigan basins have an isostatic gravity high located over the basin center which decreases with radial distance from the basin center.

The dominant feature in the Williston Basin Bouguer gravity field is a northwest-southeast striking trend of decreasing gravity anomalies to the southwest (Figure 4.5b). This feature can be directly related to the topography of the Cordilleran fold and thrust belt (Figure 4.5a). Assuming Airy isostasy and computing isostatic anomalies (Figure 4.5c), we find isostatic gravity highs over the center of the basin which decrease with increasing radii. Shorter wavelength features are superimposed on this first order trend, most notably: 1) gravity high/low paired couples mainly located in Wyoming (most likely resulting from the basement-cored Laramide thrust block uplifts and associated basins [*Hall and Chase*, 1989]) and 2) the linear rift graben central high with smaller flanking lows of the MCR in Iowa. The half-wavelength of these features (< 60 km) is clearly smaller than the half-wavelength of the Williston Basin (~800 km). By applying a low-pass filter to the isostatic anomalies we can effectively average over these short-wavelength features and minimize their signal in the longer wavelength field we want to study (Figure 4.5d). With the short wavelength features removed, the central gravity high over

the basin is even more apparent. Averaging the smoothed isotopic anomalies radially about the basin center (48°N, 103°W), the isostatic high over the basin can be seen to have an amplitude of ~25 mgals and extend out at least 600 km from the basin center (Figure 4.5e). In all quadrants but the southeast, the isostatic gravity anomalies continue to decrease beyond this distance, suggesting the effect of the basin on the gravity field may continue for as much as 800 km from the basin's center. Figure 4.5e also shows one standard deviation errors in the radially averaged isostatic anomalies. Errors are less than 10 mgals at all distances less than 650 km from the basin center, than increases at greater distances, largely due to the higher more positive isostatic anomalies of the southeast quadrant.

The Bouguer gravity anomaly field over the Michigan Basin study area (Figure 4.6b) is dominated by 1) the presence of the Proterozoic MCR forming a horseshoe-shaped pattern of rift graben highs flanked by lows and 2) by topography associated with the Appalachian Mountains (Figure 4.6a) trending northeast-southwest (in the southeast corner of the study area). As in the case of the Williston Basin, assuming Airy isostasy and computing the isostatic anomalies largely reduces the effect of topography (Figure 4.6c). However, the effect of the MCR basins are still strongly evident in the gravity anomalies. These rift basins are narrow, linear features that can be averaged over by low-pass filtering the isostatic gravity. As was true in the Williston Basin, averaging over features of less than 60 km half-wavelength should not affect the ~600 km half-wavelength of the basin we wish to study (Figure 4.6d). The resulting isostatic gravity anomalies show a central gravity high decreasing radially with distance from the basin center (Figure 4.6e). The Michigan Basin gravity signal is more complex than the monotonic decrease seen in the Williston Basin. The central gravity high decreases ~15 mgals over the first ~300 km from the basin center, than increases ~5 mgals over the next 100 km. Beyond 400 km the isostatic anomalies begin to diverge azimuthally (as seen by the different patterns that emerge when the isostatic gravity anomaly is averaged by quadrants and by the increase in errors at this distance) and probably suggests these anomalies are not solely due to the basin subsurface load.

In summary, when the effects of isostatic compensation of known (surficial) features are removed from the Bouguer gravity anomalies, both the Williston and the Michigan Basins show

a long-wavelength gravity high centered over the basin that decreases with radial distance from the basin center. The Williston isostatic gravity anomaly decreases ~25 mgals over ~600 km and may continue to decrease as radius increases, and the Michigan isostatic gravity anomaly decrease ~15 mgals over 300 km, then increase ~5 mgals from 300 to 400 km (radially) from the basin center.

IMPLICATIONS FOR BASIN-FORMING MECHANISMS

The existence of an isostatic anomaly high over the intracratonic basins is evidence for an excess mass at depth beneath the basins. If the basins were formed by either a thermal process or a phase change, an excess mass would be produced as a direct consequence of the model. However, if the basin were formed by an in-plane stress model, no excess mass is involved, and thus there should be no positive isostatic anomalies over the basin. Since these anomalies are observed, we can say with some certainty that in-plane stress models are not consistent with the data.

Thus we are left with two classes of basin-forming mechanisms able to explain both the presence of the circular intracratonic basins and the isostatic gravity high observed over them: 1) decay of thermal anomalies and 2) an increase in density due to a phase change. Reasonable mechanisms must be able to explain the localization and long duration of observed basin subsidence. In order to meet these criteria, most (if not all) phase change models invoke a localized thermal perturbation to initiate the phase change. Thus, both classes of models suggest the need for an initial thermal anomaly.

After final cooling, the average density beneath the basin must be greater than the surrounding area, producing the load that drives basin subsidence. If a phase change is occurring, this increase in density occurs as a consequence of the phase change and the increase in density is specified by the exact reaction series that is occurring. For the gabbro to eclogite phase change that is most commonly suggested [*Fowler and Nisbet*, 1985; *Haxby et al.*, 1976; *Hamdani et al.*, 1991, 1994], the final density increase of the series is 400 kg/m^3. In the absence of phase changes, (i.e. thermal decay models), a second process must be invoked to increase the

average density beneath the basin. One possible process explored in this paper is injecting asthenospheric mantle into the subcontinental lithospheric mantle.

Seismic velocity studies suggest the subcontinental lithosphere is much thicker an suboceanic lithosphere [e.g. *Lerner-Lam and Jordan*, 1988]. This increase in lithospheric thickness is accompanied by a decreased geothermal gradient, making the subcontinental lithosphere cold compared to suboceanic lithosphere. However, there is no observation of a dramatic change in the geoid between continents and oceans, so any mass excess beneath the continents (due to the colder material), must be balanced by a mass deficit, most likely compositional (the "isopycnic hypothesis") [*Jordan*, 1975, 1988]. Thus, subcontinental lithosphere is believed to be compositionally less dense and thermally more dense than suboceanic lithosphere. Because the continents and the oceans are in isostatic equilibrium, we can estimate the compositional density contrast suggested by this model (Figure 4.8). For a given continental lithospheric thickness, the density contrast ($\rho_{\text{suboceanic lithosphere}} - \rho_{\text{subcontinental lithosphere}}$) is completely specified by requiring "ordinary" subcontinental lithosphere (lithosphere unaffected by basin subsidence) to be in isostatic equilibrium with "ordinary" suboceanic lithosphere. The density contrast will thus be dependent on the thickness of the subcontinental lithosphere, with $\Delta\rho = 76$ kg/m^3 for subcontinental lithospheric thickness (l) = 200 km, $\Delta\rho = 57$ kg/m^3 for l =300 km, and $\Delta\rho = 46$ kg/m^3 for l = 400 km.

If the thermal anomaly that initiated basin subsidence was accompanied by injection of asthenospheric mantle (which forms suboceanic lithosphere when cooled) into the subcontinental lithosphere, a large mass excess (density contrast $\rho_{\text{suboceanic lithosphere}} - \rho_{\text{subcontinental lithosphere}}$) would exist after cooling that would drive basin subsidence. When the hot asthenosphere was initially injected, the chemical density contrast may not have been evident as the chemical mass excess would have largely been offset by a thermal mass deficit. However, as the injected material cooled, the thermal mass deficit decreased and the chemical mass excess became apparent, driving subsidence in the basin with a load that increased with time. (This balancing of a thermal mass deficit and a chemical mass excess may also explain how a large thermal event could occur with little or no evidence for uplift at the surface.)

Detailed modeling of the isostatic anomalies over the basin coupled with subsidence within the basin may help constrain the size and shape of the subsurface load, and may aid in choosing between the thermal anomalies and the phase change models of basin formation.

THE MODEL:

Intracratonic Basin Driving Load:

Gravity modeling is inherently non-unique, so a trade-off exists between the quality of the fit of the model to the data and the number of free parameters in the model. With this in mind, we chose a simple geometry, that of an inverted cone, which adequately simulates the physical situation of both the cooled injected material and the distribution of crust that has become eclogite (Figure 4.9). Some of the best field evidence for an inverted cone geometry of magma intrusions can be found in the Muskox intrusions located in the northwest Canadian Shield. The intrusion, located on the Arctic Circle, 110 km east of Great Bear Lake, is a 125 km long body which plunges north, exposing a funnel-shaped body with a southern feeder-dike and a northern inverted-cone-shaped mass [*Lecheminant and Heaman,* 1989]. In addition, this geometry successfully reproduces the broad features of the observed isostatic gravity anomalies and seems physically reasonable (the injected material hits a barrier and begins to concentrate at some depth within the lithosphere forming a magma "pool" which, when cooled, looks like an inverted cone.) An inverted cone is an adequate representation of the crust that has undergone a phase change if it is assumed that the phase transformation boundary is a horizontal depth and all crust deflected beneath this depth is transformed to eclogite. (This scenario more precisely suggests a bowl-shaped geometry, but to keep the number of free parameters at a minimum, this is approximated by an inverted cone).

With an inverted cone subject to the density contrast discussed above, only two free parameters are needed to completely describe the geometry: the maximum radius of the cone and the depth to the top of the cone. We require the depth of the injection to be sub-crustal since there is no evidence for crustal extension in either basin. This is especially clear in the case of the Williston Basin where no precursor volcanism is present, but is also true in the Michigan

Basin where there is no evidence for an elevated Moho. With the density contrast and the total applied load known (total applied load is constrained by basin subsidence), the height of the cone can than be computed. Thus, for a given continental lithospheric thickness, our model has only four free parameters: the elastic plate thickness, the magnitude of the total applied load, the cone radius and the depth beneath the Moho to the top of the cone. Calculation of the basin deflection requires only three of these variables; it is independent of the depth of the load. Gravity anomalies, however, are sensitive to the load depth; deeper loads produce longer wavelength, lower amplitude anomalies relative to shallower loads. Subsidence data can be used to constrain the load and cone radius (for a given elastic plate thickness). The observed isostatic gravity anomalies can then be used to constrain the depth of the load. For the modeling discussed below, the injection of suboceanic material into a continental lithospheric of thickness l = 200 km was assumed. Assuming a phase change or changing the lithospheric thickness results only in changes to the density contrast (as discussed above), which changes the height of the inverted cone. The changes in the computed gravity anomalies when the density contrast is changed are minimal, as is discussed (and shown) later in the results section.

Forward Modeling:

The present-day geometry of the basin (as expressed by the depth to the Red River or Trenton formation for the Williston and Michigan Basins, respectively) can be considered to be the result of the deflection of the lithosphere in response to some sub-surface load. Assuming constant crustal thickness, this deflection will cause variations in Moho depth, resulting in isostatic gravity anomalies, Δg_{Moho}. Isostatic gravity anomalies will also be generated by the sub-surface load itself, $\Delta g_{intrusion}$, and, if the basin is filled with sediments of a density less than the crustal density, there will be a third source of isostatic gravity anomalies, $\Delta g_{sediments}$. (In order to keep the number of free parameters to a minimum, the density of the sediments that fill the basin is assumed to be the same as the crustal density (thus eliminating one component of the isostatic gravity anomaly : $\Delta g_{sediments} = 0$. This assumption will be tested and discussed later.) Forward modeling techniques exist that allow computation of basin deflection and isostatic

gravity anomalies if the geometry of the subsurface load is known. Thus, for an assumed geometry and magnitude of the subsurface load we can compute the deflection of the Moho and the surface, and from this deflection we can compute the isostatic gravity anomalies generated by the subsurface load. Simultaneously comparing these computations for subsidence and the isostatic gravity anomalies to the observations, we can place constraints on the geometry and magnitude of the subsurface load.

The equation for the net vertical deflection, w, of a thin elastic plate overlying an invicid fluid (in the absence of horizontal loading) due to an axisymmetric load is:

$$D\left[\left(\frac{d^2}{dr^2}+\frac{1}{r}\frac{d}{dr}\right)^2 w\right] + (\rho_m-\rho_s)g\, w = P(r)$$

where D is the flexural rigidity of the plate, P(r) is the load as a function of radius, (ρ_m-ρ_s) is the density contrast above and below the plate and g is gravity (Table 1). A solution to this equation for a cylindrical load ($P(r) = P_o$ for $r < a$; $P_o = 0$ for $r > a$) has been given by *Brotchie and Sylvester* [1969]:

$$w = \begin{cases} \frac{P_o}{(\rho_m-\rho_s)g}\left[\frac{a}{\alpha}\,ker'\left(\frac{a}{\alpha}\right)ber\left(\frac{r}{\alpha}\right) - \frac{a}{\alpha}\,kei'\left(\frac{a}{\alpha}\right)bei\left(\frac{r}{\alpha}\right) + 1\right] & r < a \\ \frac{P_o}{(\rho_m-\rho_s)g}\left[\frac{a}{\alpha}\,ber'\left(\frac{a}{\alpha}\right)ker\left(\frac{r}{\alpha}\right) - \frac{a}{\alpha}\,bei'\left(\frac{a}{\alpha}\right)kei\left(\frac{r}{\alpha}\right)\right] & r > a \end{cases}$$

where *ker, kei, ber, bei* are Kelvin functions and primes denote the derivative with respect to the argument. α is a flexural parameter that depends on the flexural rigidity of the lithosphere. This can also be written as:

$w = P_o * F_{deflec}(r)$, where

$$F_{deflec}(r) = \begin{cases} \frac{1}{(\rho_m-\rho_s)g}\left[\frac{a}{\alpha}\,ker'\left(\frac{a}{\alpha}\right)ber\left(\frac{r}{\alpha}\right) - \frac{a}{\alpha}\,kei'\left(\frac{a}{\alpha}\right)bei\left(\frac{r}{\alpha}\right) + 1\right] & r < a \\ \frac{1}{(\rho_m-\rho_s)g}\left[\frac{a}{\alpha}\,ber'\left(\frac{a}{\alpha}\right)ker\left(\frac{r}{\alpha}\right) - \frac{a}{\alpha}\,bei'\left(\frac{a}{\alpha}\right)kei\left(\frac{r}{\alpha}\right)\right] & r > a \end{cases}$$

The isostatic gravity anomalies can be computed in the Fourier domain as described by *Parker* [1972]. This technique computes the gravity anomaly generated by topography on a density interface from:

$$\Delta\tilde{g}_k = 2\pi G\Delta\rho\, e^{-kz} \sum_{n=1}^{\infty} \frac{|k|^{n-1}}{n!}\, \tilde{h}_k^n$$

where $\Delta\rho$ is the density contrast on the interface, z is the depth to the interface, k is the wavenumber and h is the topography on the interface. (A tilde [~] over a variable represents the Fourier transform of that variable.) This equation can be used to generate the gravity anomaly produced at each density interface, then the results can be summed to compute the total gravity anomaly. (While this is an infinite series, convergence is rapid (as discussed by *Parker* [1972]), so only the first few terms of the summation need be retained.)

In our model, the geometry of the subsurface load is not that of a disc, but rather that of an inverted cone. The extension of the above techniques, developed for a cylindrical disc load, to the slightly more complex inverted cone geometry is trivial: a cone can be simulated numerically by combining a large number of stacked discs of decreasing radii with increasing depth (numerical tests show 10 discs are sufficient). For each disc, the gravity anomaly and deflection can be computed and added to a running total. Thus, the total basin deflection will be the sum of the deflections due to the 10 discs simulating the cone, and the total gravity anomaly will be the sum of the gravity anomalies due to topography on 10 subsurface density interfaces (one for each disc) producing $\Delta g_{intrusion}$, and the gravity anomalies due to topography at the surface, producing $\Delta g_{sediments}$, and at the Moho, producing Δg_{Moho}.

Inverse Modeling

If the exact geometry of the subsurface load were known, it would be possible to perform a linear inversion that would find the magnitude of the applied load, P_0, that best fits (in a least squares sense) the observed basin depths and observed isostatic gravity anomalies. The method

employed here is an expansion of the technique developed by *Royden* [1988] and solves simultaneously for the deflection of the basin and the resulting isostatic gravity anomalies.

To perform the linear inversion we must be able to compute the isostatic gravity anomalies in the spatial domain (see appendix). The gravity anomaly resulting from a disc load of radially varying surface density can be expressed as

$$\Delta g_n = 2\pi G z \sum_{n=0}^{\infty} \frac{(4n+1)!}{(2n)!\, n!\, n!} \frac{1}{r'^3} \left(\frac{x}{4r'^2}\right)^{2n} \int_0^a r^{(2n+1)} \sigma(r) \left(1 + \frac{r^2}{r'^2}\right)^{\left(\frac{4n+3}{2}\right)} dr$$

where the variables are as defined in the appendix.

As described above, the isostatic gravity anomaly will have three components, $\Delta g_{sediments}$, Δg_{Moho}, and $\Delta g_{intrusion}$. Assuming here for the sake of simplicity that the intrusive geometry is the shape of a disc, the contribution from $\Delta g_{intrusion}$ can be found from the above equation with $z = z_d$, the depth to the intrusive disc, and the surface density contrast equal to the applied load; or $\sigma(r) = \text{constant} = P_o$.

$$\Delta g_{intrusive} = P_o\, 2\pi G z_d \sum_{n=0}^{\infty} \frac{(4n+1)!}{(2n)!\, n!\, n!} \frac{1}{r'^3} \left(\frac{x}{4r'^2}\right)^{2n} \int_0^a r^{(2n+1)} \sigma(r) \left(1 + \frac{r^2}{r'^2}\right)^{\left(\frac{4n+3}{2}\right)} dr$$

The gravity anomalies resulting from the deflection of the Moho can be considered as arising from a disk of infinite radius whose surface density varies with amount of deflection. Thus,

$\sigma(r) = (\rho_m - \rho_c) \cdot w(r)$ or

$\sigma(r) = (\rho_m - \rho_c) \cdot P_o \cdot F_{deflec}(r)$.

Substituting this into the equation derived in the appendix leads to

$$\Delta g_{Moho} = P_o\,(\rho_m-\rho_c)\,2\,\pi\,G\,z_M \sum_{n=0}^{\infty} \frac{(4n+1)!}{(2n)!\,n!\,n!} \frac{1}{r'^3}\left(\frac{x}{4r'^2}\right)^{2n} \int_0^{\infty} F_{deflect}(r)\cdot r^{(2n+1)} \left(1+\frac{r^2}{r'^2}\right)^{\left(\frac{4n+3}{2}\right)} dr$$

where z_M is the depth to the Moho. In this formulation, Δg_{Moho} is linearly dependent on P_o. $\Delta g_{sediments}$ can be found in a similar fashion, replacing $(\rho_m-\rho_c)$ with $(\rho_c-\rho_{sed})$.

The total isostatic gravity anomaly can then be written as $\Delta g = \Delta g_{sediments}+\Delta g_{Moho} + \Delta g_{intrusion}$, or

$$\Delta g = P_o\;2\,\pi\,G \sum_{n=0}^{\infty} \frac{(4n+1)!}{(2n)!\,n!\,n!} \frac{1}{r'^3}\left(\frac{x}{4r'^2}\right)^{2n} \cdot$$

$$\left[[(\rho_m-\rho_c)\,z_M + (\rho_c-\rho_s)] \int_0^{\infty} F_{deflect}(r)\cdot r^{(2n+1)} \left(1+\frac{r^2}{r'^2}\right)^{\left(\frac{4n+3}{2}\right)} dr + \int_0^{*} r^{(2n+1)} \left(1+\frac{r^2}{r'^2}\right)^{\left(\frac{4n+3}{2}\right)} dr \right]$$

This can be rewritten as $\Delta g = P_o \cdot F_{grav}(r)$.

Using N observations of basin depth at distance r_n from the basin center and M observations of the isostatic gravity anomaly at distance r_m from the basin center, a best fit to the model may be computed by minimizing a weighted root mean square misfit between the observed and computed depths and gravity anomalies as shown below:

$$\text{Min}\left[\sum_{n=1}^{N} \left(w_{obs}(r_n) - w(r_n)\right)^2 + R \sum_{m=1}^{M} \left(\Delta g_{obs}(r_m) - \Delta g(r_m)\right)^2 \right]$$

where R is a weighting factor chosen subjectively to determine the relative importance of the basin depth data and the gravity data in fitting the observations. To find the minimum, we set the derivative (with respect to P_o, the variable we are solving for) to zero. This leads to

$$\frac{d}{dP_o}\left[\sum_{n=1}^{N} \left(w_{obs}(r_n) - P_o \cdot F_{deflec}\,(r_n)\right)^2 + R \sum_{m=1}^{M} \left(\Delta g_{obs}(r_m) - P_o \cdot F_{grav}\,(r_m)\right)^2 \right] = 0$$

Since P_o is the only unknown in this equation ($F_{deflec}(r)$ and $F_{grav}(r)$ being specified when the geometry is specified), P_o can be solved for by a matrix inversion.

As discussed above, in our model, the geometry of the subsurface load is not that of a disc, but rather that of a cone whose height is dependent on the applied load (due to the isostatic constraint). The extension of the inverse modeling techniques to a conical load is non-trivial, since the subsurface load geometry is now dependent on the applied load, making the inversion non-linear. If we consider the cone as the sum of an infinite number of discs,

$$\Delta g_{intrusive} = \int_{z_{bottom}}^{z_{top}} P_o \; 2\pi G z_d \sum_{n=0}^{\infty} \frac{(4n+1)!}{(2n)!\, n!\, n!} \frac{1}{r'^3} \left(\frac{x}{4r'^2}\right)^{2n} \int_0^{r} r^{(2n+1)} \left(1 + \frac{r^2}{r'^2}\right)^{\left(\frac{4n+3}{2}\right)} dr$$

We specify z_{top} in the model, but z_{bottom} is found from: $P_o = \Delta\rho * h$, where $\Delta\rho$ is the density contrast between suboceanic lithosphere and subcontinental lithosphere (found from isostatic considerations). This leads to limits of integration from $(z_{top} + P_o/\Delta\rho)$ to z_{top}. As P_o now appears in the integrand, the formulation is non-linear and the inversion is non-trivial.

Rather than invoking a non-linear inversion technique, we solve this equation through an iterative process that combines forward and inverse modeling as follows: 1) Assume a cone geometry (height and width) without regard to the isostatic constraint. 2) Invert for best fit load for that geometry. 3) Forward model using the best fit load found in step 2 but apply the isostatic constraint to compute cone height. (This changes the assumed geometry and thus the computed gravity). 4) Assume the geometry (cone height) suggested by the forward modeling and return to step 2. Continue iterating until the geometry used in the inversion matches the geometry produced by the forward model. Throughout this iterative process only the cone height is varied (to eventually match the isostatic constraints); density contrast, elastic plate thickness, cone radius, and depth of cone are specified at the onset an held constant. This entire iteration process is repeated for each different geometry as the cone radius, elastic plate thickness and depth to top of intrusion are varied.

RESULTS

With four free parameters, our model is successful at reproducing the major features of the data. Figures 4.10 and 4.11 show examples of computed fits to the flexure and the observed gravity anomaly due to the subsurface load of the Michigan and Williston Basins, respectively. Note that, in order to facilitate comparisons between gravity anomalies generated by the subsurface load and the observations, the observed gravity anomalies plotted here are only the contribution from $\Delta g_{intrusive}$, found by subtracting the gravity anomaly due to deflection of the Moho (Δg_{Moho}) (computed once the shape of the subsurface load is specified) from the total isostatic gravity anomaly ($\Delta g_{total} - \Delta g_{Moho} = \Delta g_{intrusive}$).

Recall that because of the non-uniqueness inherent in gravity modeling, there is a trade-off between the model fit to the subsidence data and the model fit to the gravity data (compare Figures 4.10a and 4.11a, which are tightly constrained by the subsidence data, with Figures 4.10b and 4.11b, in which the subsidence constraints have been relaxed). Keeping this trade-off in mind, some general conclusions can be drawn from the gravity model fits to the Michigan and Williston Basin isostatic anomalies.

First, the effect of changing the lithospheric thickness (and thus changing the subsurface density contrast), or assuming a phase change density contrast, has a noticeable, but minor, effect on the computed gravity anomaly (Figures 4.10a and b, 4.11a and b). A thicker lithosphere produces a smaller density contrast, requiring the injection cone to extend deeper within the lithosphere. A deeper mass excess decreases the power in the short wavelengths (thus decreasing the amplitude of the anomaly directly over the center of the basin), but increases the power at the longer wavelengths (thus increasing the amplitude further from the basin's center). Only the first of these effects is noticeable in the figures; the increase in amplitude at greater radius is distributed over a greater area (because of the circular averaging) and thus is a smaller increase at any point, making the increase in amplitude difficult to discern. Assuming a phase change density contrast (greater than those of the injection model) produces the opposite effect, decreasing the height of the cone, thus constraining all the mass to shallower depths. With this

density contrast, the magnitude of the gravity anomaly over the basin center is significantly increased, and the gravity anomaly further from the basin's center is decreased.

Second, our geometry of an inverted cone produces a gravity anomaly that matches the shape of the observed anomaly very well. Figures 4.10c and 4.11c show examples of the best fit to the observed gravity and subsidence when the geometry of a cylinder is used in the model instead of a cone. While a cylindrical geometry matches the observations in the Michigan Basin as well as a conical geometry, the same cannot be said for the Williston Basin. There the cylindrical geometry produces a gravity anomaly that significantly underestimates the observed isostatic anomalies near the basin center and falls off at a slope greater than the observations. The shape of an inverted cone is more consistent with the observations and clearly a better choice than a cylinder for the subsurface load of the Williston Basin.

Finally, the subsurface load appears to be shallow; the best fits place the load at approximately 5 km beneath the undeflected Moho (roughly 2 km beneath the deflected Moho). The best-fitting loads coupled with the isostatic constraints leads to mass distribution in the Michigan Basin (i.e. cone height) ranging between 25 and 75 km (depending on the specific geometry considered) and between 30 and 60 km in the Williston Basin. When a phase change density contrast is assumed, the best fitting loads distribute the mass over a thickness between 6 and 10 km (depending on the specific geometry considered). A deeper mass, such as one located half way between the base of the crust and the base of the lithosphere, significantly underestimates the magnitude of the high over the basin (Figure 4.10d) and the anomaly falls off at too shallow a slope to match the observations. A shallower mass (mid-crustal), on the other hand, produces too high an amplitude anomaly at the basin center and falls off at too steep of an angle, even when the constraints on subsidence are greatly relaxed; however, this may be largely a break-down of the model, as at shallow loads the specifics of the geometry of the subsurface mass become very important, and the simplification of an assumed conical shape may not be sufficient. Without more detailed knowledge of the shape of the subsurface load, we cannot rule out a shallower load. Within the limits of this model, the subsurface load is thus constrained to be at or near the base of the crust.

Michigan Basin

When looking specifically at the Michigan Basin, a number of additional conclusions can be drawn. Because gravity modeling is non-unique, a number of geometries provide equally good fits to the deflection and gravity data. These fits have some similar characteristics (most of which can be seen in Figure 4.10):

1) The elastic plate thickness is between 35 and 45 km, tightly constrained by the subsidence data. In many cases the deflection data in the center of the basin is slightly underestimated, especially with thicker elastic plates (T_e=45). This elastic plate thickness is similar to other published values, such as 40 km (flexural rigidity, D = 4.8×10^{23} Nm) found by *Haxby et al.* [1976] and 39 km (D = 4.5×10^{23} Nm) found by *Ahern and Dikeou* [1989], even though those studies assumed a disk load geometry.

2) A subsurface load radius between 200 and 250 km appears to be the most reasonable. A radius 250 km wide (Figure 4.10b) is slightly too wide of a radius to explain the subsidence and a radius of 200 km is slightly too narrow to explain the average gravity anomaly (Figure 4.10a). These fits, however, do fit the observed data within the error bounds. A larger load radius (Figure 4.10e) is unable to produce a satisfactory fit to the subsidence data. A narrower load radius (Figure 4.10f) can fit the flexural data but cannot successfully reproduce the shape of the gravity anomaly. The fact that a single cone radius cannot fit both subsidence and gravity equally well may suggest that the true geometry is not that of a perfect cone; this is further supported by the fact that a cylindrical load geometry (Figure 4.10c) is able to satisfactorily fit the gravity and subsidence of the Michigan Basin, as discussed above.

3) There are small discrepancies between the fit of the computed gravity anomaly and the observed, the most apparent being the inability of the model anomaly to reproduce or eliminate the gravity low 300 to 400 km from the basin center. Our model does produce a gravity anomaly within the error bounds of these observed signal, but cannot match the average isostatic anomaly of these features. This observation may be further evidence that the true shape of the subsurface load deviates from a perfect inverted cone; but our ability to match the shape of

the anomaly within the error bounds suggests a cone is a sufficient representation of the true geometry.

Thus, gravity modeling of the Michigan Basin suggests an inverted cone or cylinder shaped load slightly below the base of the crust with anomalously high density material distributed in a layer 25 to 75 km thick over an area essentially as wide as the basin itself.

Williston Basin

While the general conclusion of shallow load also holds for the Williston Basin, it is much more difficult to fit the specific gravity anomaly over this basin. Figure 4.11 shows some example model fits to the Williston Basin flexure and observed subsurface load gravity anomaly when the load is placed just below the base of the crust. As noted above, Figure 4.11c showed the need for a conical geometry; a cylindrical load is not sufficient. In addition, unless the flexural constraints are greatly relaxed, the predicted gravity anomaly underestimates the shape and magnitude of the observed gravity anomaly (although the computed anomaly is mostly within the error bounds). The characteristics of the models that provide the best fits to the Williston Basin gravity and flexure are:

1) An inverted cone geometries with the subsurface load located just beneath the crust, and with a radius essentially as wide as the basin itself provide the best fit to the data. In these fits, the elastic plate thickness is between 50 and 70 km, similar to results published by *Ahern and Mrkvicka,* [1984], who assumed a point load and found an elastic plate thickness of 68 km ($D = 2.41 \times 10^{24}$ Nm), and the mass is distributed over a thickness (i.e. the cone height) between 30 and 60 km thick.

2) The magnitude of the computed gravity anomaly generated by the subsurface load is always at the lower bounds of the error bars or slightly below the error bars, significantly below the average anomaly. This tendency toward underestimating the observed gravity anomalies can be seen in Figure 4.11, and was found in *all* the computed gravity anomalies for the Williston Basin. It is especially apparent when subsidence is tightly constrained (Figure 4.11a); the computed anomaly only falls completely within the error bars of the observation when the fit to

the subsidence data is relaxed, such as by allowing a greater elastic plate thickness (Figure 4.11b) or a greater total subsurface load (Figure 4.11d) than subsidence alone would warrant.

Because the computed anomaly lies at the low end of the error bars, it may seem that increasing the magnitude of the subsurface load would produce a better fit to the observation. However, increasing the magnitude of the subsurface load does not improve the fit of the computed anomaly to the observed, because increasing the load causes the amount of Moho deflection to increase as well (and thus increases the magnitude of the gravity anomaly due to Moho deflection, Δg_{Moho}). Since the Moho is flexed down, Δg_{Moho} is negative (a mass deficit due to replacement of mantle by crust), so subtracting Δg_{Moho} from the isostatic gravity anomaly produced a more positive $\Delta g_{intrusion}$. ($\Delta g_{total} - \Delta g_{Moho} = \Delta g_{intrusive}$; Δg_{total} does not change, so a more negative Δg_{Moho} produces a more positive $\Delta g_{intrusive}$.) In this way, increasing the magnitude of the subsurface load increases both the calculated gravity and the portion of the observed anomaly that must be explained by a subsurface load; resulting in little net effect on fitting the model to the data. Note that geometries can be found where the magnitude of the computed anomaly exceeds that of the observed at the basins center (usually by assuming a narrow load radius), but these models produce extremely poor fits to the observed anomaly at distances further from the basin center.

3) In most cases, the computed anomaly acceptably estimates or slightly underestimates the magnitude of the observed gravity anomaly at the basin's center, but then falls off with radial distance with a slope steeper than that observed, thus increasing the misfit of computed to observed further from the basin center (e.g. Figure 4.11a). This may suggest the subsurface load is either broader or deeper than shown in the models of Figure 4.11. Placing the load deeper in the lithosphere may help change the slope of the computed gravity anomaly, but will also decrease the magnitude of the anomaly, especially over the basin center (as more of the anomaly will be contained in the longer wavelengths), causing the magnitude to be even more underestimated (as discussed with Figure 4.10d). (Changing the depth of the anomaly, as discussed above, does not effect the computed deflection.) Broadening the cone radius increases the fit to the gravity data, but at the expense of the fit to the subsidence data. In Figure 4.11b, the

computed flexure of the lithosphere is too broad to fit the observations, predicting too little deflection in the basin center and too much deflection at the basin fringes, but even this increased radius appears to be too narrow to fit the gravity data.

Thus, the best attempts at modeling the observed gravity anomaly over the Williston Basin place the load in an inverted cone located just beneath the crust and have high density material distributed over an area approximately as wide as the basin itself. This model compares reasonably well with the observations, but tends to underestimate the magnitude of the observed isostatic anomaly.

Effect of adding sediment density

The above analysis assumed the basin was filled with sediments of the same density as the crust (thus eliminating one variable contributing to the isostatic gravity anomaly, $\Delta g_{sediments}$). If we instead assume the basin is filled with lower density sediments (ranging from 2300 to 2670 kg/m^3), the specifics of a particular model fit to the data may change, but the overall fit of computed gravity to observed does not improve. Figure 4.10g shows a fit to the gravity anomaly over the Michigan Basin using a density of 2500 kg/m^3 for the sediments in the basin. (Note that the computed fit shown in Figure 4.10g is not a best-fit in the mathematical sense, but instead a fit found with similar deflection as is seen in Figure 4.10a, in order to facilitate comparisons with Figure 4.9a and to emphasize the effects of incorporating sediment density. Inverting for the best fit will improve the fit to the gravity data, but at the expense of the fit to the subsidence.) The most obvious effect of incorporating low density sediments is the increase in magnitude of both the predicted gravity anomaly and the component of the isostatic anomaly ascribed to $\Delta g_{intrusive}$ (compare Figures 4.10a and 4.10g). When sediments are above the flexing elastic plate, the buoyancy force, $(\rho_m-\rho_{sed})gw$, is greater, requiring a larger load be applied to produce the observed deflection. This larger subsurface load produces a larger gravity anomaly. However, the low density sediments generate a isostatic gravity anomaly component ($\Delta g_{sediments}$) that largely offsets the increased load. In addition, because the sediments in the basin are much shallower than the subsurface load, $\Delta g_{sediments}$ has greater power in the shorter

wavelengths than the computed anomaly from the subsurface load. Thus, in comparison to the assumption of sediments of crustal density, when low-density sediments are incorporated the computed anomaly more poorly fits the observed anomaly directly over the basin (where the short wavelength effect of $\Delta g_{sediments}$ increases the magnitude of the isostatic gravity anomaly), but slightly improves the fit further from the basin center, especially between 250 and 350 km, where the effect of $\Delta g_{sediments}$ has died out.

Phase transitions

As mentioned above, assuming a density contrast of 400 kg/m^3, gravity modeling is able to satisfactorily fit the observed gravity and subsidence with a load thickness between 6 and 10 km thick, (depending on the assumed geometry). This thickness, however is too great to be attributed to a phase change occurring solely in crust that has been deflected below the depth of the original (undeflected) Moho. After the basins are completely formed and sediment filled, they have approximately 3 km of basement deflection, and thus also 3 km of Moho deflection. With the assumption that prior to the onset of the phase change the crust beneath the basin was similar to surrounding crust, in order to produce a 6-10 km thick zone of crust that has undergone the phase transition after basin formation, the zone of initially meta-stable gabbro that has converted to stable eclogite must be present in the lower crust at depths at least 3 km shallower than the undeflected Moho. This phenomenon must be localized beneath the basin, as the adjacent crust apparently has not undergone similar subsidence. Thus, either the phase change boundary must have migrated shallower directly beneath the basin (allowing material beneath the basin to undergo a phase change while adjacent material at the same depth does not) or the crust beneath the basin must have been anomalous at the onset, either chemically or mechanically. Based on the modeling presented here, we cannot rule out phase transitions as the driving force for basin subsidence, but the lack of a mechanism to explain why the phase transition is not occurring anywhere but beneath the basins must be address before phase transitions can be considered a viable mechanism for intracratonic basin formation.

DISCUSSION

The results of our gravity and subsidence modeling require the basin forming subsurface load be shallow, subcrustal, and essentially as wide as the basin itself. In addition, as discussed above, a thermal component is almost certainly required, both to initiate basin formation and to explain the protracted subsidence history.

One phenomenon which produces radially symmetric, localized thermal anomalies is a hot spot plume. Invoking hot spot plumes is attractive not only because they fit the required thermal criteria, but also because plumes would produce the suggested chemical density contrast. Modern-day oceanic hot spots inject asthenospheric mantle into the suboceanic lithosphere which, when completely cooled, is isostatically indistinguishable from suboceanic lithosphere that did not have a hot spot injection. Thus, the plume model would automatically inject material with a chemical density contrast into the subcontinental lithosphere.

Thermal considerations

Injection of denser suboceanic lithosphere into less dense subcontinental lithosphere would require the thermal anomaly (the plume) to heat the injected suboceanic material to a point where it is positively buoyant and will rise through the subcontinental lithosphere. Assuming the chemical density contrasts we find with our isostatic constraint, we can compute the minimum the thermal density contrast required to achieve neutral buoyancy. Using the thermal expansion equation, $\Delta\rho = \rho_m \alpha_t \Delta T$, and setting $\alpha_t = 3 \times 10^{-5}$ /°C, we can find the excess temperature (ΔT) of the injected material. For a continental lithosphere of thickness l = 200 km, ΔT = 750 °; for l = 300 km, ΔT = 570°; and for l = 400 km, ΔT = 450°. While these temperatures may seem high, such large temperature contrasts are not inconsistent with earlier results of one-dimensional thermal modeling. *Haxby et al.* [1976], for example, found a temperature contrast of 1000°C was required to reproduce the observed subsidence history of the center of the Michigan Basin. Oceanic hot spot plume observations and petrologic analysis [*Sleep*, 1990], however, suggest a 200° - 300° thermal anomaly is more realistic. These temperatures may then suggest that the

lithosphere beneath the basins is thick, and was thick at the time of basin initiation, as thicker lithospheres require more reasonable thermal anomalies.

If hot spot plumes initiated basin formation and subsequent subsidence was entirely thermal, then the gravity model we have developed here predicts a specific thermal subsidence path. We know from our modeling that we can reproduce the correct amount of final subsidence, but the predicted thermal model should also be able to reproduce the correct shape of the subsidence curve, and more importantly, the correct timing history.

Modeling the subsurface cone as a subsurface cylinder (for computational ease), the solution to the one-dimensional heat flow equation for a hot cylinder emplaced in a lithosphere with a thermal gradient that cools with time (with variables as defined in Figure 4.12) is :

$$T(z,t) = T_m \frac{z}{l} + \sum_n T_o \frac{2}{n\pi}\left[\cos\left(\frac{n\pi L}{l}\right) - \cos\left(\frac{n\pi(L+H)}{l}\right)\right] \sin\left(\frac{n\pi z}{l}\right) \exp\left(\frac{n^2\pi^2\kappa t}{l^2}\right)$$

As the hot region cools, a load is created that drives basin subsidence. Subsidence in the center of the flexurally supported basin can be found from:

$$w(0,t) = \frac{4}{\pi^2}\frac{\rho_m}{(\rho_m-\rho_c)}\alpha_t H T_o \left(\frac{a}{\alpha}\mathrm{ker}'\left(\frac{a}{\alpha}\right) + 1\right) \sum_{n=odd} \frac{1}{n^2}\left[\cos\left(\frac{n\pi L}{l}\right) - \cos\left(\frac{n\pi(L+H)}{l}\right)\right]\left(1 - \exp\left(\frac{n^2\pi^2\kappa t}{l^2}\right)\right)$$

Because we know our model produces subsidence within the range of observations (from our earlier modeling) and because we wish to compare the subsidence history predicted by different lithospheric thicknesses (and thus different ΔTs), we normalize basin deflection by the total amount of thermal subsidence. Figure 4.13 shows the resulting subsidence curve for both the Michigan and Williston Basins with lithospheric thicknesses l=200,300, and 400 km. This thermal model produces subsidence beginning approximately 20 m.y. after emplacement of the heated material with cooling continuing for more than 300 m.y., depending on lithospheric thickness: with a thinner lithospheric thickness, the thermal anomaly is dispersed more rapidly. When the anomaly is deeper (i. e. the Williston Basin), a longer period of time elapses before

subsidence begins. These simple models predict subsidence histories in the right range of those observed, although they probably overestimate the amount of time the basin subsided. This does suggest, however, that the gravity model developed is roughly consistent with the thermal constraints.

Possible Tectonic Setting for Basin Initiation

In the scenario we are developing, the synchroneity of subsidence initiation in the intracratonic basins would suggest that at some time prior to basin initiation, the North American craton was more vulnerable to mantle injection and hot spot plumes. The correlation of basin initiation to break-up of the Late Proterozoic supercontinent has also been noted. Following on the models of *Klein and Hsui* [1987] and *Hamdani et al.* [1994], we propose the timing between the events is not coincidental, but rather that it was the breakup of the supercontinent that caused basin initiation. Convection modeling of the thermal structure beneath supercontinents [e.g. Gurnis, 1988] suggests that the formation of a supercontinent causes a "thermal blanketing" effect, increasing temperatures beneath the supercontinent which eventually causes plumes to develop and rifts to form. The North American craton is unique among the fragments of the Late Proterozoic supercontinent in that it is almost entirely rimmed by rifted margins of that age, suggesting perhaps that it was the nucleus of the supercontinent from which everything else rifted off. In the only other supercontinent cycle from which we have a well preserved geologic record, (the Mesozoic supercontinent of Pangea), Africa is the cratonic fragment left almost entirely rimmed by rifts of super-continent breakup age. We thus propose Africa may be a modern-day analog to North America at the time of basin formation.

Africa is the site of the majority of continental hot spot plumes observed today, suggesting that the analogy may have some merit, but there are some obvious differences between the African hot spot swells and the intracratonic basins. Clearly surface volcanism is seen over the African hot spot swells today and there is evidently no volcanism of ages corresponding to basin initiation seen beneath either the Michigan or Williston intracratonic basins. We suggest this could mean the injected material beneath the African swells has

penetrated more deeply into the lithosphere than in the case of the North America basins, possibly because the North American craton was not stable with respect to the hot spot frame of reference after breakup of the supercontinent, as the African craton clearly has been (for at least the last 20 m.y. [*Burke and Wilson* 1972]). The fact that there are no intermediate settings between the African hot spot swells and the North American intracratonic basins can be explained because only two supercontinent cycles have occurred in the last at least 800 m.y., thus with only two observations, we cannot have intermediate members.

CONCLUSIONS

Both the Michigan and the Williston Basins are associated with long-wavelength positive isostatic anomalies. The presence of these anomalies rule out in-plane stresses as a formation mechanism for the basins. A detailed look at modeling these isostatic gravity anomalies suggests that the subsurface load driving surface subsidence is shaped like an inverted cone and is located slightly below the crust. Attempting to model these anomalies by a phase change in the lower crust requires a large area of meta-stable phases to be present solely beneath the basin or to fortuitously undergo a phase change only beneath the basin. While we can not rule out this possibility, the coincidences required make it a less likely model. Subsidence due to thermal processes and an ultimate chemistry change (from subcontinental lithosphere to suboceanic lithosphere) is our preferred model. The injected suboceanic material has enough buoyancy to reach the base of the crust, but not enough to penetrate the crust, pooling up to form the inverted cone shape observed in the isostatic anomalies. The thermal aspects of this model are consistent with observations from the basins. The injected material may be from plumes penetrating the lithosphere when the North American craton was located deep within a supercontinent (as evidenced by its many rifted margins of Late Proterozoic age. In break-up of the most recent Mesozoic supercontinent, the African craton was left with many rifted margins, suggesting its setting may be analogous to the setting of the North American craton when the intracratonic basins formed. In a way, the intracratonic basins of North America may be ancient analogs of the African hot spots of today.

APPENDIX: GRAVITATIONAL ATTRACTION OF A DISC LOAD IN THE SPATIAL DOMAIN

Following the examples of Telford [1990] and with the variables as identified in Figure A1, we can compute the gravity anomaly at point P due to a disc of radially varying surface density $\sigma(r)$ as follows:

The gravitational attraction of a point element of the disc can be found from:

$$r\,dr\,d\phi = \frac{G\,\sigma(r)\,r\,dr\,d\phi}{r''^2}$$

Since we want the gravity anomaly, all we are really concerned with is the vertical component, or

$$r\,dr\,d\phi = \frac{G\,\sigma(r)\,r\,dr\,d\phi}{r''^2}\ \frac{z}{r}$$

The anomaly due to the entire disc can then be found by integrating over all elements:

$$\Delta g = \int_0^{a}\int_0^{2\pi} \frac{G\,z\,\sigma(r)\,r\,dr\,d\phi}{r''^3}$$

Now $\frac{1}{r''^3}$ can be expanded into a series of Legendre Polynomials:

$$\frac{1}{r''^3} = \frac{1}{r'^3}\left[\frac{r'}{r}P'_0(u) + P'_1\ (u) + \left(\frac{r}{r'}\right)P'_2 + \left(\frac{r}{r'}\right)^2 P'_3 + \cdots\right] \quad r' \geq r$$

$$\frac{1}{r''^3} = \frac{1}{r^3}\left[\frac{r}{r'}P'_0(u) + P'_1\ (u) + \left(\frac{r'}{r}\right)P'_2 + \left(\frac{r'}{r}\right)^2 P'_3 + \cdots\right] \quad r' \leq r$$

where $u = \cos\gamma$ and primes on the Polynomial terms represent the first derivative of that polynomial. Note that from geometric considerations $u = \cos\gamma = \frac{x}{r'}\cos\phi$. Simplifying:

$$\frac{1}{r''^3} = \frac{1}{r'^3}\left[\sum_{n=0}^{\infty}\left(\frac{r}{r'}\right)^{n-1}P'_n(u)\right] \quad r' \geq r$$

$$\frac{1}{r^3} = \frac{1}{r^3}\left[\sum_{n=0}^{\infty}\left(\frac{r'}{r}\right)^{n-1}P'_n(u)\right] \quad r' \leq r$$

The even order polynomials, P_0, P_2, P_4, ... contain only even powers of u (thus cos γ). so their derivatives contain only odd powers of cos γ. When integrated between 0 and 2π, odd powers of cos γ will vanish, leaving only odd polynomials to contribute to the sum.

A well established equation for the first derivative of the odd Legendre Polynomials (see Kellogg, 1953 for example):

$$P'_{2n+1}(u) = \sum_{k=0}^{n}(-1)^k \frac{1\cdot3\cdot5\ \cdots(4n-2k+1)}{2^k\,k!\,(2n-2k)!}\left(u^{2n-2k}\right)$$

$$P'_{2n+1}(u) = \sum_{k=0}^{n}(-1)^k \frac{1\cdot3\cdot5\ \cdots(4n-2k+1)}{2^k\,k!\,(2n-2k)!}\left(\frac{x\cos\phi}{r'}\right)^{2n-2k}$$

Combining this with integral 1: for r' > a :

$$\Delta g = G\,z\sum_{n=0}^{\infty}\sum_{k=0}^{n}(-1)^k \frac{1\cdot3\cdot5\ \cdots(4n-2k+1)}{2^k\,k!\,(2n-2k)!}\int_0^{a}\int_0^{2\pi}\frac{\sigma(r)\,r^{2n+1}\cos^{2n-2k}\phi\ x^{2n-2k}}{r^{4n+3-2k}}\,d\phi\,dr$$

now, $\int_0^{2\pi}\cos^{2n-2k}\phi\ d\phi$ can be computed analytically from a table of integrals:

$$\int_0^{2\pi}\cos^{2n-2k}\phi\ d\phi = \frac{2\pi}{2^{2n-2k}}\left(\frac{(2n-2k)!}{(n-k)!(n-k)!}\right)$$

Computing the first term: k = n

$$\int_0^{2\pi}\cos^{0}\phi\ d\phi = 2\pi$$

$$\Delta g_0 = G\, z\, (2\pi) \sum_{n=0}^{\infty} (-1)^n \frac{1\cdot 3\cdot 5 \cdots (2n+1)}{2^n\, n!} \frac{1}{r'^{2n+3}} \int_0^a r^{2n+1}\, \sigma(r)\, dr$$

$$\Delta g_0 = \frac{2\pi G z}{r'^3} \int_0^a r\, \sigma(r) \left[\sum_{n=0}^{\infty} -1^n \frac{1\cdot 3\cdot 5 \cdots (2n+1)}{2^n\, n!} \left(\frac{r}{r'}\right)^2 \right] dr$$

Now, the binomial theorem says:

$$(1+x)^n = 1 + nx + \frac{n(n-1)}{2!}x^2 + \frac{n(n-1)(n-2)}{3!}x^3 + \cdots$$

For n = -3/2,

$$(1+x)^{\frac{3}{2}} = 1 - \frac{3}{2}x + \frac{\frac{3}{2}\,\frac{5}{2}}{2!}x^2 + \frac{\frac{3}{2}\,\frac{5}{2}\,\frac{7}{2}}{3!}x^3 + \cdots$$

$$(1+x)^{\frac{3}{2}} = \sum_{n=0}^{\infty} (-1)^n \frac{1\cdot 3\cdot 5 \cdots (2n+1)}{2^n\,(n)!} x^n$$

$$\text{so } \Delta g_0 = \frac{2\pi G z}{r'^3} \int_0^a r\, \sigma(r) \left(1 + \frac{r^2}{r'^2}\right)^{\frac{3}{2}} dr$$

Computing second term: k = n-1

$$\int_0^{2\pi} \cos^2\phi \; d\phi = \pi$$

$$\Delta g_1 = G\, z\, (\pi)\, x^2 \sum_{n=1}^{\infty} (-1)^{n-1} \frac{1\cdot 3\cdot 5 \cdots (2n+3)}{2^{n-1}\,(n-1)!\; 2!} \frac{1}{r'^{2n+2+3}} \int_0^a r^{2n+1}\, \sigma(r)\, dr$$

Now, binomial theorem for $(1+x)^{\frac{7}{2}}$

$$(1+x)^{\frac{7}{2}} = \sum_{n=1}^{\infty} (-1)^{n-1} \frac{7\cdot 9\cdot 11 \cdots (2n+3)}{2^{n-1}\,(n-1)!} x^{n-1}$$

so

$$\Delta g_1 = \frac{3\cdot5\cdot \pi G z x^2}{2!\, r'^7} \int_0^a r^3 \sigma(r) \left(1 + \frac{r^2}{r'^2}\right)^{\frac{7}{2}} dr$$

Computing the third term: k - n-2:

$$\int_0^{2\pi} \cos^4\phi \; d\phi = \frac{3}{4}\pi$$

$$\Delta g_2 = G z \left(\frac{3}{4}\pi\right) x^4 \sum_{n=2}^{\infty} (-1)^{n-2} \frac{1\cdot3\cdot5 \cdots(2n+5)}{2^{n-2}\,(n-2)!\; 4!} \frac{1}{r'^{2n+7}} \int_0^a r^{2n+1} \sigma(r)\; dr$$

$$\Delta g_2 = \frac{3\cdot5\cdot7\cdot9 \cdot\frac{3}{4} \pi G z x^4}{4!\, r'^{11}} \int_0^a r^5 \sigma(r) \left(1 + \frac{r^2}{r'^2}\right)^{\frac{11}{2}} dr$$

Generalizing to all n terms:

$$\Delta g_n = \frac{1\cdot3\cdot5 \cdots(4n+1)\, 2\pi G z x^{2n}}{2^{2n}\, n!\; n!\; r'^{(4n+3)}} \int_0^a r^{(2n+1)} \sigma(r) \left(1 + \frac{r^2}{r'^2}\right)^{\left(\frac{4n+3}{2}\right)} dr$$

and simplifying:

$$\Delta g_n = 2\pi G z \sum_{n=0}^{\infty} \frac{(4n+1)!}{(2n)!\; n!\; n!} \frac{1}{r'^3} \left(\frac{x}{4r'^2}\right)^{2n} \int_0^a r^{(2n+1)} \sigma(r) \left(1 + \frac{r^2}{r'^2}\right)^{\left(\frac{4n+3}{2}\right)} dr$$

Comparisons of $\Delta g_{spectral}$ (computed following Parker [1972] and discussed in the forward modeling section) and $\Delta g_{spatial}$ (above equation) shows that a large number of terms in the summation must be kept in order to accurately compute $\Delta g_{spatial}$. Our summation goes from n=0 to 200, which, for all tested cases comes within 1% of $\Delta g_{spectral}$.

It can be shown with similar algebraic manipulations that the equations for $r' < a$ are identical.

REFERENCES

Ahern, J. L., 1992, Mechanical modeling of the Williston Basin constrained by COCORP seismic reflection profiling, *EOS Transactions of the American Geophysical Union*, **73**, p. 321.

Ahern, J. L., and P. J. Dikeou, 1989, Evolution of the lithosphere beneath the Michigan Basin, *Earth Planet. Sci. Lett.*, **95**, 73-84.

Ahern, J. L., and S. R. Mrkvicka, 1984, A mechanical and thermal model for the evolution of the Williston Basin, *Tectonics*, **3**, 79-102.

Bond, G. C., P. A. Nickeson, and M. A. Kominz, 1984, Breakup of a supercontinent between 625 Ma and 555 Ma: new evidence and implications for continental histories, *Earth Planet. Sci. Lett.*, **70**, 325-345.

Brown, L., L. Jensen, J. Oliver, S. Kaufman, and D. Steiner, 1982, Rift structure beneath the Michigan Basin from COCORP profiling, *Geology*, **10**, 645-649.

Brotchie, J. F., and R. Sylvester, 1969, Crustal flexure, *J. Geophys. Res.*, **74**, 5240-5252.

Burke, K. and J. T. Wilson, 1972, Is the African plate stationary?, *Nature*, **239**, 387-390.

Committee for the Gravity Anomaly Map of North America, 1987, Gravity anomaly map of North America, *Geol. Soc. of Amer.*, 5 sheets, scale 1:5,000,000.

Ells, G. D., 1962, Structures associated with the Albion-Scipio oil field trend, *Mich. Geol. Survey*.

Fowler, C. M. R., and E. G. Nisbet, 1985, The subsidence of the Williston Basin, *Can. J. Earth Sci.*, **22**, 408-415.

Gurnis, M., 1988, Large-scale mantle convection and the aggregation and dispersal of supercontinents, *Nature*, **322**, 695-699.

Haid, J. H., 1991, Tectonic subsidence analysis of the Williston Basin, *Master's thesis*, University of Saskatchewan.

Hajnal, Z. C. M. R. Fowler, R. F. Mereu, E. R. Kanasewich, G. L. Cumming, A. G. Green, and A. Mair, 1984, An initial analysis of the Earth's crust under the Williston Basin; COCRUST experiment, *J. geophys. Res.*, **89**, 9381-9400.

Hall, M. K. and C. G. Chase, 1989, Uplift, unbuckling and collapse; flexural history and isostasy of the Wind River Range and Granite Mountains, Wyoming, *J. Geophys. Res.*, **94**, 17581-17593.

Hamdani, Y., J.-C. Mareschal, and J. Arkani-Hamed, 1991, Phase changes and thermal subsidence in intracontinental sedimentary basins, *Geophys. J. Int.*, **106**, 657-665.

Hamdani, Y., J.-C. Mareschal, and J. Arkani-Hamed, 1994, Phase change and thermal subsidence of the Williston Basin, *Geophys. J. Int.*, **116**, 585-597.

Haxby, W. F., D. L. Turcotte, and J. M. Bird, 1976, Thermal and mechanical evolution of the Michigan Basin, *Tectonophysics*, **36**, 57-75.

Hinze, W. J., and D. W. Merritt, 1969, Basement rocks of the southern peninsula of Michigan, *Michigan Basin Geol. Soc.*, pp. 28-59.

Howell, P. D., and B. A. van der Pluijm, 1990, Early history of the Michigan basin: sunsidence and Appalachian tectonics, *Geology*, **18**, 1195-1198.

Jordan, T. H., 1975, The continental tectosphere, *Rev. Geophys. Space Phys.*, **13**, 1-12.

Karner and Watts, 1982, On isostasy at Atlantic-type continental margins, *J. Geophys Res.*, **87**, 2923-2948.

Karner, G. D., M. S. Steckler, and J. A. Thorne, 1983, Long-term thermo-mechanical properties of the continental lithosphere, *Nature*, **304**, 250-253.

Kellogg, O. D., 1953, Foundation of potential theory, Dover Publication, New York.

Kennedy, G. C., 1959, The origin of continents mountain ranges and ocean basins, *Am. Sci.*, **97**, 491-504.

Kent, D. M., 1987, Paleotectonic controls on sedimentation in the northern Williston Basin, Saskatchewan, in Longman, M. W., ed., 1987, Williston Basin: anatomy of a cratonic oil province, *Rocky Mountain Association of Petroleum Geologists*, 45-56.

Klein, G. deV., and A. T. Hsui, 1987, Origin of cratonic basins, *Geology*, **15**, 1094-1098.

Knapp, J. H., D. J. Baird, D. N. Steer, J. J. Walters, L. D. Brown and K. D. Nelson, 1993, The COCORP Williston Basin surveys: deep reflection profiling of ancient continental margins, *EOS Transactions of the American Geophysical Union*, **74**, p. 443.

Kruse, S. E., and L. H. Royden, 1994, Bending and unbending of an elastic lithosphere: The Cenozoic history of the Apennine and Dinaride foredeep basins, *Tectonics*, **13**, 278-302.

Le Cheminant, A. N., and L. M. Heaman, 1989, "Mackenzie igneous events, Canada: Middle Proterozoic hotspot magmatism associated with ocean opening", *Earth Plan. Sci. Lett*, **96**, 38-48.

Lyon-Caen, H., and P. Molnar, 1983, Constraints on the structure of the Himalaya from an analysis of gravity anomalies and a flexural model of the lithosphere, *J. Geophys. Res.*, **88**, 8171-8191.

Lyon-Caen, H., and P. Molnar, 1985, Gravity anomalies, flexure of the Indian plate and the structure, support and evolution of the Himalaya and Ganga basin, *Tectonics*, **4**, 513-538.

Milbert, D. G., and D. G. Schultz, 1993, GEOID93: A new geoid model for the United States, *EOS Transactions of the American Geophysical Union*, **74**, p. 96.

National Geophysical Data Center, 1988, ETOPO-5 bathymetry/topography data, Data Announcement 88-MGG-02, Natl. Oceanic and Atmos. Admin., U.S. Dep. Commer., Boulder, Colo.

Nelson, K. D., D. J. Baird, J. J. Walters, M. Hauck, L. D. Brown, J. E. Oliver, J. L. Ahern, Z. Hajnal, A. G. Jones, and L. L. Sloss, 1993, Trans Hudson Orogen and Williston Basin in Montana and North Dakota: new COCORP deep profiling results, *Geology*, **21**, 447-451.

Nunn, J. A., and N. H. Sleep, 1984, Thermal contraction and flexure of intracratonal basins: a three-dimensional study of the Michigan Basin, *Geophys. J. R. astro. Soc.*, **76**, 587-635.

Parker, R. L., 1972, The rapid calculation of potential anomalies, *Geophys. J. R. astro. Soc.*, **31**, 447-455.

Porter, J. W., R. A. Price, and R. G. McGrossman, 1982, The western Canada Sedimentary Basin, *Phil. Trans. R. Soc. Lond., A*, **305**, 169-192.

Quinlan, G., 1987, Models of subsidence mechanisms in cratonic basins and their applicability to North American examples, in *Sedimentary Basins and Basin Forming Mechanisms, Can. Soc. Petrol. Geol., Mem.*, **12**, 463-481.

Royden, L., 1988, Flexural behavior of the continental lithosphere in Italy: constraints imposed by gravity and deflection data, *J. Geophys. Res.*, **93**, 7747-7766.

Sleep, N. H., 1990, Hotspots and mantle plumes: some phenomenology, *J. Geophys. Res.*, **95**, 6715-6736.

Sleep, N. H., J. A. Nunn, and L. Chou, 1980, Platform basins, *Ann. Rev. Earth planet. Sci.*, **8**, 17-34.

Stewart, J. H., 1972, Initial deposits in the Cordilleran geosyncline: evidence of a late Precambrian (850 m.y.) continental separation, *Geol. Soc. of America, Bulletin*, **83**, 1345-1360.

Stewart, J. H., 1976, Late Precambrian evolution of North America: plate tectonics implication, *Geology*, **1**, 11-15.

Telford, W. M., L. P. Geldart, and R. E. Sheriff, 1990, Applied Geophysics, 2nd edition, Cambridge University Press, N.Y.

Ullrich, L. and R. Van der Voo, 1981, Minimum continental velocities with respect to the pole since the Archean, *Tectonophysics*, **74**, 17-27.

Zhu, T. and L. W. Brown, 1986, COCORP Michigan surveys: reprocessing and results, *J. Geophys. Res.*, **91**, 11477-11495.

Table 1. Variables used in computations

ρ_m	density beneath the Moho	3200 kg/m^3
ρ_c	density of the continental crust	2670 kg/m^3
g	acceleration of gravity	9.8 m/s^2
G	gravitational constant	6.67x10^{-11} Nm^2/kg^2
D	flexural rigidity $D = ET_e^3/12/(1-\nu^2)$	
	where	
	E = Young's modulus	8.53x10^{10} N/m^2
	ν = Poisson's ratio	0.25
α	flexural parameter $\alpha = (4D/\Delta\rho g)^{1/4}$	

FIGURE CAPTIONS

Figure 4.1: Location of the four intracratonic basins of North America (stippled) and spatial relationship to major orogenic belts. After *Quinlan* [1987]

Figure 4.2: Subsidence history of the four intracratonic basins of North America. After *Hamdani et al.* [1994]

Figure 4.3: Map of the Williston Basin area, with depth to basement shown at 500 meter contour intervals. Edge and outliers of the Cambrian Deadwood Formation indicated by hachured pattern; edge of Paleozoic formation indicated by dashed line. After *Crowley et al.* [1985]

Figure 4.4: Map of the Michigan Basin area, with depth to basement shown at 1 km contour intervals. After *Howell and van der Pluijm* [1990]

Figure 4.5: a) Topography of the Williston Basin study area. Contour interval is 250 meters. A black dot marks inferred current center of the Williston Basin. A large circle shows a radius of 800 km about the center of the basin. b) Bouguer gravity anomaly of the Williston Basin study area. Contour interval is 25 mgals. c) Isostatic gravity anomaly of the Williston Basin study area. Contour interval is 15 mgals. d) Modified isostatic gravity anomaly of the Williston Basin study area (see text for details). Contour interval is 15 mgals. e) Radial isostatic gravity anomaly (black dots) obtained by circularly averaging about the center of the Williston Basin. Also shown is the average isostatic gravity by quadrants and one standard deviation of the radial averaging

Figure 4.6: a) Topography of the Michigan Basin study area. Contour interval is 100 meters. A black dot marks inferred current center of the Michigan Basin. A large circle shows a radius of 800 km about the center of the basin and a smaller one shows a 400 km radius. b) Bouguer gravity anomaly of the Michigan Basin study area. Contour interval is 20 mgals. c) Isostatic gravity anomaly of the Michigan Basin study area. Contour interval is 20 mgals. d) Modified isostatic gravity anomaly of the Michigan Basin study area (see text for details). Contour interval is 20 mgals. e) Radial isostatic gravity anomaly (black dots) obtained by circularly averaging about the center of the Michigan Basin. Also shown is the average isostatic gravity by quadrants and one standard deviation of the radial averaging

Figure 4.7: a) Radially averaged depth to the Upper Ordovician Red River Formation in the Williston Basin with one standard deviation errors. b) Depth to the Middle Ordovician Trenton Limestone Formation in the Michigan Basin with the same errors as computed in the radially averaging of the Williston Basin.

Figure 4.8: Schematic diagram of the isostatic constraint. All three columns are constrained to hold equal mass. See text for details.

Figure 4.9: Schematic diagram of the gravity model. See text for details.

Figure 4.10: Comparison of the model gravity anomalies and basin deflections (solid lines) with observations (symbols) in the Michigan Basin. Note that the observed gravity anomaly is $\Delta g_{intrusive}$, as discussed in the text. a) Model computed with tight constraints on the deflection. Maximum cone radius (a) = 200 km, elastic plate thickness (T_e) = 35 km. Solid line: continental lithosphere of thickness l = 200 km (height of cone (h) = 45 km), long dashed line: l = 300 km (h = 57 km), intermediate

dashed line: l = 400 km (h = 75 km), short dashed line: phase change model, (h = 9 km) b) Model computed with relaxed constraints on deflection. a = 250 km, T_e = 35 km, Solid line: l = 200 (h = 30 km), long dashed line: l = 300 km (h = 42 km), intermediate dashed line: l = 400 km (h = 55 km), short dashed line: phase change model, (h = 6.5 km) c) Model computed with cylindrical geometry, a = 175 km, T_e = 35 km, l = 200 km (h = 24 km). d) Model computed with deep anomaly (top = 125 km) a = 200 km, T_e = 35 km, l = 200 km (h = 45 km). e) Model computed with increased load radius, a = 300 km, T_e = 45 km, l = 200 km (h = 24 km), f) Model computed with decreased load radius, a = 150 km, T_e = 35 km, l = 200 km (h = 70 km) g) Model computed with the effects of sediment loading incorporated ρ_{sed} = 2500 kg/m^3, a = 200 km, T_e = 35 km, l = 200 km (h = 57 km)

Figure 4.11: Comparison of the model gravity anomalies and basin deflections (solid lines) with observations (symbols) in the Williston Basin. Note that the observed gravity anomaly is $\Delta g_{intrusive}$, as discussed in the text. a) Model computed with tight constraints on the deflection. a = 350 km, T_e = 55 km Solid line: continental lithosphere of thickness l = 200 (height of cone (h) = 37 km), long dashed line: l = 300 km (h = 49 km), intermediate dashed line: l = 400 km (h = 61 km), short dashed line: phase change model, (h = 7 km) b) Model computed with relaxed constraints on deflection. a = 450 km, T_e = 75 km, Solid line: l = 200 (h = 31 km), long dashed line: l = 300 km (h = 42 km), intermediate dashed line: l = 400 km (h = 53 km), short dashed line: phase change model, (h = 6 km) c) Model computed with cylindrical geometry, a = 300 km, T_e = 55 km, l = 200 km (h = 24 km). d) Model computed with relaxed constraints on deflection showing effect of increasing load magnitude. a = 450 km, T_e = 65 km, l = 200 km (h = 37 km),

Figure 4.12: Geometry and definition of variables used in the thermal calculation.

Figure 4.13: Results of one-dimensional thermal modeling. Normalized subsidence (relative to total thermal subsidence) is plotted as a function of time since emplacement. Bold lines show theoretical curves based on gravity modeling fits of the Williston Basin. Plain lines show theoretical curves based on gravity modeling fits of the Michigan Basin. In both sets of lines, solid lines represent cooling of a 200 km thick continental lithosphere (l = 200 km) , long dashed lines are for l = 300 km, and short dashed lines are for l = 400.

Figure A1: Geometry and definition of variables used in the derivation of the gravitational attraction of a disc load in the spatial domain.

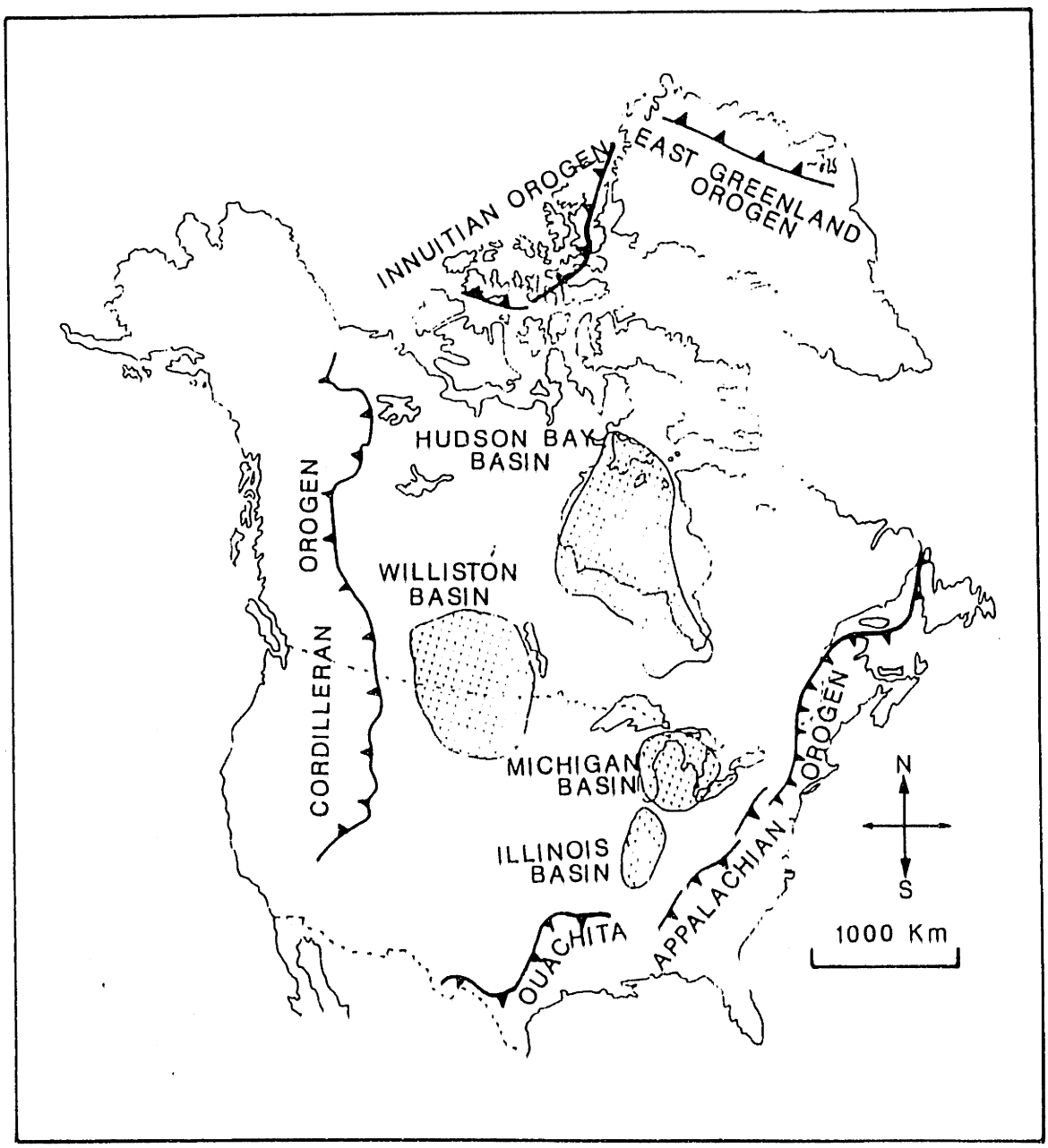
INNUITIAN OROGEN
EAST GREENLAND OROGEN
HUDSON BAY BASIN
WILLISTON BASIN
CORDILLERAN OROGEN
MICHIGAN BASIN
ILLINOIS BASIN
OUACHITA
APPALACHIAN OROGEN
N
S
1000 Km

Figure 4.1

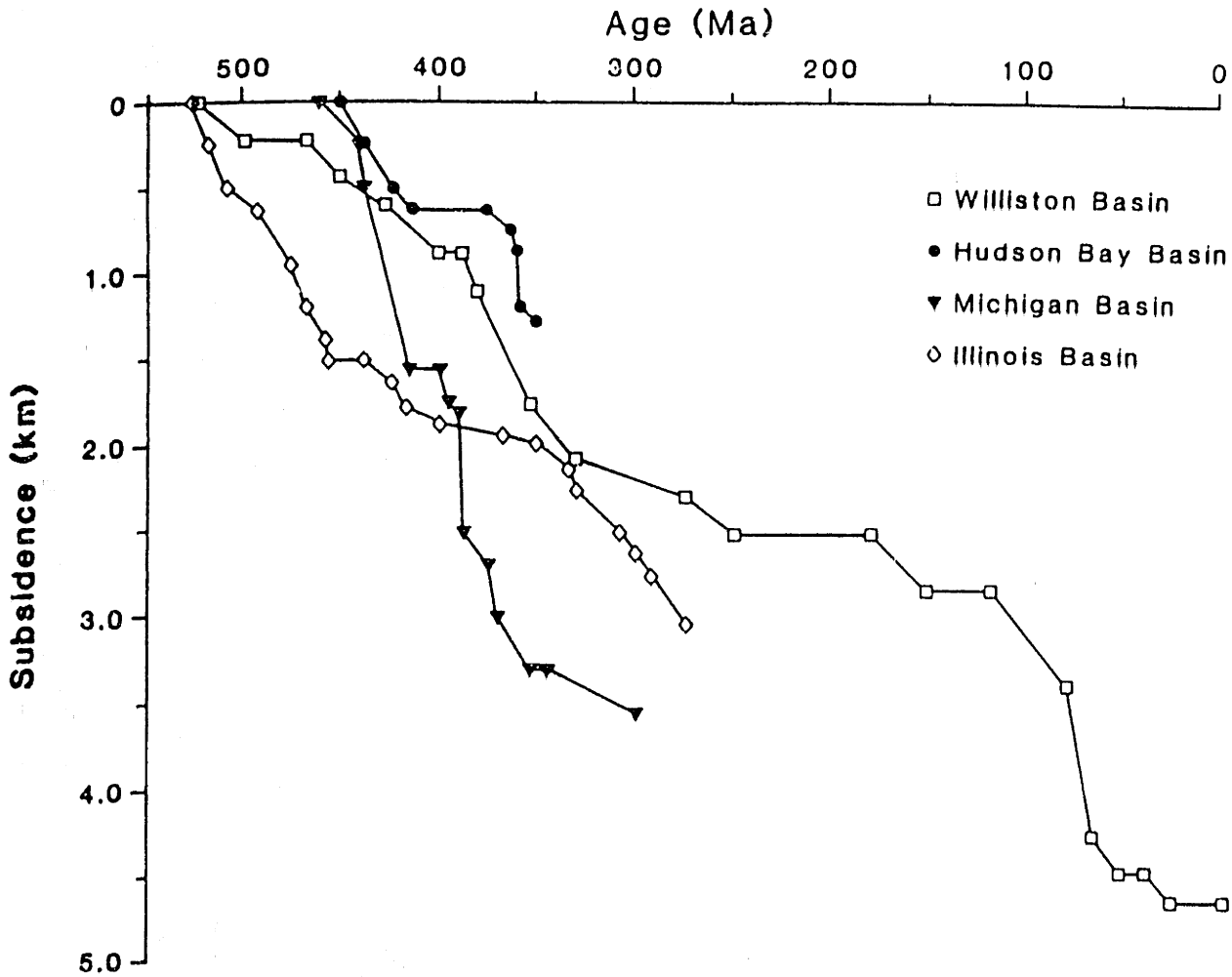
Age (Ma)
500
400
300
200
100
0
0
1.0
2.0
3.0
4.0
5.0
Subsidence (km)
Williston Basin
Hudson Bay Basin
Michigan Basin
Illinois Basin

Figure 4.2

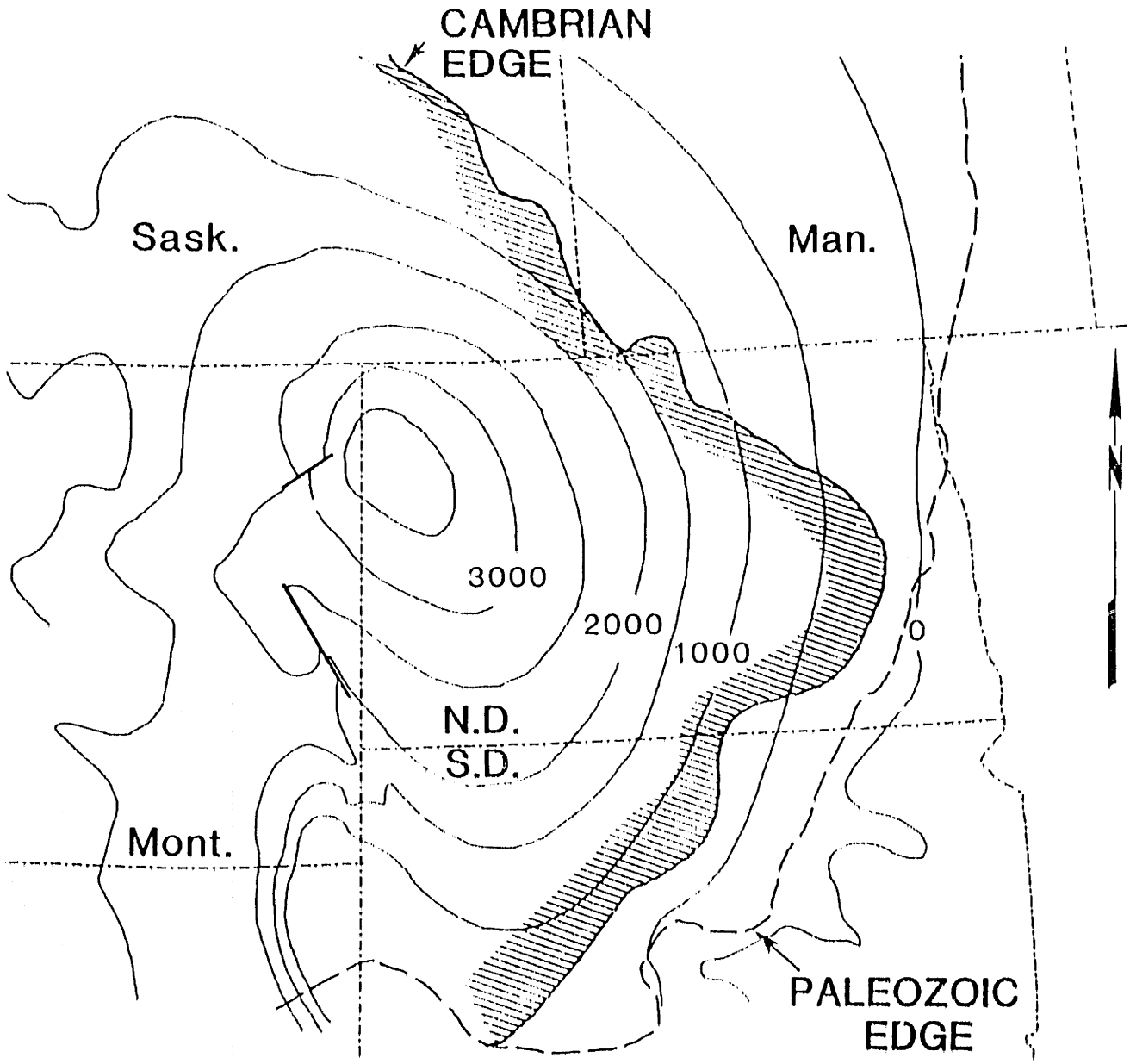
CAMBRIAN
EDGE
Sask.
Man.
3000
2000
1000
0
N.D.
S.D.
Mont.
PALEOZOIC
EDGE

Figure 4.3

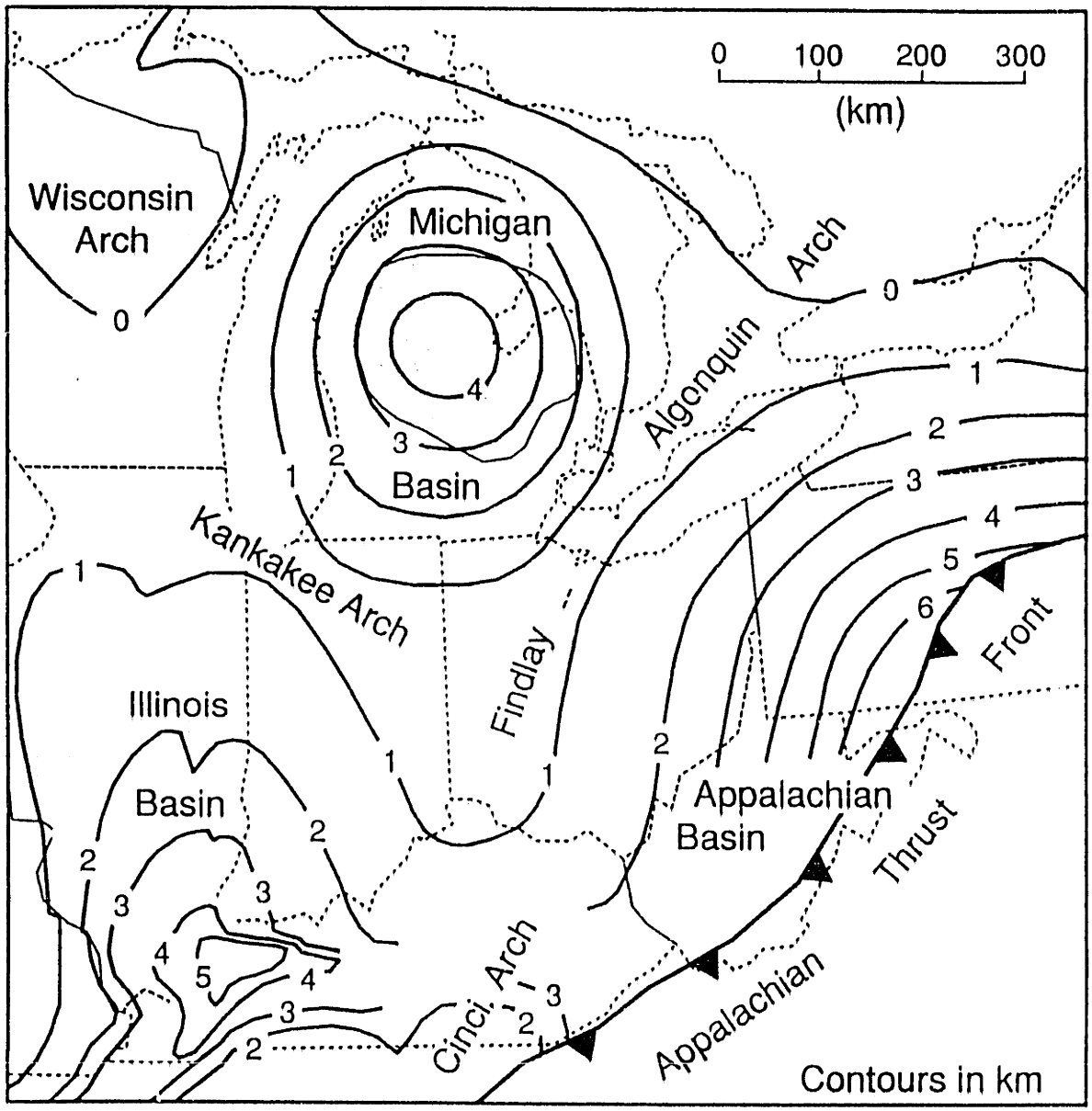
0 100 200 300
(km)
Wisconsin Arch
Michigan Basin
Algonquin Arch
Kankakee Arch
Findlay Arch
Illinois Basin
Appalachian Basin
Cincinnati Arch
Appalachian Thrust Front
Contours in km

Figure 4.4

Williston Topography

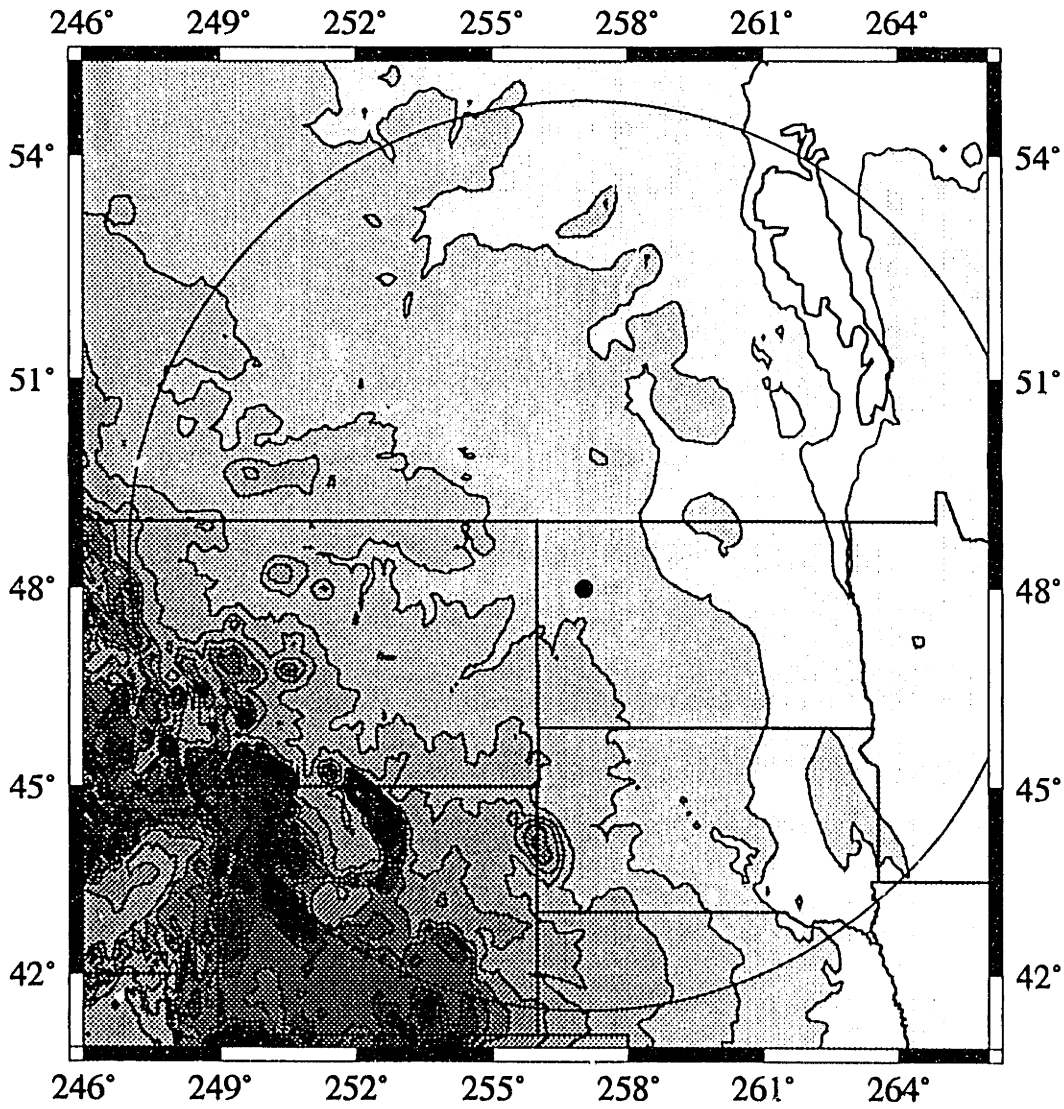

Circle shows 800 km radius

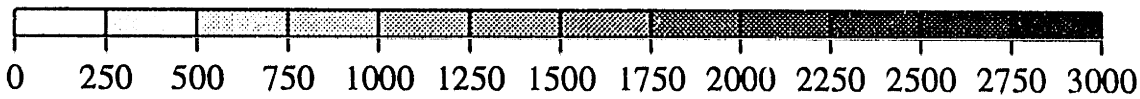

meters

Figure 4.5a

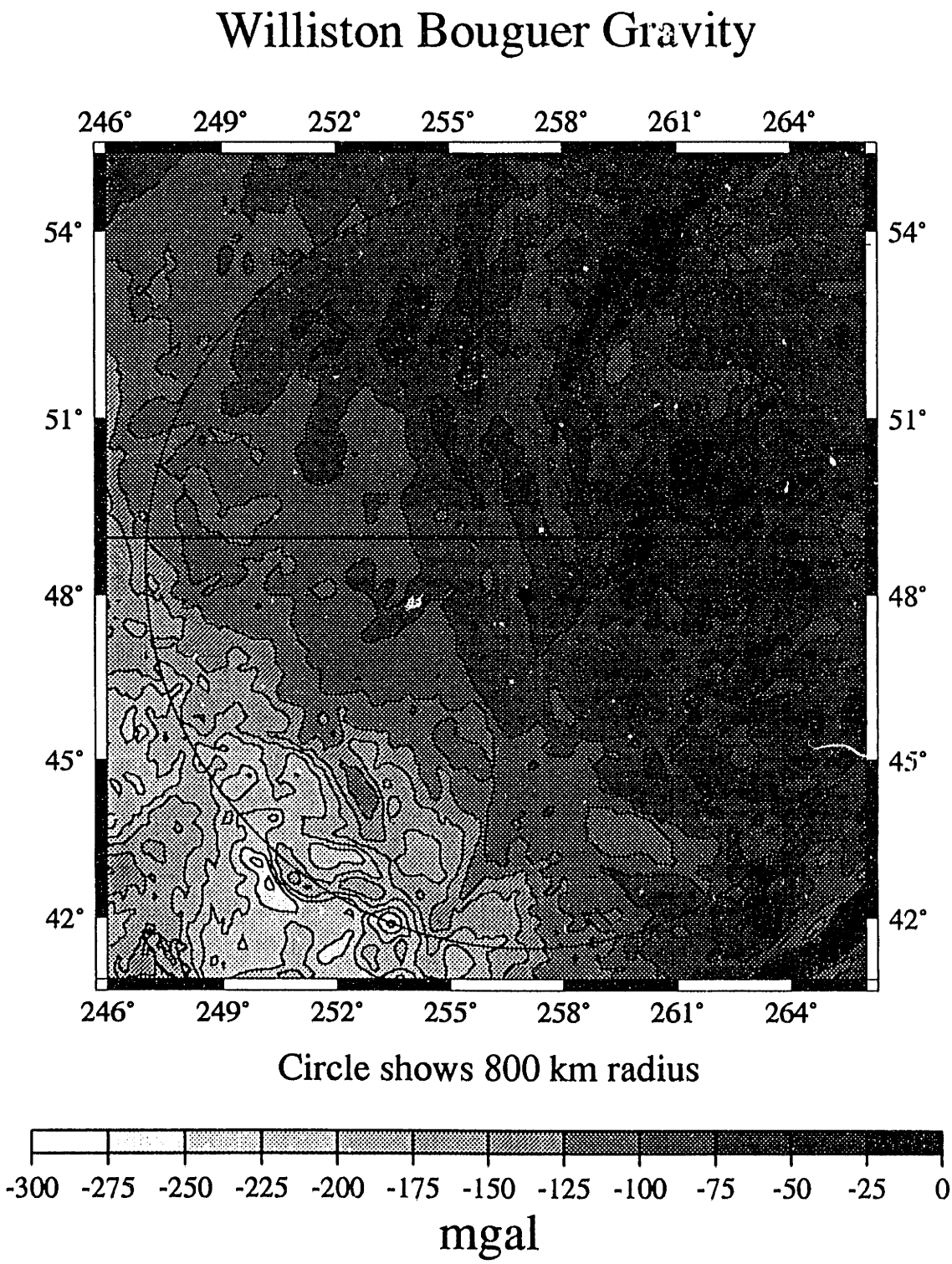
Williston Bouguer Gravity
246°
249°
252°
255°
258°
261°
264°
54°
51°
48°
45°
42°
Circle shows 800 km radius
-300
-275
-250
-225
-200
-175
-150
-125
-100
-75
-50
-25
0
mgal

Figure 4.5b

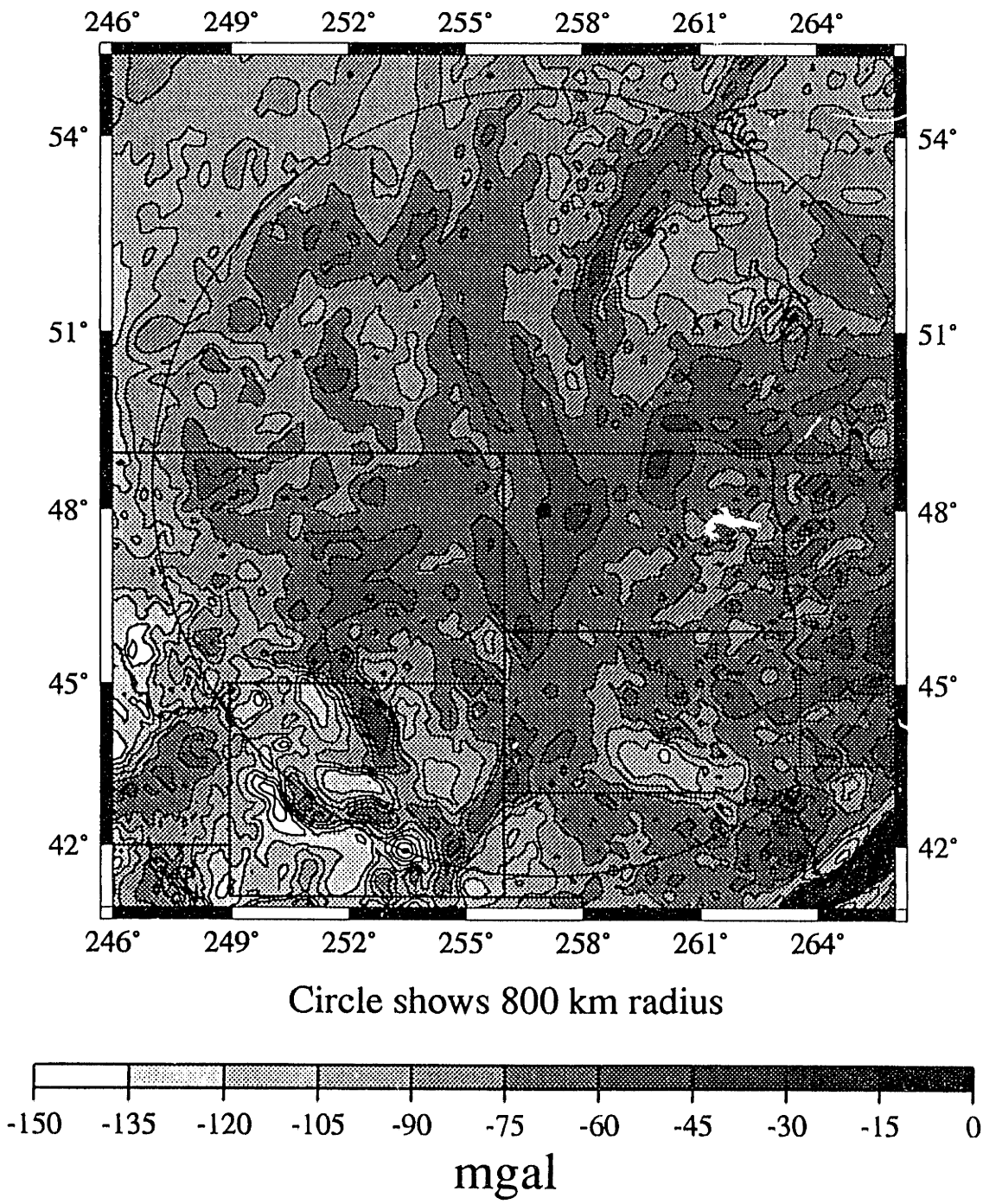
Williston Isostatic Gravity
246°
249°
252°
255°
258°
261°
264°
54°
51°
48°
45°
42°
Circle shows 800 km radius
-150
-135
-120
-105
-90
-75
-60
-45
-30
-15
0
mgal

Figure 4.5c

Williston Modified Isostatic Gravity

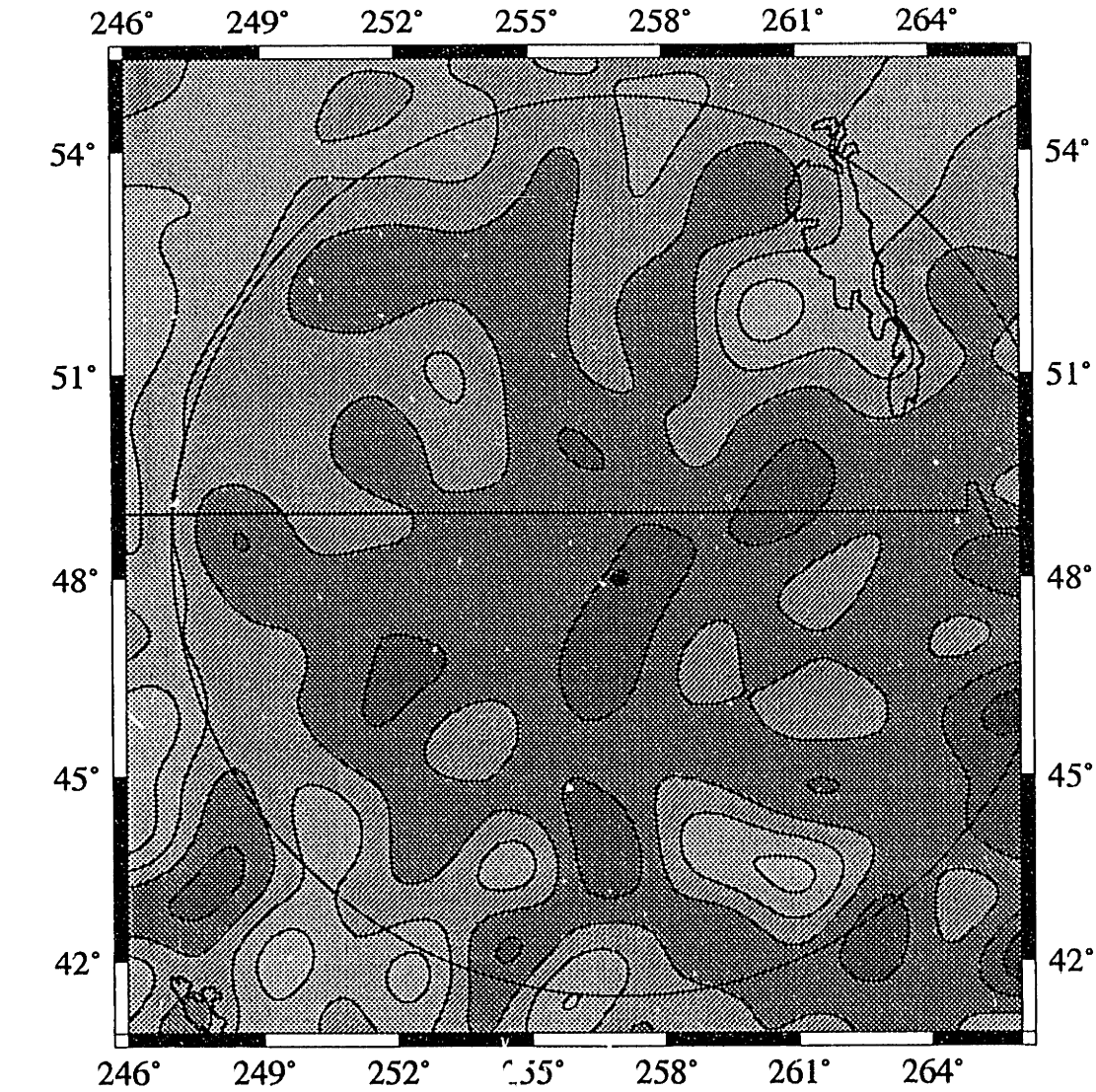

Circle shows 800 km radius

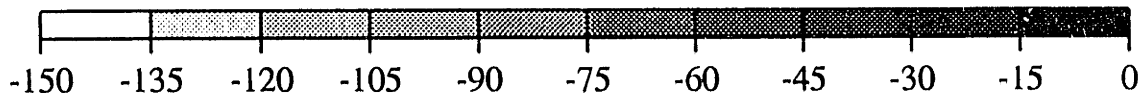

mgals

Figure 4.5d

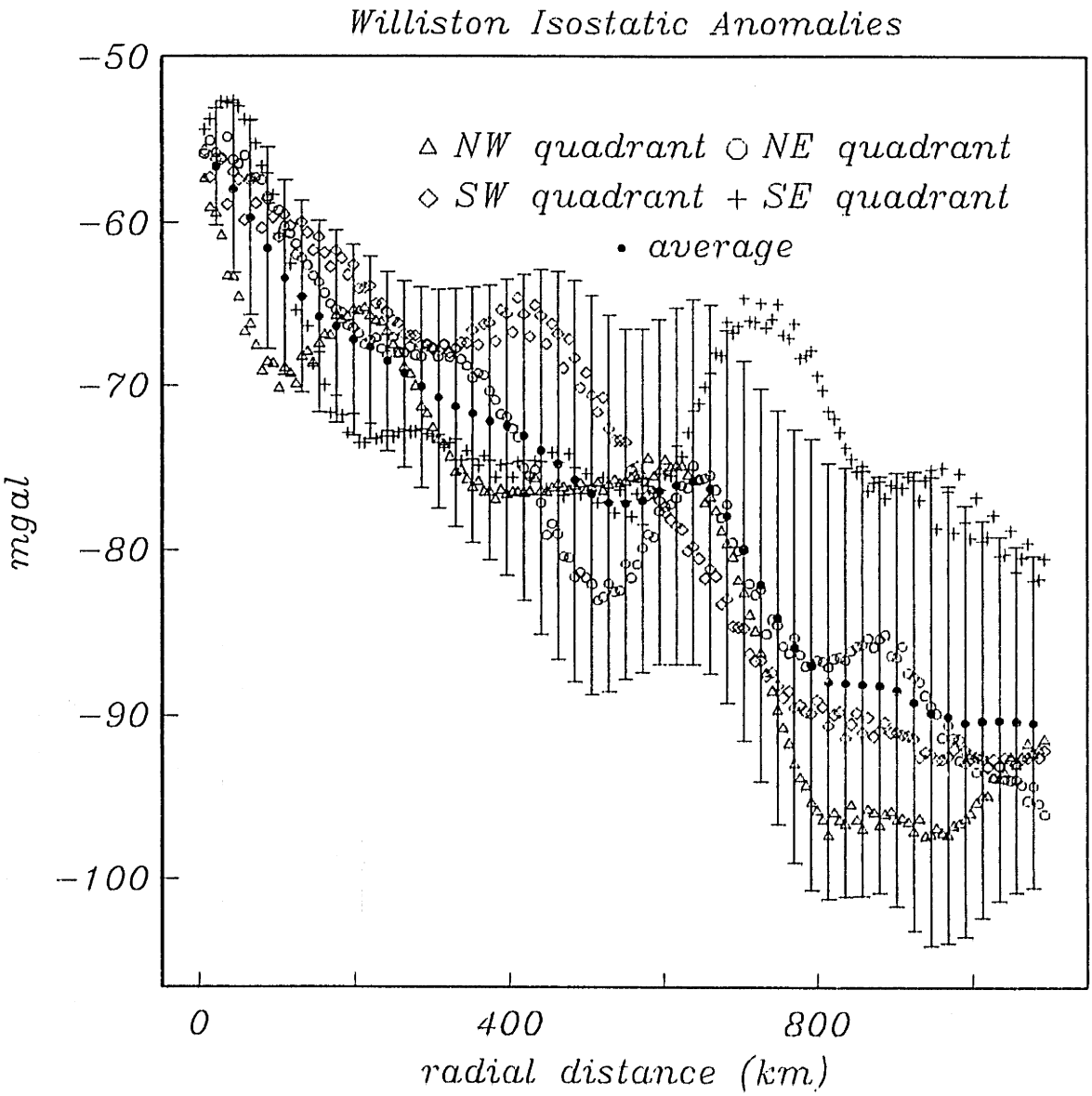
Williston Isostatic Anomalies
△ NW quadrant ○ NE quadrant
◇ SW quadrant + SE quadrant
• average
−50
−60
−70
−80
−90
−100
mgal
0
400
800
radial distance (km)

Figure 4.5e

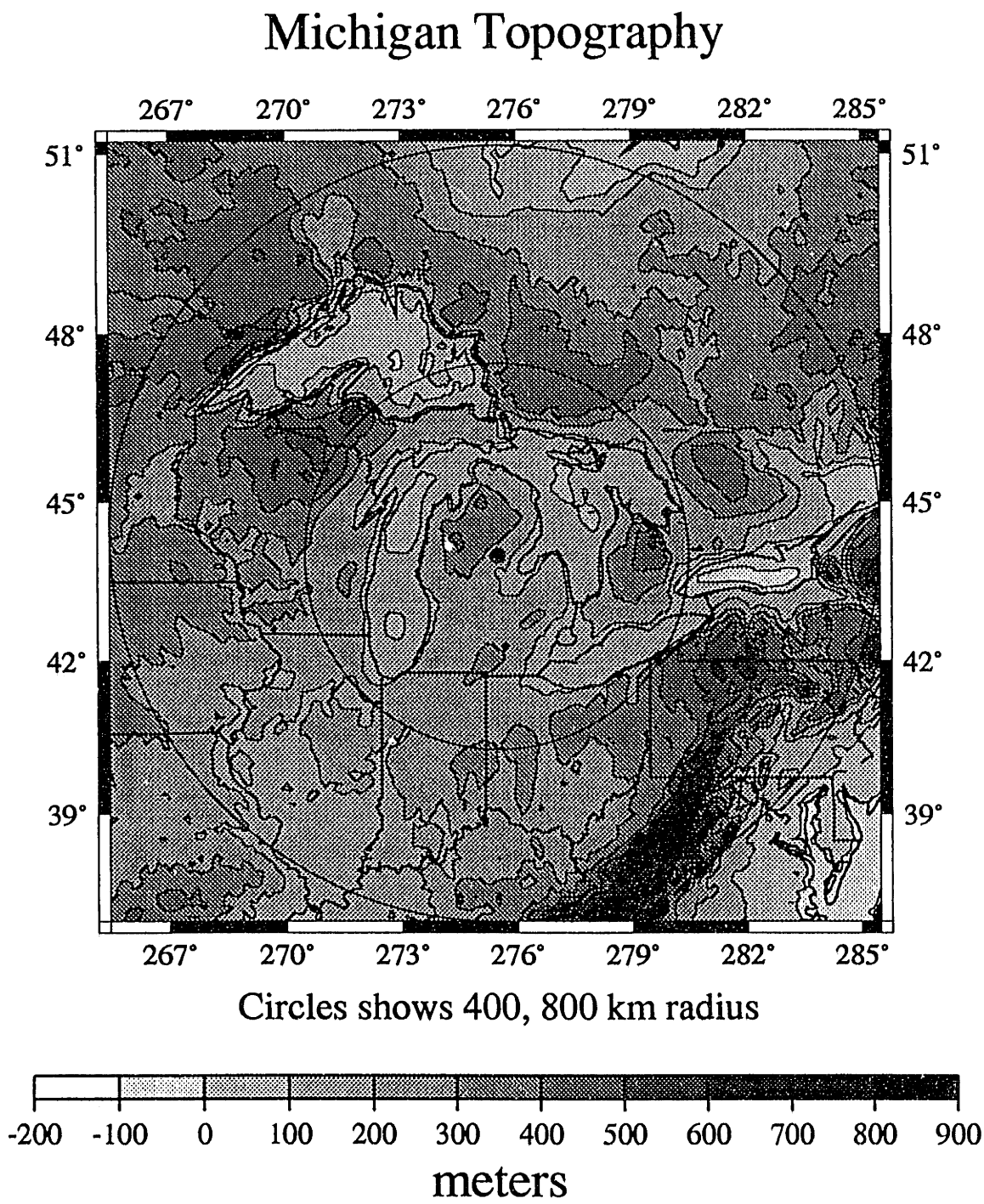
Michigan Topography
267°
270°
273°
276°
279°
282°
285°
51°
48°
45°
42°
39°
Circles shows 400, 800 km radius
-200
-100
0
100
200
300
400
500
600
700
800
900
meters

Figure 4.6a

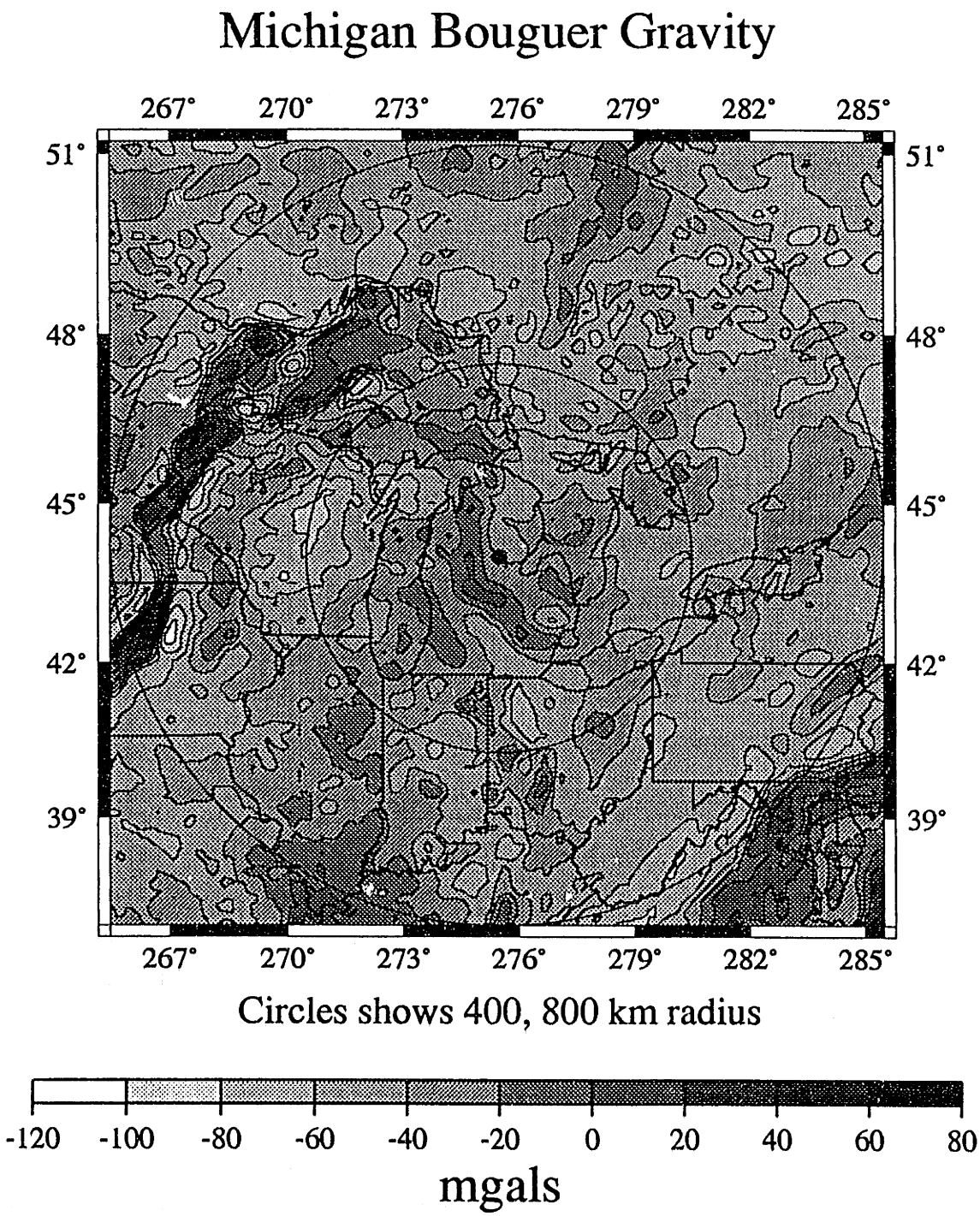
Michigan Bouguer Gravity
267°
270°
273°
276°
279°
282°
285°
51°
48°
45°
42°
39°
Circles shows 400, 800 km radius
-120
-100
-80
-60
-40
-20
0
20
40
60
80
mgals

Figure 4.6b

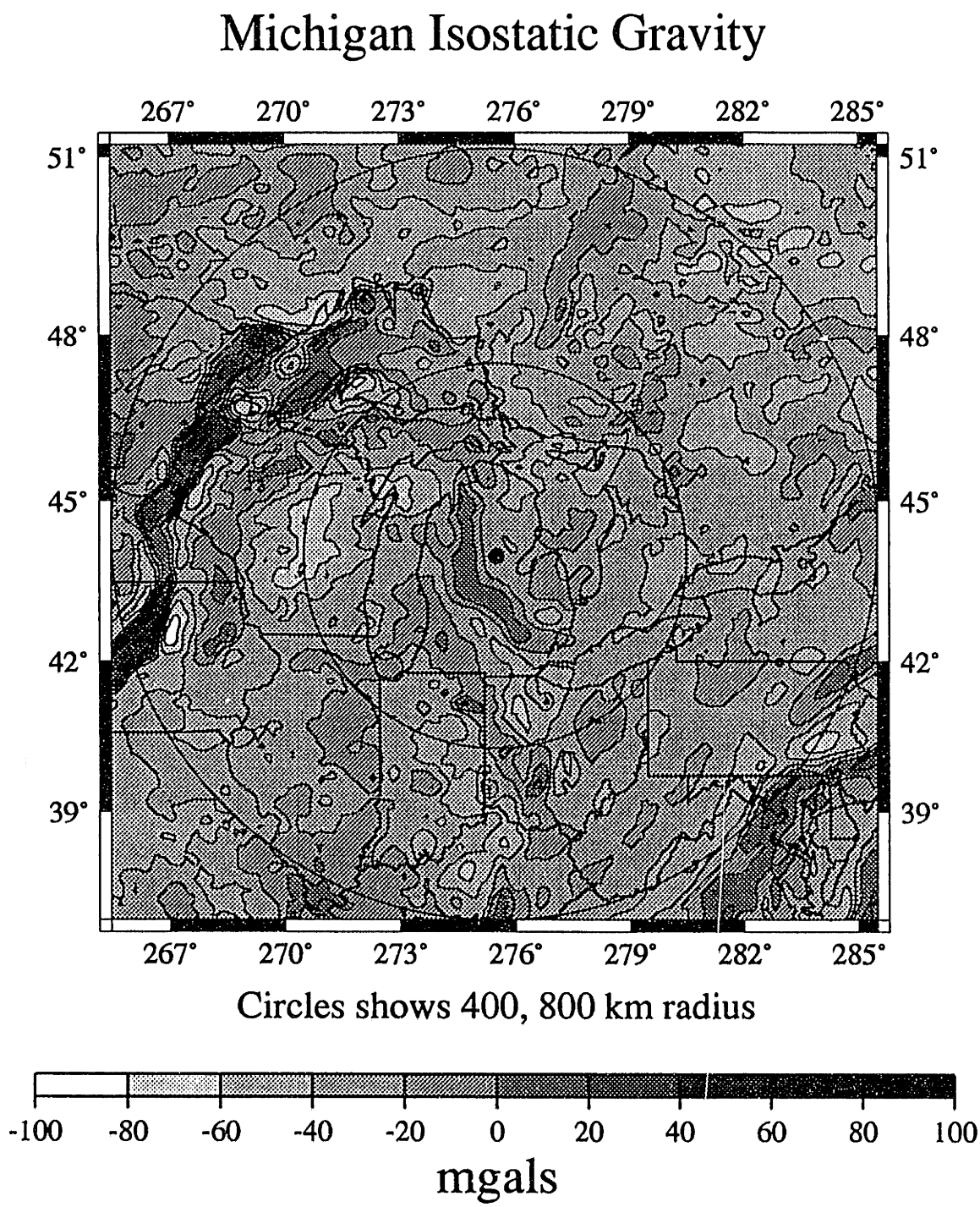
Michigan Isostatic Gravity
267°
270°
273°
276°
279°
282°
285°
51°
48°
45°
42°
39°
Circles shows 400, 800 km radius
-100
-80
-60
-40
-20
0
20
40
60
80
100
mgals

Figure 4.6c

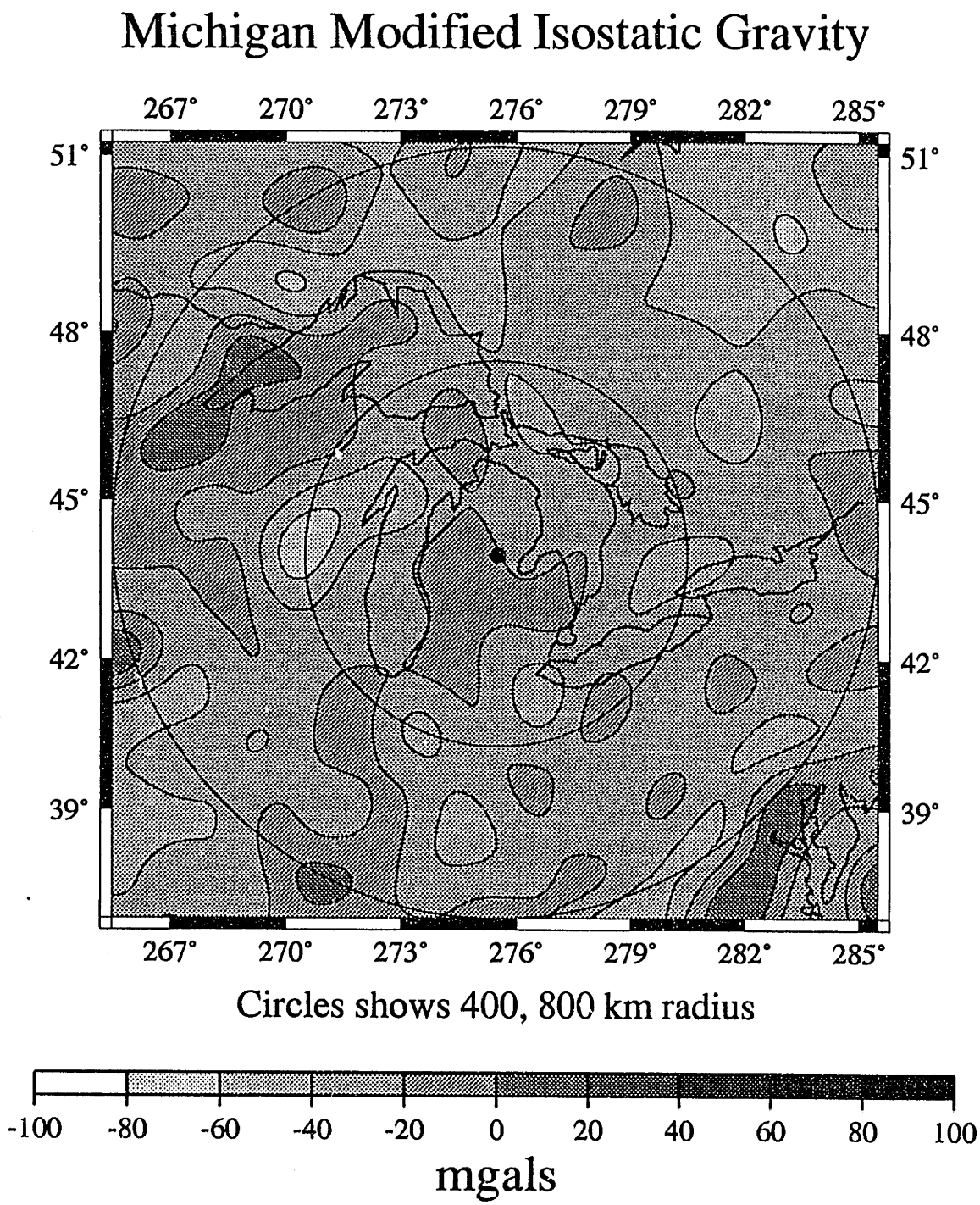
Michigan Modified Isostatic Gravity
267°
270°
273°
276°
279°
282°
285°
51°
48°
45°
42°
39°
Circles shows 400, 800 km radius
-100
-80
-60
-40
-20
0
20
40
60
80
100
mgals

Figure 4.6d

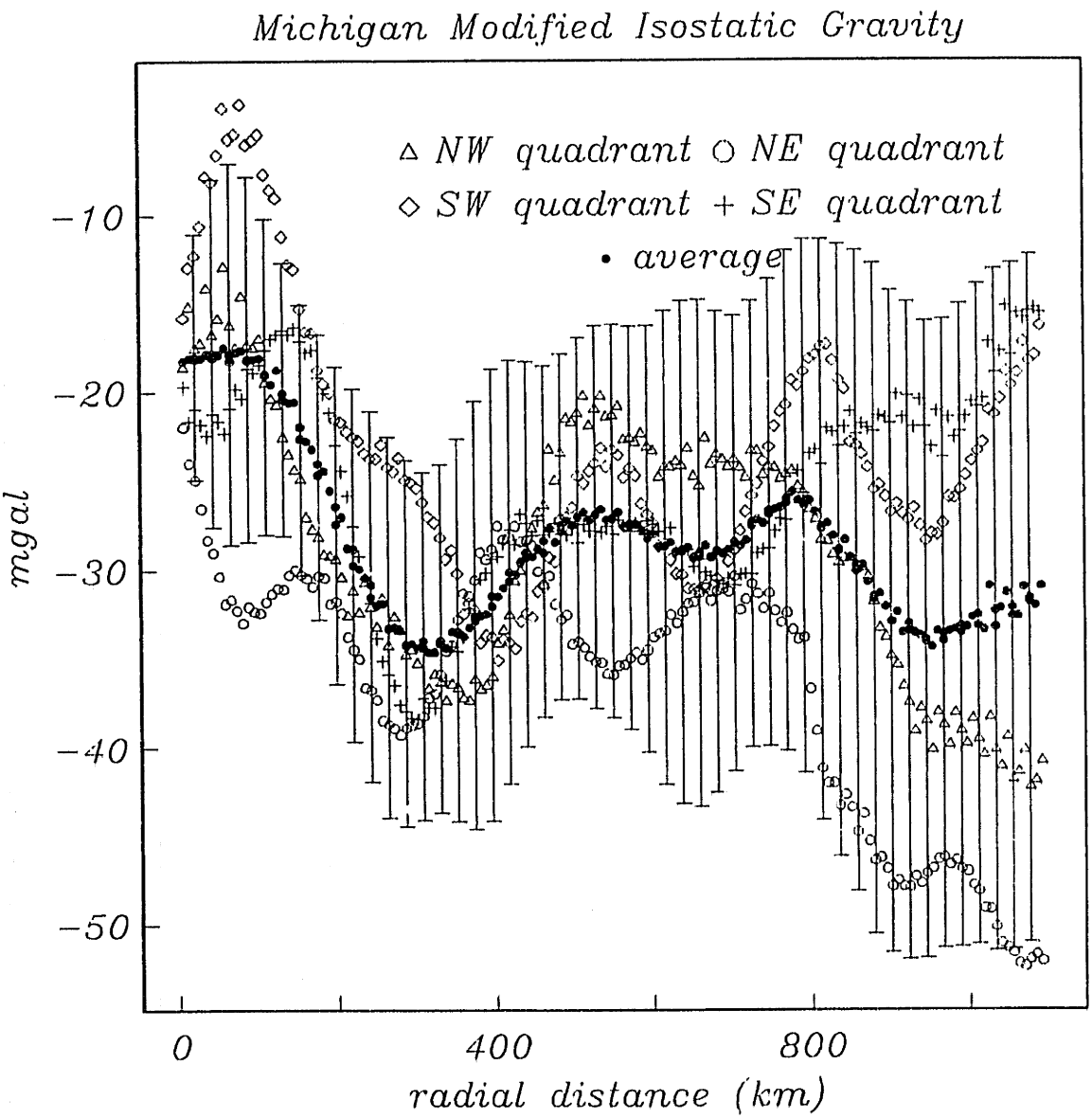
Michigan Modified Isostatic Gravity
△ NW quadrant ○ NE quadrant
◇ SW quadrant + SE quadrant
• average
-10
-20
-30
-40
-50
mgal
0
400
800
radial distance (km)

Figure 4.6e

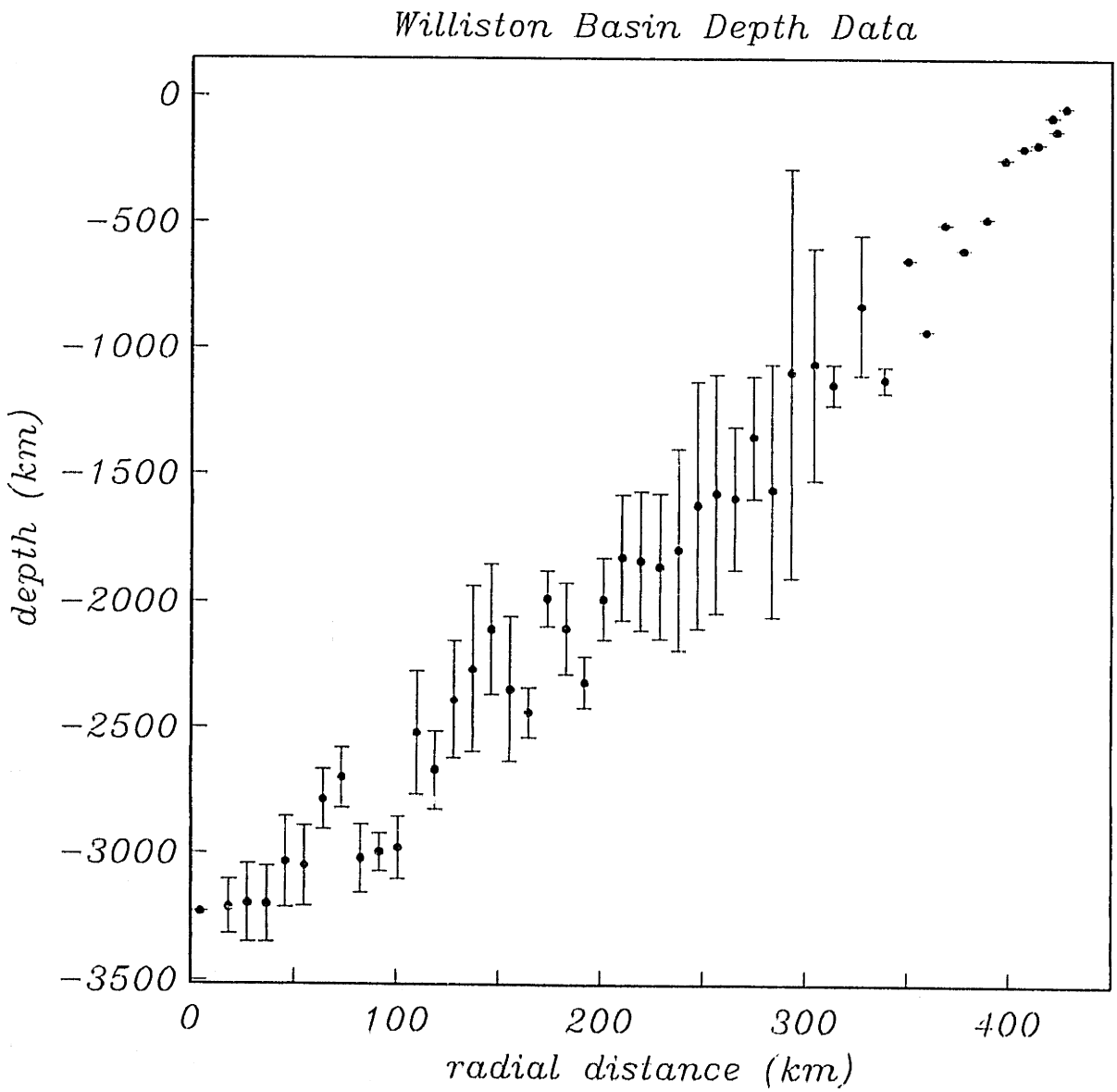
Williston Basin Depth Data
0
-500
-1000
-1500
-2000
-2500
-3000
-3500
depth (km)
0
100
200
300
400
radial distance (km)

Figure 4.7a

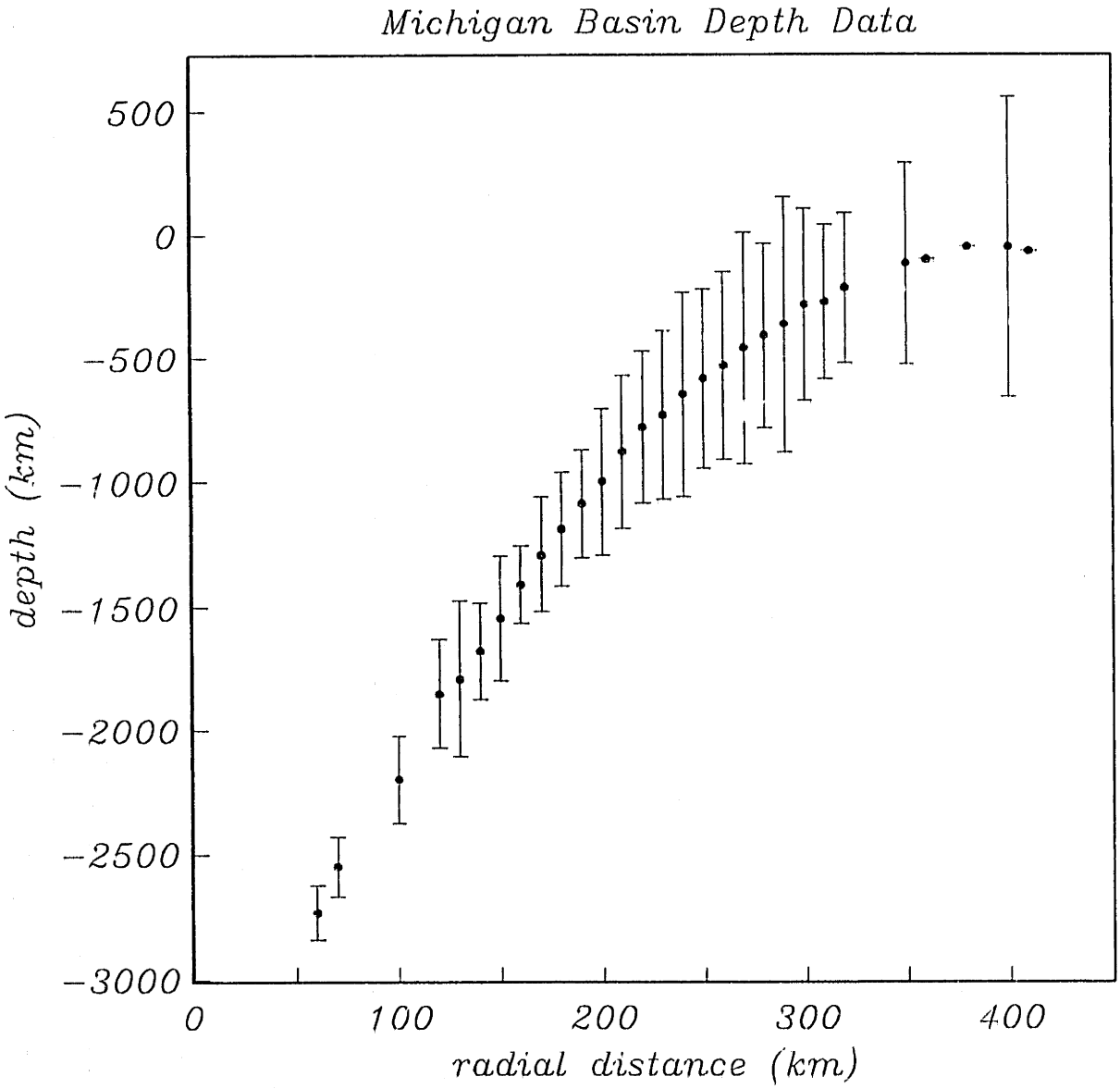
Michigan Basin Depth Data
500
0
-500
-1000
-1500
-2000
-2500
-3000
depth (km)
0
100
200
300
400
radial distance (km)

Figure 4.7b

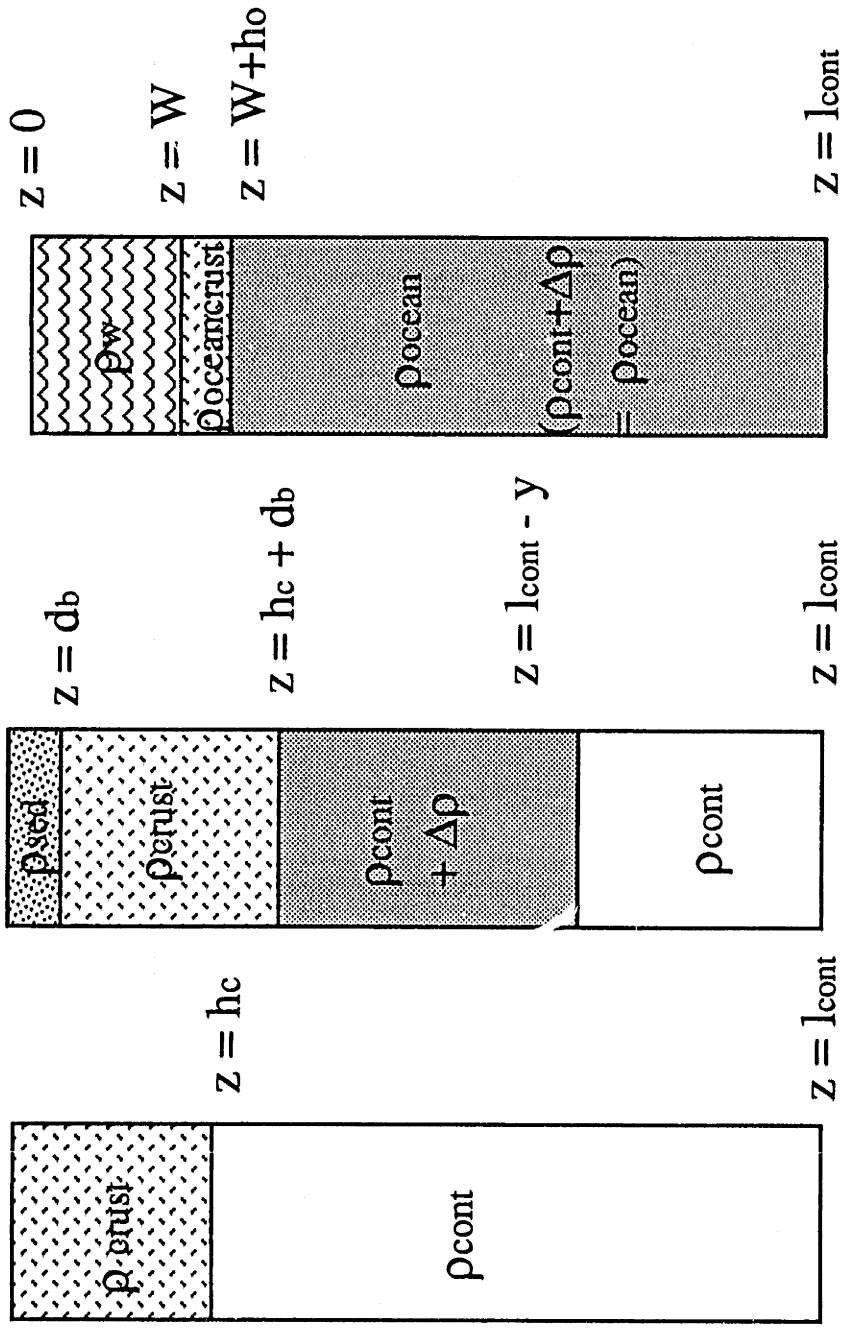
z = 0
z = W
z = W+ho
z = db
z = hc + db
z = lcont - y
z = lcont
z = hc
z = lcont
ρsed
ρcrust
ρcont + Δρ
ρcont
ρcrust
ρcont
ρw
ρoceancrust
ρocean
(ρcont+Δρ = ρocean)

Figure 4.8

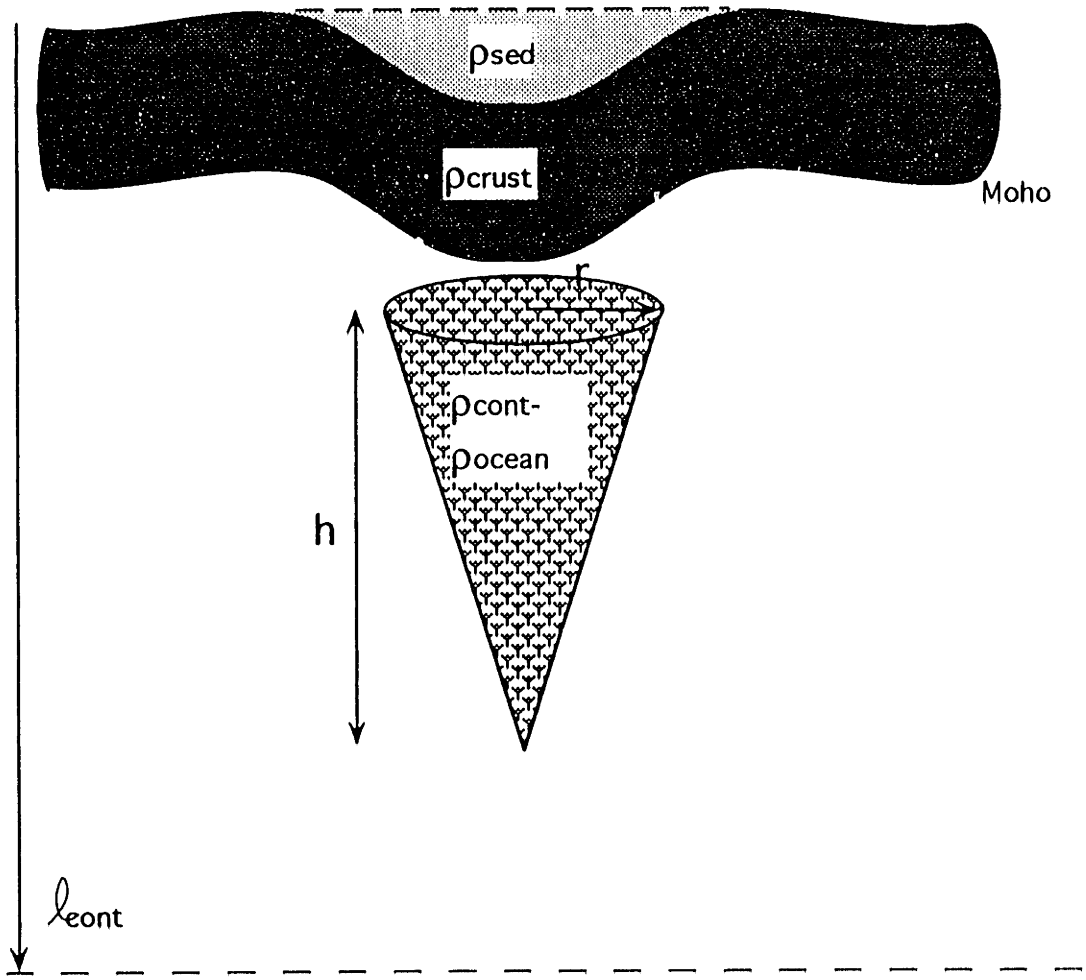

Figure 4.9

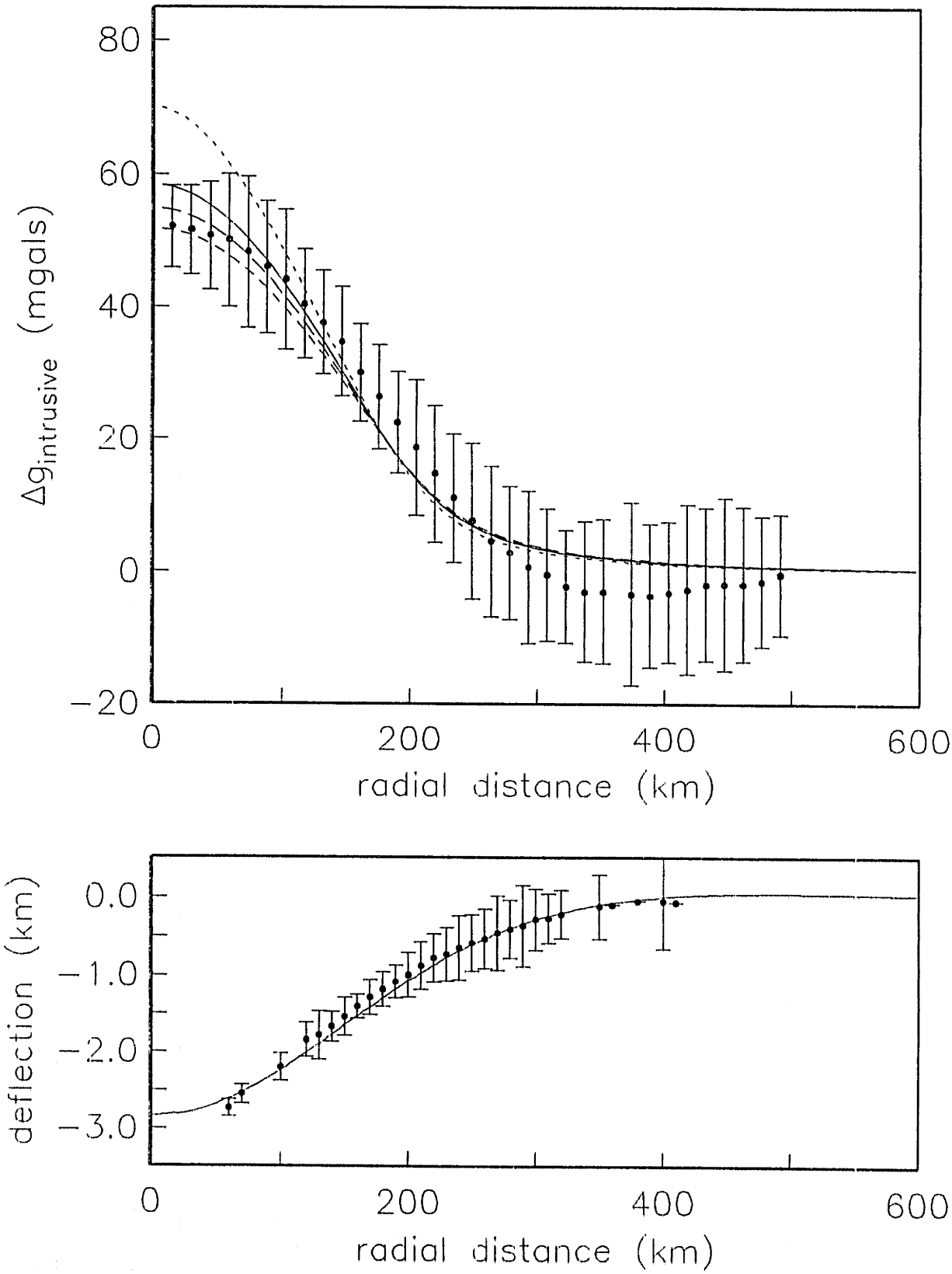
80
60
40
20
0
−20
$\Delta g_{intrusive}$ (mgals)
0
200
400
600
radial distance (km)
0.0
−1.0
−2.0
−3.0
deflection (km)
0
200
400
600
radial distance (km)

Figure 4.10a

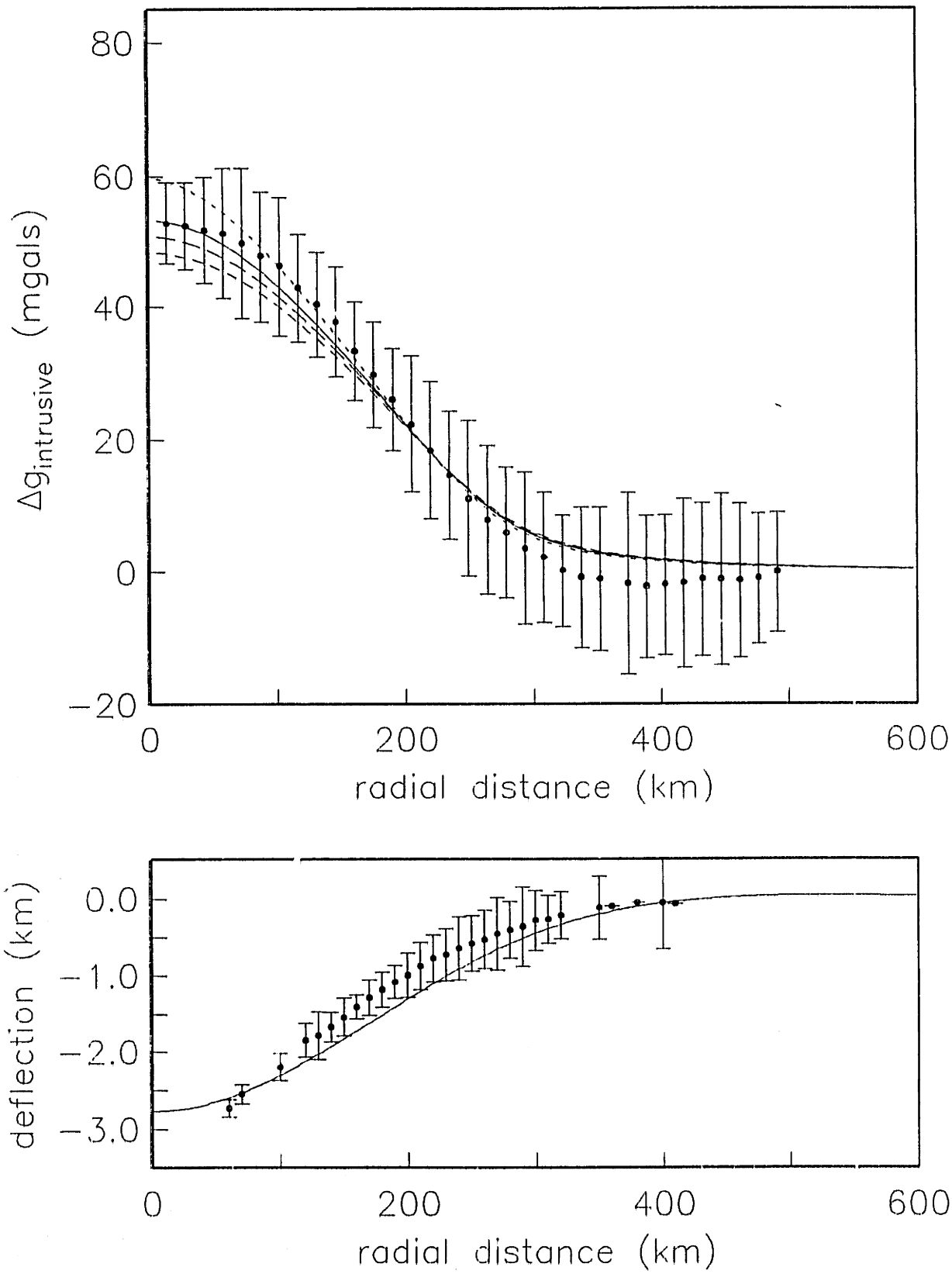
80
60
40
20
0
−20
$\Delta g_{intrusive}$ (mgals)
0
200
400
600
radial distance (km)
0.0
−1.0
−2.0
−3.0
deflection (km)
0
200
400
600
radial distance (km)

Figure 4.10b

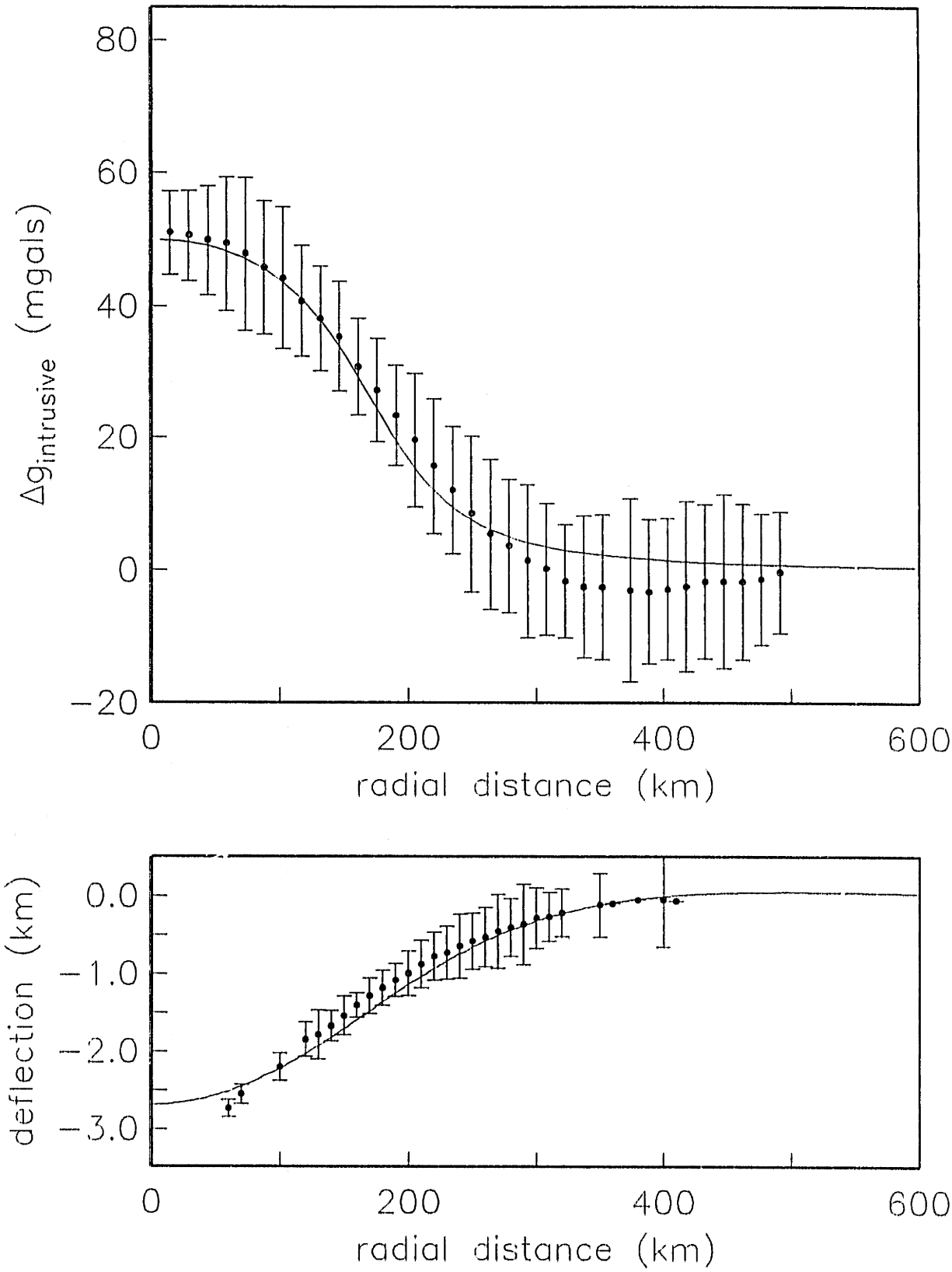
80
60
40
20
0
−20
$\Delta g_{intrusive}$ (mgals)
0
200
400
600
radial distance (km)
0.0
−1.0
−2.0
−3.0
deflection (km)
0
200
400
600
radial distance (km)

Figure 4.10c

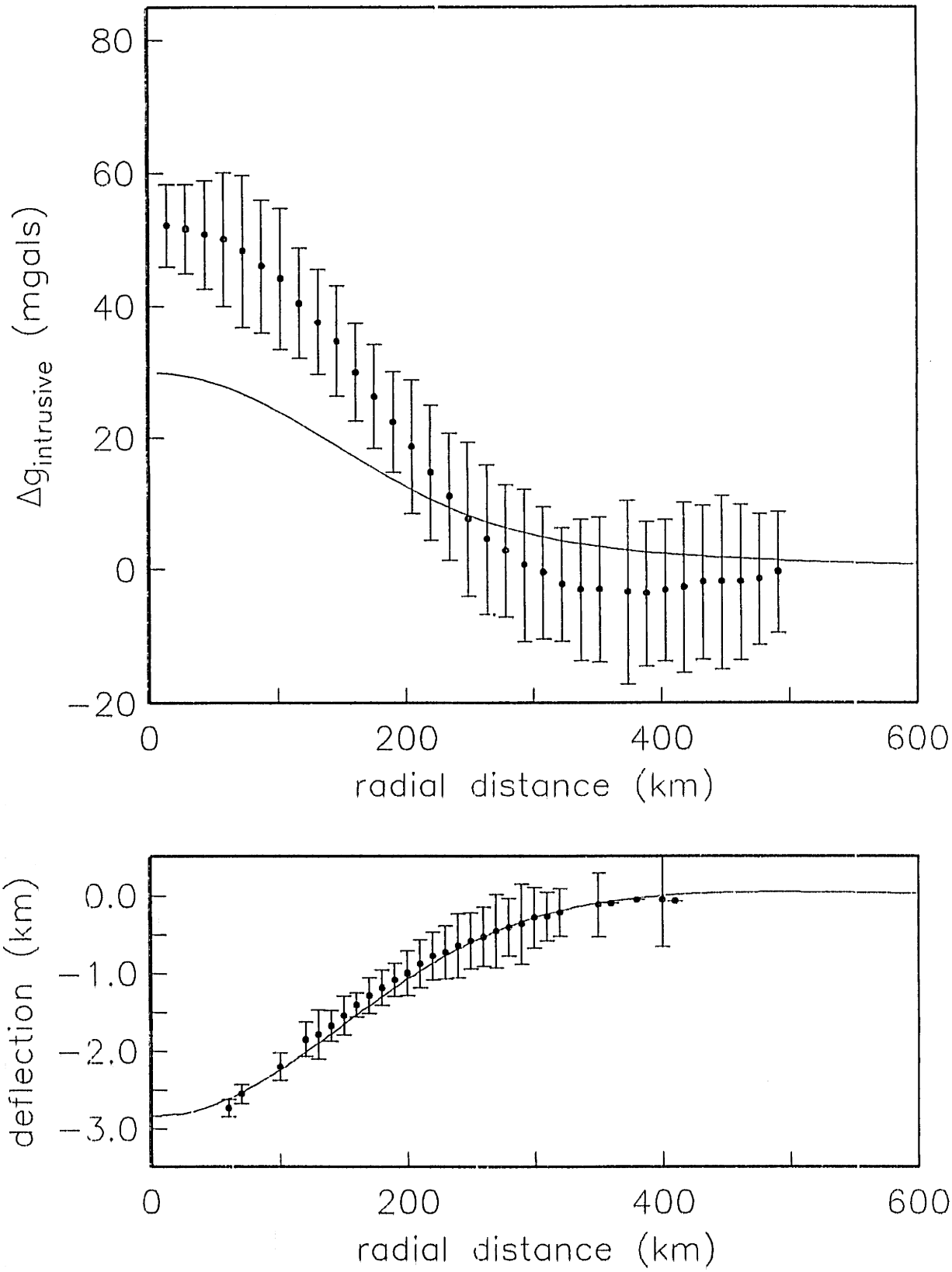
80
60
40
20
0
−20
$\Delta g_{intrusive}$ (mgals)
0
200
400
600
radial distance (km)
0.0
−1.0
−2.0
−3.0
deflection (km)
0
200
400
600
radial distance (km)

Figure 4.10d

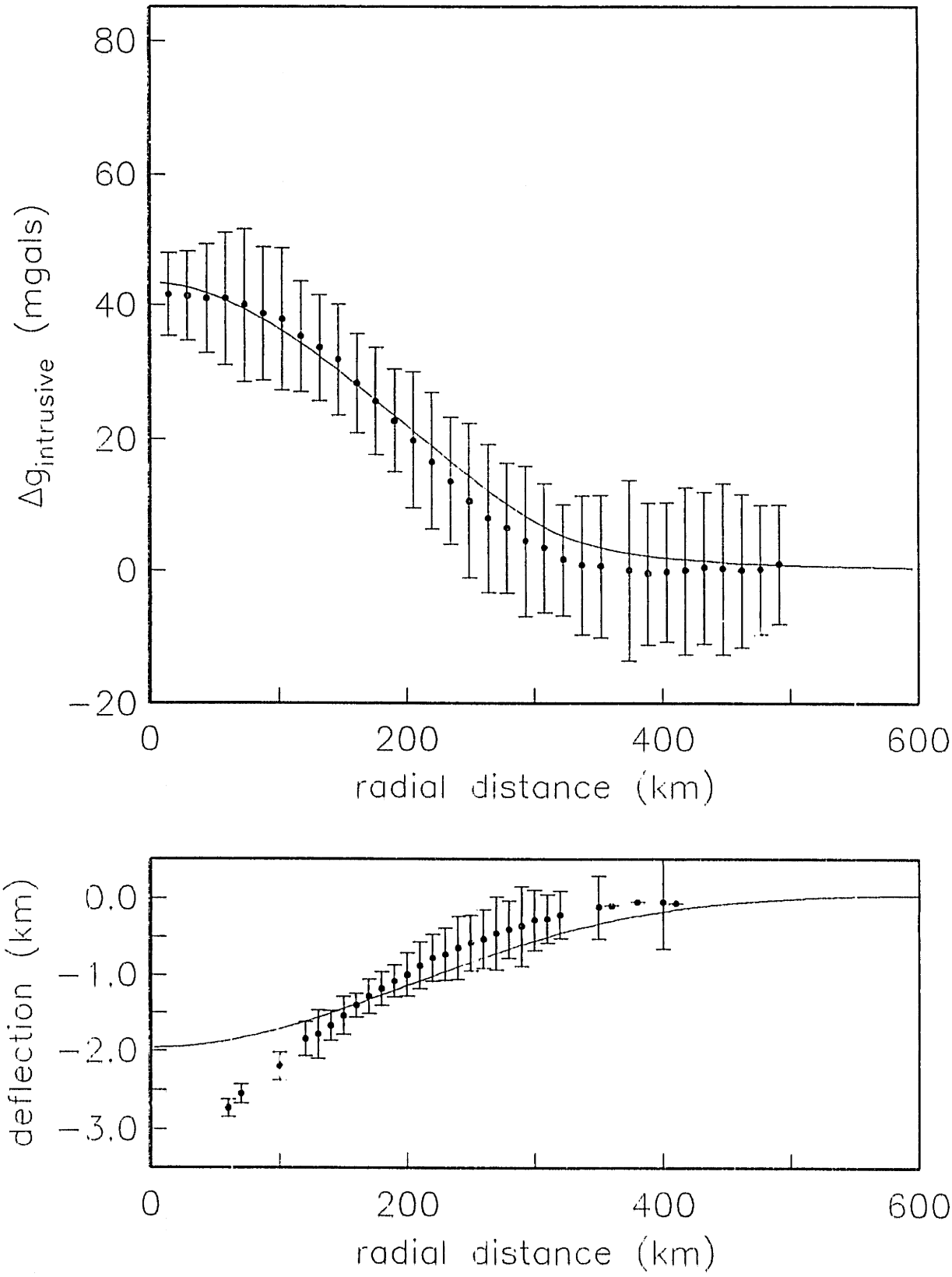
80
60
40
20
0
−20
$\Delta g_{intrusive}$ (mgals)
0
200
400
600
radial distance (km)
0.0
−1.0
−2.0
−3.0
deflection (km)
0
200
400
600
radial distance (km)

Figure 4.10e

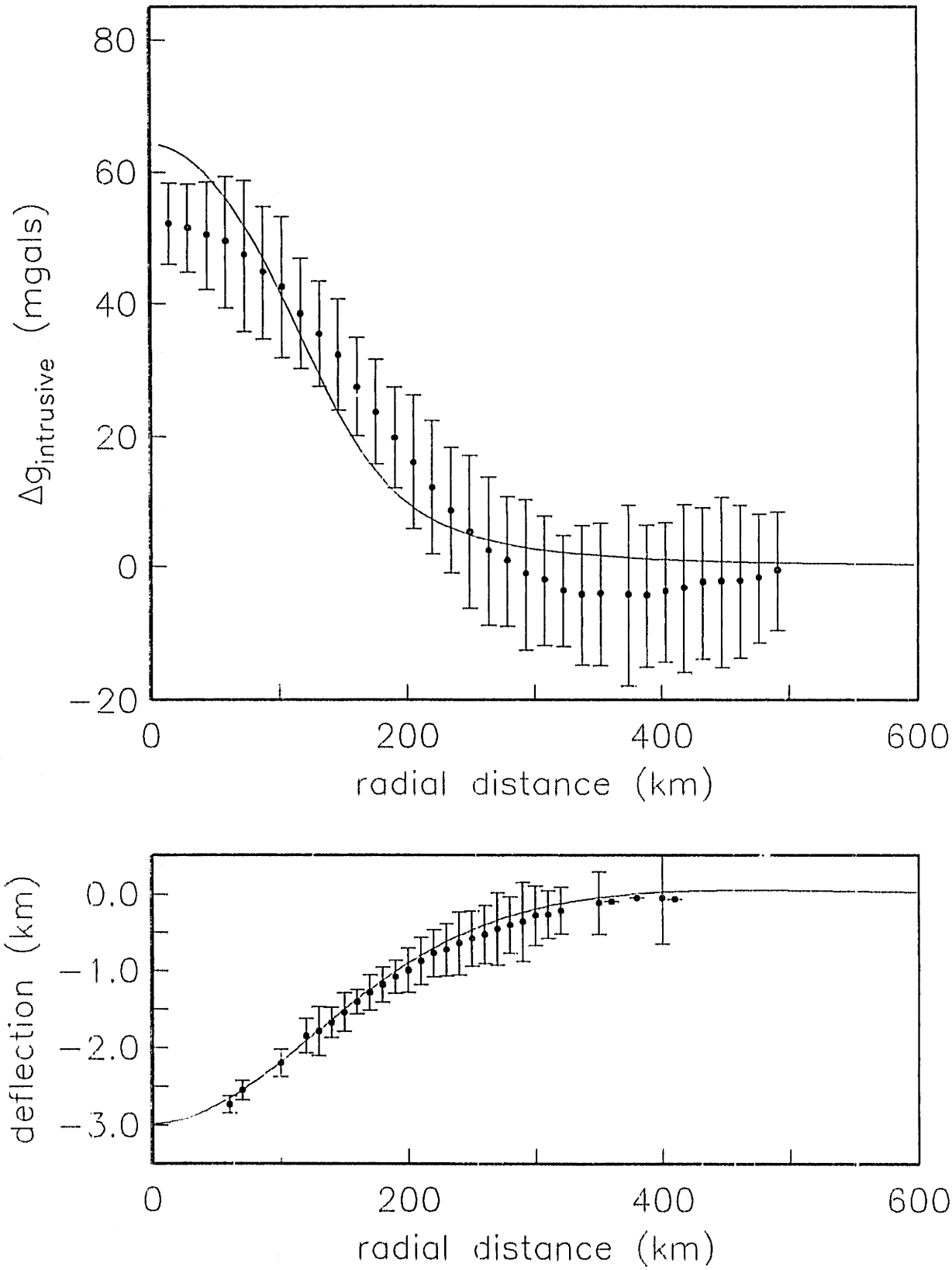
80
60
40
20
0
−20
$\Delta g_{intrusive}$ (mgals)
0
200
400
600
radial distance (km)
0.0
−1.0
−2.0
−3.0
deflection (km)
0
200
400
600
radial distance (km)

Figure 4.10f

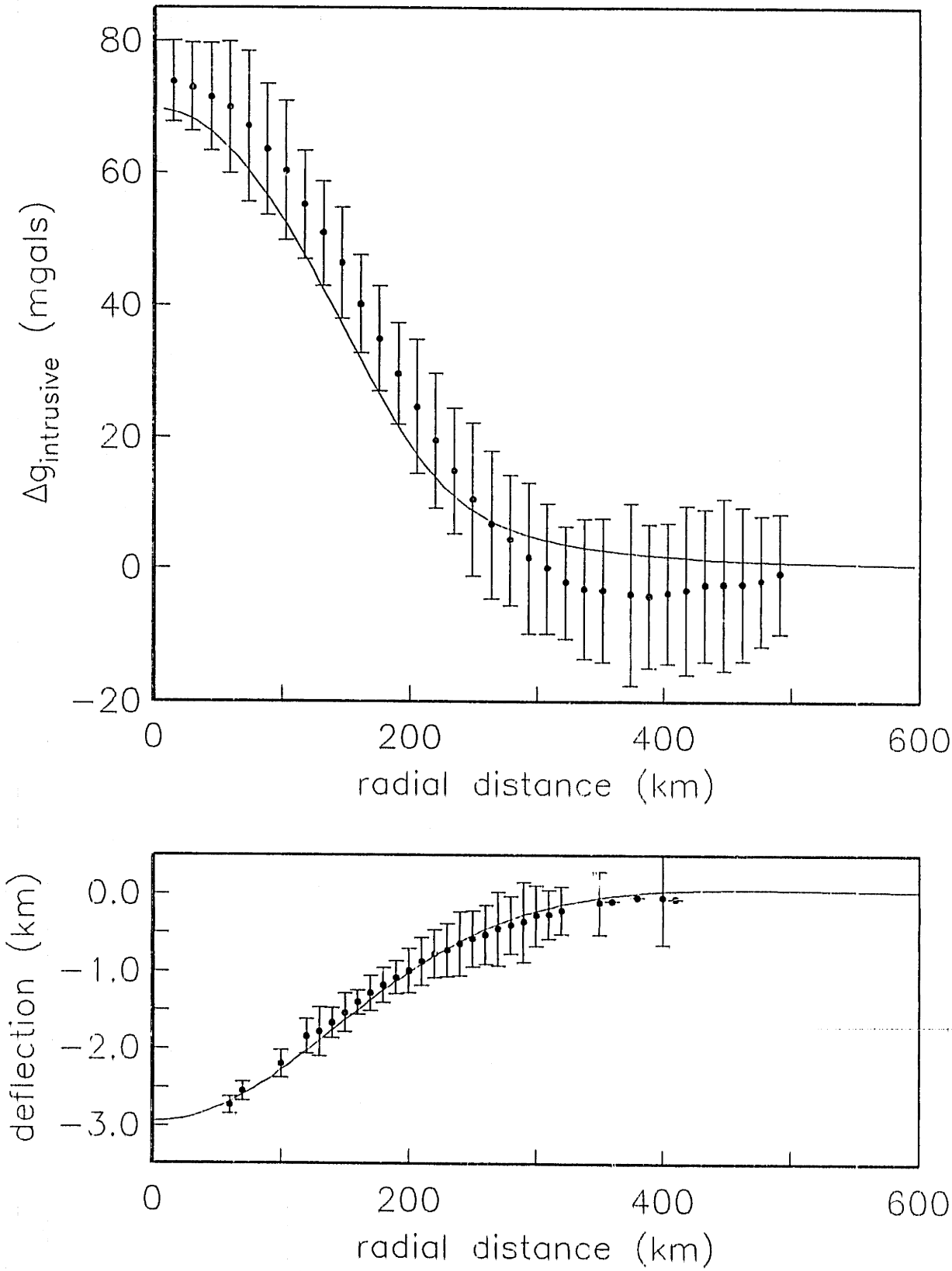
80
60
40
20
0
−20
$\Delta g_{intrusive}$ (mgals)
0
200
400
600
radial distance (km)
0.0
−1.0
−2.0
−3.0
deflection (km)
0
200
400
600
radial distance (km)

Figure 4.10.g

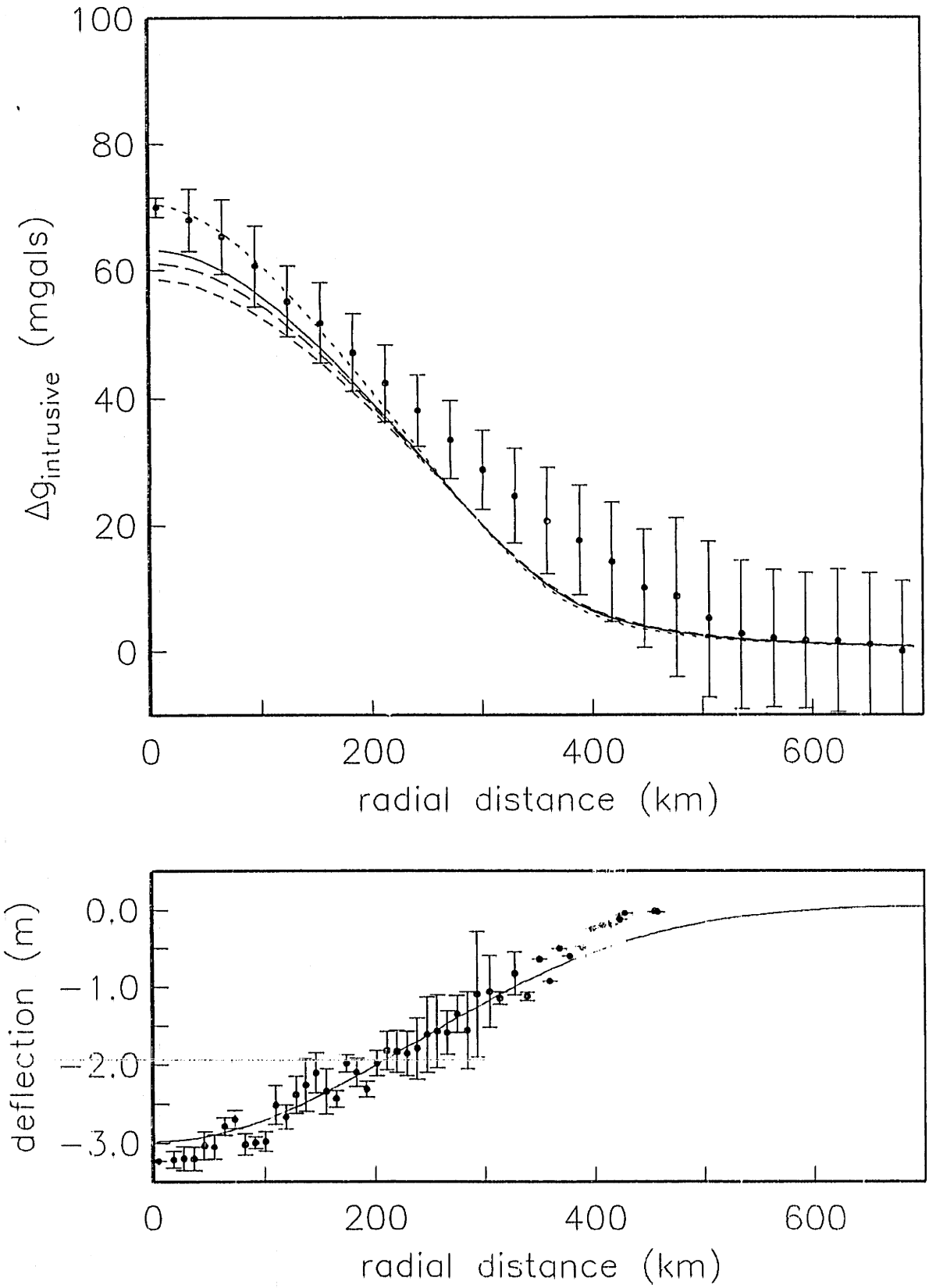
100
80
60
40
20
0
$\Delta g_{intrusive}$ (mgals)
0
200
400
600
radial distance (km)
0.0
−1.0
−2.0
−3.0
deflection (m)
0
200
400
600
radial distance (km)

Figure 4.11a

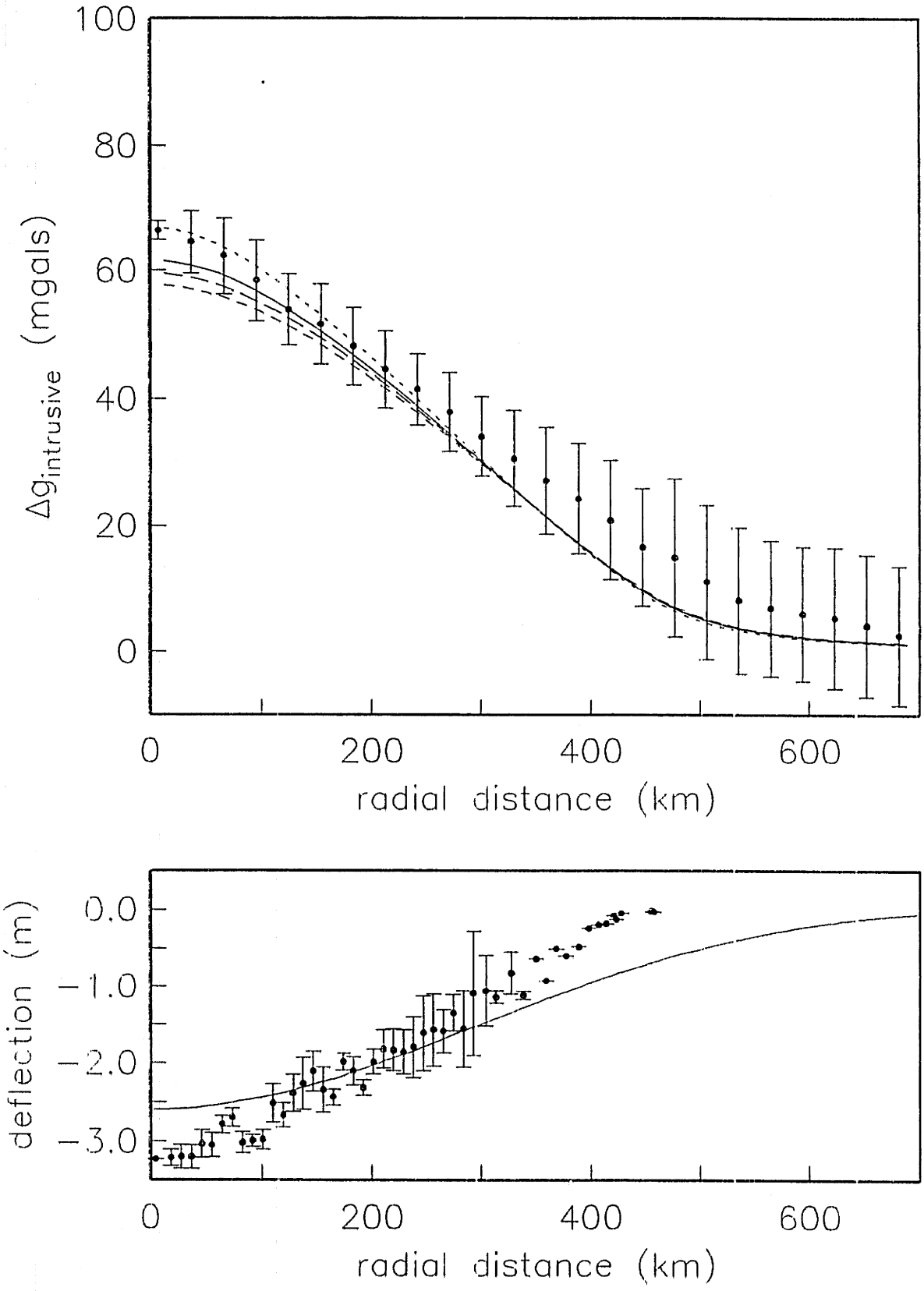
100
80
60
40
20
0
$\Delta g_{intrusive}$ (mgals)
0
200
400
600
radial distance (km)
0.0
−1.0
−2.0
−3.0
deflection (m)
0
200
400
600
radial distance (km)

Figure 4.11b

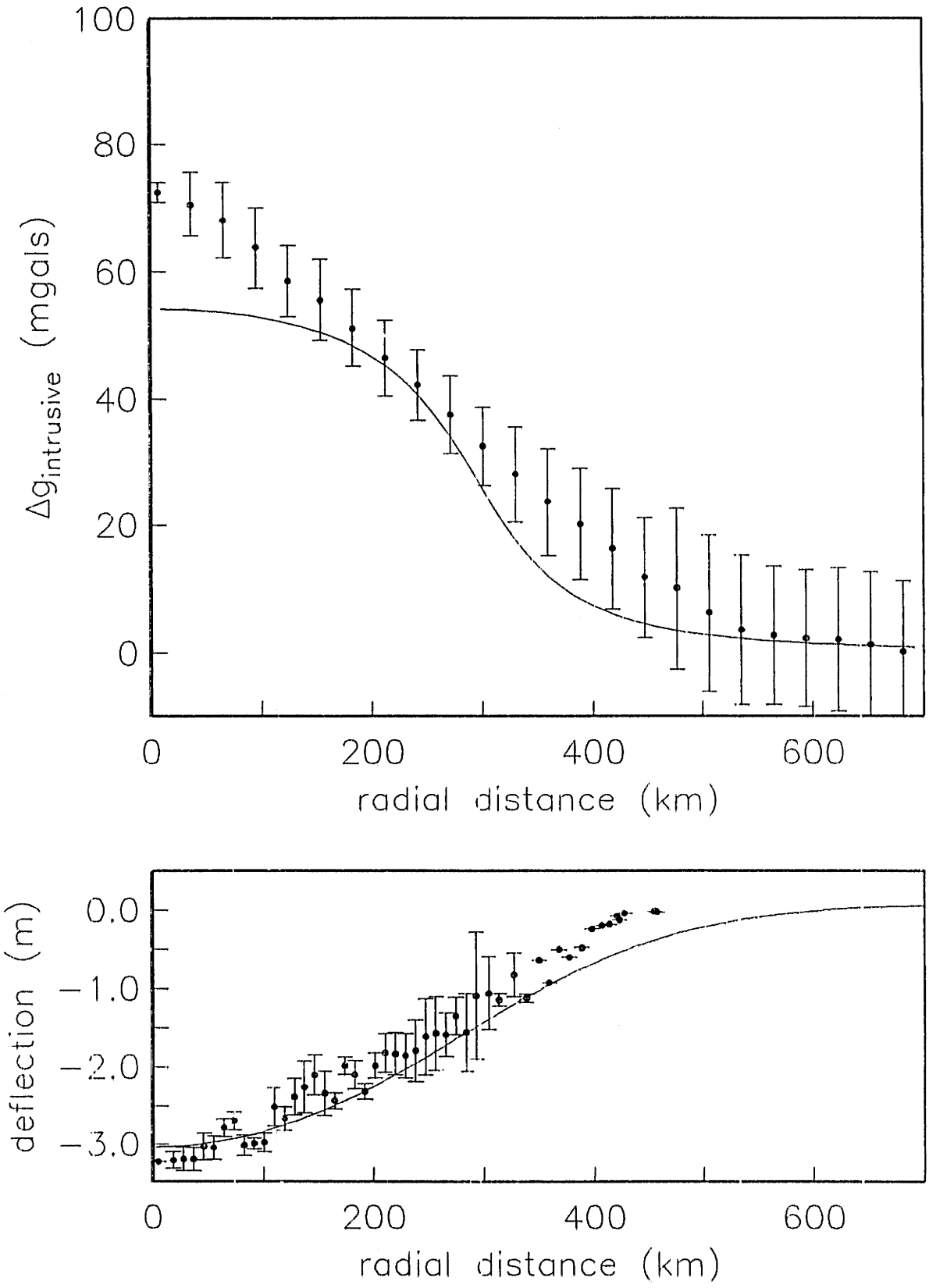
100
80
60
40
20
0
$\Delta g_{intrusive}$ (mgals)
0
200
400
600
radial distance (km)
0.0
−1.0
−2.0
−3.0
deflection (m)
0
200
400
600
radial distance (km)

Figure 4.11c

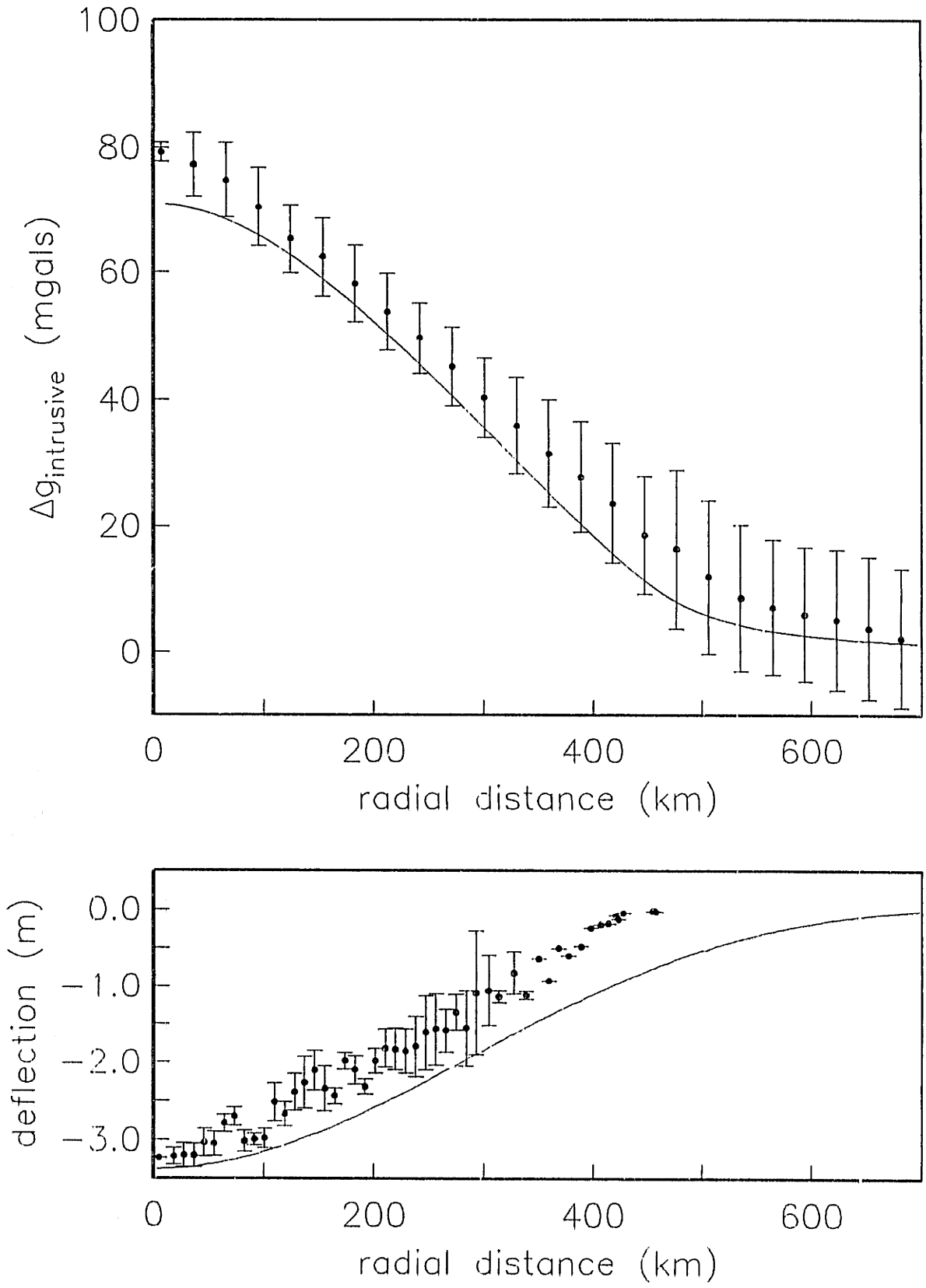
100
80
60
40
20
0
$\Delta g_{intrusive}$ (mgals)
0
200
400
600
radial distance (km)
0.0
−1.0
−2.0
−3.0
deflection (m)
0
200
400
600
radial distance (km)

Figure 4.11d

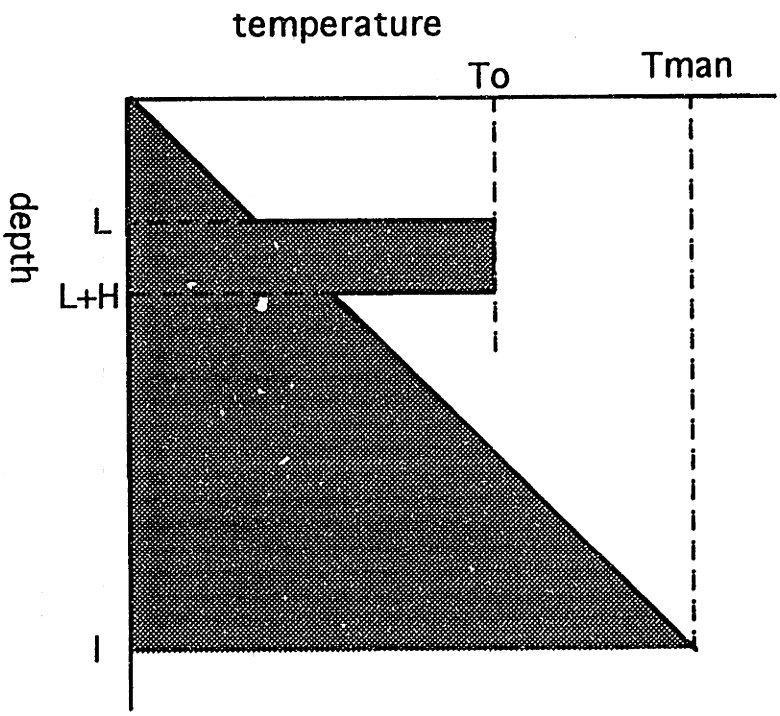

Figure 4.12

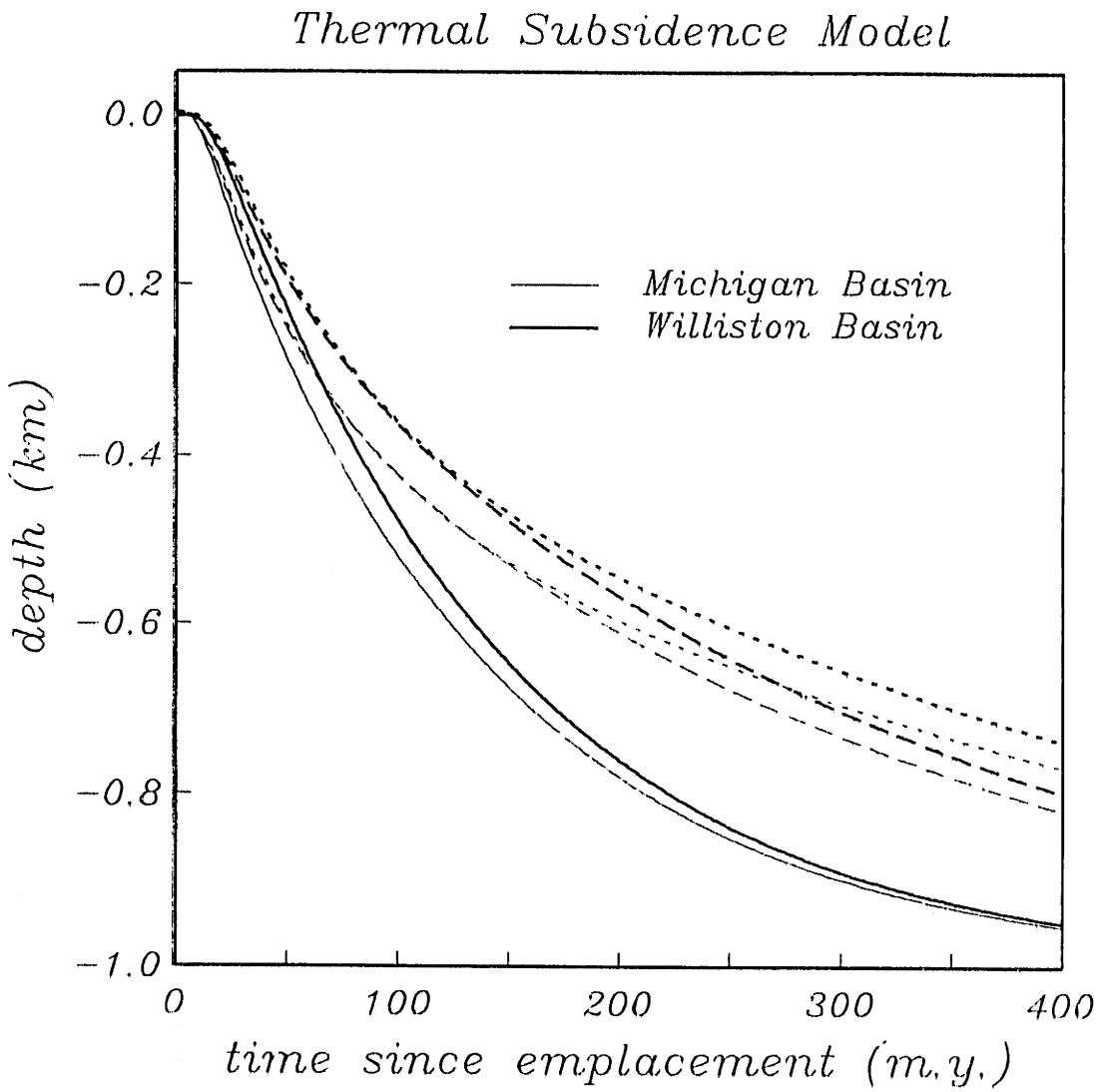
Thermal Subsidence Model
0.0
-0.2
-0.4
-0.6
-0.8
-1.0
depth (km)
Michigan Basin
Williston Basin
0
100
200
300
400
time since emplacement (m.y.)

Figure 4.13

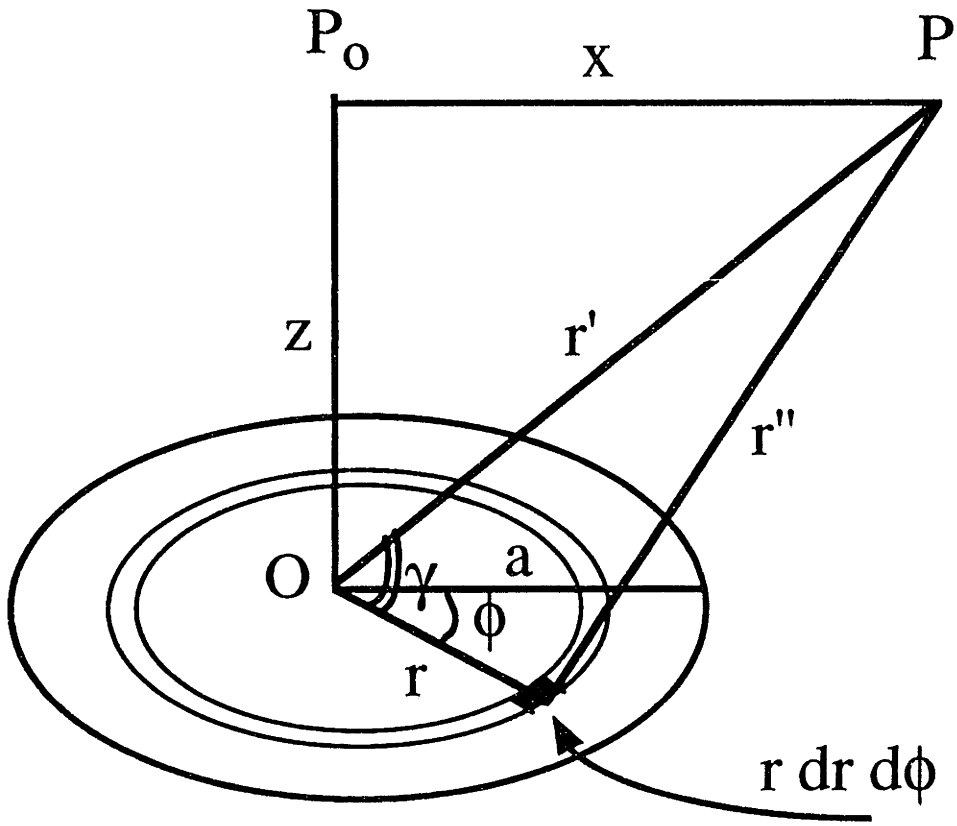

Figure A1

CHAPTER FIVE

SOME CONCLUSIONS REGARDING MANTLE UPWELLINGS (HOT SPOTS) BENEATH CONTINENTAL LITHOSPHERE

One of the main focuses of this thesis is how the continental lithosphere transforms the processes and forces of mantle dynamics into the geology and morphology we see at the surface. The main surface expression of mantle downwellings, subduction zones, is considered in the second chapter, which investigated how subduction of heterogeneous continental lithosphere may be different, both spatially and temporally, from subduction of the (relatively) homogenous oceanic lithosphere The surface expression of mantle upwellings, hot spots (or mantle plumes), is considered in chapters three and four and the combined results of these two studies suggest some general conclusion can be drawn about how mantle upwellings are transformed by continental lithosphere.

The present-day distribution of hot spots (Figure 5.1) suggests there is an important distinction between oceanic and continental lithosphere in determining where there is a surface expression of a mantle upwelling. Figure 1 shows two different compilations of present-day hot spot locations [*Sleep*, 1990, *Richards et al.*, 1988]. In both cases, the majority of hot spots are observed in the oceans; large areas of continental lithosphere, including all of Asia and South America, are completely devoid of hot spots. Continental hot spots are present, as demonstrated by Yellowstone and the African hot spots, but even when the greater surface area of oceanic lithosphere is accounted for, there is a notable deficit of continental hot spots. This deference toward surface manifestation of hot spots on oceanic lithosphere could be the result of two distinct processes depending on whether the distribution of hot spots is controlled by lower mantle dynamics or by plume interaction with the lithosphere. If lower mantle dynamics control the location of

hot spots, this preference of hot spots on oceanic lithosphere suggests the distribution of continental and oceanic lithosphere may be fundamentally controlled by (or a fundmental control on) lower mantle dynamics, as a connection between the lower mantle and the lithospheric plates must exist such that upwellings beneath the present-day location of continental lithosphere are minimized. (A second explanation for lower mantle control is possible, that the present-day distribution of continents fortuitously (and coincidently) matches the present day zone of upwellings within the lower mantle without any connection between the two distributions. This explanation requires a very large coincidence.) The alternative explanation, that it is differences between the continental and oceanic lithosphere itself that is causing the dearth of continental hot spots, is the assumption made in this chapter. With this assumption, the continental lithosphere is in effect "filtering out" mantle plumes to produce the observed deficit.

Some continental hot spots, however, do have a surface expression, so in at least some cases, the continental lithosphere does not completely filter out the effect of a mantle upwelling. I propose that there are two primary cases in which mantle plumes beneath continental lithosphere will not be completely filtered out, and thus will have a surface expression: 1) when the mantle plume is strong and 2) when the plume impinges on continental lithosphere that remains stable with respect to the hot spot frame of reference for an extended period of time. To support this hypothesis, this chapter will briefly present evidence for a modern hot spot and an ancient analog to the hot spot for both types of plume. Yellowstone is a classic example of a strong present-day plume beneath the continental lithosphere; it will be discussed in some detail first. Following Yellowstone, the track of the New England hot spot plume will be presented as an example of a strong continental hot spot plume in the geologic record. The African hot spots are an example of a the second class of continental hot spot, being located beneath continental lithosphere that paleoreconstructions show has been stable with respect to the hot spot frame of reference for at least 20 m.y. Finally, the intracratonic basins of North America, which,

as discussed in more detail in Chapter 4, all formed at roughly the same time and slightly after a time when little or no motion relative to the hot spot frame or reference is required by paleoreconstructions, will be discussed as an ancient analog the African hot spots.

We begin by considering the Yellowstone hot spot plume. The Yellowstone hot spot affords an excellent opportunity to compare the physical properties and observations of a strong mantle plume located beneath continental lithosphere with the physical properties and observations of a strong mantle plume located beneath oceanic lithosphere. As we shall see, in all the parameters compared here, Yellowstone is completely analogous to its oceanic counterparts, suggesting that there is no difference between the mantle plumes themselves.

As discussed in more detail in Chapter 3, Yellowstone has mainly been defined as a hot spot on the basis of its track of age-progressive volcanics; no "swell" feature in either the topography or the Bouguer gravity is apparent (Figure 3.1). There is, however, a large geoid anomaly (estimated between +8 and 12 meters) centered directly over Yellowstone (Figure 5.2), that, coupled with the volcanic age track in the opposite direction of plate motion, provides strong evidence for the presence of an active hot spot. The lack of observable topographic swell is due in large part to small scale pre-existing tectonic features unrelated to the hot spot rendering the long wavelength topographic uplift undetectable. By carefully considering and filtering out (or smoothing over) the tectonics feature of the Yellowstone region that precede the impingement of the hot spot plume, we can isolate the effect of the hot spot on the topography. As shown in Chapter 3, we find hot spot related uplift of about 1200 m elevation over a 400 km half-wavelength, the "swell" (Figure 3.2). Having isolated a topographic swell that can be ascribed to the hot spot, we can use a technique that essentially applies a pair of linear filters to the swell's wavelength and magnitude information to constrain the depth of compensation. For Yellowstone the depth of compensation is found to be 70 ± 10 km (see Figure 3.3).

We now have four physical properties that we ascribe directly to the mantle plume located at Yellowstone: a positive geoid anomaly (+8 m), a topography anomaly magnitude (+1200 m) and wavelength (400 km half-wavelength), and a depth of compensation (70 ± 10 km). We can compare these four properties of Yellowstone with the same properties of four strong oceanic hot spots, namely those located at Hawaii, the Marquesas, Cape Verde and Bermuda (Figure 5.3). These swells are listed in order of decreasing strength (as defined by their hot spot flux, discussed below), with the Cape Verde plume being approximately the same strength as the Yellowstone plume. As can be seen in Figure 5.3, in all four measured properties, the Yellowstone hot spot falls well within the range observed for oceanic swells, suggesting that the plume beneath Yellowstone is no different than other strong plumes located beneath oceanic lithosphere. Since this plume is no different than oceanic plumes, it may suggest that what is different (and causing the apparent lack of continental hot spots) is the continental lithosphere; and Yellowstone's surface expression is only detectable because the plume itself is strong. Alternatively, this similarity between the Yellowstone plume and oceanic plumes may suggest that the lithosphere beneath Yellowstone is more like oceanic lithosphere than cratonic continental lithosphere, possibly a result of the large amount of extension the western United States has undergone.

One way the strength of a hot spot plume can be quantified is through a property called the plume "buoyancy flux", or simply the hot spot flux. This is a quantity defined by *Sleep* [1990] that uses surface observables (such as shape and size of the hot spot swell) to determine the amount of anomalous buoyant material generated beneath the swell as a function of time. *Sleep* quantified the hot spot flux for 37 hot spots with the most easily isolated topographic swells (those shown in Figure 5.1a). Figure 5.4 shows a histogram of the distribution of hot spot flux. Hawaii is immediately obvious as a site of extreme hot spot flux, almost three times greater than the next strongest plume. The five hot spots of the Pacific Superswell (including the Marquesas) form then next group of

significantly stronger than average plumes. These six extremely strong plumes together account for 40% of the total generated hot spot flux. The remaining 31 plumes are divided into 4 bins by strength. Yellowstone is in the strongest remaining bin, which also includes Cape Verde and Bermuda. Thus, using hot spot flux as a measurement of plume strength, compared to the majority of present-day hot spots, Yellowstone is a strong plume, which may be why it is detectable even though located beneath continental lithosphere.

As a second example of a plume located beneath continental lithosphere that was strong enough to have a surface expression, consider the track of the New England hot spot (Figure 5.5). This plume, currently active today in the western Atlantic Ocean (located beneath the Corner Seamounts (Figure 5.5a), has a traceable continental track in the igneous intrusives beginning in the White Mountains and increasing in age through the Monteregian Hills, finally disappearing west of Montreal (Figure 5.5b). (See *Sleep*, [1990b] for a more detailed look at the chronologic evidence for a hot spot track in the igneous provinces.) Because this hot spot has both a continental and an oceanic track, we can determine the strength of the plume when it first appeared in the ocean (creating the Bear Mountain seamount) and use that strength as an estimate for the plume strength when it was last beneath the continent. From looking at how the subsidence of the ocean floor deviates from that of the predicted age-subsidence relationship [*Parsons and Sclater*, 1977], and ascribing that deviation to hot spot processes, *Sleep* found that the hot spot flux at the Bear Mountain seamount was 2 Mg/sec. This strength would make it the seventh strongest plume today (after Hawaii and the Superswell hot spots) if it were currently active at that strength. (In reality, the strength of the plume has decreased along its Atlantic track and its present day strength is among the weakest hot spots.) Thus, when the plume was first beneath the ocean, forming the Bear Seamount, and presumably just prior, when it was beneath continental New England and left a hot spot trace, the New England hot spot was a strong hot spot.

The second situation in which hot spots located beneath continental lithosphere may have a surface expression is when the continental craton has been stable with respect to the hot spot frame of reference for an extended period of time. The present-day example of this case is the hot spots beneath the African craton. At least three plumes (East Africa [*Ebinger et al.*, 1991], Dafur [*Crough*, 1982a], and Hoggar [*Crough*, 1982b]) beneath Africa have surface expressions, including topographic swells, geoid highs, anomalous volcanism and, in one case, continental rifting. That the African craton has been relatively stable with respect to the hot spot frame of reference is well established; computations of current plate motions relative to the hot spot frame of reference (Figure 5.6) [*Gripp and Gordan*, 1990] show small velocities across the majority of the African plate, and reconstructions of plate motions through the Cenozoic show little or no plate motion relative to the hot spot frame of reference for at least the last 20 m.y. [*Burke and Wilson*, 1972]. Thus, on the only craton that has been relatively stable with respect to the hot spot frame of reference, hot spots beneath the continental lithosphere have produce discernible surface expressions.

An example from the geologic record that may be the surface expression of hot spots beneath continental lithosphere that has been stable with respect to the hot spot frame of reference for an extended period of time is the intracratonic basins of North America. These four basins, the Williston, Michigan, Hudson Bay and Illinois Basins, are large, circular basins containing several kilometers of subsidence that all began subsiding at approximately the same time. As developed in more detail in Chapter 4, these basins may be the result of hot spot related injection of more dense suboceanic lithosphere into the less dense subcontinental lithosphere, which, when cooled, produces and excess mass that drives the basin subsidence.

As the gravity and flexural modeling in Chapter 4 shows, the subsurface mass beneath the Williston and Michigan Basins is a subcrustal load shaped like an inverted

cone. Such a geometry is similar to what would be expected if heated (buoyant) material rose through the lithosphere and pooled at the base of the crust (as it would not have enough buoyancy to penetrate the crust). The injected material may have been able to penetrate so high within the lithosphere because the lithosphere may have been at rest with respect to the injection source (the mantle plume) for an extended period of time. Paleo-reconstructions of the minimum velocity of the North American craton at the time in question (roughly 500 to 700 Ma) require almost no motion [*Ullrich and Van der Voo*, 1980] (Figure 5.7); suggesting that finding a 20 m.y. period of no absolute motion is not unreasonable.

Thus, the geologic record coupled with active geology suggests that hot spots may penetrate the continental lithosphere and have a surficial expression of either they are strong plumes (as demonstrated by the Yellowstone and the New England plumes) or if they formed when the continental craton is at rest with respect to the hot spot frame of reference for an extended period of time (as demonstrated by the African hot spots and may also be demonstrated by the intracratonic basins of North America). The hot spots that do penetrate and have a continental surface expression appear to be completely analogous to their oceanic counterparts, suggesting the plumes themselves are no different and the preferential distribution of hot spots on oceanic lithosphere (as compared to continental lithosphere) is a function of the lithosphere and not the plumes.

References

Burke, K. and J. T. Wilson, 1972, Is the African plate stationary?, *Nature*, **239**, 387-390.

Crough, S. T., 1981a, Free-air gravity over the Hoggar Massif, Northwest Africa: evidence for alteration of the lithosphere, *Tectonophysics*, **77**, 189-202.

Crough, S. T., 1981b, The Dafur Swell, Africa: gravity constraints on its isostatic compensation, *Geophys. Res. Lett.*, **8**, 877-879.

Ebinger, C. J., T. D. Bechtel, D. W. Forsyth, and C. O. Bowin, 1989, Effective elastic plate thickness beneath the East African and Afar plateaus and dynamic compensation of the uplifts, *J. Geophys. Res.*, **94**, 2883-2901.

Gripp, A. E. and R. G. Gordon, 1990, Current plate velocities related to hotspots incorporating the NUVEL-1 global plate motion model, *Geophys. Res. Lett.*, **17**, 1109-1112.

Parsons, B. and J. Sclater , 1977, An analysis of the variation of ocean floor bathymetry and heat flow with age, *J. Geophys. Res.*, **82**, 803-827.

Richards, M. A., B. H. Hager and N. H. Sleep, 1988, Dynamically supported geoid highs over hotspots: observations and theory, *J. Geophys. Res.*, **93**, 7690-7708.

Sleep, N. H, 1990a, Hotspots and mantle plumes: some phenomenology, J. *Geophys. Res.*, **95**, 6715-6736.

Sleep, N. H., 1990b, Montegerian hotspot track: a long-lived mantle plume, *J. Geophys. Res.*, **95**, 21,983-21990.

Ullrich, L. and R. Van der Voo, 1981, Minimum continental velocities with respect to the pole since the Archean, *Tectonophysics*, **74**, pp. 17-27.

FIGURE CAPTIONS

Figure 5.1: Global distribution of hot spot plumes, from two different compilations. a) after Sleep [1990a] b) after Richards et al. [1988]

Figure 5.2: Geoid anomaly over Yellowstone and surrounding area, contour inervals are 2 meters. A yellow dot locates the inferred current location of the Yellowstone hot spot plume.

Figure 5.3: Comparison of four physical properties of the Yellowstone hot spot (grey symbols) with the same physical properties measured at four different oceanic swells (black symbols), from left to right: Hawaii, the Marquesas, Cape Verde and Bermuda

Figure 5.4: Histogram of hot spot flux for the currently active hot spots.

Figure 5.5: After Sleep, [1990b], oceanic (a) and continental (b) track of the New England seamont plume. Striped area of (b) is area of anomalous igneous activity. Large plutons are shown in black

Figure 5.6: Current plate motions in the hot spot frame of reference, from the NUVEL-HS2 model (bold arrows) and the RM2 model (plain arrows). After Gripp and Gordan, [1990]. The African plate is outlined.

Figure 5.7: Mimimum required plate velocites throughout the Paleozoic and Proterozoic for the North American craton. Bold ticks delineate the time of interest, the period from .5 to .8 b.y.

Hotspot Distribution

(from Sleep, 1990)

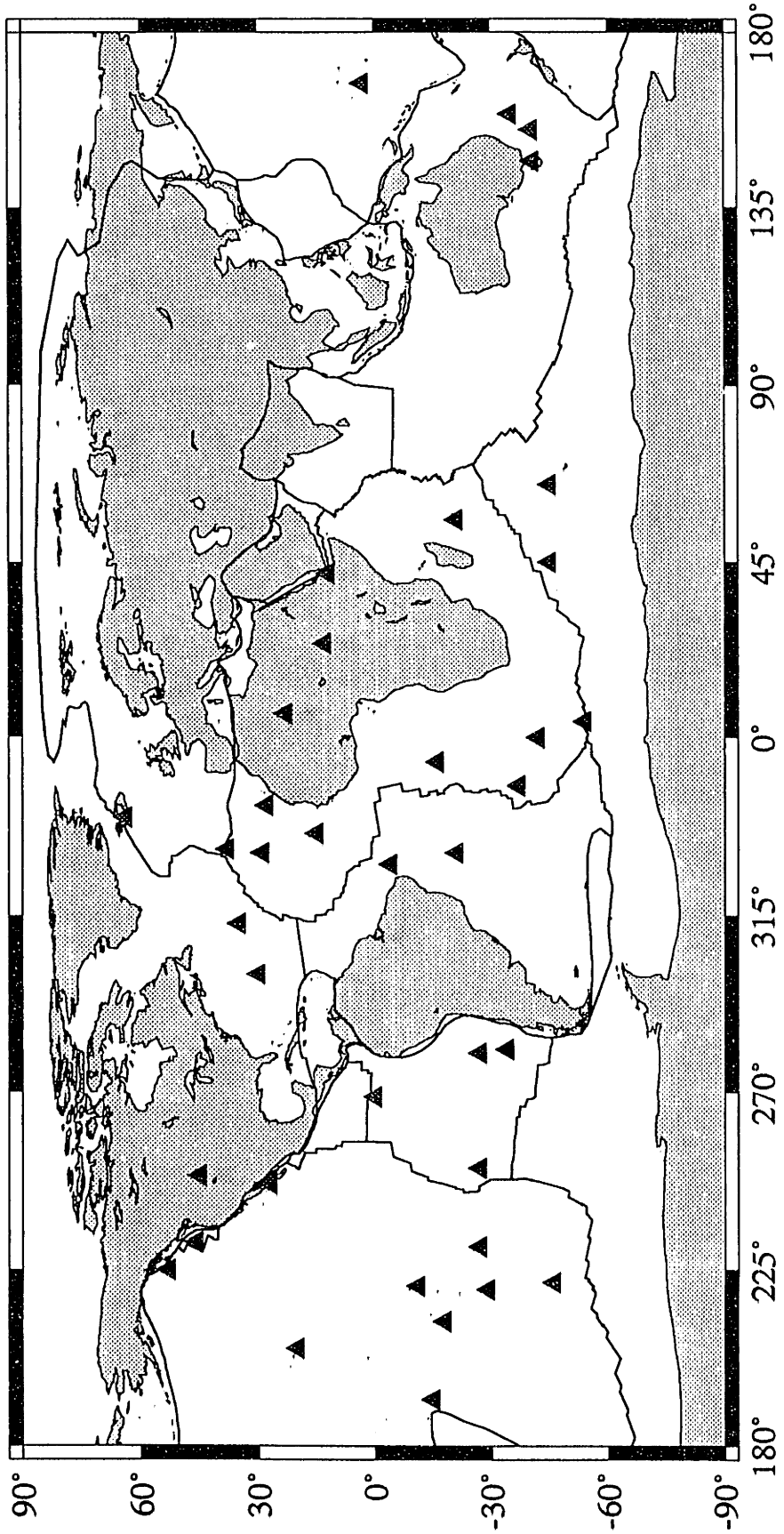

Figure 5.1a

Hotspot Distribution

(from Richards et al. 1988)

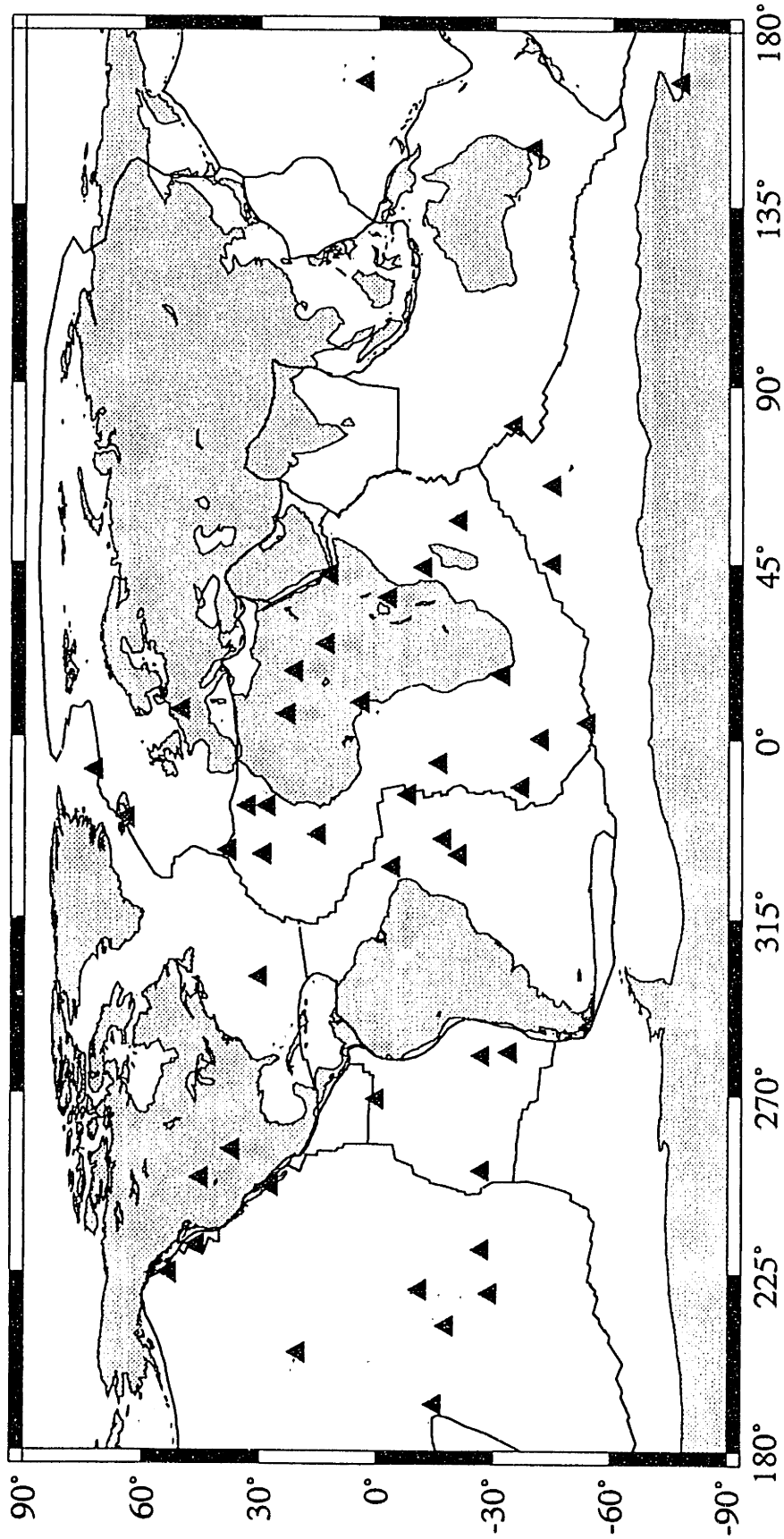

Figure 5.1b

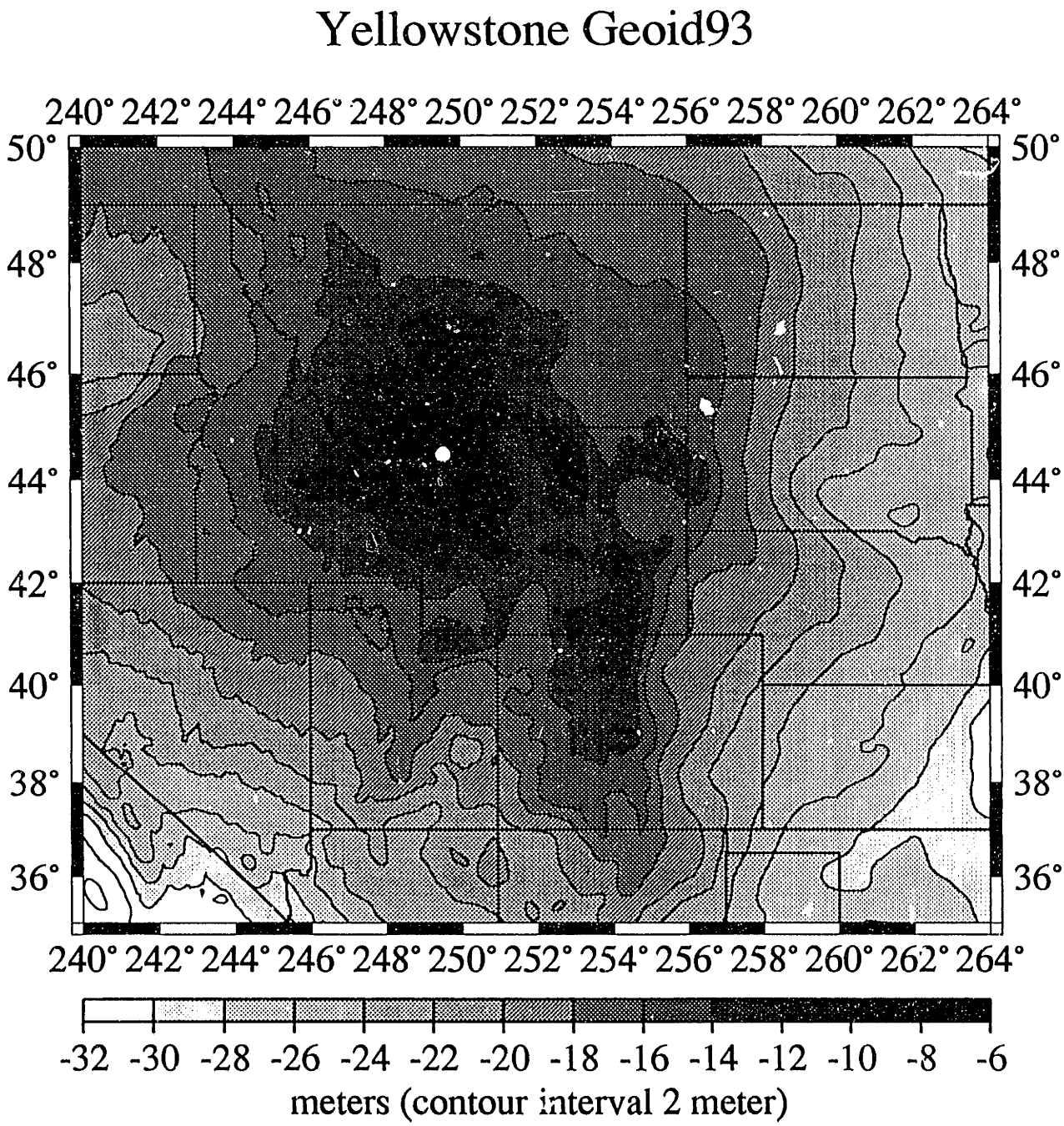
Yellowstone Geoid93
240° 242° 244° 246° 248° 250° 252° 254° 256° 258° 260° 262° 264°
50°
48°
46°
44°
42°
40°
38°
36°
-32 -30 -28 -26 -24 -22 -20 -18 -16 -14 -12 -10 -8 -6
meters (contour interval 2 meter)

Figure 5.2

Yellowstone vs. Oceanic Swells
Depth of Compensation (km)
Swell Half-Wavelength (km)
Geoid Anomaly (m)
Topographic Anomaly (m)
Hawaii
Marquesas
Yellowstone
Cape Verde
Bermuda
0
20
40
60
80
100
0
200
400
600
800
1000
1200
0
3
6
9
12
15
0
500
1000
1500
2000
2500

Figure 5.3

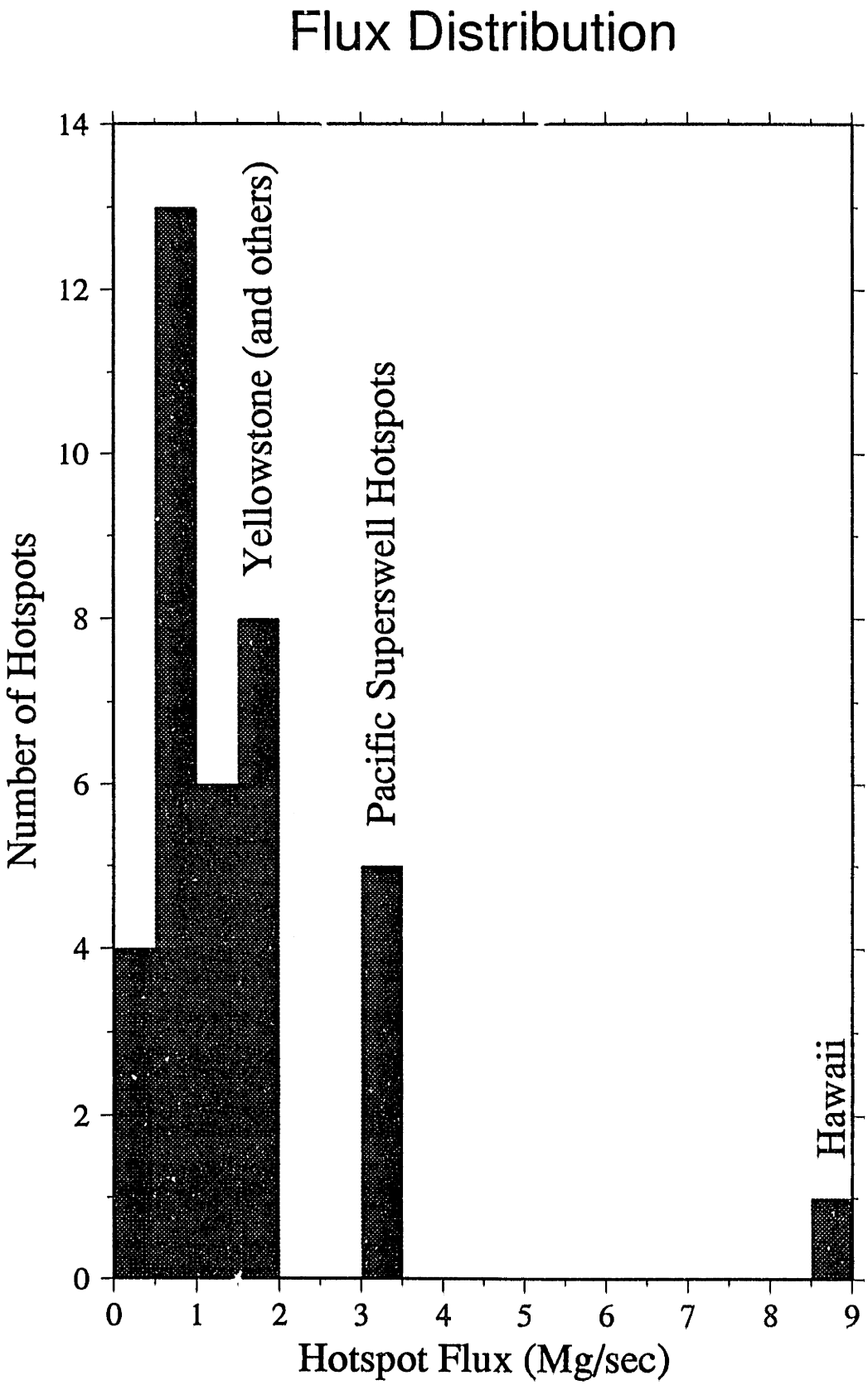
Flux Distribution
Number of Hotspots
Hotspot Flux (Mg/sec)
Yellowstone (and others)
Pacific Superswell Hotspots
Hawaii
0
2
4
6
8
10
12
14
0
1
2
3
4
5
6
7
8
9

Figure 5.4

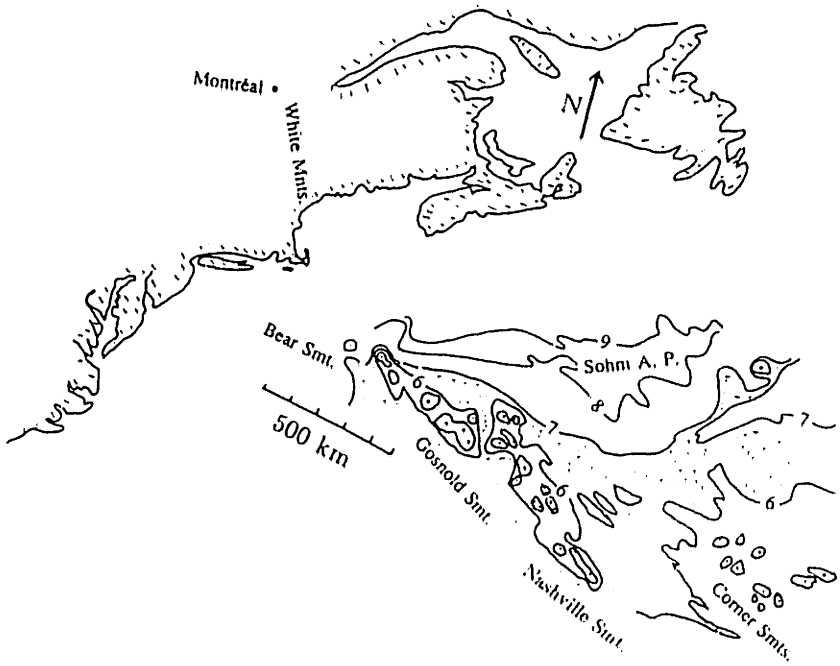
Montréal
White Mnts.
N
Bear Smt.
500 km
Gosnold Smt.
Sohm A. P.
9
8
7
6
Nashville Smt.
Comer Smts.

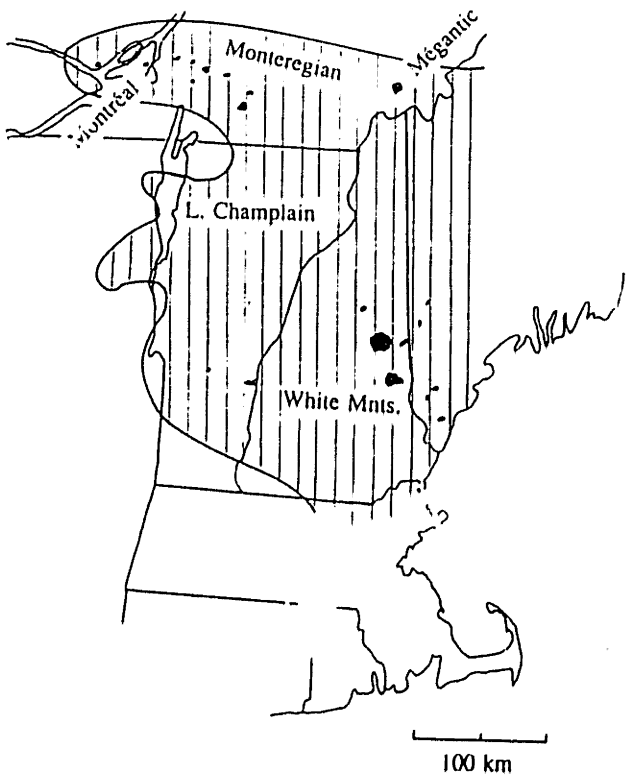
Monteregian
Mégantic
Montréal
L. Champlain
White Mnts.
100 km

Figure 5.5

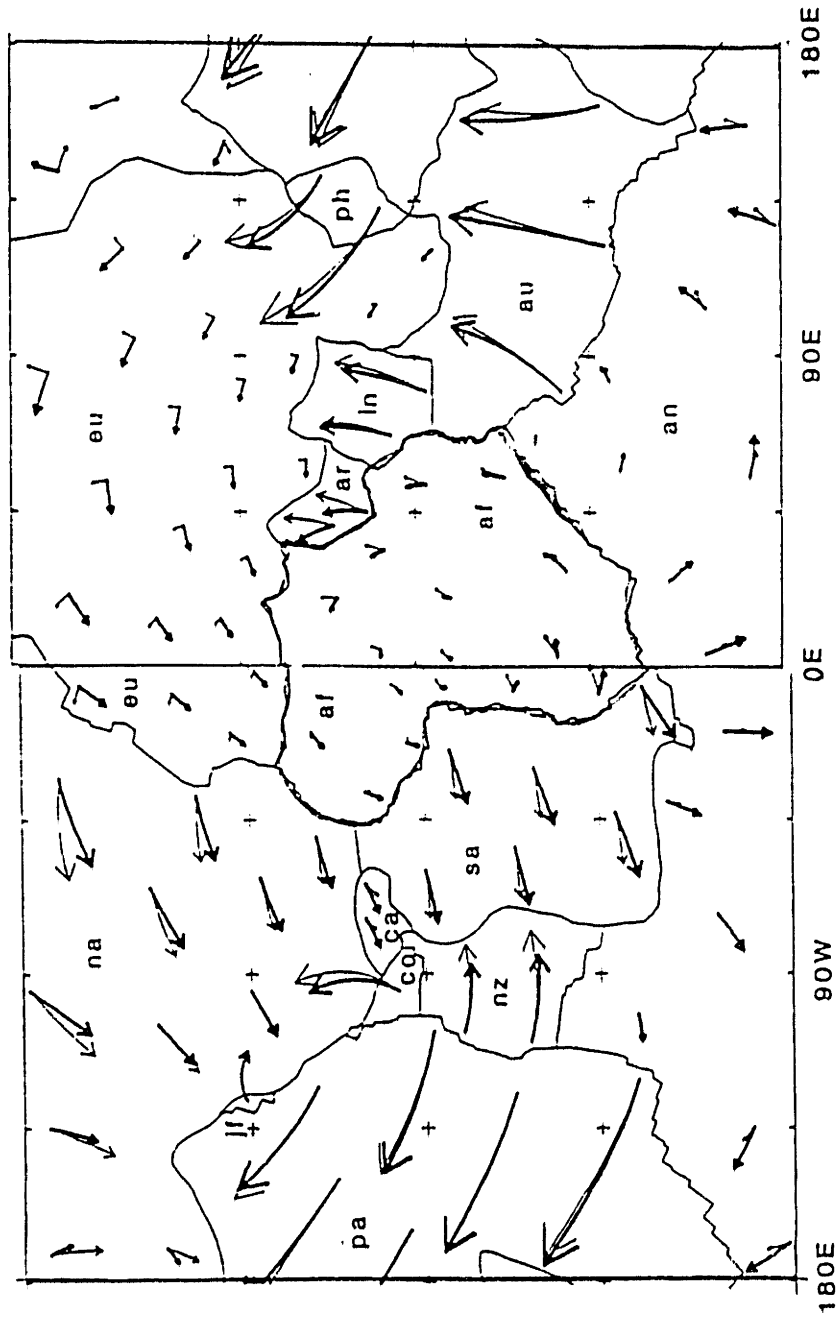

Figure 5.6

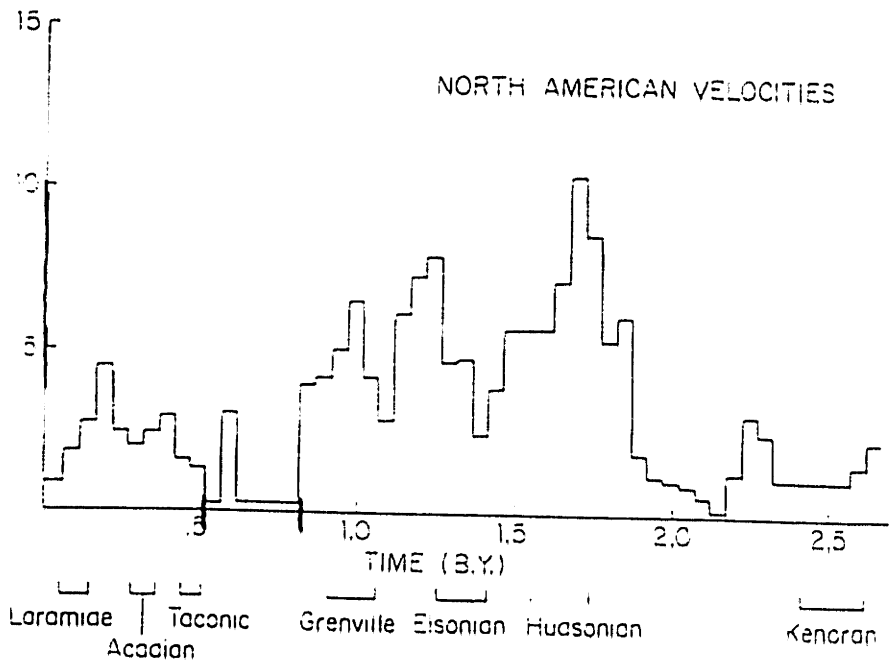
15
NORTH AMERICAN VELOCITIES
1.0
1.5
2.0
2.5
TIME (B.Y.)
Laramide
Acadian
Taconic
Grenville
Elsonian
Hudsonian
Kenoran

Figure 5.7